THE UNIVERSITY *of* EDINBURGH

Trace Element Incorporation in Silicate Melts and Glasses at High Pressure

Charlotte J. L. de Grouchy

Doctor of Philosophy
The University of Edinburgh
22nd August 2016

Abstract

Trace elements are highly fractionated during large-scale melting associated with planetary differentiation events. The resulting partition coefficients are used to constrain a range of geological processes and are known to be influenced by pressure, temperature, and compositional changes in crystalline structures. Although recent studies have shown that melt compositional changes affect the partitioning of trace elements, the degree to which these ratios are influenced by alterations in the melt structure, especially with increasing pressure, is poorly constrained due to the difficulty of collecting structural information on bonding environments *in situ*. A basic understanding of how these elements are incorporated in silicate melts is critical to interpreting early planetary differentiation and crust forming events. This thesis presents results from both x-ray diffraction and absorption techniques on trace element (Y, Zr, Lu and Nd) incorporation in silicate melt structures. The structure of two rare Earth element doped model end member silicate liquids, a highly polymerised haplogranite (Si-Al-Na-K-O) and a less polymerised anorthite-diopside (Si-Al-Mg-Ca-O), have been studied. The results are the first to identify trace rare Earth element (REE) incorporation in silicate melts at high pressure using x-ray diffraction techniques.

The local melt structure around Y and Zr in a highly polymerised haplogranite has been studied using x-ray absorption spectroscopy up to 8 GPa and 1650 K. Both elements appear to adopt 8-fold coordination within the melt structure with no variation over the pressure range studied. This was also found for the Lu bonding environment in the same composition where the coordination number of Lu-O was found to be 8, with a bond distance $r_{\mathrm{Lu-O}} = 2.36$ Å in the haplogranite melt. At low pressures, < 5 GPa, the bonding environment of Lu-O was found to be dependent on composition with coordination decreasing to $CN_{\mathrm{Lu-O}} = 6$ and $r_{\mathrm{Lu-O}} = 2.29$ Å in the anorthite-diopside melt. This compositional variance in coordination number at low pressure is consistent with observations made for

Y-O in glasses at ambient conditions and is coincident with a dramatic increase in the partition coefficients previously observed for rare Earth elements (REE) with increasing melt polymerisation. However, an abrupt change in both Lu-O coordination and bond distance is observed at 5 GPa in the anorthite-diopside melt, with $CN_{\mathrm{Lu-O}}$ increasing from 6 to 8-fold and $r_{\mathrm{Lu-O}}$ from 2.29 to 2.39 Å. This occurs over a similar pressure range where a reduction in the reported heavy REE partition coefficients is observed.

X-ray diffraction experiments up to 60 GPa and 2000 K have also been performed on the incorporation of the larger light REE, Nd, in basaltic-like melts. The results presented show that incorporation within the anorthite-diopside composition is dependent on the size of the REE. Nd-O initially shows the same 6-fold coordination as Lu-O at ambient conditions, although the change to 8-fold coordination appears to occur at considerably lower pressure between 1-2 GPa. Coordination change in both cases can be attributed to collapse of the silicate network and an increase in the average number of available 'crystal like' sites in the liquid, with ionic radius of the REE controlling at which pressure the preference for these sites in the melt occurs. Published mineral-melt partition coefficients for Nd, with major mineral phases such as garnet, show very little variation with pressure, in contrast to Lu. The difference in structural incorporation of Lu and Nd in the melts presented in this thesis could explain this partitioning behaviour.

Overall this thesis highlights that important structural changes of the trace element bonding environment in silicate melts occur with both compositional variation and pressure. Melt structural changes with pressure cannot be neglected in predictive models of trace element behaviour, and using a single melt term to normalise the effects of melt on trace element partitioning will not accurately predict partitioning behaviour at depth during magma formation or differentiation.

Lay Summary

Melting processes within the Earth generate molten silicates that have produced crustal rocks since the formation of the Earth, and act as the main conduits for element transport between the mantle, crust and atmosphere. Understanding the structures of molten silicates therefore provides important insight into crust formation and mantle evolution through time. As melting occurs from a predominantly solid mantle, elements are partitioned between the crystal and melt phases. Elements at very low concentrations in the mantle, called trace elements, produce distinctive partitioning ratios. These ratios are used to understand many geochemical processes including how and when the first crust on Earth was formed, as well as assessing the depth of modern day melting in volcanic systems. In order to understand how these trace element ratios can be interpreted, knowledge of both the crystal and melt structures of the phases involved at the conditions of melt formation (high pressure and temperature) is important in order to predict how other elements might behave within mineral-melt systems.

In this work, silicates are studied in their molten state at high pressure by compressing small samples between specialised anvils to create pressures found deep inside the Earth, and melting is generated by laser and resistive heating techniques. The internal structure of the melt is probed using intense x-rays generated at synchrotron facilities. This study focuses on the local environment of some trace elements (Lu, Nd, Y and Zr) within the silicate melt structure, and how this local structure changes with pressure within silica-rich and silica-poor melts. Changes within the trace element local environment are observed at high pressure in the silica-poor compositions, and the different behaviour of trace elements between the various compositions is observed.

Declaration

I declare that this thesis was composed by myself, that the work contained herein is my own except where explicitly stated otherwise in the text, and that this work has not been submitted for any other degree or professional qualification except as specified.

Parts of this work have been published in [1].

(*Charlotte J. L. de Grouchy, 22nd August 2016*)

Acknowledgements

This PhD thesis could not have been completed without the support and encouragement of many different people and although there isn't space to name them all here I hope they know who they are and how much their friendship has meant to me. I would like to thank my PhD supervisor Chrystèle Sanloup for all her guidance, support and enthusiasm for this project, for always being there but also teaching me the importance of becoming an independent researcher. Without her training in high pressure techniques I would not have been able to carry out this work. I would also like to thank the rest of the research group, James, Holly, and Ben, for many scientific discussions and friendly chats, especially during some very late nights on experiments.

My thanks go to all the beamline scientists at central facilities who have helped with this work: Dominik Daisenberger (I-15 Diamond Light Source), Yosio Kono (HP-CAT, Advanced Photon Source), Clemens Prescher (formally at the Advanced Photon Source), Innokenty Kantor (formally at the European Synchrotron Radiation Facility) and Nicolas Guignot (PSICHE, Soleil). Without whom I wouldn't have learnt many of the things necessary to complete this thesis.

I would like to thank the Condensed Matter Centre for Doctoral Training (CM-CDT) for financial funding of this project, and the opportunity to meet new people from across the CM-CDT. Particularly Carole who became my writing buddy, and without our many days sitting in various coffee shops this thesis would still be unwritten. Thank you to all of the friends I have made in Edinburgh, particularly my office mates, who have always been there through the good and bad with hugs and a glass of wine, you are all amazing.

A huge thank you to my family for their love, support, and encouragement to pursue my heart and strive for new things, and for always being there when things don't go to plan. And lastly, but by no means least, I thank with all my heart my fiancé Geoff without whom I could not have made it through the last four years. Thank you for always being there, supporting and encouraging me when I doubted myself, never failing to give me the confidence to carry on, and putting up with me while I wrote this thesis!

Funding Acknowledgements

This thesis was supported by the Engineering and Physical Sciences Research Council (EPSRC) with PhD studentship funding from the Condensed Matter Doctoral Training Centre (CM-CDT) under grant number EP/G03673X/1. This work was also in part supported by the European Research Council under the European Community's Seventh Framework Programme (FP7/20072013 Grant Agreement No. 259649 to Chrystèle Sanloup).

Portions of work in Chapter 8 were performed at GeoSoilEnviroCARS (The University of Chicago, Sector 13), Advanced Photon Source (APS), Argonne National Laboratory. GeoSoilEnviroCARS is supported by the National Science Foundation - Earth Sciences (EAR-1128799) and Department of Energy-GeoSciences (DE-FG02-94ER14466). Portions of work in Chapters 5, 7 and 8 were performed at HPCAT (Sector 16), Advanced Photon Source (APS), Argonne National Laboratory. HPCAT operations are supported by DOE-NNSA under Award No. DE-NA0001974 and DOE-BES under Award No. DE-FG02-99ER45775, with partial instrumentation funding by NSF. Both the above research experiments used resources of the Advanced Photon Source, a U.S. Department of Energy (DOE) Office of Science User Facility operated for the DOE Office of Science by Argonne National Laboratory under Contract No. DE-AC02-06CH11357.

We thank Diamond Light Source for access to beamline I-15 (EE9022) that contributed to the results presented here in Chapters 5 and 7. We acknowledge the European Synchrotron Radiation Facility (ESRF) for provision of synchrotron radiation facilities and the use of beamline BM-23. Results collected from ESRF during ES189 are presented in Chapter 6. We acknowledge SOLEIL for provision of synchrotron radiation facilities during experiment 20130198 which are presented in Chapter 5.

Glossary of Abbreviated Terms

AnD $Anorthite_{36}$-$Diopside_{64}$

BE Boron-epoxy

CN Coordination number

DAC Diamond anvil cell

EDXD Energy dispersive x-ray diffraction

EXAFS Extended x-ray absorption spectroscopy fine-structure

G(r) Radial distribution function

HPG Hapologranite

HREE Heavy rare Earth elements

LH-DAC Laser heated diamond anvil cell

LREE Light rare Earth elements

MD Molecular dynamics

P Pressure

PEP Paris-Edinburgh press

Q/k Momentum vector in reciprocal space (Q convention in XRD, k convention in EXAFS)

r/R Interatomic distance in real space (r convention in XRD, R convention in EXAFS)

REE Rare Earth elements

rh-DACs Resistively heated diamond anvil cells

S(Q) Structure factor

T Temperature

TC Thermocouple

XAS X-ray absorption spectroscopy

XANES X-ray absorption near edge structure

XRD X-ray diffraction

Contents

List of Figures

List of Tables

Chapter 1

Introduction

1.1 Silicate Melts at High Pressure and Temperature

Silicate melts have had an important role in geological processes since the formation of the Earth. Although the Earth is predominantly made up of solid silicate mantle (84% by volume), melting processes are the cause of volcanic activity and subsequent crust formation, as well as the transport and recycling of elements out of and within the mantle. During the formation of the Earth it is thought that heavy bombardment by meteorites and decay of short-lived isotopes (Fe and Al) could have caused the Earth to have been extensively molten during planetary differentiation. These melting processes have left distinctive trace element partitioning signatures within the core, mantle and crust that are used to interpret early differentiation and crust forming events [2]. Silicate melts are dominantly comprised of Si, O, Al, Mg, Ca, and Fe (Table 1.1) and are formed in the present day during partial melting and fractional crystallisation. Melting can be caused via a number of mechanisms, including adiabatic melting (Figure 1.1B), increasing the mantle temperature via the addition of hot material (Figure 1.1C), or lowering of the solidus by the addition of volatiles (Figure 1.1D). Magma is most commonly produced at mid-ocean ridge and subduction margins and two end member compositions can be used to describe most melting processes (Table 1.1). These are: (1) Basaltic, which is the most common melt composition representing the first stages of melting of an olivine-rich mantle. Basaltic melts

Composition	SiO_2	Al_2O_3	Na_2O	K_2O	TiO_2	FeO	MgO	CaO
Basaltic melts	45-52	12-18	3-4	<1	1-2	3-8	4-7	9-11
Granitic melts	70-77	11-13	3-5	3-5	<1	2-3	< 1	∼1

Table 1.1 *Oxide compositions in weight % for typical end member melt compositions [3].*

are low in silica and form oceanic crust. (2) Granitic melts which represent the last stages of fractional crystallisation or re-melting of existing crust. These are silica rich as SiO_2 is concentrated in the melt phase during crystallisation.

Partial melting is thought to occur at distinctive locations within the mantle (Figure 1.2), predominantly at depths <5 GPa during crustal formation, but also at boundary layers, such as below the crust, at 410 km at the top of the transition zone [5], at the 660 km discontinuity [3, 6], and potentially at the core-mantle boundary [7, 8] (Figure 1.2). As these melts are fluids, they are one of the main sources of bulk transport for elements between the core, mantle, crust and atmosphere and therefore it is important to understand how the properties of these melts behave at the conditions at which they form. Most present day melts are formed at temperatures between 1200-1800°C (unless volatiles are present), and at lower pressures (<5 GPa) [3]. However, during planetary formation these melts may have occurred across a much more extensive range, particularly down to the base of the upper mantle at 25 GPa (see original reference for magma ocean theory [9] to review by [10]).

In order to study the *in situ* properties of silicate melts, access to high pressure (P) and temperature (T) conditions is required. This neccesitates the use of specialised experimental techniques, including diamond anvil cells (DAC) and large volume presses. Pressure is obtained by compressing the sample (loaded into a deformable gasket) between anvils which may be made from tungsten carbide, diamond, or other hard materials. The conditions which can be generated are limited by the material and size of the anvils but typically ranges from 1-30 GPa for large volume press experiments [11], and up to 400 GPa for DAC at ambient temperature [12]. X-ray diffraction can then be used to determine the structure of materials under these conditions and for over 10 years this has been a common technique for studying silicate liquids (see initial study by [13] to the current highest $P - T$ range by [14]), although studies are still more common on silicate glasses recovered to ambient conditions due to the difficulties

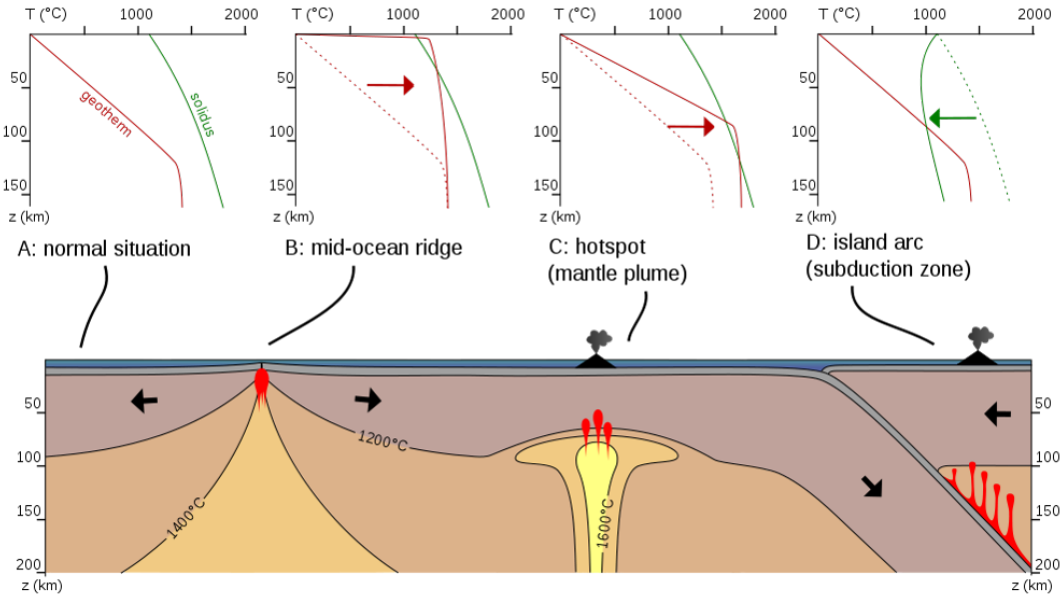

Figure 1.1 *Schematic figure of the crust, upper mantle solidus temperatures and the geotherm. A: Normal geotherm and solidus temperatures for typical crust. B: Adiabatic melting where geotherm temperature exceeds the solidus due to crustal thinning at mid-ocean ridge settings. C: Melting due to upwelling of hot material. D: Melting caused by the influence of volatiles, such as water, lowering the mantle solidus temperature locally. From [4].*

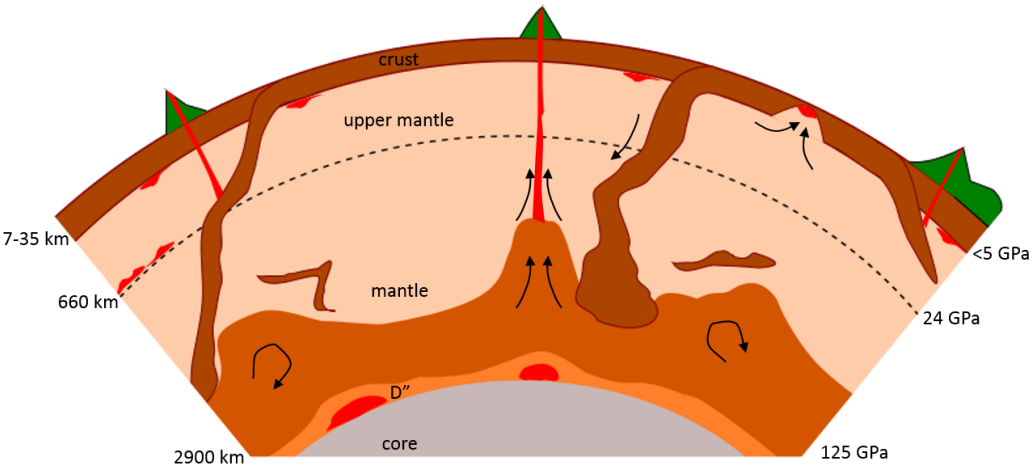

Figure 1.2 *Schematic figure representing the possible basic structure of the crust and upper mantle of the Earth including depths and subsequent pressures in GPa. Locations of suggested partial melting regions are shown in red.*

of obtaining high enough signal intensity on liquids, and maintaining stable high $P-T$ conditions. Recent shock measurements can also access melting at high $P-T$ (5-130 GPa and >1700 K for silicates in [15]), although limitations in the Q-range and signal intensity prevent elements at low concentrations from being defined. To obtain necessary signal intensity, intense x-ray sources are required with a suitable wavelength only possible at certain synchrotron sources. By using these sources, x-ray diffraction has been used to identify interesting changes in both the glass and melt structures of silicates at high pressure [14, 16–20].

1.2 Trace Elements

Trace elements have long been used to determine and trace different geological processes through time. These include, dating early crust formation, understanding the $P-T$ conditions of melting and crystallisation, and tracking the movement and recycling of elements and minerals through the core, mantle and crust [21, 22]. Trace elements, particularly rare Earth elements (REE), are of use to the geochemical community because of their distinctive partitioning due to their atomic radii and charge. REE of the lanthanide series, which are generally 3+ in charge, undergo radial contraction with increasing atomic number which results in distinctive partitioning trends (see Chapter 2.2 for further details). A long standing controversy that is regularly addressed with trace element partitioning data is that of the chondritic Earth. This debate surrounds whether the composition of the bulk silicate Earth differs from that of chondrites, and how to explain discrepancies between trace element ratios. The key trace element pairs used to propose theories surrounding this are predominantly Lu/Hf and Nd/Sm [2, 23–26]. Another use of Lu and Hf isotopes is for dating early Earth crust formation [27–30]. Trace elements are particularly useful as they do not influence chemical reactions of the system and have distinctive partitioning behaviours in mineral/melt systems depending on the conditions of melting. Partitioning studies both at ambient and high pressure have identified that the melt composition can strongly influence partitioning ratios, and therefore that structural changes within melts must influence trace element behaviour [31–37]. However, there is little understanding on why these changes in partitioning occur, and how they are influenced by changes in the structure of melts at high $P-T$. Understanding the incorporation of trace elements into melt structures and the influence on partitioning is, therefore, critical for the interpretation of

their behaviour during Earth formation and other geological events.

As most structural studies on the incorporation of trace elements in silicates have been made at ambient pressure, the influence of pressure on the melt structure and subsequent trace element incorporation is poorly understood. It is well known that major elements within silicate melts undergo coordination changes with pressure [14, 16, 20, 38] and this thesis aims to understand how REE are incorporated into silicate melt structures, and the influence of pressure on their behaviour. By understanding this behaviour, further information can be incorporated in models to predict how trace elements behave at extreme conditions. Experimental studies that have previously aimed to unravel REE incorporation in silicate melts have focused predominantly on ambient pressure glasses using x-ray absorption techniques [39–41]. This method is limited by reliance on models based on reference compounds, and it can only provide information on the local structure around a specific trace element rather than the overall silicate network. This thesis explores the structures of representative end-member compositions of silicate melts *in situ* at their conditions of formation and shows the development of the use of x-ray absorption and diffraction, including both angle and energy dispersive techniques, in the identification of rare Earth elements within melt structures. The compositions chosen represent model end members for the first and last stages of present day melting in order to understand how the basic properties of silica-rich and silica-poor melts influence trace element incorporation. This thesis presents the first work of its kind to identify trace elements directly in a silicate liquid structure at high pressure using x-ray diffraction.

1.3 Thesis Outline

There are nine chapters in this thesis following this introduction. Three of these introduce the background, concepts, data treatment and instrumentation used or developed for this study. Four contain new data collected and analysed to further the fundamental understanding of this research topic, and a final conclusion and discussion of possible future work is presented. An outline of each chapter is given below:

Chapter 2) Silicate Liquids and Glasses. This chapter provides a background for the motivation behind this study and the importance of trace

elements in a geological context. It introduces what is currently understood about the structure of silicate melts, and covers current understanding and knowledge of how trace elements behave and what is required to improve current partitioning models.

Chapter 3) A Review of Structural Probes for Liquids and Glasses. The theories of x-ray diffraction and absorption that are used in this study are covered, and the formalisms that will be mentioned throughout this thesis are described. The specific use of x-ray diffraction to probe liquid structures is also described.

Chapter 4) Instrumentation and Data Treatment. The instrumentation required to carry out the experimental work in this thesis is detailed in this chapter, including all high pressure-temperature techniques and the synchrotron sources used. This chapter is a combination of existing techniques that are well established and the development work completed in this thesis to improve existing methods for data collection on silicate liquids. A description of the data analysis process and methodology used in the results chapters is also given.

Chapter 5) An X-ray Diffraction Study of Haplogranitic Melts. These results present the structure of haplogranitic (HPG) melts and glasses up to 12 GPa using x-ray diffraction. This includes identification of the first nearest neighbour distances up to 3 Å including Si-O and the possible change in Al-O coordination. The influence of water on the structure is discussed as well as the implications for medium range order and the compressibility of silica-rich liquids compared to their glasses at the same pressure.

Chapter 6) Trace Elements in Haplogranitic Melts Using X-ray Absorption. X-ray absorption techniques are used to study the incorporation of Br, Y and Zr within the haplogranite melt structure up to 8 GPa. Work presented on Br was completed by both the author and Dr. Benjamin Cochain as a preliminary study on trace element incorporation in silicate liquids. This resulted in the publication of 'Bromine speciation in hydrous silicate melts at high pressure' [1] which is presented in Publications at the end of this thesis. Results on Y and Zr present the local structure of these elements within the HPG, and Y is used as a proxy for Lu incorporation which is discussed in Chapter 7.

Chapter 7) Structure of Lutetium-doped Melts and Glasses. The first data on trace element incorporation in silicate melts at high pressure using x-ray diffraction techniques is presented. The structural incorporation of Lu in end

member (basaltic and granitic-like) melts is discussed, including coordination and bond distances of Lu-O up to 6 GPa (granitic melts) and 8 GPa (basaltic-like melts). This chapter shows the difference between Lu incorporation in silicate melts with varying degrees of polymerisation and the influence of pressure on the structural incorporation of heavy rare Earth elements.

Chapter 8) Structure of Neodymium-doped Melts and Glasses. These results present the local environment of Nd within the basaltic-like melt introduced in Chapter 7. Structural data were collected up to 35 GPa in the liquid and 60 GPa in the glass using laser heated diamond anvil cells. The results show that there is differing behaviour of Nd, a light rare Earth element, compared to Lu in de-polymerised melt structures.

Chapter 9) Conclusions and Future Work. The conclusions of this thesis are presented with the overall implications of the results summarised. Ideas for further study on this topic that could be developed based on the work presented in this thesis are discussed.

Chapter 2

Silicate Liquids and Glasses

Silicate glasses and melts have unique structural and chemical characteristics compared to their crystalline counterparts, and it is the structure of these melts that determines their physical properties, such as viscosity and density, as well as their incorporation of different elements. The physical and chemical properties of glasses are known to vary with chemical composition, or increasing temperature and pressure [42, 43], such as observed in silica glass where the Si-O bond length and Si coordination increase between 20-35 GPa [16]. This has also been observed within the melt at 15-35 GPa, and for other cations such as Fe in basaltic melt compositions [14, 19]. In order to understand the properties of silicate liquids, their structures at the conditions of magma formation at depth must be understood. Although a limited amount of information exists for silicate melt structures due to the difficulties presented by *in situ* data collection, structural studies on glasses provide a starting picture of the silicate network.

2.1 Amorphous Silicate Structures

The non-crystalline nature of silicate glasses and melts means there is no long-range periodicity; however, silicate glass and liquid networks do have a short and medium range order [44] due to the network forming nature of components. In order to interpret structural measurements made by x-ray diffraction and absorption some understanding of silicate melt structures is required. The basic unit of any silicate glass or liquid is the silica tetrahedron [42]. These consist

of four oxygens surrounding one silicon atom, producing a unit of SiO_4^{4-} (Figure 2.1C). These tetrahedra behave as relatively rigid units within the structure and can covalently link into polymerised networks by sharing oxygens (Figure 2.1). In crystalline SiO_2 and silicate minerals these tetrahedra link to form chains, rings, sheets, and a variety of 3D networks [45]. The oxygens that share corners with two adjacent tetrahedra are described as 'bridging' oxygens, and those that are not involved in bonding between tetrahedra are known as 'non-bridging'. In silicate glasses and melts the general structure is determined by the nature of the silicate network which depends on the silica content of the melt [42]. As a glass or melt can inherently be more disordered than a crystal, this network has greater flexibility and ring structures can be formed in a variety of sizes, from highly polymerised interconnected networks to predominantly separate SiO_4^{4-} and $Si_2O_7^{6-}$ units (Figure 2.1A) [46].

In amorphous SiO_2 the 2D network has been visualised by tunneling electron microscopy [47] and can be seen to be a completely interconnected polymerised network of tetrahedra (Figure 2.2). These tetrahedra form 'cages' (or 'rings' in two-dimensions) within the structure depending on the number of tetrahedra involved in each ring and how connected they are. In crystalline SiO_2 these rings are nearly always 6-member; however in the glass and melt these range from 4-10 membered [47] (Figure 2.2), with the most common ring size of between 5-8 members [46] (Figure 2.1B). These rings produce voids of varying size with much less regularity than that of crystalline structures. Six-member rings tend to be of a diameter of the order $\sim$2.2 Å and >8-membered rings could have diameters >5 Å [47]; the size of these rings is likely to determine which other atoms present in the structure can be accommodated within them. In a lower silica content melt the tetrahedra are less interconnected and voids are present in the structure that are not completely enclosed by the network tetrahedra (Figure 2.1A).

Natural silicate melts contain electro-positive elements (Na, K, Ca, Mg, Fe etc.) which modify the silicate network from the basic SiO_2 model. These network modifiers can produce non-bridging oxygens by breaking the polymerised network due to their large atomic radius and positive charge. These atoms are also thought to be accommodated within the rings and between polymerised chains in silica rich networks but are more easily accommodated within the lower silica content melts due to the higher number of non-bridging oxygens. Some 4+ cations such as Ti can act as network modifiers and network formers by replacing Si^{4+} in the network [48].

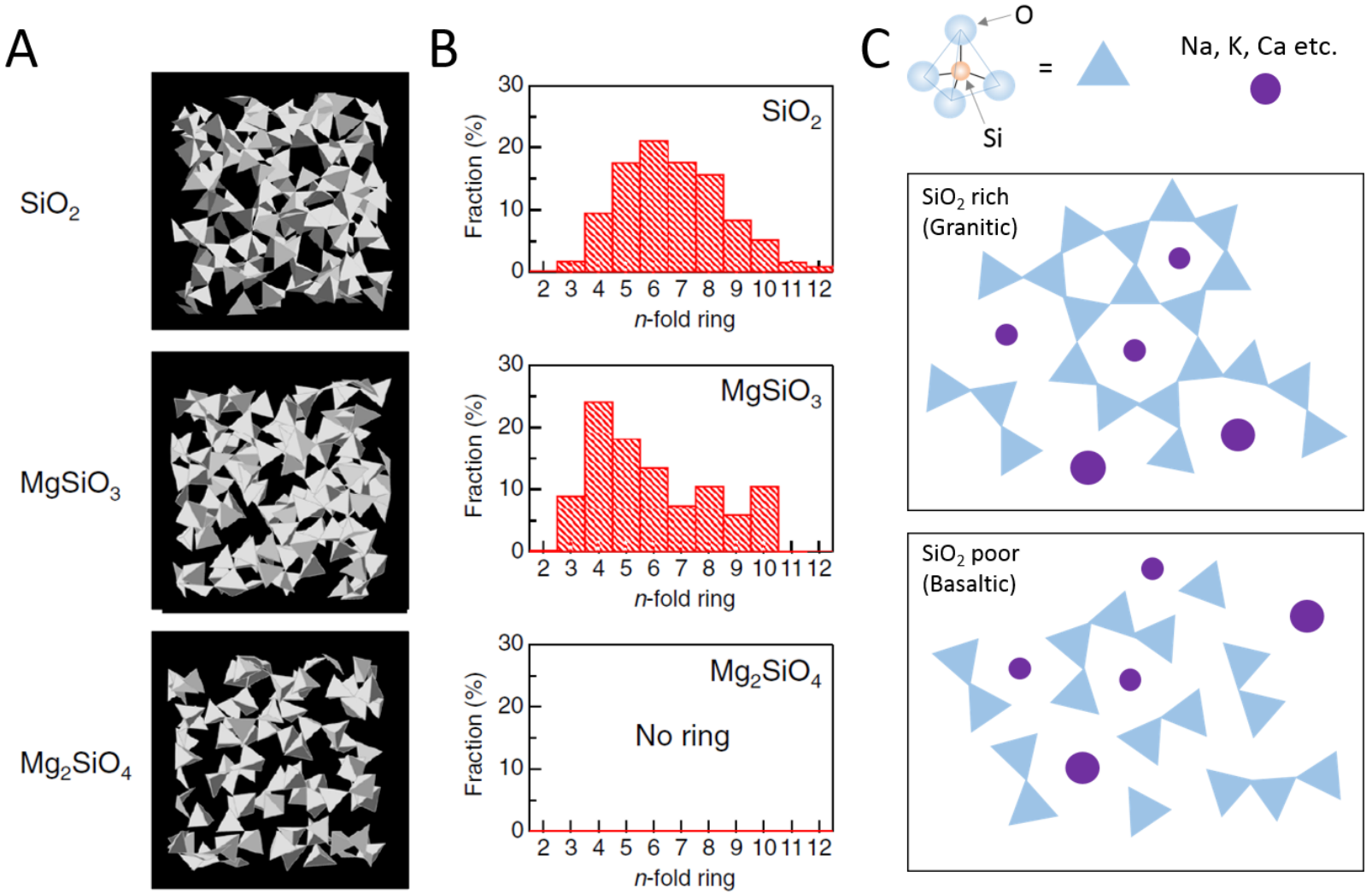

Figure 2.1 *A: Modelling by [46] showing the number of interconnected tetrahedra in silica melts with decreasing SiO_2 content, from SiO_2 glass to Mg_2SiO_4. B: The ring statistics obtained from models in A. From [46]. C: Schematic representation of a silica rich (top) and silica poor (bottom) melt network.*

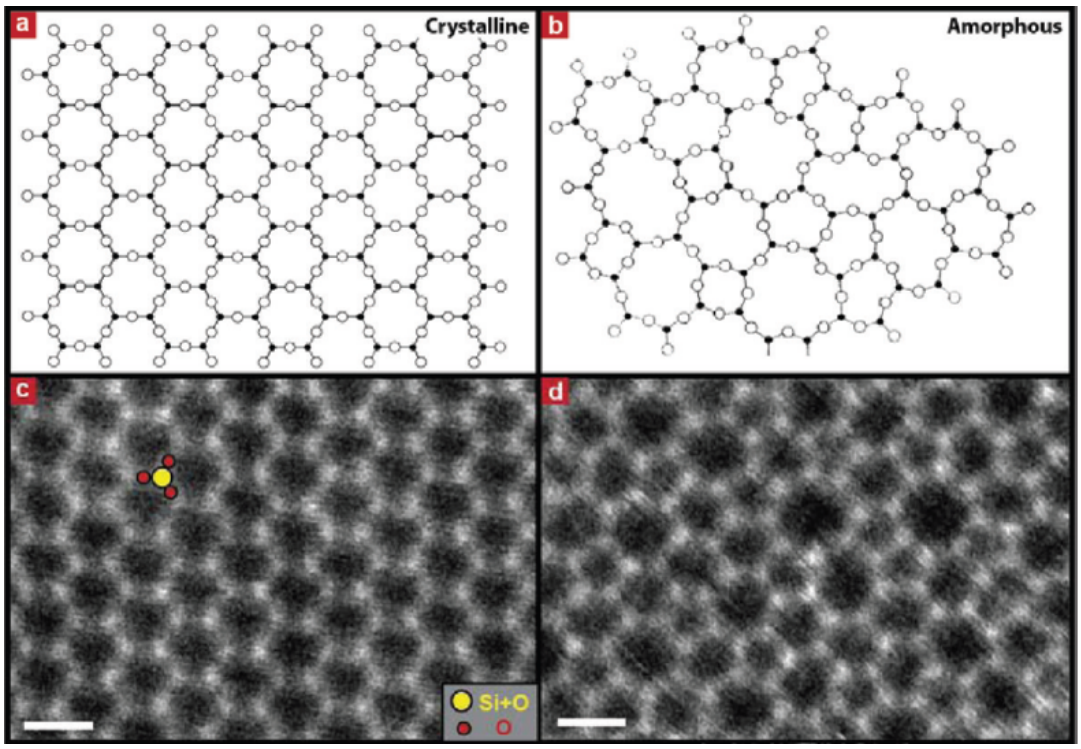

Figure 2.2 *From [47]. Models for the 2D network of crystalline SiO_2 (a) and glass (b), with experimental 2D STEM images collected by [47] for crystalline (c) and amorphous (d) SiO_2. Scale bar in C is 5 Å.*

In order to probe the structure of silicate liquids, the structure factor and radial distribution functions, obtained through x-ray diffraction, are used in this thesis (Chapter 3). The short range structure of a melt is considered to extend to 3 Å, which covers the first nearest neighbour distances [44]. The radial distribution function gives the probability of finding an atom at a certain distance from another in r-space and can provide information on bond distances (Figure 2.3) and the coordination of nearest neighbour atoms, where coordination is defined as the number of nearest neighbours surrounding an atom. Due to the inherent thermal motion present in melts, the structure is flexible and over the time of a measurement only the average structure is recorded [44]. As the liquid lacks long range periodic order coordination numbers can be more varied than those found in most minerals, and coordination such as '5-fold' can occur due to a mix of coordination numbers from 4-6 as well as the greater flexibility and irregularity of the sites formed by the rings of varying size [42].

Studies have shown that some intermediate range order exists in amorphous silicates due to the structures formed by the interconnected tetrahedral units [50–53]. This intermediate structure arises from quasi-lattice planes that exist

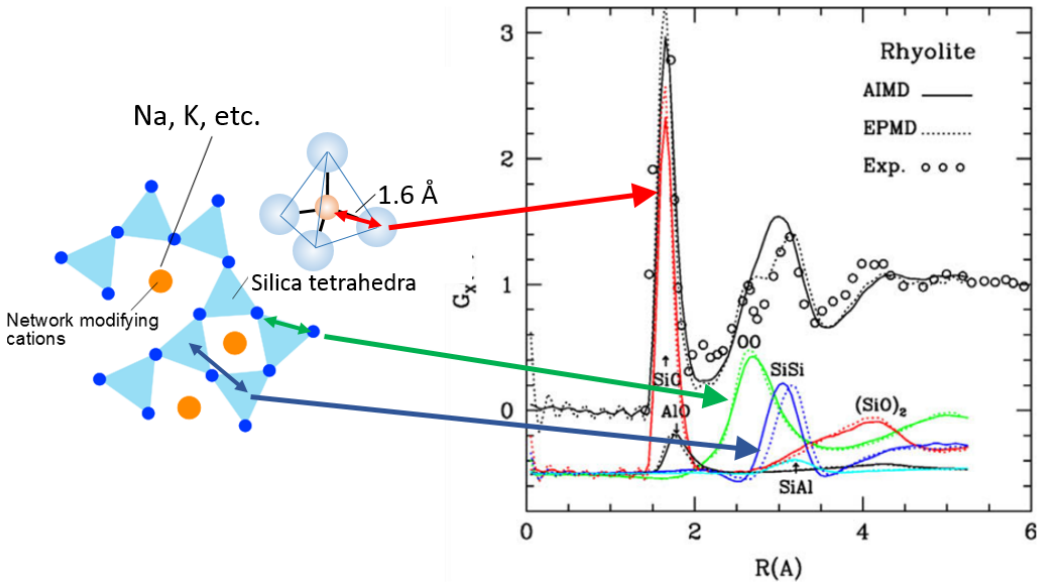

Figure 2.3 *Information obtained on the short-range order in silicate glasses and liquids from the radial distribution function. A schematic melt network is shown with the bond distances marked that can be identified in the radial distribution function (right from [49]).*

due to the rings (Figure 2.4) as seen in silicate glass. This medium range order can be probed by the first sharp diffraction peak (FSDP) of the structure factor in reciprocal space [51, 53, 54]. The origin of the FSDP, although still debated, is thought most likely to arise from intermediate periodicity within silicate networks. Salmon [51] has shown that if the FSDP is Fourier transformed to real space, an oscillatory function with a period of $2\pi/Q_1$ (where Q_1 is the position of the FSDP in the reciprocal space) is produced (Figure 2.4). This periodicity depends on the size of the cages and therefore the spacing between the psuedo-lattice planes. The FSDP is less broad than other peaks in the structure factor and as such it is considered 'Bragg' like, reflecting the intermediate order within the glass [50]. The introduction of network modifying cations shifts the FSDP to higher Q as the polymerised network of rings is distorted and broken up, causing increased diversity in the number of ring members and a decrease in the medium range order compared to vitreous silica [54].

2.2 Trace Elements in Silicate Liquids

Trace elements are defined as those elements in concentrations <0.1 wt.% within a given system and are usually of the order parts per million (ppm) or parts

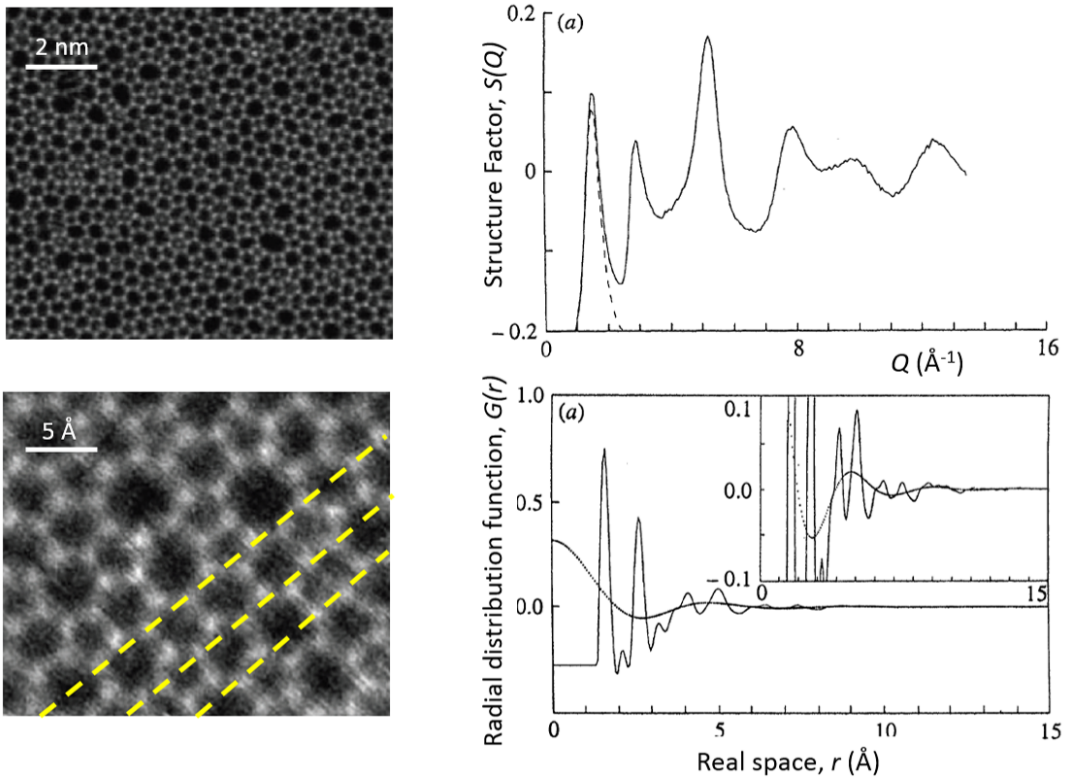

Figure 2.4 *Left: TEM images from [47] with quasi-lattice planes caused by the tetrahedral network shown. Right: Structure factor of SiO_2 glass with FSDP marked by dashed line. The long wavelength oscillatory function after the Fourier transform of the FSDP only is shown compared to a full radial distribution function of SiO_2 glass, from [51].*

per thousand [55]. In this study the trace elements used (predominantly rare Earth elements) are found in minor concentrations as non-network forming cations. Trace elements can often partition between phases in a measurable and predictable manner and it is these partition coefficients that are of importance for understanding certain properties of geological systems. Two groups of trace elements will be discussed in this thesis: (1) Rare Earth elements (REE), which include the lanthanides and Y as these tend to exhibit similar chemical properties. These are divided into two sub-groups, the heavy REE (HREE) including Tb-Lu, and the light REE (LREE) from La-Gd. The H/LREE distinction arises from the lanthanide contraction and therefore density of the atoms. (2) High field strength elements (HFSE), which although they can include the REE, here will be reserved for Hf, Zr and other 4+ cations which have a small radius compared to ionic charge [55]. When partial melting occurs, trace elements partition between the different phases in the system. The ratio of element concentration, C, between the mineral and the melt is known as the partition coefficient of a two-phase mineral-melt system, D, [55] and is defined for an element k by

$$D^k_{mineral} = \frac{C^k_{mineral}}{C^k_{melt}}. \tag{2.1}$$

In geological systems an average D is summed for all co-existing mineral phases within one melt composition. When the concentration in the mineral phase is greater than the melt, D>1, the element k is compatible and prefers to stay within the mineral phase. For D<1 it is incompatible and will preferentially incorporate in the melt [3]. Trace elements have different partition coefficients depending on their size and ionic charge and therefore often have distinctive partitioning ratios (D^k/D^j). The systematic partitioning of trace elements provides three important tools for petrologists and geochemists: (1) The fraction of partial melting can be determined providing the T of melting, (2) the residual mineralogy of the system during melting can be determined and provides a P range for melt genesis, and (3) radioactive element partitioning can provide a tool for dating events in the Earth's history [55].

Partitioning takes place largely during processes such as partial melting and fractional crystallisation that occur during crust formation and would have been present during planetary differentiation. Partioning ratios are known to depend on multiple factors: temperature and depth of formation, mineral and melt composition, volatile content, and oxygen fugacity (see [41] and references

within). The preferential enrichment of incompatible elements in the melt can help identify the degree of melting and the sequence of crystallisation, providing insight into the evolution of the melt since its formation [55].

REE are considered refractory lithophile due to their preference for incorporation in silicate rather than sulphide or metal phases, and their high condensation temperatures [26]. Due to these properties one of the biggest uncertainties in Earth science that REE ratios are used for understanding is the composition of the bulk silicate Earth, and whether it is 'chondritic' (i.e. average refractory element ratios are identical to those found in chondrite meteorites). Research surrounding this is based on the radioactive decay of two key element pairs, ^{176}Lu-^{176}Hf and ^{146}Sm-^{142}Nd [2, 23–26]. In these pairs, the larger radii daughter elements (^{176}Hf and ^{142}Nd) partition more strongly into any melt phase during crystallisation or melting, compared to the smaller parent elements. This leads to elevated ϵ_{Hf} and ϵ_{Nd} values where ϵ_x is the ratio between the radiogenic daughter and unradiogenic isotope of the same element (^{177}Hf and ^{144}Nd) normalised to the 'Chondritic Uniform Reservoir' (CHUR). This means unradiogenic $\epsilon_{Hf,Nd}$ values <0 are assumed to be caused by an enriched (greater ^{177}Hf or ^{144}Nd) mantle source, with a radiogenic $\epsilon_{Hf,Nd}$ >0 indicating a depleted mantle reservoir [56]. There are many controversies surrounding the chondritic model for the bulk Earth as experimental determination of trace element ratios produces a complicated picture. One of the paradoxical trace element ratios is that of Sm/Nd, where the measured mantle ratio is approximately 6% higher than chondritic values [26]. This requires the presence of a hidden reservoir that formed early during Earth history, or the superchondritic model where the bulk Earth is assumed to have isotopic values higher than chondrites. The hidden reservoir model is difficult to reconcile with existing heat flow models or mantle plume signatures and as the moon and Earth have identical ^{142}Nd/^{144}Nd values, this reservoir would have to have been formed and isolated before the moon forming impact [26]. ^{176}Lu-^{176}Hf partitioning also adds to this controversy [28, 30, 56–58]; un-radiogenic Hf signatures in >3.9 Gyr zircons of terrestrial rocks indicate extraction from an enriched mantle source ($>^{177}$Hf), although debate surrounding the appropriate decay constant to use can also suggest a highly depleted mantle source [28], requiring extensive crust to be present very soon after Earth formation. All these studies assume the behaviour of Lu/Hf and Sm/Nd partitioning at depth in the early Earth is the same as measured today in partitioning experiments. However, if partitioning ratios were strongly influenced by P due to alterations in the melt structure this could significantly change predicted models for early crust

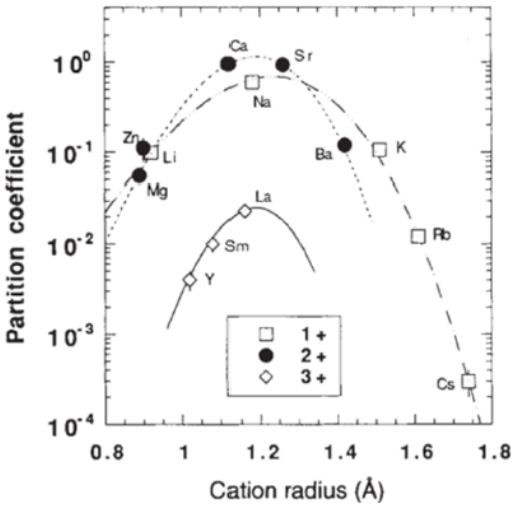

Figure 2.5 *Plot of partition coefficient (D) against cation radius for a series of 1+, 2+ and 3+ cations, with the parabolic relation highlighted. From [60].*

extraction and differentiation. For example, if structural changes in the melt at depth cause less partitioning of Lu from unradiogenic Hf at depth during first crust extraction, this could produce a depleted mantle signature even though no prior crustal extraction had taken place.

2.2.1 The Lattice Strain Model

It was first recognised by Onuma [59] that plots of partition coefficients for some trace elements give a parabolic dependence on cation radius (Figure 2.5), with a minimum when the two isovalent cations have a similar radius. Blundy and Wood [60] took this further and by using energetic models for crystal strain by Brice [61], they proposed a model that quantifies a partition coefficient for a series of isovalent cations substituting into a specific lattice site (Equation 2.4).

This 'lattice strain model' attempts to quantitatively describe trace element partitioning as a function of temperature, pressure, bulk composition and the properties of the cation site in the mineral lattice. This model is based on the strain energy of the site when cation substitution occurs, where E is the apparent Young's Modulus that defines the stiffness of the crystal lattice site. The strain energy around the cation site is proportional to the size difference between the host and the substituting cation; if the cation is larger than the original host ion on the site then the strain energy will be positive as greater strain will be exerted

on the mineral structure. Brice [61] related mechanical strain (ΔG_{strain}) to E of the crystal through

$$\Delta G_{strain} = 4\pi E N_A \left[\frac{r_0}{2}(r_k - r_0)^2 + \frac{1}{3}(r_k - r_0)^3 \right]. \tag{2.2}$$

Blundy and Wood [60] argue that as the melt is much more compressible than the crystal lattice, the strain energy within the melt is much lower and does not need to be considered, making $\Delta G_{strain} \approx \Delta G_{exchange}$ [62], where $\Delta G_{exchange}$ is the Gibbs free energy associated with the exchange of a cation k between the melt and the mineral. The free energy of fusion (ΔG_{fusion}) is the Gibbs free energy associated with the partitioning of the host cation within the structure as a function of P and T, and for an ideal exchange of cations when $r_k = r_0$ the ΔG_{fusion} can be thought of as a 'strain free' partitioning event, D_0, for a given P, T and composition. The overall partition coefficient energetics for a cation k, D_k, is controlled by the ΔG_{strain} and ΔG_{fusion} by

$$D_k = exp \left[\frac{\Delta G_{fusion} - \Delta G_{exchange}}{RT} \right], \tag{2.3}$$

where T is temperature (K) and R is the universal gas constant. Blundy and Wood [60] made the relation between these ideas by substituting Equation 2.3 into Equation 2.2, and applying the condition that for a cation of radius r_k equal to the host cation radius (r_0) the ΔG_{fusion} can be described by D_0. This gives the expression for the partition coefficient D_k as

$$D_k^{min/melt} = D_0^{min/melt} exp \left[\frac{-4\pi E_x N_A (\frac{r_0}{2}(r_k - r_0)^2 + \frac{1}{3}(r_k - r_0)^3)}{RT} \right]. \tag{2.4}$$

The implications for this are extensive as it provides a tool for predicting partition coefficients for similarly charged cations in a crystal lattice. However, although the D_0 term in equation 2.4 does rely on P, T, and the composition of both the relevant melt and mineral phases, there is no explicit term that describes or quantifies the effect of melt structural changes. As shown by [33, 35, 37, 63] variations in the melt can have a strong influence on partitioning (Section 2.2.2 and 2.2.3). Some studies [37, 64, 65] have included a separate melt term based on the energetics or elasticity of the melt site. Imai *et al.* [37] showed that if the melt site was considered to be as large as the crystal lattice site in a peridotite melt-

olivine system, the effect of the melt on partitioning could not be neglected at high pressures. The current models by van Westrenen and Draper [66], Draper and van Westrenen [67], and Wood and Blundy [65], although specifically including the possible effect of the melt at pressures up to 6 GPa, contain parameters based on measured partitioning data for the system of interest, and are only successful for predicting REE partitioning within a system of the same mineralogy (garnet and clinopyroxene respectively). Not only does this require experimental values of the partition coefficients for each different melt composition, but even when the melt composition remains fixed, structural changes within the melt at high $P-T$ in the deep Earth could severely change the partitioning of certain elements. As reviewed by Sanloup [43] and developed further in this study, magmas are highly compressible, particularly at shallow mantle conditions (<5 GPa). Therefore the hypothesis that their elasticity and compressibility is negligible compared to crystal structures must be revisited and any structural changes around the trace element sites need to be documented if a truly predictive model is to be established.

2.2.2 Compositional Changes

Several studies have shown that variations in the melt composition do influence partitioning [33, 37, 63]. The compositional study by Prowatke and Klemme [33] directly observed a change in partitioning ratios correlated to a change in melt composition. By increasing the Aluminium Saturation Index ($ASI = Al_2O_3 = (Na_2O + K_2O + CaO)$) of their glass they observed a two orders of magnitude increase in partition coefficients in accessory minerals for trivalent REE such as Lu, Y, and La, with HFSE such as Hf and Zr unaffected. It was concluded that by increasing the ASI of the glass, the polymerisation of the melt was increased, which influenced the number of non-bridging oxygens available to bond with the trivalent cations. Other compositional studies have also shown a preference for REE to enter less polymerised melt structures [32, 34]. Schmidt [34] studied partitioning between gabbroic and granitic melts at low pressure and showed that trivalent REE have a strong preference for gabbroic melts. This was related to the required high (6-8) coordination and, therefore, a preference to enter the more open structure.

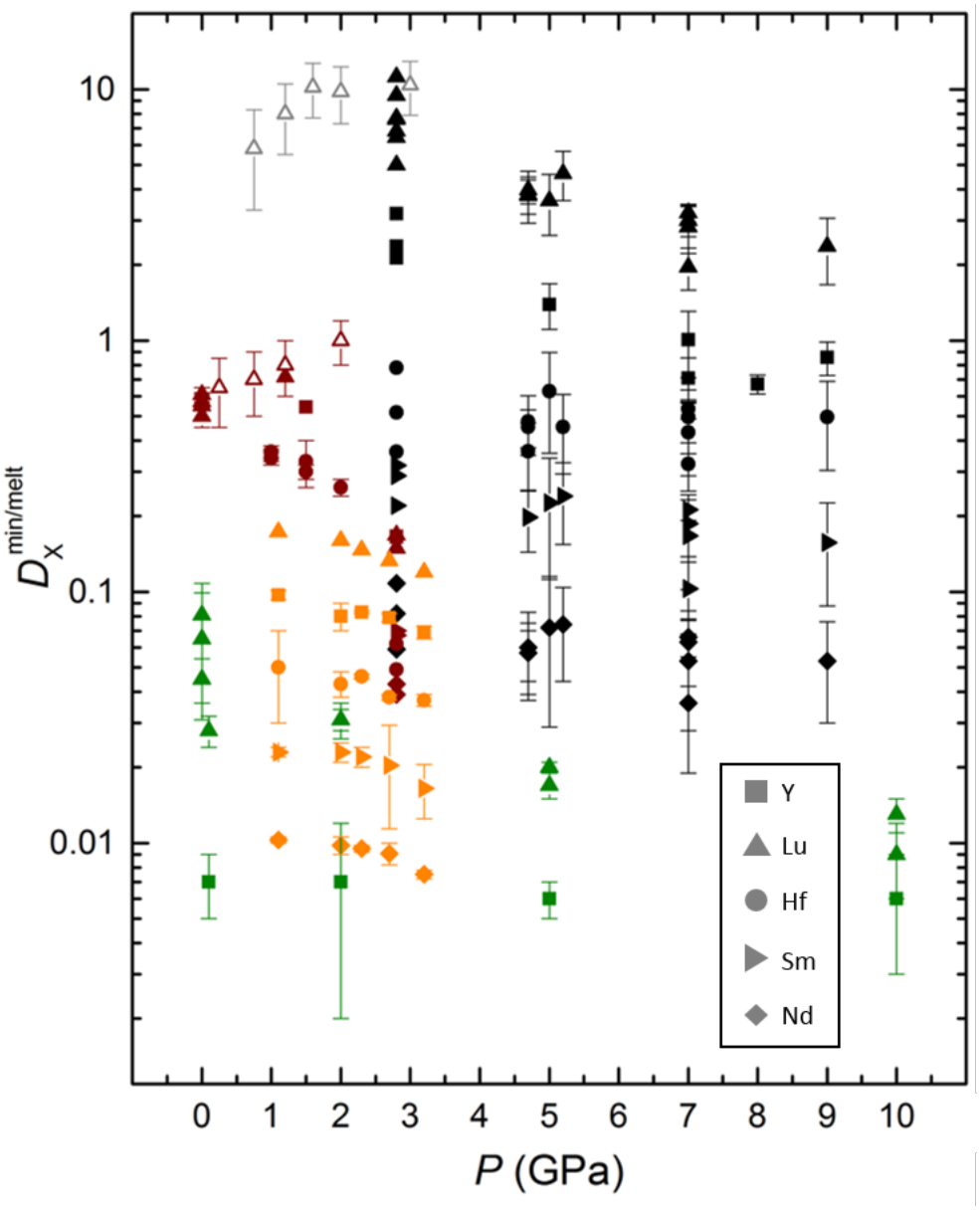

Figure 2.6 *Major mineral-melt partition coefficient data ($D_X^{min/melt}$) for Lu (triangle), Nd (diamond), Y (square), Hf (circle) and Sm (right-triangle) with pressure. Data presented are from studies where the composition was consistent over all P-T conditions. Other studies (i.e. [68]) have varying starting compositions that may mask any P effects. Colours indicate mineral in equilibrium with glass after experiment (Black: garnet, Grey: sphene, Red: clinopyroxene (cpx), Orange: orthopyroxene (opx), Green: olivine). Data is taken from [37, 69–75]. Error bars are taken from references where possible and for those not shown are smaller than the symbol size. Filled symbols are crystals coexisting with a melt of 44-50 % SiO_2 and open symbols are with andesitic melts of $SiO_2 \gtrsim 60$ %*

2.2.3 High Pressure

Different studies present varying results on the impact of pressure on partition coefficients. In general studies on REE partitioning with pressure show a decrease with pressure in REE compatibility between minerals and basaltic-like melts (Figure 2.6) [37, 69, 71]; although Green and Pearson [72] reported an opposite trend for clinopyroxene-andesitic melts, measuring a small increase in compatibility for REE to 2 GPa, which is most likely due to the higher silica content of the melt. Draper *et al.* [69] proposed that an increase in the majorite component of garnets in chondritic melts at 5 GPa causes a large decrease in partition coefficient for the HREE with a compatibility plateau after 5 GPa. However this trend is not observed for lighter REE such as Nd (Figure 2.6) where the D_{Nd} remains relatively constant up to 10 GPa. This was also true for high field strength 4+ cations such as Hf and Zr. This would suggest that at P >5GPa partition coefficients between HREE and LREE or 4+ cations may become similar. Although the transition to majorite may influence partitioning, the possibility of melt structural changes at these pressures was not considered. Imai *et al.* [37] also observed a decrease in HREE partition coefficients between olivine and peridotitic melt for some 3+ cations, including Lu, with increasing pressure between 5-10 GPa, although for Y which is very incompatible in olivine there was little affect of pressure on partitioning. Studies by Westrenen and Draper [66, 67] present an opposing view to the decrease of partition coefficients with P, and suggest that thermodynamically, if other variable factors are removed, the partition coefficients in the garnet-basalt system increase with P. The data shown in Figure 2.6 does include studies with variations in temperature as can be seen by the range of partition coefficients at similar pressures. The uncertainty regarding the effect of increasing pressure on partition coefficients

A decrease in compatibility is particularly noticeable for clinopyroxene and basaltic melts where the partition coefficients appear to decrease rapidly with pressure up to 3 GPa from ambient (Figure 2.6). The largest decrease observed for the elements in this study is for Nd, where the partition coefficient drops by an order of magnitude (from 0.7 to 0.05) by 3 GPa, with the smallest change for Y. This data suggests that there is a trend in REE partitioning behaviour with pressure that depends on the cation radius. Although changes in the crystal lattice may be the cause of this, Imai *et al.* [37] proposed that elasticity of the cation site in the melt structure might effect partitioning as, in the case of olivine, changes on the crystal lattice alone would not produce a large enough

effect, but currently no evidence for structural changes within the liquid has so far been presented. Studies on silicate glasses, and more recently liquids, have shown that structural alterations for major elements do occur within the liquid with increasing pressure. This has been well documented for Si-O coordination which increases from 4 to 6 above 15-35 GPa [14, 16] and the change in Al-O coordination to 50% 6-fold coordination by 12 GPa [20, 38]. This thesis is the first to monitor the effect of minor element incorporation in silicate melts at high pressure in an attempt to improve our understanding of why such pressure affects on partitioning are observed.

2.2.4 Structural Incorporation in Glasses

Simon *et al.* [41] have investigated the local structural effects of yttrium (Y) in silicate glasses using Extended X-ray Absorption Fine Structure (EXAFS) at ambient conditions. They studied the bonding environment of Y within the same glasses as [33] in order to isolate the structural effect on Y with increasing aluminium saturation index (polymerisation) of the glass. They discovered that increasing melt polymerisation leads to an increase in Y coordination (CN) from 6 to 8, with a corresponding increase in average bond distance from 2.28 to 2.38 Å. Ponader and Brown [39] observed a similar compositional variance with $CN_{\mathrm{La-O}}$ increasing from 7 to 9 in the higher polymerised melt, and $r_{\mathrm{La-O}}$ also lengthening from 2.42 to 2.59 Å. In contrast though they observed a coordination decrease for Yb and Gd with increasing melt polymerisation. However, Simon *et al.* [41] note that the EXAFS processing methods used by [39] may produce artificially low values for CN. Observations by Farges [40] show an increase in coordination with polymerisation for Th at 1-3 wt.% levels and Th/U partitioning ratios in zircon are attributed to the increase in compatibility of Th in the presence of highly polymerised melts. Keppler and Rubie [76] presented some of the first results on the change in Co and Ni coordination at high pressure in quenched silicate melts, and proposed that the coordination increase from 4 to 6 would cause a distinct change in partitioning. For silica-rich melt compositions an increase in partitioning is observed for Lu with increasing P (open symbols on Figure 2.6), this could be attributed to the greater polymerisation of the melt structure. All these studies indicate that important structural changes of minor elements can occur within the melt, not just the crystal lattice, and could impact REE local structure and partitioning. Nevertheless, to date all these studies have been carried out on quenched glass systems and not *in situ* at the conditions of melt

formation.

Chapter 3

A Review of Structural Probes for Liquids and Glasses

This chapter gives an introduction to the theory of x-ray diffraction and absorption, and subsequently how these techniques are applied to amorphous solids and liquids. The functions that need to be derived in order to interpret liquid and amorphous diffraction data are defined, and the difference between energy dispersive and angle dispersive diffraction will be introduced.

3.1 X-ray Diffraction

X-ray diffraction (XRD) is a well known tool for studying solids and solving crystal structures, and since the 1990s techniques have advanced enough that it has become an increasingly common tool for looking at liquid and amorphous silicate structures [44]. With the development of synchrotron radiation, which provides a high flux of polarized x-rays, the short-medium (<6 Å) average structures of liquids can be identified through pair distribution function analysis.

X-ray diffraction is the process of scattering incident photons, with wavelengths between 0.1-10 nm, of electromagnetic radiation by a sample. In contrast to solids, for amorphous materials, instead of resolving atomic positions exactly only the time-resolved probability of finding atoms at a certain distance from another can be found. In a structure of known composition, this can be ideal for estimating bond lengths and the coordination of elements. X-ray diffraction utilises the

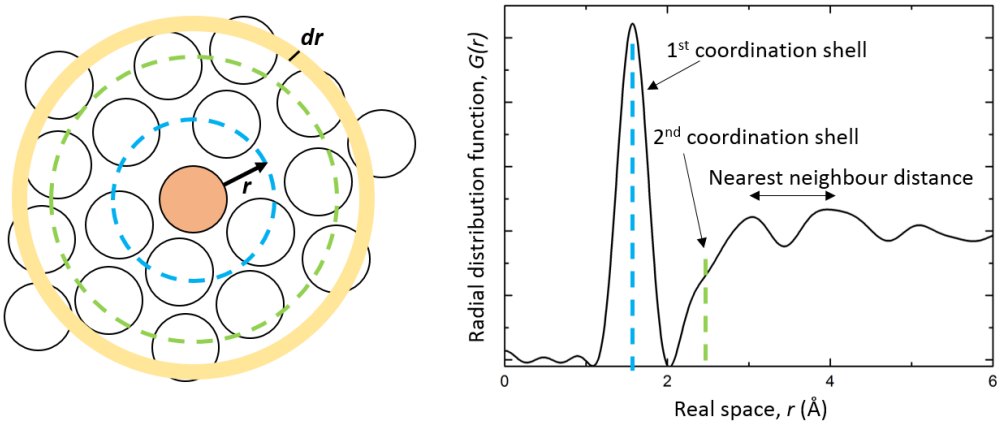

Figure 3.1 *General schematic of the radial distribution function (RDF), known as the $G(r)$, and measurement of nearest neighbour interactions between atoms. Each correlation distance is represented by an oscillation in the RDF.*

behaviour of a material to scatter x-rays from the electron cloud of an atom. This scattering occurs from a spatially extended distribution rather than a point source, as in neutron diffraction where diffraction is from the atomic nucleus [77]. The radial distribution function is given by $4\pi r^2\rho(r)$, where $4\pi r^2\rho(r)dr$ is the average number of nearest neighbours between r and $r + dr$ away from the the central atom (Figure 3.1). Peaks in the $G(r)$ correspond to different bond distances that are present within the sample (Figure 3.1). All the work in this thesis is carried out on non-crystalline substances in glass or liquid form, therefore the theory of x-ray diffraction will be presented only in relation to scattering in non-crystalline materials and a full description of scattering from crystals will not be covered. The main texts followed in this chapter are those of chapters 1 and 10 in reference [77] and developed by [78]. A classical approach to x-ray diffraction theory is described rather than a fully quantum mechanical derivation, as this is not required and provides a similar approximation [77].

3.1.1 Theory

Given an x-ray wavelength of between 0.1-10 nm and an atomic size of 0.05-0.5 nm, the radiation wavelength used is of the order of the interatomic spacing, and therefore can provide information on the distribution of atoms in space. If an incoming incident beam of energy, I_0, interacts with an atom, the scattering vector, $\boldsymbol{Q}$, is defined by the incoming and scattered wave vectors, $\boldsymbol{k_1}$ and $\boldsymbol{k_2}$, by

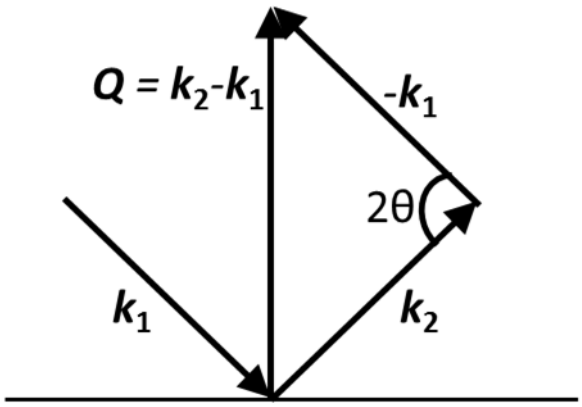

Figure 3.2 *Definition of the scattering vector, $\boldsymbol{Q}$, in relation to wave vectors $\boldsymbol{k_1}$ and $\boldsymbol{k_2}$.*

$\boldsymbol{Q} = \boldsymbol{k_2} - \boldsymbol{k_1}$ where $|\boldsymbol{k_1}| = 2\pi/\lambda$ and $|\boldsymbol{k_2}| = 2\pi/\lambda$ depending on the wavelength of the incident and scattered beam (Figure 3.2). For elastic scattering it is assumed that the incident energy is much greater than any energy exchange that happens at the sample which leads to $k_1 \approx k_2$. If the scattered beam is at an angle θ to a point source scatterer then the magnitude of the wave vector, or momentum transfer, $\boldsymbol{Q}$, is given by

$$Q = |\boldsymbol{Q}| = \frac{4\pi}{\lambda} sin(\frac{2\theta}{2}). \tag{3.1}$$

If the wavelength of the experiment is fixed and a detector is placed at distance R from the sample it will be possible to collect all the scattered radiation as a function of Q that falls on the detector. It is from this Q dependant spectra that a structure factor for the sample can be calculated as shown below. To understand how a structure factor for a complex or polyatomic system can be derived it is useful to first consider scattering from a free electron and build up through scattering from a single atom. The following derivation of the scattering from a single atom uses cgs notation for simplicity. Coherent and incoherently scattered waves will be addressed as both have implications for diffraction measurements. For coherent (elastic) scattering, classical electrodynamic theory states that an electron which experiences a periodically changing electric field on interaction with incident x-ray radiation will be excited to periodic vibrations and emit electromagnetic radiation of the same frequency. The electric field of an electron

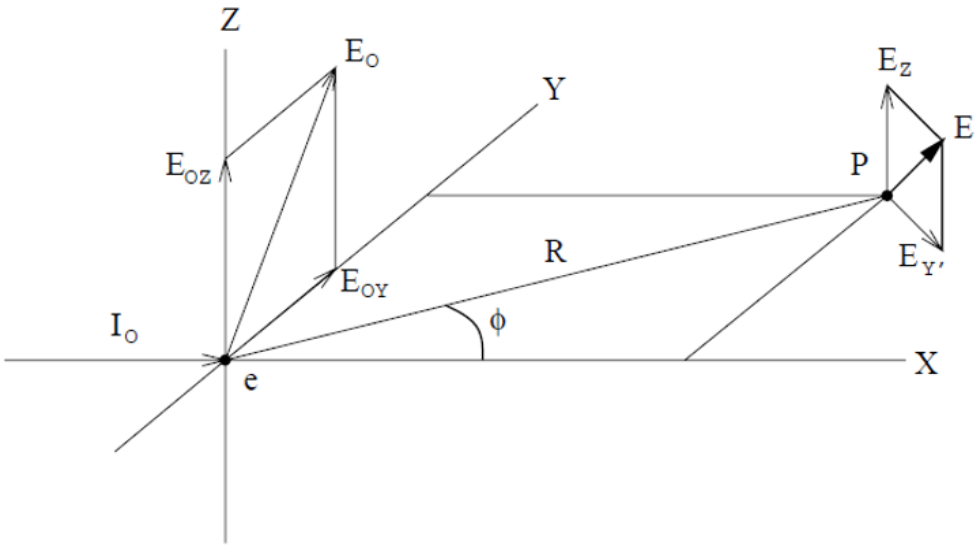

Figure 3.3 *Representation of classical scattering by an incoming beam, I_0, for a single free electron at the origin and measurement at P. From [77].*

at the origin in Figure 3.3 can be given by

$$\boldsymbol{\epsilon_0} = \boldsymbol{E_0} \sin 2\pi v t, \tag{3.2}$$

where v is the frequency of the incident beam I_0, t is time, and $\mathbf{E}_0$ is the amplitude of the wave oscillating in the YZ plane. In order to understand x-ray scattering the radiation at point P at a distance R from the electron is considered. The electron will have a force exerted on it due to the electric field which induces an acceleration,

$$\boldsymbol{a} = \frac{q\ \boldsymbol{\epsilon_0}}{m}, \tag{3.3}$$

where m and q are the mass and charge of the electron in this case. An electric field at point P will be induced from the acceleration of the electron which can shown by

$$\boldsymbol{\epsilon} = \frac{q\ \boldsymbol{a} \sin\alpha}{c^2 R}. \tag{3.4}$$

Figure 3.3 shows the direction of this field relative to the electron and point P, where α is the angle between the acceleration and R, and c is the velocity of light. The resultant electric field is therefore a direct consequence of the acceleration

component $\boldsymbol{a}\sin\alpha$ caused by the frequency of the incoming x-ray radiation. The amplitudes of the separate components (Figure 3.3) of the oscillatory motion can be expressed in terms of the directions of motion of the field

$$\boldsymbol{E_{Y'}} = \frac{q^2 \boldsymbol{E_{0Y}}}{mc^2 R}\cos\phi, \tag{3.5}$$

and

$$\boldsymbol{E_Z} = \frac{q^2 \boldsymbol{E_{0Z}}}{mc^2 R}. \tag{3.6}$$

The overall amplitude $\boldsymbol{E}$ at point P can then be obtained by summing the individual vectors, and in order to express the average electric field they must be averaged over all directions in the YZ plane, which produces

$$\langle \boldsymbol{E^2} \rangle = \langle \boldsymbol{E_0^2} \rangle \frac{q^4}{m^2 c^4 R^2}\Big(\frac{1+\cos^2\phi}{2}\Big). \tag{3.7}$$

The measured intensity picked up by a detector at P is given by the intensity, I, which is defined as the mean energy per unit area per unit time. This intensity can be calculated from $\boldsymbol{E}$, which is the amplitude of the electric field in cgs units, through the conversion

$$I = \frac{c}{8\pi}\langle \boldsymbol{E}^2 \rangle, \tag{3.8}$$

which yields the Thomson scattering equation for the measurable intensity from the classical scattering of a free electron,

$$I = I_0 \frac{q^4}{m^2 c^4 R^2}\Big(\frac{1+\cos^2\phi}{2}\Big). \tag{3.9}$$

This represents the polarised energy of a scattered electron with $(1+\cos^2\phi/2)$ from the initially unpolarized incident x-ray beam. However, when considering atoms, the scattering does not occur from a single electron but from an electron cloud which it is assumed has a spherical symmetry around the nucleus. This scattering takes two forms: (1) Classical elastic scattering with no change in wavelength. (2) Compton (inelastic scattering) which will be discussed in Section 3.1.2. To calculate the elastic scattering from an entire atom we consider the

electrons to represent a spherical cloud of negative charge represented by a charge density, ρ. The electron density of an atom is assumed to be the sum of the individual electron densities and is therefore related to the atomic number, Z, of each element. Due to some partial destructive interference as the scattered waves interact in the cloud the charge density decreases with increasing angle θ away from the incident beam. The average charge density of the cloud, $\rho(r)$, depends on distance r from the nucleus and assumes spherical symmetry. The atomic scattering factor, f, represents the number of electrons within an atom of atomic number Z that will scatter the incident radiation. This can be given by

$$f = \sum_{n=1}^{Z} \int_0^{\infty} 4\pi r^2 \rho(r) \frac{\sin Qr}{Qr} dr. \tag{3.10}$$

The intensity of coherent scattering from each electron bound in an atom is directly related to the Thomson scattering of a free electron and the scattering power of the electron cloud. Calculated values using wave mechanics and charge density distributions have been tabulated for the coherent scattering factors for each atom and are given in references such as [79–81]. The scattering power varies inversely with the electron cloud and is therefore always Z at $\theta = 0$, decreasing exponentially with increasing Q (Figure 3.4A). This scattering therefore dominates at low angles whereas the opposite is true of incoherent scattering (Section 3.1.2). Using the scattering factor above, the coherent scattered intensity of an electron cloud around one atom is

$$I_{coh} = I f^2, \tag{3.11}$$

where the f^2 arises because the formalism for f was developed in terms of scattering amplitudes and not wave intensities. This result assumes that the wavelengths used for diffraction are far from any absorption edge and therefore no corrections for absorption edge effects of the sample are required, which is true for the diffraction results presented in this thesis. In terms of the intensity measured from a sample of atoms m and n, this is then given by

$$I(Q) = \sum_{m=1}^{N} \sum_{n=1}^{N} f_m(Q) f_n(Q) \exp[\frac{2\pi i}{\lambda} \boldsymbol{(k_2 - k_1).r}_{mn}]. \tag{3.12}$$

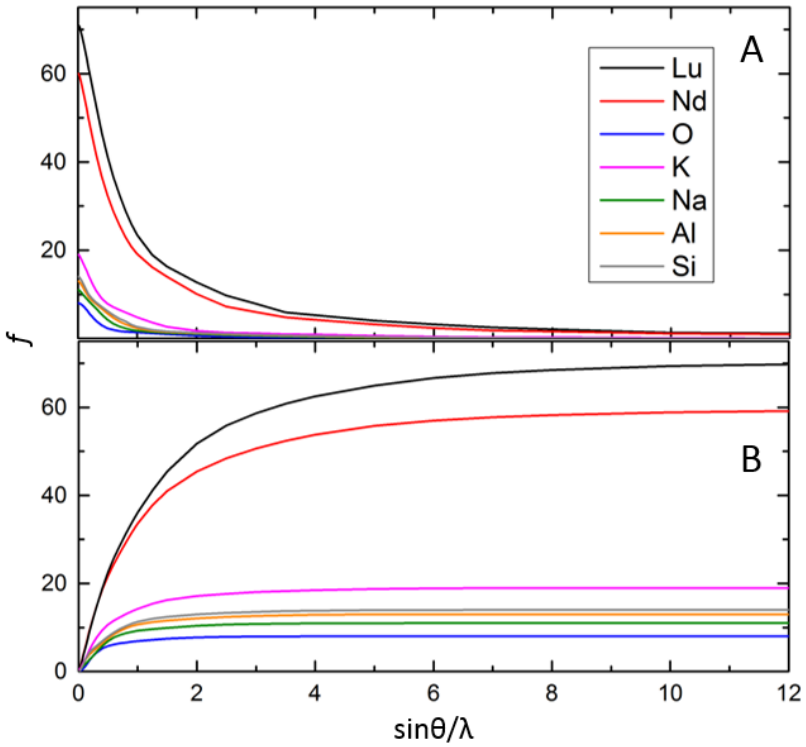

Figure 3.4 *A: Self-scattering profiles, $f(Q)$, from atoms used in this study. B: Incoherent (Compton) scattering profiles for the same atoms.*

3.1.2 Compton Scattering

In reality, collisions are not perfectly elastic and scattering from the spatially extended electron cloud causes the incoming x-ray to lose energy. This reduction in energy increases the wavelength of the scattered photon and is termed inelastic (or Compton) scattering [82]. As momentum is not conserved no regular interference patterns are produced, and inelastic scattering produces a background that varies depending on the size of the atom (Figure 3.4B). The Compton effect, or change in wavelength, $\lambda^{'}$, caused by inelastic scattering is given by

$$\lambda^{'} = \lambda + \frac{h}{mc}(1 - cos\phi) \tag{3.13}$$

which results from scattering away from the incident axis and states that the change in wavelength is independent of the incoming photon energy. Although it is very weak compared to elastic scattering this contribution must be removed from diffraction patterns before structural measurements can be made (Chapter 4.5.2).

3.1.3 Scattering from Non-crystalline Materials and Liquids

Monatomic Formalism

As this thesis addresses only materials of a non-crystalline nature, which are therefore anisotropic, it is possible to spherically average over all orientations in the sample as $exp(i\mathbf{Q}\ .\ \mathbf{r}) = sin(Qr)/Qr$. Following the previous derivation, and reference [78], the scattering theory for a monatomic amorphous sample is presented. Equation 3.12 over all space becomes

$$I(Q) = \sum_{m}\sum_{n} f_m f_n \frac{\sin Qr_{mn}}{Qr_{mn}}, \tag{3.14}$$

where f_{m} and f_{n} are the atomic scattering factors for the m and n^{th} atoms and r_{mn} is the distance between those atoms. The double sum comes from summing over all the pairs of atoms in the sample over all possible orientations. This is the first formal theory for studying non-crystalline materials with diffraction techniques

and was presented by Debye [83]. The coherent x-ray scattering for one type of atom, with N disordered atoms in a material can be defined as

$$I_{coh}(Q) = Nf^2(Q)\Big(1 + \sum_{m \neq n} \frac{\sin Qr_{mn}}{Qr_{mn}}\Big). \tag{3.15}$$

In order to obtain the scattering for the x-ray detector sample volume, S, an average atomic density, $\rho(r)$, term can be introduced that represents the average number of atoms in the volume, dV, illuminated by the x-rays at a distance, r, from the central atom. This is integrated in order to sum over the sample volume by

$$I_{coh}(Q) = Nf^2(Q)\Big(1 + \int_S \rho(r)\frac{sinQr}{Qr}dV\Big). \tag{3.16}$$

An average atomic density, ρ_0, constant over the sample volume and 0 at any other location, is defined for S. By adding a term where this average density represents scattering from the sample at small angles, and subtracting the average from the density function, the integral is not limited to the sample volume and the experimentally observable scattering is given by

$$I_{coh}(Q) = Nf^2(Q)\Big(1 + \int_0^\infty [\rho(r) - \rho_0]\frac{\sin Qr}{Qr}4\pi r^2 dr\Big). \tag{3.17}$$

The structure factor, $S(Q)$, which represents the normalised amplitude of the waves scattering from a sample is derived by

$$S(Q) = \frac{I_{coh}(Q)}{Nf^2(Q)} = 1 + \int_0^\infty [\rho(r) - \rho_0]\frac{\sin Qr}{Qr}4\pi r^2 dr. \tag{3.18}$$

The $S(Q)$, which is a Fourier transform of the electron density, can then be Fourier transformed to real space using a sine transform to obtain the pair distribution function, $G(r)$, as follows

$$G(r) = 4\pi r^2\rho(r) = 4\pi r^2\rho_0 + \frac{2r}{\pi}\int_0^\infty [S(Q) - 1]\frac{\sin(Qr)}{Qr}dQ, \tag{3.19}$$

which oscillates around 1 as r approaches infinity. In this thesis the $S(Q)$ and $G(r)$ are the main tools for extracting structural information about the silicate melt

structures. Other studies may present the $G(r)$ in different formats, including the differential correlation function, $D(r), F(r) = 4\pi r\rho_0 G(r)$ which oscillates around 0 at high r, or the total correlation function where $G(r)$ approaches ∞ at high r.

Polyatomic Formalism

This derivation still follows the work of [78] to expand the monatomic theory to polyatomic materials with more than one atom type. For a polyatomic system, Equation 3.15 becomes

$$I_{coh}(Q) = N\sum_{p} f_p^2(Q) + \sum_{m}\sum_{n\neq m} f_m(Q)f_n(Q)\frac{sinQr_{mn}}{Qr_{mn}} \tag{3.20}$$

where p and q represent atoms in a stoichiometric unit of the sample and m and n index all atoms in the illuminated sample volume, S. N is the number of compositional units made up of p and q atoms in the sample. As in the monatomic case an average atomic density function is introduced that represents the average number of atoms of type p at r distance away from atoms of type q in a chosen volume. This produces the integral equation over volume dV

$$I_{coh}(Q) = N\sum_{p} f_p^2(Q) + N\sum_{p}\sum_{q}\int_S f_p(Q)f(Q)\rho_{p,q}(r)\frac{sinQr}{Qr}dV. \tag{3.21}$$

In the case of polyatomic systems it is critical to define parameters that represent the average conditions within a sample volume, particularly an effective molecular density function, $\rho_{poly}(Q,r)$, that represents the density within the sample due to the differing concentrations, $c_{p,q}$, of each atom. In order to formulate this term an effective electronic form factor, $f_{eff}(Q)$, and effective atomic number, $K_{p,q}(Q)$, are required for the density function given by

$$\rho_{poly}(Q,r) \equiv \frac{\sum\sum K_p(Q)K_q(Q)\rho_{p,q}(r)}{Z_{total}^2}, \tag{3.22}$$

with

$$f_{eff}(Q) = \frac{\sum f_p(Q)c_p}{Z_{total}}, \tag{3.23}$$

where Z_{total} is the atomic number of a compositional unit and equals $\sum K_p(Q)$, which is given by

$$K_p(Q) = \frac{f_p(Q)}{f_{eff}(Q)}. \tag{3.24}$$

The form factors for the individual atoms are the same as described for the monatomic case, and can be found in literature where they have been calculated from theoretical scattering [79–81]. If the Q dependency of $K_p(Q)$ is not removed, this will prevent the density function being transformed to real space due to its dependency on both r and Q, contrary to the monatomic case. However, the Q dependency of $K_p(Q)$ can be removed if it is assumed that an average effective atomic number can be defined for the entire Q-range to be studied. For this case the effective molecular density function becomes

$$\rho_{mol}(r) = \frac{\sum\sum K_p K_q \rho_{p,q}(r)}{Z_{total}^2}, \tag{3.25}$$

and the coherent scattering from Equation 3.20 can then be written as

$$I^{coh}(Q) = N f_e^2(Q)\left\{ \sum_p K_p^2 + Z_{total}^2 \int_S \rho_{mol}(r) \frac{\sin Qr}{Qr} dV \right\}, \tag{3.26}$$

which can be Fourier transformed as it only depends on r. As in the monatomic formalism the average atomic density for the sample is defined as ρ_0, and by ignoring any small angle scattering the structure factor is found by

$$S(Q) = \frac{I^{coh}(Q)}{N Z_{total}^2 f_{eff}^2(Q)} = 1 + \int_0^\infty [\rho_{mol}(r) - \rho_0] \frac{\sin Qr}{Qr} 4\pi r^2 dr, \tag{3.27}$$

and the $S(Q)$ can be Fourier transformed to real space by

$$G(r) = 4\pi r^2 \rho_{mol}(r) = 4\pi r^2 \rho_0 + \frac{2r}{\pi} \int_0^\infty [S(Q) - 1] \frac{\sin(Qr)}{Qr} dQ, \tag{3.28}$$

which may be expressed as the sum of the partial radial distribution functions, $g_{p,q}(r)$,

$$G(r) = \frac{\rho_{mol}}{\rho_0} = \sum_p \sum_q \frac{K_p K_q}{Z_{total}^2} g_{p,q}(r). \tag{3.29}$$

From above we can also represent the $S(Q)$ as the sum of individual $S_{p,q}(Q)$ functions as

$$S(Q) - 1 = \sum_p \sum_q \frac{K_p K_q}{Z_{tot}^2}(S_{p,q}(Q) - 1), \tag{3.30}$$

where the individual ion-ion structure factors can be given by

$$S_{p,q}(Q) = 1 + \rho_0 \int_0^\infty (g_{p,q}(r) - 1)\frac{\sin Qr}{Qr} 4\pi r^2 dr. \tag{3.31}$$

These partial structure factors and radial distribution functions are similar to that found by following the Faber-Ziman ([84]) formalism where

$$S(Q) - 1 = \sum_p \sum_q \frac{c_p c_q f_p(Q) f_q^*(Q)}{|\sum_p c_p f_p(Q)|^2}[S_{p,q}(Q) - 1] \tag{3.32}$$

and it can be seen that the fractional term in Equation 3.32 is the representation of the effective factors described in Equations 3.23 and 3.24. By describing these functions as a sum of their partials it is possible to understand how to extract further information on individual ion-ion coordination numbers, $CN_{p,q}$, from the radial distribution function. This can be extracted, as the average number of q atoms in a shell between r to $r + dr$ around p atoms is found by integration of the partial radial distribution function as

$$CN_q = 4\pi\rho_0 c_q \int_{r1}^{r2} g_{p,q}(r) r^2 dr. \tag{3.33}$$

The extraction of the $S(Q)$ from collected sample intensity will be addressed in Chapter 4.5.

3.1.4 Angle Versus Energy Dispersive X-ray Diffraction

X-ray diffraction patterns can be collected via two techniques. The first and most commonly used is angle-dispersive where diffraction from the sample is collected over all angles of θ. This means that the wavelength of incident radiation is kept fixed and a monochromatic x-ray beam would be used on a synchrotron.

Detectors in this case can collect over multiple angles and the limit is defined by the opening of the cell assembly, distance from the detector, and the wavelength used to collect the pattern. For example higher energy will give access to higher theta and higher Q through the formula

$$Q = \frac{4\pi}{\lambda} sin\theta. \tag{3.34}$$

For energy dispersive x-ray diffraction (EDXD), λ is varied and θ is fixed so that data is collected over a range of energies, which can be converted to Q through $Q = 4\pi E \sin\theta/12.3984$. In order to access high Q, and not be limited by the range of energies available from the source, data can be collected at a variety of fixed angles over the full energy range. These data can then be fit together for progressively higher Q as θ is increased. Even though theoretically much higher Q than angle dispersive diffraction can be collected for the same type of pressure cell, EDXD does have limitations in that the data has to be normalised and fit together which can cause unreal artefacts in the subsequent $S(Q)$. Collection times for EDXD are also considerably longer than those required for angle dispersive diffraction, and can be of the order of >2 hours compared to 60 s or less for angle dispersive data collection.

3.2 X-ray Absorption Spectroscopy

X-ray absorption fine structure (XAS) is the process by which x-rays are absorbed by atoms near the electron binding energy, and the description below follows the work of [85]. XAS is specific to one type of atom in the sample as the energy is selected to target the absorption edge of the atom of interest. This behaviour means that XAS is therefore sensitive to the oxidation state, coordination and distance of the chosen atom and its nearest neighbours. XAS can be considered as two different regimes, (1) XANES which is the near-edge spectra <30 eV of the absorption edge, (2) EXAFS which are the extended x-ray absorption fine structure oscillations at >30 eV from the edge (Figure 3.5). In EXAFS, the oscillations provide more quantitative information than XANES on the local structure around the element of interest, and is the technique used in this study. The advantage of EXAFS over XRD is that it is chemically selective, and the element of interest can be at very minor concentrations if there is a high incident energy and a thick enough sample.

At the absorption edge of electrons at the core level (1s or 2p), if the incoming energy exceeds their binding energy then a photo-electron is ejected from this level and out of the atom, creating a photo-electron with wave number k (absorbing atom in Figure 3.5). An absorption edge at this energy is observed for each particular element as the electrons are promoted from the core level to the continuum. When a neighbouring atom is considered, the excited photo-electron will scatter from the electrons of this neighbour and alter the predicted absorption energy as it returns to the core-level hole. The probability that x-rays will be absorbed is given by Beer's Law that $I = I_0 e^{-\mu t}$, where I_0 is the incoming x-ray intensity, I is the intensity collected after the sample, t is the sample thickness and μ is the absorption coefficient. μ is dependant on the sample's atomic number, Z, sample density, ρ, atomic mass, M, and incident x-ray energy. It can be plotted as a smooth function of energy using the relation

$$\mu \approx \frac{\rho Z^4}{M E^3}. \tag{3.35}$$

After absorption of the energy and electron promotion, the excited state will decay back to the empty level and produce x-ray fluorescence. XAS can be measured either in transmission or fluorescence, and in this thesis only transmission will be discussed. To obtain information about one specific element, well documented energies are chosen that target the absorption edge of the particular element of interest. Depending on the energy of the edge the K, L and M-edge energies can be used. The absorption of x-rays at the core binding energy gives rise to a sharp jump that is unique in energy for all elements (Figure 3.5). XAS provides information on the absorption coefficient, μ, at or just after the absorption edge energy and I is measured after the sample and compared with the incident x-ray energy, I_0, to provide μ as a function of energy through

$$\mu(E) = log\Big(\frac{I_0}{I}\Big). \tag{3.36}$$

The EXAFS equation that considers only oscillations above the absorption edge is given as a function of energy by

$$\chi(E) = \frac{\mu E - \mu_0(E)}{\Delta\mu_0}, \tag{3.37}$$

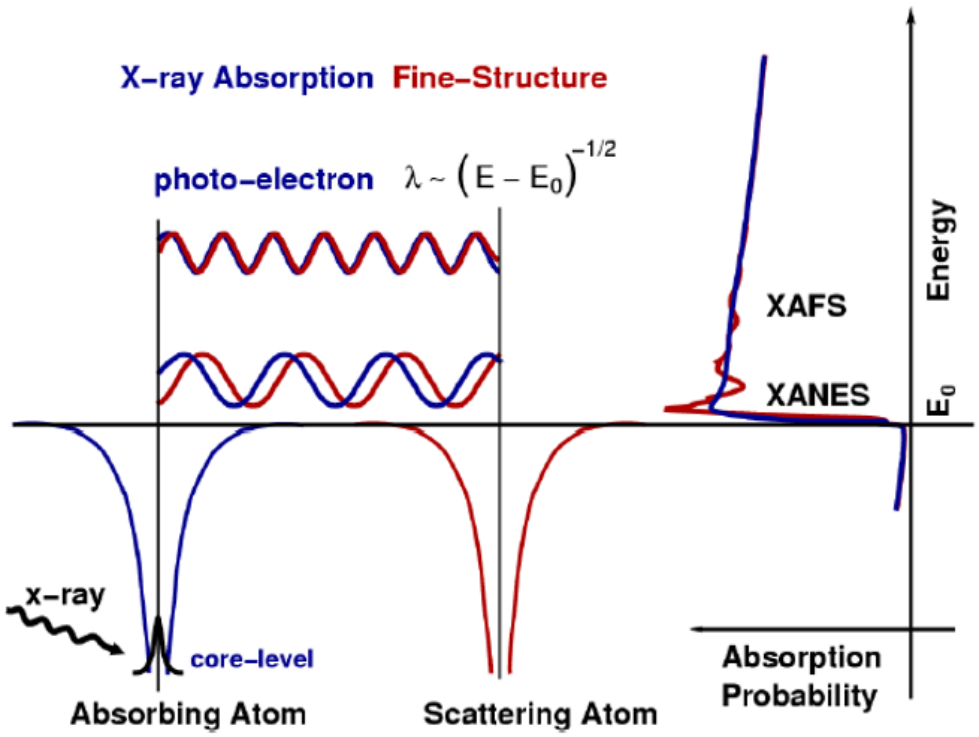

Figure 3.5 *From [85]. Photo-electric process is shown where an absorbing atom absorbs x-rays with the energy of a bound core electron E_0 and excites a core electron to the continuum, with wave number proportional to $\sqrt{E - E_0}$ (presented in blue). This causes an absorption profile for one atom given by the blue curve. XAS occurs because the photo-electron scatters from a neighbouring atom and then returns to absorbing atom with a modulated wave, giving rise to the red oscillations.*

where $\mu_0(E)$ is the absorption of an individual atom at the chosen energy and is defined by a background function of the ideal absorption profile of one atom (blue function in Figure 3.5) and $\Delta\mu_0$ is the jump in energy at the absorption edge when $E = E_0$. However, it is common to describe EXAFS in terms of the photo-electron that has been created during the absorption process, and the wave number in k-space for this photo-electron can be defined as

$$k = \sqrt{\frac{2m(E - E_0)}{\hbar^2}}, \tag{3.38}$$

for absorption edge energy, E_0, and the electron mass m. The oscillations produced in the EXAFS are then a direct result of the photo-electron wave number and are given by $\chi(k)$. Different nearest neighbour interactions and shells of atoms produce varying frequencies that are apparent in $\chi(k)$ which can be modelled by the EXAFS equation

$$\chi(k) = \Sigma_j \frac{N_j f_j(k) e^{-2k^2\sigma_j^2}}{kR_j^2} sin[2kR_j + \delta_j(k)], \tag{3.39}$$

where N is the number of nearest neighbours of atom j, and the scattering properties of the nearest neighbours are represented by their $f(k)$, the amplitude, and $\delta(k)$, the phase shift. R is the interatomic distance between the central atom and coordinating shell and σ^2 is the disorder parameter, especially prevalent at high temperatures. If the EXAFS of well known structures are obtained and the phase shift and scattering amplitudes are calculated, the EXAFS equation allows determination of N, R and σ^2 for substances where the structure is not documented. Although k in XAS is the momentum transfer and the same parameter as Q used in XRD formalism, this thesis shall always present XAS data in k and XRD data in Q as this is the generally presented format for these kind of studies.

Chapter 4

Instrumentation and Data Treatment

This chapter consists of five main sections that serve as an overview of the equipment used in this thesis and the main data processing techniques. Synchrotron sources used to obtain the data collected in this thesis are presented in 4.1 and 4.2. An overview of the general experimental techniques and high pressure cells used are covered in 4.3, and the data analysis methods used throughout this work are introduced in 4.5. Sections 4.3 and 4.5 contain both existing techniques as well as those developed for work in this thesis, including calibration of the resistive heaters for diamond anvil cells. This chapter aims to provide the relevant experimental information used throughout this thesis so that only specific experimental details are provided at the beginning of the appropriate chapters.

4.1 Synchrotron X-ray Sources

Synchrotron radiation facilities provide a high flux of x-rays that can be used to study the structure of materials, including liquids. Synchrotrons typically inject electrons into the main storage ring from previously accelerated electrons in a linear accelerator and booster ring configuration. Within the booster ring electrons are accelerated up to 3 GeV before they are injected into the main storage ring. Insertion devices and bending magnets are used in the main storage

ring to keep the accelerated electrons in a curved path. X-ray radiation is emitted and sent to each beamline from the accelerated electrons as they change direction. Within individual beamlines specialised optics in the first hutch are used to focus the high energy x-rays that are required for experiments. The beam is collimated, focused using mirrors, and the wavelength of the required x-rays is tuned at the beamline using a monochromator. On most of the insertion device beamlines used in this study KB (Kirkpatrick-Baez) mirrors are used to further focus the beam on to a focal point at the sample position. In order to maximise both the Q-range and signal intensity from the sample a compromise between higher energy wavelengths (λ), that will produce a longer Q-range, and lower energy wavelengths that will maximise the sample:background ratio, is required. For low scattering silicate liquids it was found in this study that energies between 38-42 keV provide a Q-range of $\geqslant$12 Å^{-1}, and a high enough scattering intensity from low Z samples. Good resolution in Q-space is vital for studying silicate liquids and amorphous materials, particularly for minor elements, to obtain high enough resolution in order that all the individual element contributions can be resolved. Different beamlines at differing synchrotron sources were used in this study and these are presented briefly below, with the experimental instrumentation on each beamline useful to this study highlighted.

4.2 Diffraction Instrumentation

4.2.1 I15 - Diamond Light Source

I15 at the Diamond Light Source (DLS) utilises an insertion device that provides x-rays in the range of 20-80 keV. The energy is selected by a Si(111) monochromator, and high pressure resistively heated diamond anvils cell are loaded directly on to the diffraction stage. For this study a beam of 42 keV was used, and a Perkin Elmer image plate detector was placed at 262 mm from the sample in order to access the maximum possible Q-range of 12 Å^{-1}. The x-ray beam is focused down by vertical and horizontal mirrors to a beamsize of 70×70 μm.

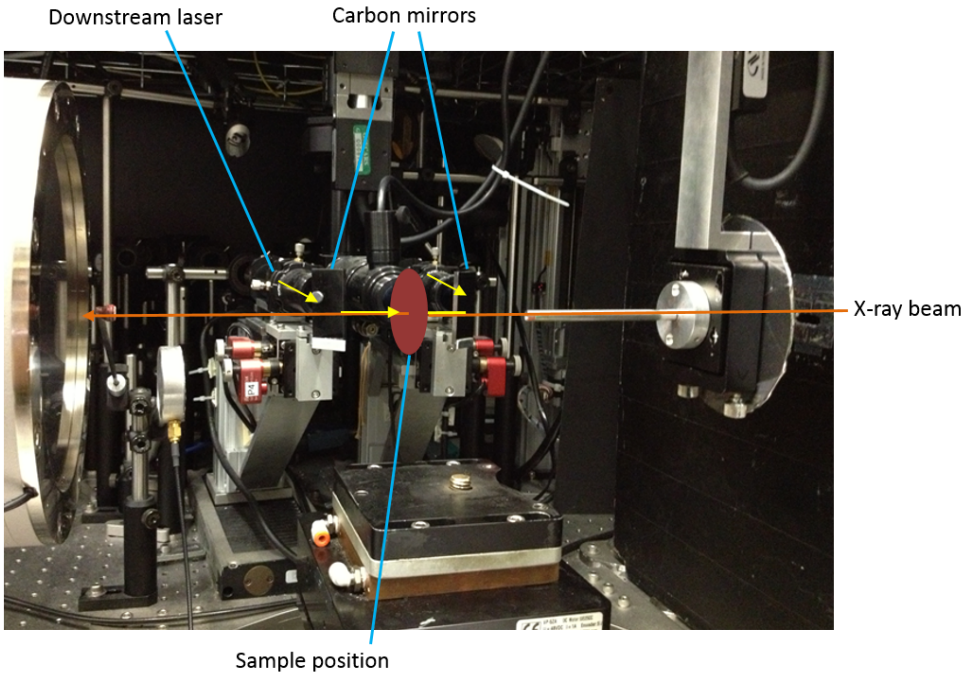

Figure 4.1 *Setup for DAC laser heating system on 13-IDD at the APS. The laser pathway on to the sample is shown by the yellow arrows. They arrive through specially aligned optics and are reflected on to the sample using carbon mirrors.*

4.2.2 13-IDD - Advanced Photon Source

13-IDD is part of the GeoSoilEnviroCARS (GSECARS) sector and is an insertion device beamline at the Advanced Photon Source (APS). It specialises in high pressure laser heating which enables conditions of the Earth's deep interior to be studied. A monochromatic beam of λ=40 keV was used with a 2D MAR-345 CCD detector which allowed between 11-12 $Å^{-1}$ in Q-space to be accessed. A YAG laser was used to heat the sample from both sides using carbon mirrors (Figure 4.1), this produces a relatively uniform temperature gradient and homogeneous sample temperature with full melting throughout the thickness of the sample (20 μm). The disadvantage of this technique is that alignment of the x-ray beam and lasers here is crucial to detect the melt signal but the carbon mirrors used to align the lasers produce a high background signal which must be removed. With the sample signal already so low this introduces further complications to the data processing (as detailed in Section 4.5.2).

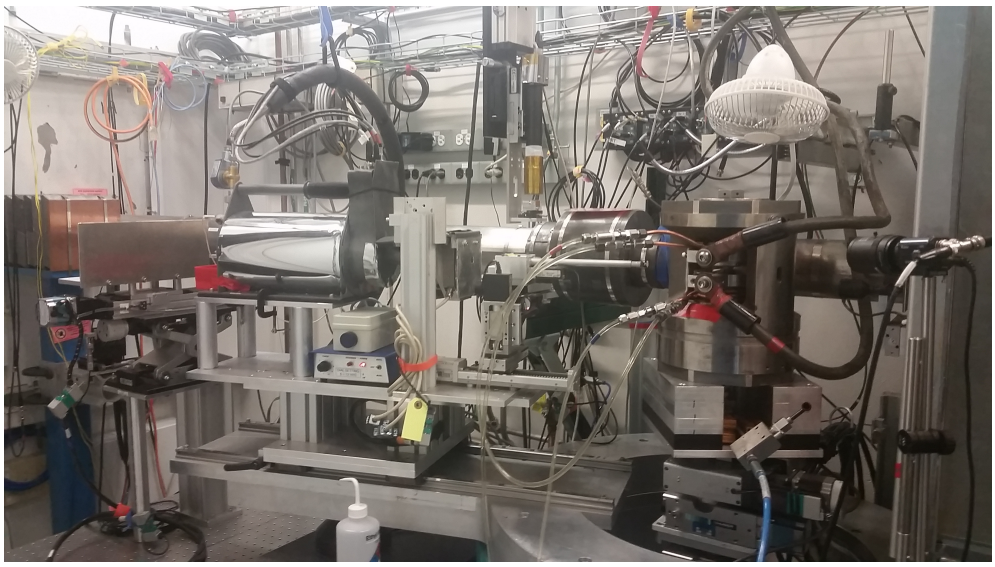

Figure 4.2 *Paris-Edinburgh press installed on 16-BM-B.*

4.2.3 16-BM-B - Advanced Photon Source

This beamline has a large volume Paris-Edinburgh press (PEP) installed for high pressure and temperature x-ray diffraction (Figure 4.2). Unlike the previous beamlines described it uses a white beam which consists of a range of energies. In this case energy dispersive x-ray diffraction data is collected on an indium solid state detector. Diffracted x-rays are filtered by slits so that only the wavelengths diffracted from the sample centre are collected, this produces a very minimal background and enhanced signal intensity which makes this an excellent beamline for studying low scattering samples. Another advantage of the PEP is that it provides very stable melting for a large (1 mm^3) sample volume, which produces high signal intensity even at temperatures >2000 K at 6-7 GPa.

4.2.4 BM-23 - European Synchrotron Radiation Facility

BM-23 at the European Synchrotron Radiation Facility (ESRF) is an x-ray absorption spectroscopy (XAS) beamline and can accommodate high pressure equipment, in this study a Paris-Edinburgh press. It operates in 16-bunch mode with an average current in the storage ring of 200 mA. It is a bending magnet beamline, but due to the fixed energy required for XAS the signal intensity is reasonable. K, L and M-edges of elements with atomic numbers from 22-76 can be probed for absorption measurements. The transmitted signal is measured by

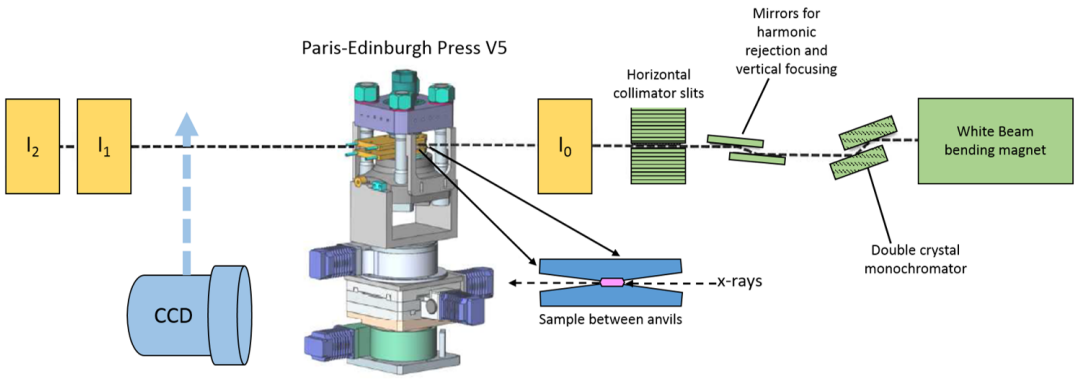

Figure 4.3 *Experimental setup for BM-23 including the use of mirrors and collimator slits to focus the incident x-ray beam. The XRD detector that can be moved in and out accordingly is highlighted as well as the XAS transmission collection chambers before and after the sample chamber, I_0-I_2. Adapted from [86].*

an ion chamber (I_1 on Figure 4.3) after the sample, and the $log(I_0/I_1)$ provides the absorption with energy, $\mu(E)$. X-ray diffraction can also be measured on the sample using a MAR-CCD detector in order to estimate the $P-T$ conditions and identify melting. A reference channel I_2 (Figure 4.3) allows simultaneous collection of the transmission from a sample and reference material.

4.3 High Pressure Techniques

In order to study silicate liquids at the conditions of formation in the Earth, high pressure and temperature conditions must be generated for the experiment. These techniques are discussed below along with the advantages and disadvantages of different setups that have applications to this study.

4.3.1 The Diamond Anvil Cell

The diamond anvil cell (DAC) is commonly used in experiments for generating high pressures. The advancements since its design in 1965 have changed the field of high pressure research with pressures exceeding >700 GPa reported in 2015 [87] using double staged anvils with nanopolycrystalline diamond semi-balls. The force in a DAC is generated from the two opposed diamond culets with the sample contained within a usually metallic gasket between the tips (Figure 4.4A). Diamonds are an excellent material for use as anvils as their hardness enables the

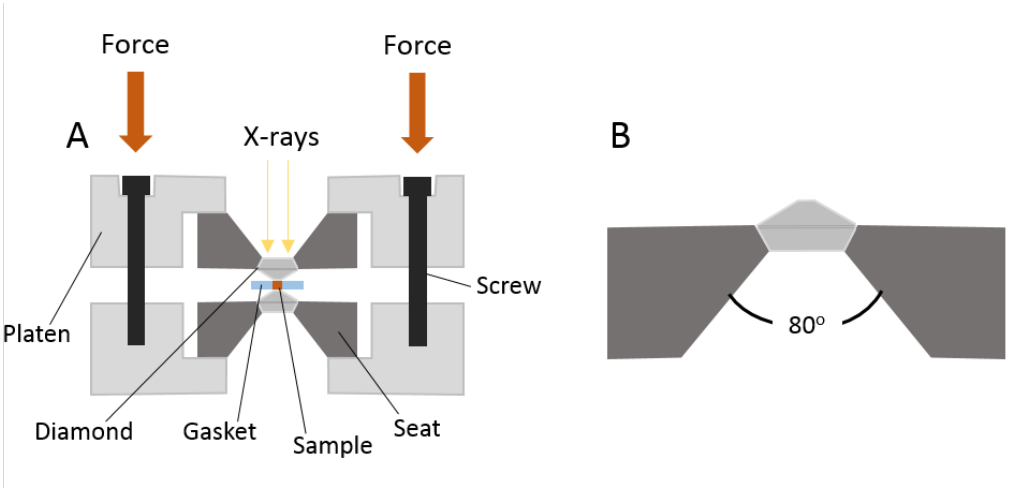

Figure 4.4 *A: Schematic design of a four-post diamond anvil cell. B: Boehler-Almax seat design with wide angle opening.*

generation of very high pressures, and their transparency to x-rays and other radiation also allows access to the samples at high pressure. Although there are many cell designs the four-post Mao-Bell symmetric design was used in this work. The force on the culets is generated via tightening of four screws which applies force to the platens that hold the seats (Figure 4.4A). Pressure is monitored via Raman spectroscopy of a ruby inserted into the sample chamber (Section 4.3.5). The diamonds are fixed with stycast on to tungsten carbide seats which provide high mechanical strength and do not require the x-rays to pass through them. As the samples in this study are not rotated during diffraction, the Q-range achievable is limited by the opening angle of the DAC seats. For liquid diffraction a high Q-range is essential, therefore wide angle opening Boehler-Almax seats [88] are used (Figure 4.4B) which open with an aperture angle of ∼70-80°. These seats also provide greater support for the diamonds and can easily access pressures up to 120 GPa.

Rhenium gaskets were used in this thesis for all DAC measurements in order to contain the sample radially during uniaxial pressure generation from the anvils. As this uniaxial stress is high, conditions within a DAC are often not hydrostatic and a pressure transmitting medium can be used to minimise shear stress on the sample. In this thesis as the samples are amorphous or molten, a P-transmitting medium was not used as liquids are unable to support shear stress. The gasket is pre-indented to the appropriate thickness so that a small hole can be drilled in the centre of the culet. The sample and pressure calibrants (Section 4.3.5) are loaded into the hole and the cell is closed. Heating of the sample can be

generated by laser or resistive heating and both will be discussed below. Due to the DAC designs used in this thesis x-rays are always passed through the back of the diamonds and through the gasket hole so no scattering from the gasket or seats should be present (Figure 4.4A).

4.3.2 Resistively Heated Diamond Anvil Cells

Internal resistively heated DACs (rh-DACs) are advantageous for low scattering liquids as the entire sample is heated, which maximises the signal intensity from the melt. The heaters function via a current flowing through a metallic resistance heater. Resistive heaters used here were developed with platinum wire. Pt was chosen due to its high ductility as it is easy to coil thin wires, as well as its oxidation behaviour, as only a very thin PtO_2 layer is formed at T>4-500°C which disappears with further heating [89]. The heater is placed around the sample chamber and to minimise oxidisation of the wire and diamonds at high temperature, a flow of noxal gas ($Ar/H_2 5\%$) was passed over the diamonds during the experiment. To prevent the heating coil touching the cell body the heater is encased in heatproof cement with a large enough central hole for the gasket (Figure 4.5). An external heater is also used in conjunction to raise the temperature of the entire cell body. Temperature was read by a K-type thermocouple inserted close to the tip of the diamond and sample chamber. One limitation of rh-DACs is that the temperature is limited to $\leqslant 1000^o$C but even at these temperatures oxidation and failure of the diamond anvils can occur rapidly.

Heating Calibration

The resistive heating cell assemblies were made by coiling a 250 μm diameter Pt wire with at least 20 turns around a 10 mm outer diameter alumina ring. It was critical to ensure that the coils were very evenly spaced with no contacts to prevent any shorts when a current was applied. More accurate coiling and coil spacing greatly increased the stability of the current during heating and the length of the heater life-span. The ends of the wires were coiled around a 1.5 mm diameter molybdenum tube in order to make a connection for the heating cables. This coil was then placed within a pyrophyllite disk cut to the dimensions of the cell body to provide as much insulation as possible (Figure 4.5). Sheets of mica were placed between the pyrophyllite and cell body to minimise any risk of

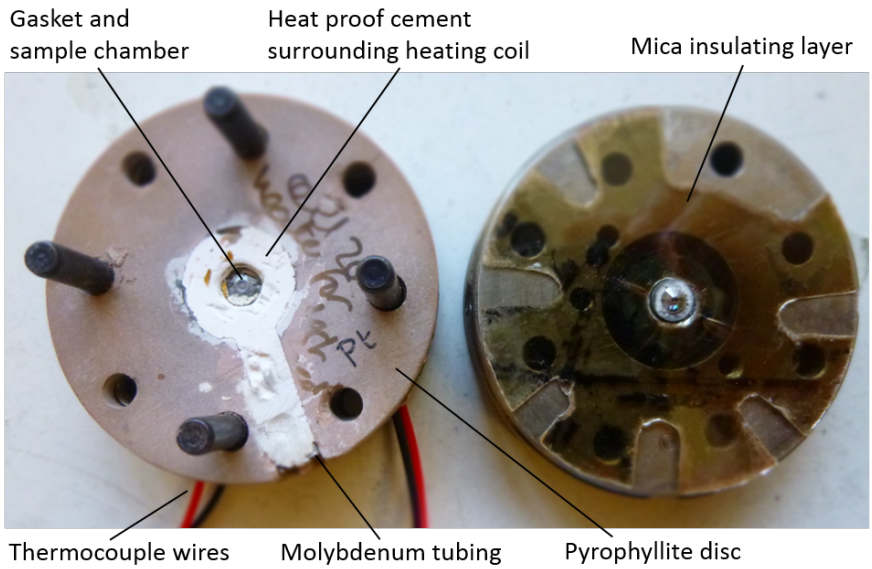

Figure 4.5 *Heater contained within a pyrophyllite disk and placed on open diamond anvil cell. Aspects from the discussion in the text are highlighted in the figure. The cell body is 5 cm across for scale.*

contact between the cell and heater. The coil and ring leave a 5 mm diameter free middle where the diamonds and gasket can be accessed (Figure 4.5). K-type thermocouples (TC) were used to measure the temperature in the centre of the heater and were placed as close as possible to the edge of the diamond culet (Figure 4.6), without direct contact with the diamonds to avoid incorrect T measurements due to heat conduction by the diamonds. As the Pt wire heating coils had not previously been used they required calibration in order to estimate the error on the thermocouple temperature, and any temperature variation that might occur as distance from the sample chamber increased. Two methods were used to constrain the errors on temperature:

1) **Samples of known melting temperature:** Samples of known melting T, lead (327.5°C), aluminium (660.3°C), and sodium carbonate (851°C), were placed within separate holes drilled in the gasket (Figure 4.7 top). Visual observations during heating were used to see at what point the samples became molten (Figure 4.7a-d). The power and temperature readings were noted at this time to monitor if the T reading was within the expected melting T for each sample (Figure 4.8). Two thermocouples were placed at either side of the culet (Figure 4.6) in order to measure how T varied with thermocouple placing. One thermocouple placed directly at the edge of the culet (TC1, ideal position) as close to the sample chamber as possible and another 1-2 mm further away (TC2 max. distance). The

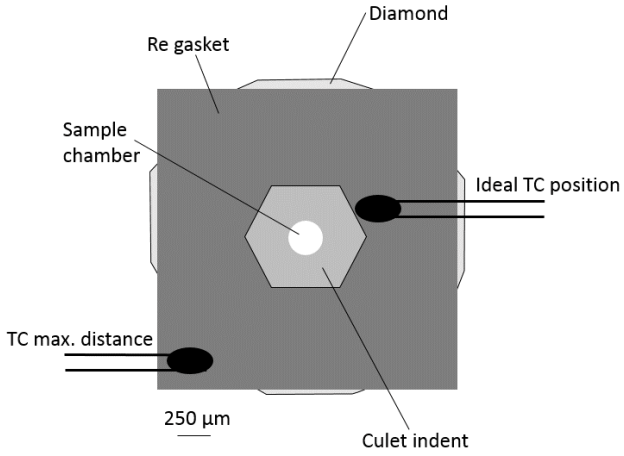

Figure 4.6 *Position of thermocouples (TC) around the sample during testing. Ideal position is as close as possible to the sample chamber (upper TC) but not touching the diamond culet. The worst position is furthest away from the sample chamber (approx. 1-2 mm) and is represented by the bottom TC at the edge of gasket.*

thermocouples were secured in position by heatproof cement. In this calibration, sample melting was monitored via video and samples were observed continually during heating (Figure 4.7). After 3 runs with different heaters it could be seen that the average power required to melt the sample produced a temperature reading on the thermocouple closest to the sample within 10-20°C of the expected melting temperatures. However, temperature varied by up to 50°C with a 2 mm increase in TC distance away from the centre. With the TC diameter at approximately 0.6 mm the size of the TC itself should not dramatically affect the T measurements. With this information, during the experiment it was essential to know that the TC was fixed as close to the sample chamber as possible, and heatproof cement was used to glue the wire covering in the same position before each cell was closed.

2) **Pt/NaCl Calibration:** Pt and NaCl were both loaded in separate holes in the gasket and the cell was gently closed to keep the P at ambient conditions but sealed. X-ray diffraction was collected approximately every 100^{o}C from the TC readings at I-15 at the Diamond Light Source. From diffraction patterns, the lattice parameter, a, of both Pt and NaCl were extracted and equations of state for each sample were used to calibrate both pressure and temperature (Section 4.3.5). This process was repeated at different pressures and the average temperatures calculated for four experiments are shown in Figure 4.9. At each diffraction measurement the power and TC readings were also monitored to compare to the

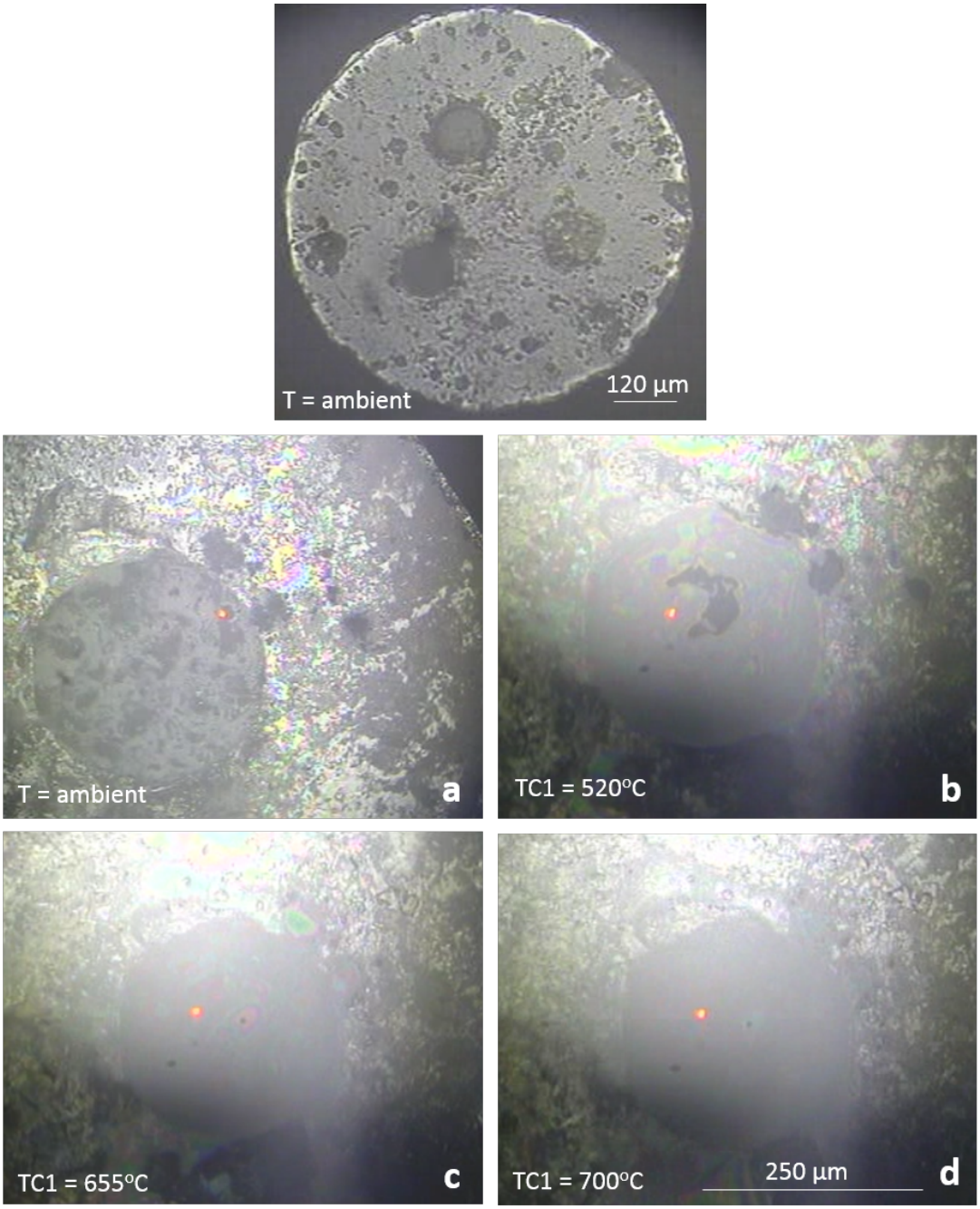

Figure 4.7 *Top: 800 µm gasket drilled with 3 holes and filled with samples of known melting T as described in text (from top clockwise: NaCl, Pb and HPG sample). a-d: One example of melting of the HPG sample during a heater test to determine an estimate of the melting T. See darker patches and crystals at lower temperatures (a-b), which disappear upon heating until the sample is homogeneous in d.*

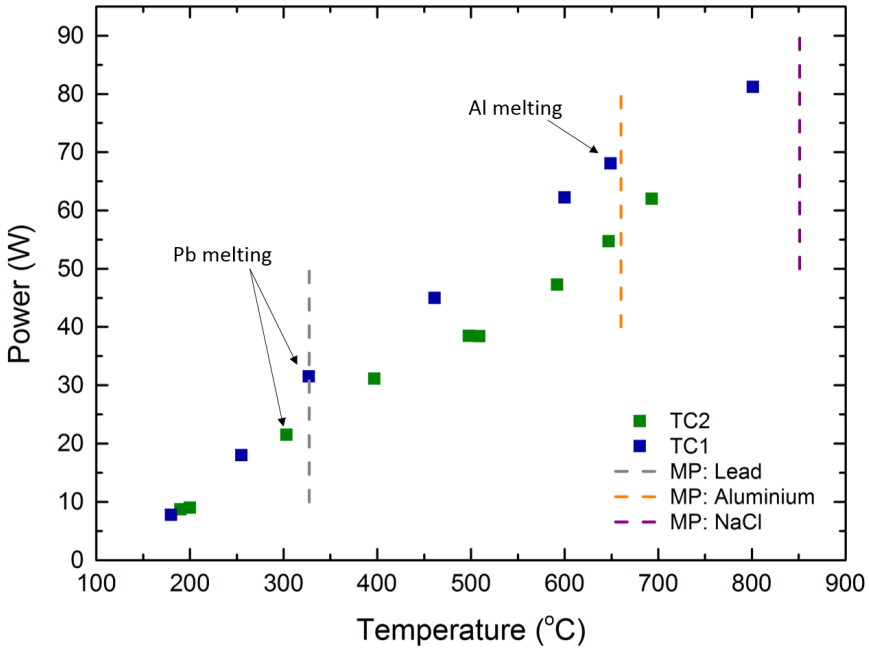

Figure 4.8 *Average from 3 experiments with thermocouples (TC) placed at different distances from the sample. TC1 placed as close to sample chamber as possible (Figure 4.6 ideal position). TC2 1-2 mm away (Figure 4.6 max. distance). Dashed lines represent known melting temperatures of Pb, Al and NaCl.*

derived temperatures. These results are in good agreement and have a similar gradient to those of the measurements in Figure 4.8.

In both tests it can be seen that there is an error up to 50°C that must be considered on all measurements. This comes from the risk of the TC distance from the sample not being ideal and the error from the two different calibration methods (Figure 4.10).

Improvements to Resistive Heaters

In order to increase the temperatures reached by the resistive heaters, a higher resistivity, ρ, would be required. Resistivity is affected by length and cross sectional area of the material in question through $\rho = R.A/L$, where R is the resistance of the material, A is the cross sectional area, and L is the length. Platinum wire was used due to its high resistance and relative inertness, which prevents oxidation even at high temperature. Oxidation of the wire would decrease the efficiency of the heater so materials such as W, Pb and Ti, even though they have a higher resistance, would oxidise too quickly on heating. Mo

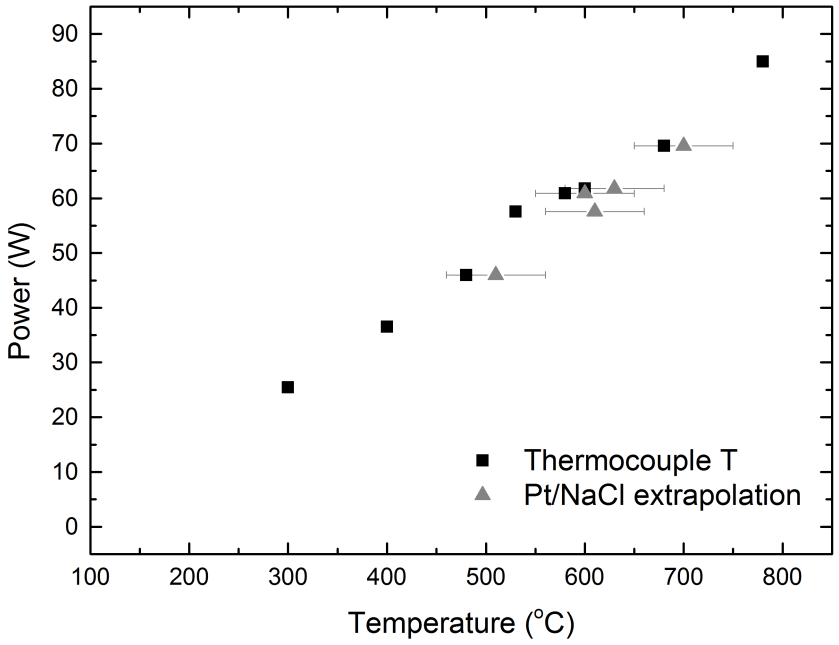

Figure 4.9 *Pt/NaCl calibration points plotted with the T read by the thermocouple (TC1) at the same power.*

wire was trialled in this study and did not seem to regularly reach as high temperatures as the Pt heaters, most likely due to the difference in oxidation behaviour of Mo, which continues to oxidise above T >400°C [90], and difficulty in accurately coiling it, as it is less ductile than Pt. Two improvements could be made to increase the resistivity of the Pt wire heaters: (1) a greater number of coils would increase the length of the wire; (2) thinner wire to decrease the cross sectional area. This would also increase the number of coils that could be wound around the alumina ring. In order to achieve a higher number of coils with a wire <250 μm in diameter, this would require extremely precise coiling, possibly using a machine, to ensure regularity of coil spacing and prevent damaging the thin wire. As Pt wire is malleable it is much easier to work with than other metals; however any small defects in the wire will increase the chance of failure with increasing power. Another possible method to improve radiation to the gasket/sample chamber would be not to cover the inside of the coil with heat proof cement; however this has limitations as it is essential the heater does not come into contact with the gasket, and the cement acts as an insulator to keep the radiative heat within the sample chamber.

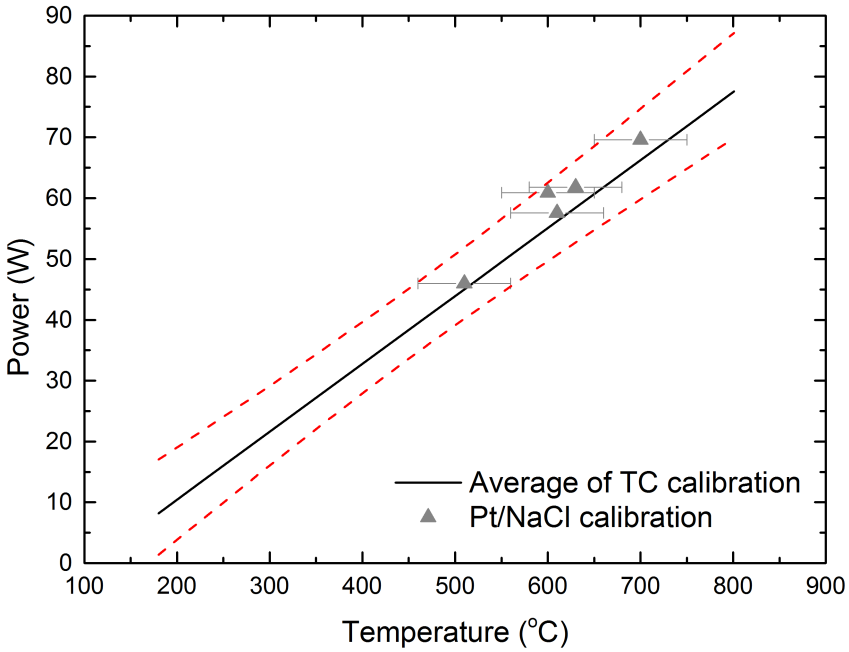

Figure 4.10 *TC calibration using a best fit average of all the heater test data from Figure 4.8, and the error on the line of best fit (red dashed lines). Pt/NaCl calibration points plotted on this show they lie within error of the average for temperature versus power.*

4.3.3 Laser Heated Diamond Anvil Cell

The laser heated DAC requires an unmodified diamond anvil cell with heating generated by lasers from an external setup on the beamline. Samples used in laser heating experiments using a YAG laser are required to be thin enough to melt with the laser (<50 μm), and contain a metal coupler homogeneously distributed within the sample that absorbs the laser wavelength. In the case of laser heating, as the diamonds are such good thermal conductors, a thermal insulation layer is required between the sample and diamonds and in this study SiO_2 was used. Even though exceedingly high temperature conditions can be generated with laser heating it can be difficult to estimate or target temperature accurately. The other disadvantage over rh-DACs is the very localised heating of the sample (the size of the laser spot is often <20 μm). This induces large temperature gradients and can cause diffusion or reaction between the sample and thermal insulation layers during heating. In this study, Nd was used as the laser coupler as it has an excitation wavelength appropriate for the YAG laser used on GSECARS, and its efficiency as a coupler is described in Chapter 8.

4.3.4 Paris-Edinburgh Press

Other techniques that can generate less extreme pressures and high temperatures are large volume presses. The Paris-Edinburgh press (Figure 4.11) can generate pressures routinely up to 15 GPa [91] at ambient temperature, and high temperatures up to 2300 K at 10 GPa [92]. The PEP has the advantage of a large sample volume (up to 2 mm^3), which for low scattering samples provides excellent signal intensity. In chapters 5 and 6 the V-type press is used with individual details discussed within the chapters. In general the sample is contained within a deformable gasket compressed by two shaped, opposed tungsten carbide anvils (Figure 4.11). The hemispherical sample chamber provides a large sample volume but requires good gasket design to reduce the risk of blow out at high pressure, especially during heating. High temperature conditions are generated by resistive heating through an internal graphite furnace (Figure 4.12). During heating, current is sent through the circuit at a constant rate and the temperature was monitored using previous thermal expansion calibrations by [92, 93]. In this study two general gasket designs were used: (1) Boron-epoxy (BE) 7/2.4 mm (where this is the ratio between the outer cell and heater diameter) after [94] (Figure

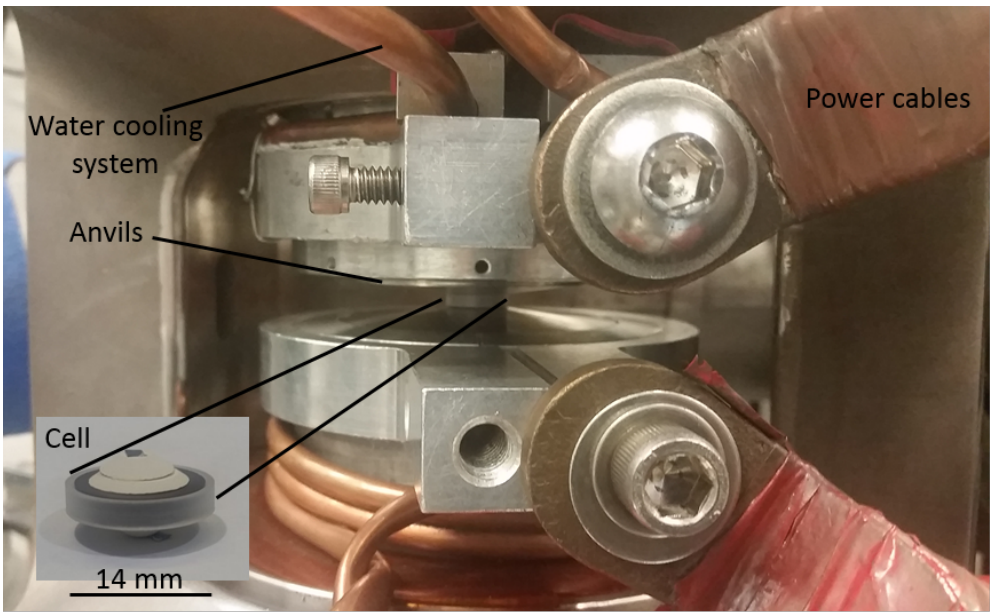

Figure 4.11 *PEP anvil setup, including heating cables, water cooling system and a 3/14 mm zirconia cell design (design B from 4.12).*

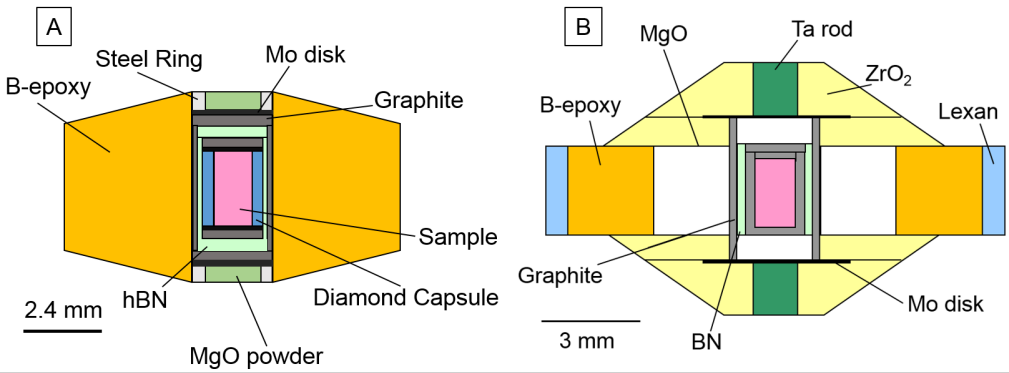

Figure 4.12 *PEP basic cell designs used in thesis. A: From [94] 7.2/2.4 mm boron-epoxy gasket design. B: From [93] using zirconia cap design.*

4.12A); (2) zirconia caps and MgO by [93] of 14/3 mm (Figure 4.12B).

MgO or BN act as a P-transmitting medium to the sample and the BE gaskets in both cases are designed to slightly extrude outward with P but contain the sample within a confining P. The low scattering and absorption of the BE makes it an ideal gasket medium as a high signal intensity, with little or no background, is obtained from the sample. Modifications were made to these cell assemblies for individual experiments and these are discussed in the relevant experimental chapters (5 and 6). Due to the decrease in space between the anvils at high pressure and strain on the gasket, the maximum pressure achievable in the PEP experiments for this study is 8 GPa at 2000 K.

4.3.5 High Pressure Calibration

In this study two standard techniques for determining the pressure on the sample have been used: (1) ruby fluorescence (DAC only), (2) the internal pressure standard method (PEP and DAC). These are described briefly below.

Ruby Fluorescence

In DAC experiments one regularly used method of determining pressure within the sample chamber is that of ruby fluorescence [95]. A small (<5-8 μm) ruby is inserted into the sample chamber, it must be carefully placed away from the centre of the sample so it does not interfere with diffraction measurements, but also not too close to the edge of the gasket so that it may be squeezed by the gasket as this will not represent the pressure on the sample. Ruby is Cr^{3+} doped Al_2O_3 and electronic transitions of the Cr^{3+} ions cause distinctive emission lines [95]. At ambient pressure and temperature these emission lines can be seen via use of laser-induced fluorescence at R_1 =692.86 nm and R_2 =694.25 nm. As pressure increases the Cr^{3+} ion environment is altered and this produces a shift in the emission spectra as the emitted wavelength changes. The calibration used in this study is that of Mao *et al.* [96] and is valid over all the pressure range in this thesis. Pressure, P in megabars, can be determined by

$$P = \frac{A}{B}\left\{\left[1 + \left(\frac{\Delta\lambda}{\lambda_0}\right)\right]^B - 1\right\}, \tag{4.1}$$

where difference between the R_1 wavelength at ambient conditions, λ_0, and at high pressure, is $\Delta\lambda$, and A and B are constants of 19.04 and 7.665 respectively. The limitation of ruby fluorescence in this study is that at high temperatures the the R_1 emission has a large temperature dependence and results in large errors in the P calibration for inaccuracies in T of >5 K. Broadening of the R_1 and R_2 peaks also occurs above ~550 K so that they cannot be individually distinguished [97]. This level of accuracy in T measurements was not achievable in this study and therefore, ruby fluorescence is used initially at ambient temperature to target a starting P in DAC experiments, but during the experiment an internal calibrant is used to monitor any P changes with temperature.

Internal Pressure Calibrant

In this case pressure is determined through the known equation of state (EOS) of a pressure standard inserted in the sample chamber. Using x-ray diffraction the cell volume and lattice parameters can be determined and subsequently the P can be estimated using these parameters in the EOS. As for ruby, the standard must not react with the sample and should not undergo any phase changes in the pressure range of interest unless they are well documented. These pressure standards typically include transition metals or compounds with a simple structure. In this study Pt and NaCl were used in the DAC experiments, with hexagonal-BN (hBN) and MgO used in the PEP experiments.

Platinum (Pt) placed within the sample chamber was monitored via x-ray diffraction during the experiment. Pt adopts a face-centered cubic structure which has distinct (111) and (200) Bragg peaks that can be monitored with P as the positions of these peaks shift as the crystal is compressed. A third-order Birch-Murnaghen EOS which relates the volume change within the sample to the pressure using a calculated bulk modulus from previous calibrations is then used to estimate P through

$$P_{300K} = \frac{3K_0}{2}\left[\left(\frac{V_0}{V}\right)^{7/3} - \left(\frac{V_0}{V}\right)^{5/3}\right]\left(1 - \frac{3}{4}[4 - K_0^{'}]\left[\left(\frac{V_0}{V}\right)^{2/3} - 1\right]\right), \qquad (4.2)$$

where V_0 is the original crystal volume in Å^3 of Pt at ambient conditions, V is the volume determined from the lattice parameters measured at high P, and K_0 is the bulk modulus ($K_0^{'}$ is the derivative). After ambient temperature measurements have been made this provides P_{300K}, and using a temperature correction the pressure at high $P-T$ can be determined through $P = P_{300K} + P_{HT}$ where P_{HT} is the thermal correction for high temperature measured by $\delta V/\delta T$ at a constant pressure or estimated theoretically. The pressure is also constrained by the minimum P on the sample as determined by ruby fluorescence at ambient conditions. The pressure of the sample was determined at ambient temperature, with a Pt calibrant, using the pressure-volume relations of [98], and during high temperature measurements a thermal correction from [99] was applied to account for thermal expansion. A small beamsize must be used at high P to avoid contamination of the sample diffraction by the P-standard as the sample chamber is reduced in size. NaCl was also used as a P-standard during resistive heating

calibrations (Section 4.3.2) and the same EOS methodology was used, using the bulk modulus and first P-derivative from [100] and the thermal expansion parameters from [101]. This was in order to solve for unknown P and T by obtaining the lattice parameters for both NaCl and Pt and solving simultaneously. For the PEP experiments, MgO or hBN x-ray diffraction patterns were used as pressure standards using parameters from [102] and [103], with a Pt foil also inserted into the sample chamber in some cases. In all cases as many Bragg peaks as possible were fit in order to determine the most accurate lattice parameters.

4.4 Glass Preparation

The haplogranite (HPG) and anorthite$_{36}$-diopside$_{64}$ (AnD) glasses were synthesised by mixing together the appropriate amounts of reagent grade oxides (SiO_2, Al_2O_3, MgO) and carbonates (K_2CO_3, Ca_2CO_3, Na_2CO_3) from Alfa Aesar with purity >99.99%. The oxide and carbonate powders were initially dried in the furnace at 1000 K and 450 K respectively, to remove any water or organic contaminants. The mixed powders were ground in an agate pestle and mortar and decarbonated for 12 hours at 1273 K on a slow ramp. They were then fused at 1873 K in a platinum crucible for 1 hour. The molten glass was quenched by immediately placing the crucible into cold water. The glass was checked for the absence of crystals, crushed and re-ground under acetone and finally fused again three times to ensure homogeneity. Trace elements for Chapters 6, 7 and 8 were added in the form of high purity Y_2O_3, ZrO_2, Lu_2O_3 or Nd_2O_3 (>99.99%) at the desired concentration to a portion of the ground glass in order to have both a doped and plain sample of each composition for comparison. The mixture was ground for 1 hour, and fused once more in a platinum crucible followed by water quenching. This glass was crushed, re-ground, and fused 3 times at 1873 K to ensure homogeneous distribution of any trace elements. All glasses were free from bubbles and show no signs of crystallisation. The samples were crushed to a fine homogeneous powder before being loaded.

In order to lower the melting temperature of the haplogranite to access melting at temperatures achievable in a resistive heated diamond anvil cell (<1000 K), water was added to the sample via high pressure addition using a piston-cylinder. Platinum capsules were welded containing finely ground haplogranite with 10 wt.% H_2O and held for 4 hours at 2 GPa and 1670 K to ensure full homogenisation. The samples were fast quenched by immediately cutting power

to the press. Final totals of water were between 8-10% over 4 runs measured using Raman spectroscopy and final electron microprobe totals.

4.5 Angle Dispersive X-ray Diffraction Data Treatment

This section will describe the processes required to correct the raw intensity data before analysis of the diffraction data (as presented theoretically in Chapter 3) can be undertaken. These corrections include initial image plate processing, polarisation and normalisation corrections, removal of incoherent scattering, and integration to reciprocal space in order to obtain the function $I(Q)_{coh}$ as given in Chapter 3.1.3, which contains information solely from the scattering between the atoms in the sample.

4.5.1 Image Plate Processing

For diamond anvil cell experiments during diffraction Bragg peaks arise due to scattering from the single crystal diamond anvils. These usually occur at distances of $>5\,\text{Å}^{-1}$ and appear as distinct spots on the image plate (Figure 4.13b). At different sample angles the scattering can be minimised and before each final measurement is taken the cell is rotated by up to 2-3° in X to minimise the diamond diffraction (Figure 4.13b-c). As only data from the sample signal should be processed, the initial data processing step is to remove these Bragg peaks from the image plate. This can be done by applying a mask in FIT2D [104] or Dioptas [105] to the peaks (Figure 4.13d). It is important to mask enough of the surrounding area so no pixels are left on the image plate with contributions from diamond scattering. By applying this mask only to the selected areas the remaining image plate can then be integrated and the liquid signal is not compromised due to the radial nature of the image. A dark image plate (Figure 4.13a), which is the scattering on the detector when no beam is present, is collected before each measurement for the same length of time as the sample scan, this is automatically removed from the sample image plate in order to remove any inherent detector noise.

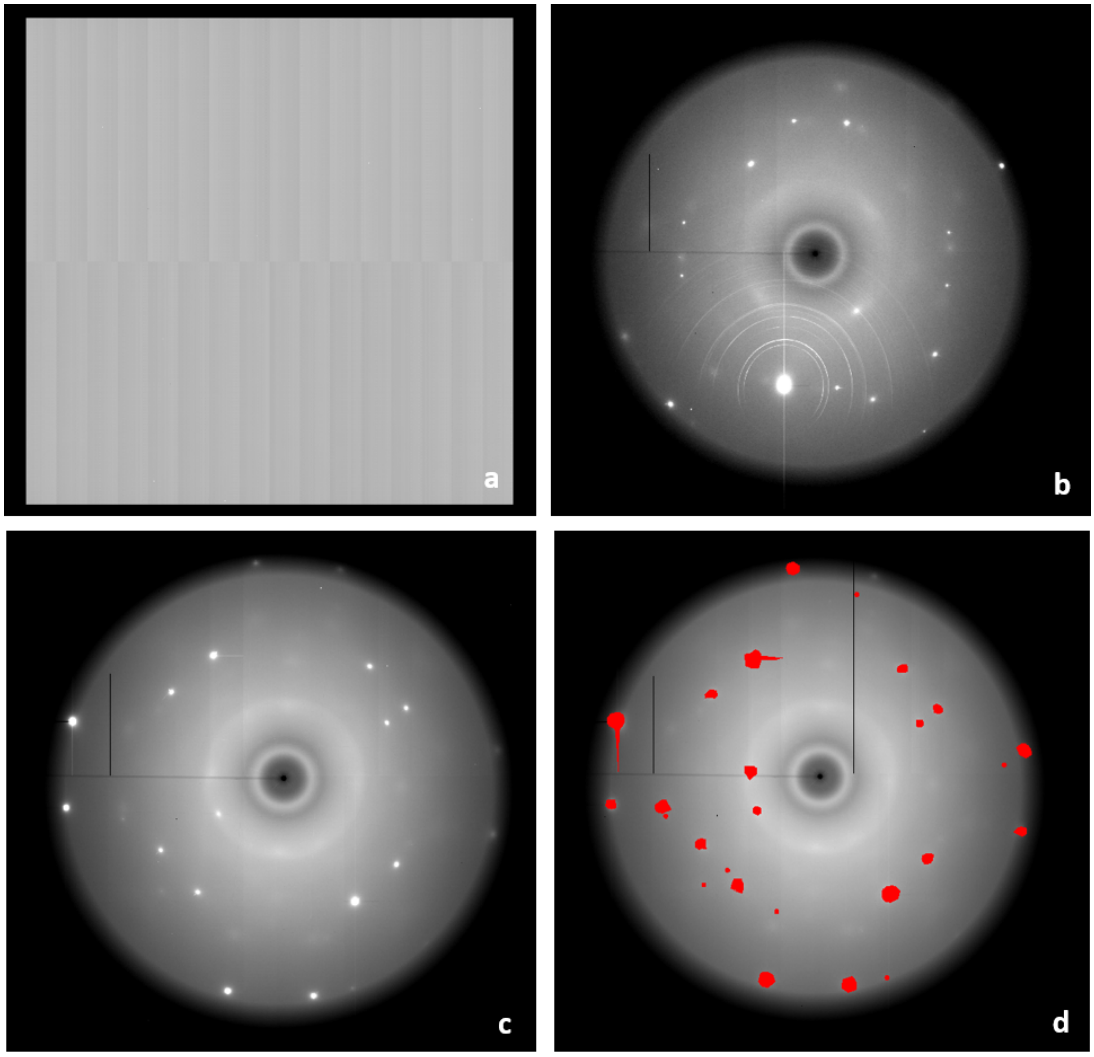

Figure 4.13 *Image plates on Dioptas [105]. a: Dark image collected after each data point. b: Example of severe diamond diffraction before rotation in X. c: Image plate with suitable diamond Bragg peaks after 0.1-0.4˚rotation in X centring. d: Image plate for c with mask applied (red). The black horizontal line is the beamstop, this can be masked or not as long as the same mask is applied to the background diffraction pattern.*

4.5.2 Structure Factor Extraction

The measured experimental intensity, $I(Q)_{meas}$, contains scattering by both the sample and background contributions. In order to isolate the intensity that contains only the coherent structural information, $I_{coh}(Q)$, corrections for background intensity, $I_B(Q)$, incoherent scattering, $I_{inc}(Q)$, and attenuation, $A(Q)$, from the sample must be made to the measured intensity which can be given by

$$I(Q)_{meas}P(Q) = \frac{A(Q)}{\alpha}(I_{coh}(Q) + I_{inc}(Q)) + XI_B(Q). \tag{4.3}$$

$I_{inc}(Q)$ is the sum of the self, $\sum c_y f_y(Q)^2$, and Compton scattering, $\sum c_y C_y(Q)$, where these sum over all the species in the sample and c_y is the concentration of species y [44]. $A(Q)$ is the attenuation caused by the thickness of the sample, with $P(Q)$ the correction to account for polarisation of the x-ray beam at the synchrotron. X and α are scale factors and normalisation parameters respectively and are discussed in more depth below.

Polarisation Corrections

Both FIT2D [104] and Dioptas [105] apply corrections for the incident beam polarisation. This accounts for the polarisation, $P(Q)$, which arises from the different perpendicular and parallel x-ray beam intensities caused by the beamline optics. The polarisation is measured on a standard of known structure, CeO_2, before the experiment. By using the known Bragg peak positions for CeO_2, the distance between the sample stage and detector can also be calculated and used during integration of the image plate. The image plate is radially integrated to a one-dimensional diffraction pattern given in 2θ where θ is half the angle between the incident and diffracted beam. The patterns are also normalised to a constant incident beam flux by measuring the flux on the detector. In x-ray diffraction, usually geometrical effects from the sample, particularly the attenuation of the x-ray beam, $A(Q)$, due to the sample thickness, t, need to be considered. However, due to the very low absorption of the sample, and t is of the order $<80\,\mu$m with a scattering angle 2θ $<30°$, the value of this function is $<0.01\%$ of the signal intensity and makes no difference to the overall sample function.

Background Removal

Background removal, $I_B(Q)$, for DAC experiments is possibly the most important step in the data analysis. This is not required for the EDXD PEP experiments in this thesis due to the very low background signal because of the soller slits on the beamline. Empty DAC background patterns are collected to measure the scattering contribution from the single crystal diamond anvils, which has been filtered by the gasket aperture and surrounding air. In order to remove this from the sample signal correctly the empty cell scans must be collected for the same length of time under identical conditions. As the aperture of the gasket hole has an effect on the background function this can be difficult if the gasket is damaged or deformed during heating. The image plate must have the same mask applied to it to ensure no features in either pattern are because of the radial integration and the same corrections for polarisation and flux normalisation should be applied. After integration the background should scale to the sample (plus background) signal and both should be equal at approximately 25-30 2θ (Figure 4.14) where there is no longer any diffraction from the sample itself, and contributions from the cell should be identical in both cases. The background can be scaled slightly if necessary (parameter X in Equation 4.3), but this should be minimal. If the background is appropriate it can be removed successfully; however, if a large scale factor >5% is required the data needs to be discarded.

Normalisation

As described in Chapter 3 the data are corrected for the effect of the inelastic (Compton) and self scattering of the atoms in the sample. The total incoherent scattering for the sample is calculated through

$$I_{inc} = \sum_{sample} c_y C_y(Q) + \sum_{sample} c_y f_y(Q)^2. \tag{4.4}$$

The sample signal is scaled to this function as shown in Figure 4.15A so that the sample function oscillates around the incoherent scattering intensity at the highest 2θ angles. By removing the self and Compton scattering contributions from the diffraction pattern the underlying scattering from the individual constituent atoms are removed, leaving the $S(Q)$ dependant only on the scattering between the atoms. The normalisation factor required to scale

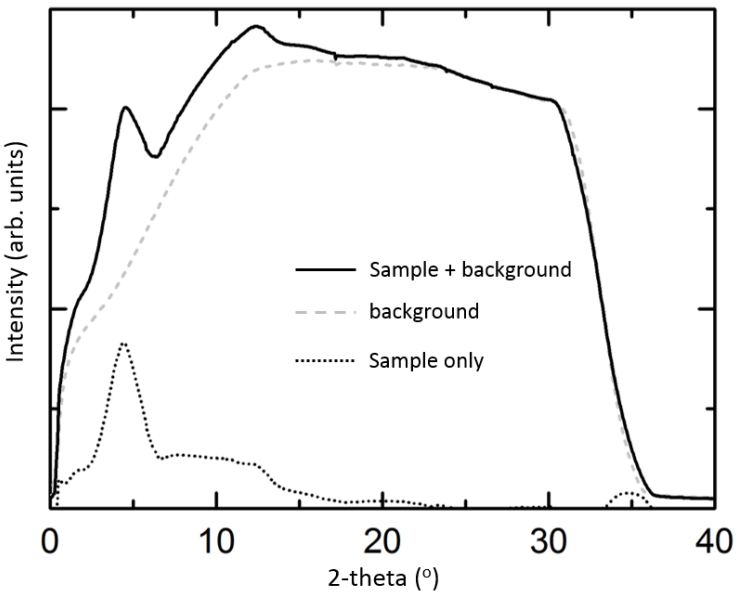

Figure 4.14 *Process of background scaling and removal for haplogranite glass within a resistively heated DAC, background must be scaled to sample pattern at 30 2θ where there should be no scattering from these samples. Background is then subtracted from the sample plus background spectra.*

the sample intensity is given by α, following the method of Krogh-Moe and Norman [106, 107], and can be calculated using the limit that as $\lim_{r\to 0} G(r) = 0$, $\sin(Qr) = Qr$ and therefore

$$-2\pi^2 n_0 = \int_0^{Qmax} \big[S(Q) - 1\big] Q^2 dQ, \tag{4.5}$$

and following from Equation 4.3 the total scattering in the sample chamber is given by

$$I_{sample}(Q) = \frac{A(Q)}{\alpha}\big[I_{coh} + I_{inc}\big], \tag{4.6}$$

which can be rearranged to find the normalisation constant α for the coherent scattering through

$$\alpha = \frac{-2\pi^2 n_0 + \int_0^{Qmax} I_{inc}(Q) Q^2 dQ}{\int_0^{Qmax} I(Q)_{samp} Q^2 dQ}. \tag{4.7}$$

Incorrect normalisation can produce significant artefacts within the Fourier

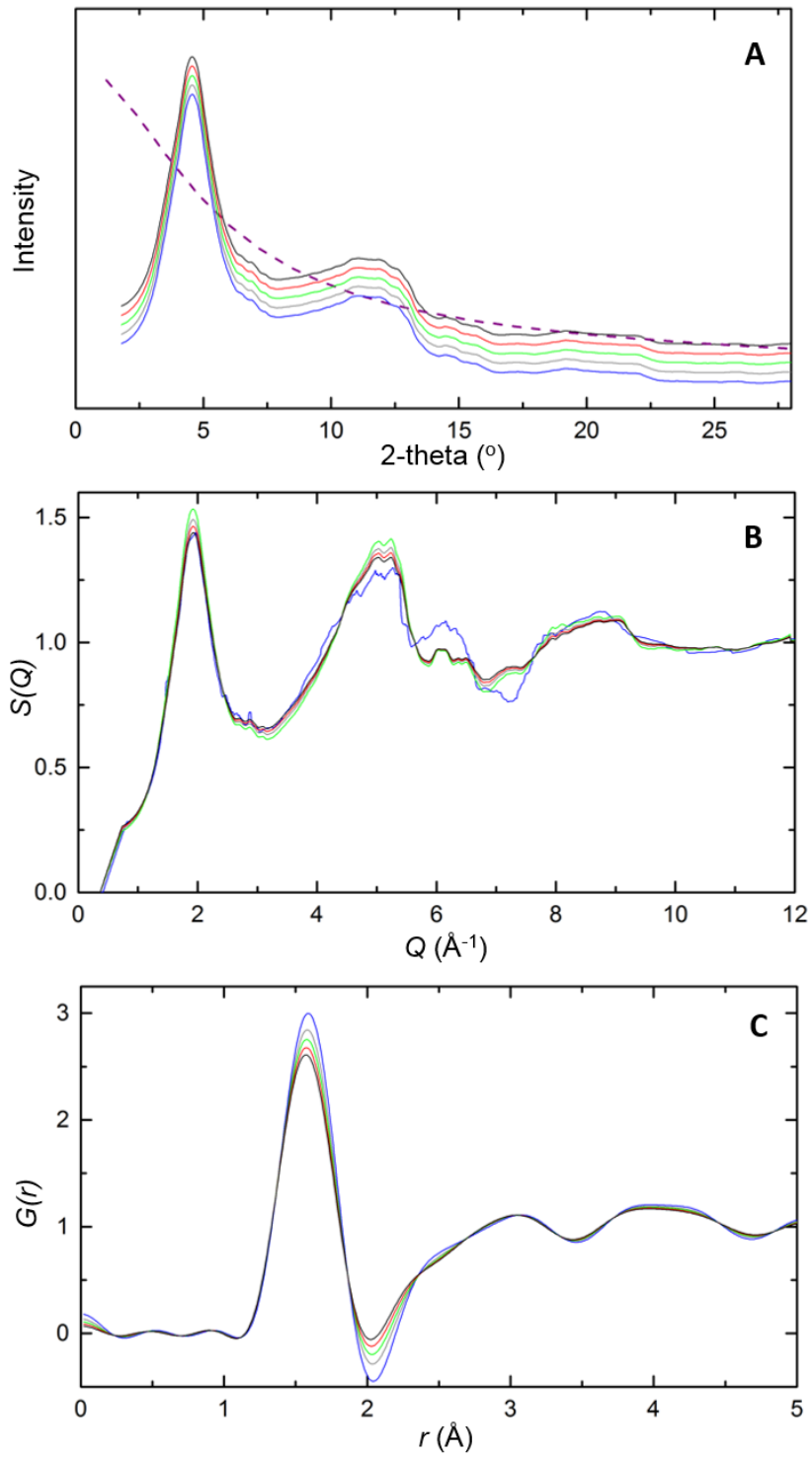

Figure 4.15 *A - Diffraction patterns in theta with different normalisation. Purple dashed line represents the sum of the self and Compton scattering. The black spectra in A (oscillating around the incoherent scattering at 2-theta>20) is best normalised. This can be seen in B and C, the subsequent $S(Q)$ and $G(r)$, by the lack of artefacts and minimal oscillations at low r in C.*

transformed $G(r)$; this can occur if the background is incorrectly scaled to the data or normalisation of the data to the self and Compton scattering is wrong. This leads to errors in the $S(Q)$ and $G(r)$ as peaks and oscillations will misrepresent the true structure. In Figure 4.15 it is shown that the diffraction pattern after background removal should oscillate around the self scattering above $25\,2\theta$ otherwise peaks in the $S(Q)$ have artificial intensities (Figure 4.15B) and this is seen in the $G(r)$ through unreal intensities in the first peak and larger oscillations at r <1 Å (Figure 4.15C). This highlights the importance of having data to at least 11 $Å^{-1}$ to be able to be sure this procedure is done correctly. At high Q there should be no signal from the sample and the only signal will be from the incoherent scattering. Normalisation errors are most easily introduced by incorrect background subtraction so it is critical to ensure the correct background has been collected at the conditions of the sample measurement.

4.5.3 Radial Distribution Function Extraction

To obtain the $S(Q)$ and $G(r)$ as theoretically described in Chapter 3, after normalisation the structure factor, $S(Q)$, can be obtained as in Equation 3.27 by

$$S(Q) = \frac{I^{coh}(Q)}{f_{eff}(Q)^2}, \tag{4.8}$$

and Fourier transformed to the $G(r)$ as described in Equation 3.28. Once the $G(r)$ has been obtained, it is possible to estimate coordination number and bond distance of the individual correlations within the $G(r)$ if the data is of high enough quality. These interactions, $g(r)_{\text{ind}}$, arise from correlations between pairs of atoms such as Si-O, O-O, Na-O, and K-O. In order to estimate coordination number and bond distance for the correlations present, fits were made to the $G(r)$ using the following relations:

$$G(r) = \sum g(r)_{\text{ind}} = \frac{Z_{total}^2}{n_0 \sum K^2} \sum_i \frac{x_i A_i}{\sigma_i \sqrt{2\pi}} exp\left(\frac{-(r-d_i)^2}{2\sigma_i^2}\right), \tag{4.9}$$

where

$$A_i = \frac{CN_i}{\int \frac{4\pi r^2}{\sigma_i\sqrt{2\pi}} exp - \left(\frac{(r-d_i)^2}{2\sigma_i^2}\right) dr}. \tag{4.10}$$

The coordination number for the individual ion-ion contributions, CN_i, is related to the integral under each individual Gaussian by the density, n_0, and concentration, x_i, of the species. The interatomic distance is d_i and $\sigma_i = k\sqrt{d_i}$ defines the width of the Gaussian using an adjustable parameter k [108]. For polyatomic materials a representative concentration can be made and a density estimated that enables the coordination of each pair of atoms to be predicted. The analysis is typically limited to r <3 Å due to the overlapping nature of the contributions. This allows peaks of well defined width and height to be very well approximated by a Gaussian distribution. At higher correlations the contributions from second interactions feature and make this process much more difficult. For strongly overlapping contributions a single Gaussian can be fit made up of the individual contributions to represent correlations at higher distances approximately if this is required.

4.5.4 Self-consistency Checks

Self-consistency checks [109, 110] were performed on all the data to ensure the $S(Q)$ and $G(r)$ after processing were consistent and reliable. These included (1) ensuring the $S(Q)$ followed the sum rule $\int_0^\infty [S(Q) - 1]Q^2 dQ = -2\pi^2 n_0$ in the limit that $r = 0$, (2) that low-r oscillations were minimised as ($G(r = 0) = 0$), and (3) the reverse Fourier transform of the calculated $G(r)$ can reproduce with reasonable accuracy the input $S(Q)$. For (1), the sum-rule arises from the small angle approximations $\sin Qr = Qr$ and, if normalisation of the $S(Q)$ is correct, should be satisfied. In order to confirm that proper normalisation had been carried out the $S(Q)Q^2 - Q^2$ was integrated as seen in Figure 4.16. Due to the limits of experimental work the ideal limits of 0 to ∞ are unachievable; however at higher Q the function should oscillate evenly around 0 and therefore no further addition to the integral will be made.

Process (2) is due to the $r_{\min}$ limit, where no atomic interactions can take place beneath the limit of closest approach, and therefore for $r = 0$, $G(r) = 0$. In this case the oscillations at $r < r_{\min}$ should be minimal and any oscillations

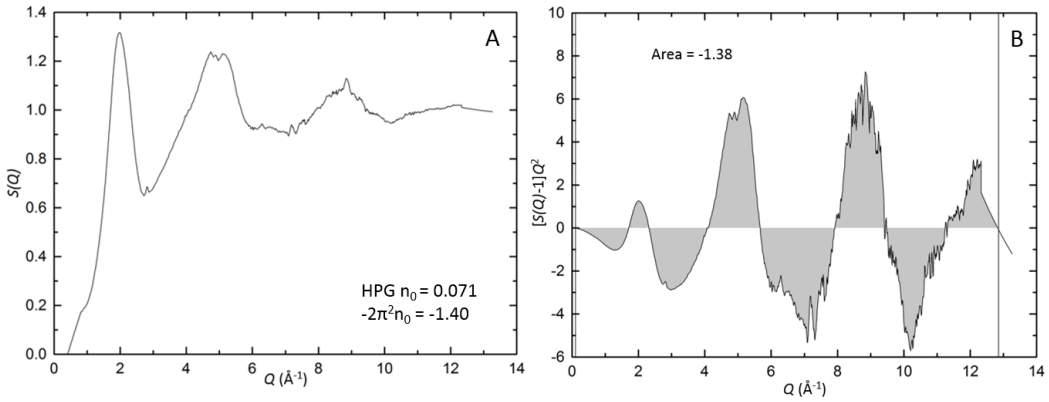

Figure 4.16 *A: $S(Q)$ for haplogranite glass. B: Self-consistency sum-rule check on A, showing integration under area of the curve over the maximum Q-range.*

present at this limit are artefacts of the Q_{max} Fourier transform limit. These oscillations should be minimised by varying the $S(Q)$ limit as discussed below. For (3), the reproducibility of the $S(Q)$ through an inverse Fourier transform of the obtained $G(r)$ proves that the $G(r)$ is reasonable and no artificial oscillations have been introduced during the Fourier transform process. As seen in Figure 4.17 the inverse Fourier transforms (solid lines) reproduce the original $S(Q)$ used to calculate the $G(r)$ with reasonable accuracy and no major oscillations are introduced.

Influence of the Q_{max} Cut-off

The termination of the $S(Q)$ can have severe impacts on the $G(r)$ during the Fourier transform, as depending on the Q_{max} cut-off artificial oscillations can be introduced to the $G(r)$. This is because an ideal Fourier transform requires the limits to be from Q =0 to $Q = \infty$ but cannot be adhered to practically. A Q-range as long as possible should be collected until there is visibly no signal left from the sample at high Q, and at this point the $S(Q)$ must oscillate around 1. The best Q_{max} can be found by Fourier transforming the data at various Q_{max} distances and minimising any unreal oscillations. Artificial oscillations tend to be characterised by their regular wavelength, often a characteristic wavelength of $4\pi/Q_{max}$, and appearance at the same position relative to real peaks over all r. A Q_{max} compromise must be reached where artificial oscillations are reduced, but where no damping or broadening of the real contributions is introduced (Figure 4.18).

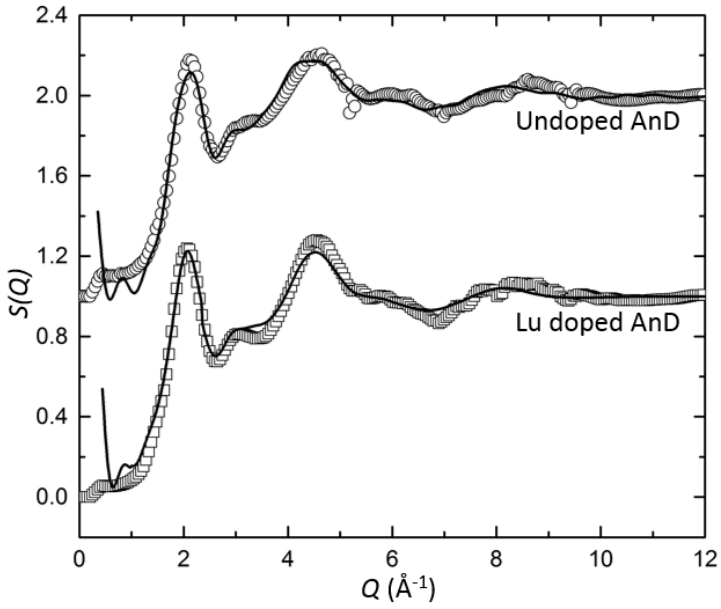

Figure 4.17 *$S(Q)$ for Lu-doped and undoped collected data (symbols) obtained in a Paris-Edinburgh press with reverse Fourier transform $S(Q)$ obtained from the calculated $G(r)$ (solid lines).*

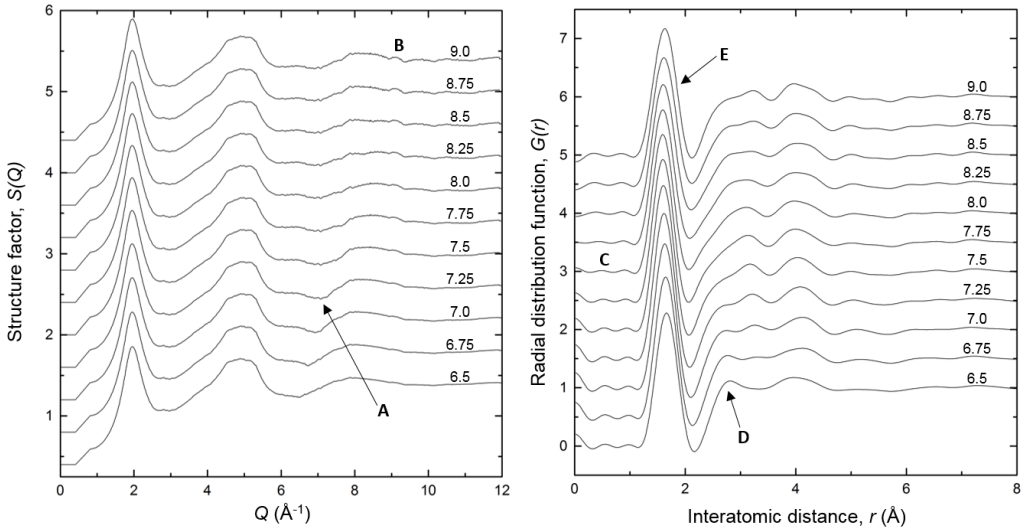

Figure 4.18 *Result of variations in Qmax Fourier transform limit. Feature A - artefact from forcing Q_{max} before oscillations in sample are complete. B - Location of cut-off in Q. C - $G(r)$ with minimal oscillations below r_{min}. D - Artificial peak produced by short cut-off distance and feature A in $S(Q)$. E - Width and position of the Si-O peak generated by longest Q_{max} distance.*

This can be observed by monitoring the width and position of the first peak relative to the first peak in a $G(r)$ Fourier transformed over the longest possible Q_{max} (Figure 4.18E). In Figure 4.18 peak E can be seen to increase in position, decrease in height and broaden as the cut-off distance is decreased. This is due to feature A in the $S(Q)$ which is introduced by cutting the $S(Q)$ too soon before signal from the sample is minimised. By testing a range of Q_{max} values, the aims are: (1) To minimise the oscillations at low r below the first peak (C in Figure 4.18) and, (2) identify which oscillations are introduced as artefacts by testing multiple cut-off distances. Particular care on the Q_{max} distance must be taken when identifying minor element correlations, to be certain these are not artefacts (feature D in Figure 4.18) and a Q_{max}=8.5 Å^{-1} was chosen via this method for all the HPG results in this chapter, and is consistently used throughout the rest of this work in order that no correlations were produced from using a variety of Q_{max} distances. This distance preserves the first peak position and height of the longest Q_{max} distance, and minimises oscillations at low r introduced by uneven oscillations at high Q (Figure 4.18 feature B). This value is identical to the best Q_{max} found by [78].

4.6 Energy Dispersive X-ray Diffraction Data Treatment

For energy dispersive data, as the measurements are taken at fixed detector angles (2θ angles of 2°, 2.7°, 3.5°, 5°, 7°, 10°, 15°, 20°, 27°, 35°) over a wide range of energy, E, this allows collection up to 20 Å^{-1} in reciprocal space where $Q = 4\pi E \sin\theta/12.398$. Peaks in the diffraction pattern slightly obscure the liquid signal at certain energies; these arise from Bragg peaks of the graphite sample chamber and fluorescence from indium on the detector and elements within the sample. Fluorescence peaks can be identified as they occur consistently at the same energy. These peaks are removed before data analysis by erasing their contributions and the data is extrapolated via a cubic spline between the remaining data. This process can be seen in Figure 4.19 (left).

The scaling of the individual structure factors is achieved by fixing the oscillations of the data at highest Q to oscillate around 1, as they must by definition (Figure 4.19 right). The other structure factors are then scaled accordingly in reverse order from highest Q. After merging, an error weighted spline is fit to the data in

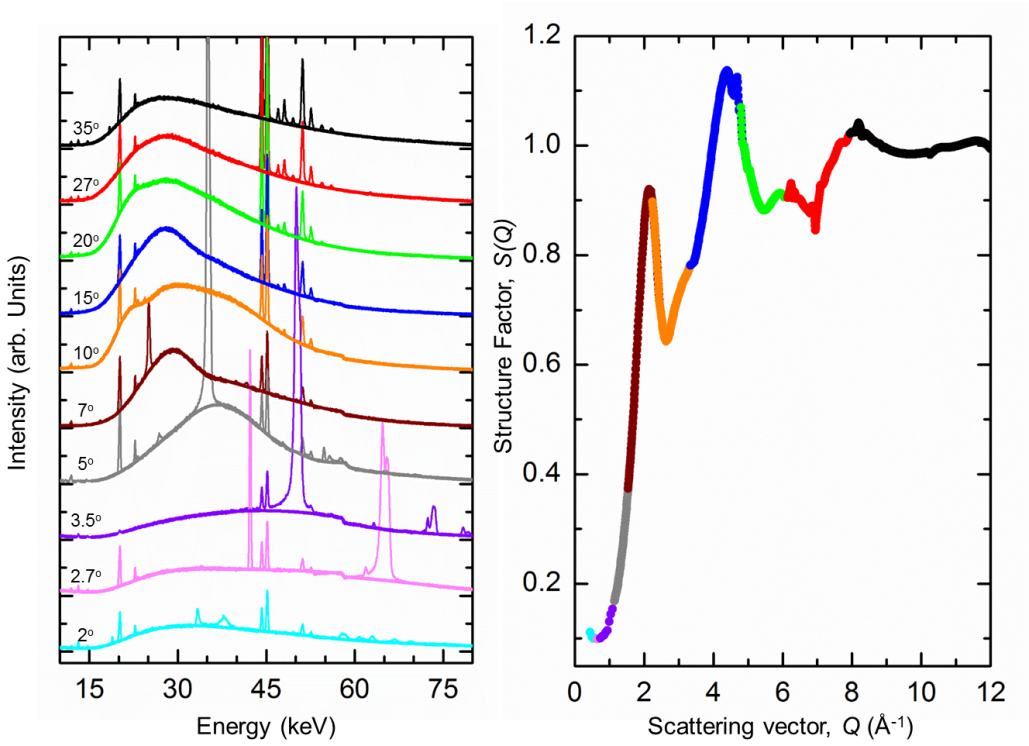

Figure 4.19 *Left: Energy dispersive x-ray diffraction patterns for anorthite-diopside showing each collection angle and Bragg peaks. Fits to baseline curve show final data after peak removal that were used in $S(Q)$ extrapolation. Energy range used for analysis was between 25-55 keV. Right: Structure factor, $S(Q)$, obtained after data processing by a spline of each collection angle (shown by colours of spectra which are the same in both figures).*

order to obtain an evenly spaced $S(Q)$ distribution. This fitting uses only parts of the individual $S(Q)$ that overlap in order that they can be fit together. This overlapping can introduce artefacts so special care must be taken to ensure these artefacts do not influence the final $G(r)$; these can be identified if regular spaced cosine oscillations are observed with increasing amplitude towards low r. The $G(r)$ is then obtained by Fourier transform of the spline smoothed $S(Q)$.

4.7 X-ray Absorption Data Treatment

XAS (x-ray absorption spectroscopy) data is collected in energy (eV) over a given range, selected to cross the absorption edge of the element of interest. A brief description of the necessary data processing techniques to obtain EXAFS oscillations in k-space, that can be used to extract information on bond distances and coordination in real space, is presented below. Firstly, any glitches are removed by deleting the outlying data point and fitting a spline between the two on either side. As these steps are so insignificant for one point in 100 eV there should be no visible impact on the spectra. Only glitches arising from one incorrect intensity caused by detector effects should be removed.

Once the glitches have been removed the data is normalised to an edge jump of 1 in order to compensate for the varying thickness of the samples and any change in concentration. Normalisation is done by fitting pre- and post-edge functions over the same range in energy to normalise the pre-edge to 0 and the post-edge to 1 (Figure 4.20). The pre-edge function should be fit as close to the edge jump as possible before any inflection occurs; this is to ensure the region is representative of the pre-edge gradient because data collection is concentrated here and before this the gradient can be unrepresentative. The post-edge should be fit over as long a range as possible from highest energy collected to the start of the first visible EXAFS oscillations. These ranges should be consistent between data sets to ensure normalisation is regular and the edge jump and first oscillations are not incorrect.

The normalised spectra are compared with the reference sample collected on the channel after the sample to check that no drift in energy has occurred due to fluctuations on the beamline or experimental effects. As seen in Figure 4.21 if the reference sample edge position has moved from the initial scans collected at the start of the experiment, the shift in position of the edge and the reference

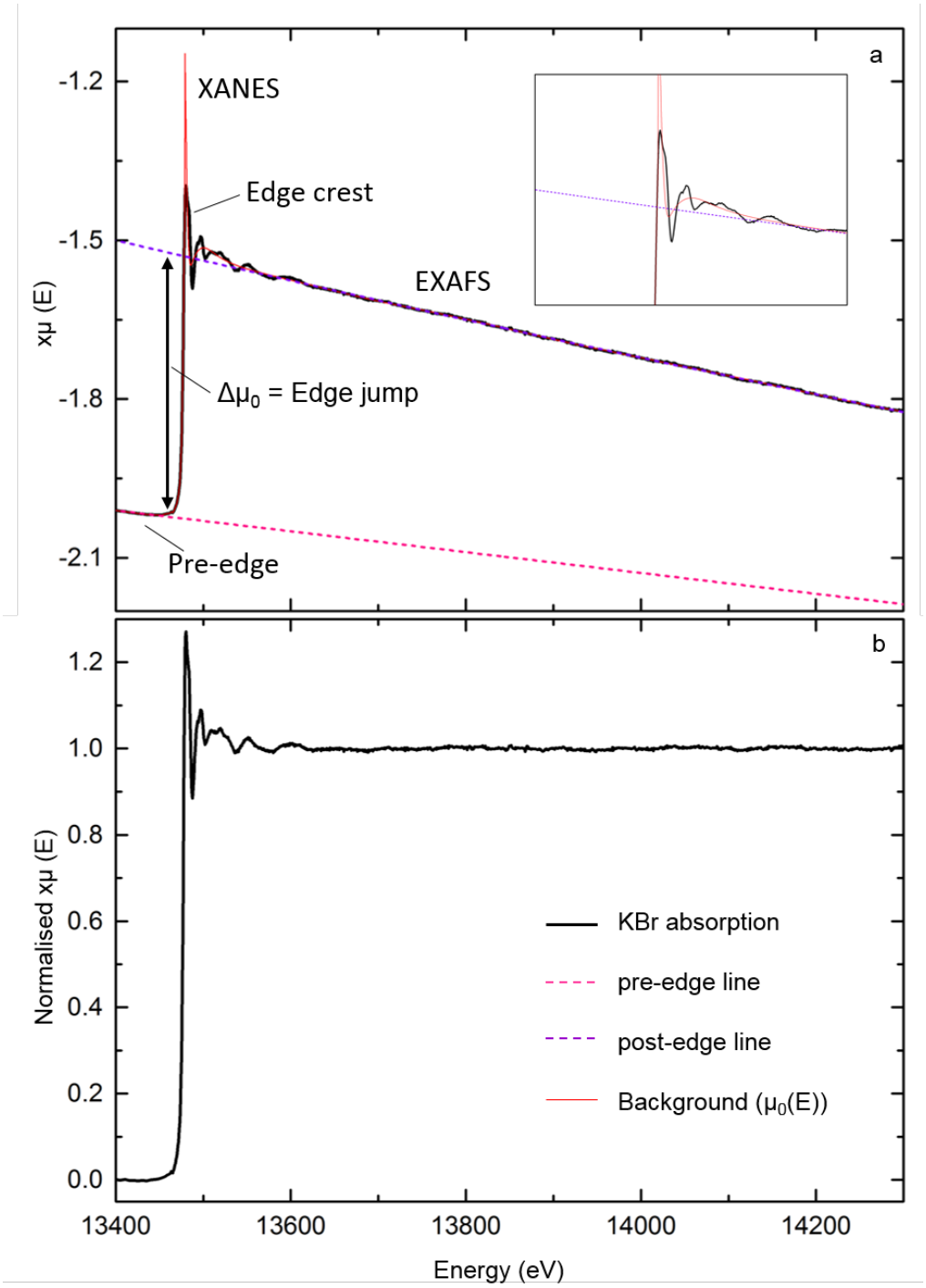

Figure 4.20 *a: Collected XAS spectra for a bromine reference compound, highlighting XANES and EXAFS regions, and features of the absorption edge. The modelled absorption for one atom of Br is given in red as the background function. The dashed lines represent the pre and post-edge fits required to normalise the data.*

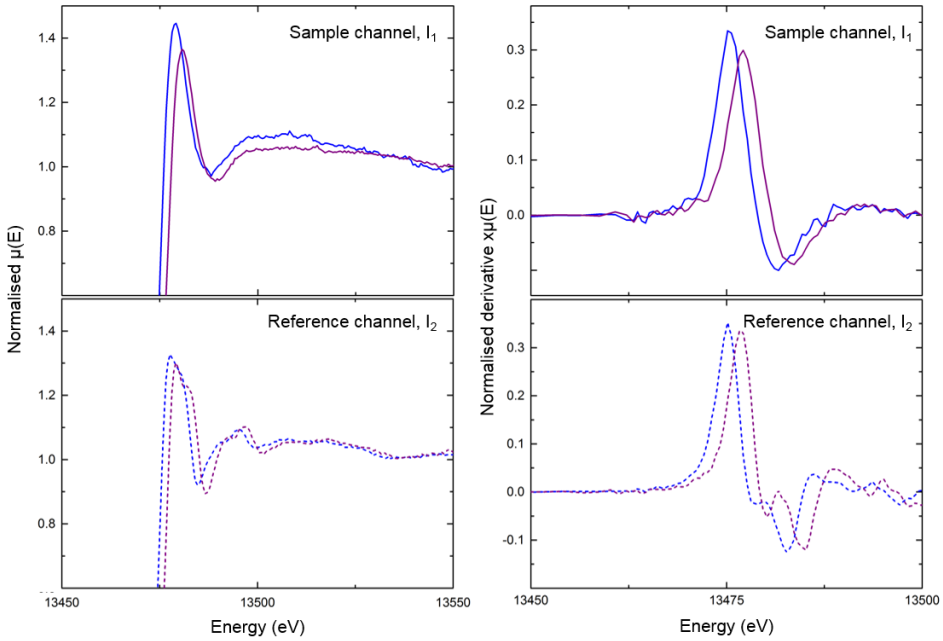

Figure 4.21 *EXAFS spectra normalised (left) and derivatives (right) for Br doped granite samples and the NaBr reference, collected 6 hours apart. Reference spectra (lower panels) also show edge drift in the edge position, indicating that drift is not sample dependant and needs to be corrected for before analysis.*

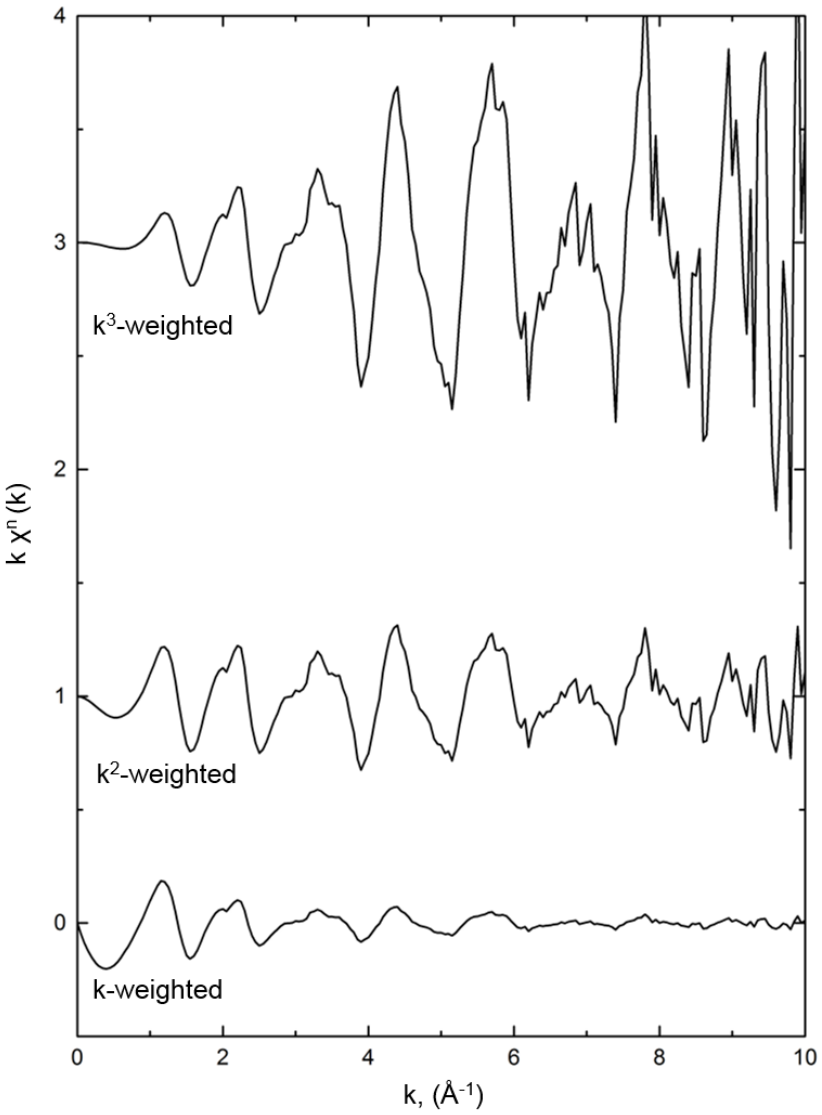

Figure 4.22 *The same bromine reference compound plotted with different k-weights to highlight the exaggeration of low or high k oscillations and compensate for any amplitude decay.*

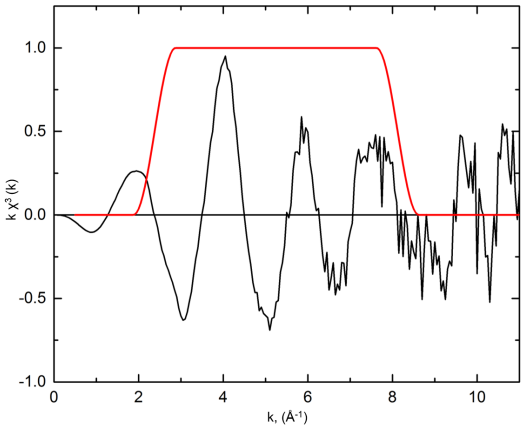

Figure 4.23 *k^3-weighted spectra with Hanning window for region of Fourier transform highlighted in red. The window has been chosen to coincide with where the data cross Y=0.*

must be an experimental shift rather than real, and both the reference and data should be adjusted. This can be clearly seen in both the edge position and first derivative. The data must be adjusted by the same amount as required to move the reference on to its original edge position prior to the beginning of the experiment. If the sample has shifted but the reference is consistent with the edge at the initial position then the shift can be considered as real.

A background function is applied to the normalised spectra using a cubic spline in a technique developed by Ravel and Newville [111] (Figure 4.20a). This spline approximates the post-edge spectra for one isolated atom of the element of interest, in order to remove any low frequency oscillations and leave the signal only from the XAS interactions. The function is chosen by applying a minimum background distance, R_{bkg}, below which there should be no oscillations as it is less than the diameter of one atom in the sample. This forces the oscillations below this distance to 0. Once all these processing steps have been completed, the data can be viewed in k-space and weighted appropriately (Figure 4.22) to compensate for any amplitude decay with increasing energy as the EXAFS oscillations decay quickly with k. Energy and k are related through

$$k = \sqrt{\frac{2m(E - E_0)}{\hbar^2}}. \tag{4.11}$$

As given theoretically in Chapter 3.2 a Fourier transform is performed to distinguish nearest neighbour shells in real space. The transform is carried out using a window over a chosen distance in k-space (Figure 4.23) in order

to minimise artificial oscillations that arise at high energy from noise in the spectra. The chosen window should then be used over all the experimental data to ensure consistency between the data points. In most cases, high $P-T$ data will be Fourier transformed over a much smaller range (typically up to 7-8 Å^{-1}), compared to reference or glass spectra (up to 10-15 Å^{-1}). The minimum distance is chosen as just above that of the R_{bkg} distance and it is important to select the window boundaries at the same value of Y, i.e. where Y=0 (Figure 4.23).

Chapter 5

An X-ray Diffraction Study of Haplogranitic Melts

This chapter describes the results of the structural determination of haplogranitic glasses and melts up to 12 GPa using x-ray diffraction techniques. The nearest neighbour Si-O and Al-O correlations are monitored to 12 GPa and density changes between the glass and melt are discussed. The results show that in strong glass forming networks, with high SiO_2 content, the glass structure is analogous to that of the melt.

5.1 Introduction

Haplogranitic melts are synthesised to represent highly silicic magmas similar to the last stages of melting during fractional crystallisation. They predominantly contain Si and Al oxides combined with alkali metals such as Na and K. These can be found in such environments as subduction zones and other crustal formation settings [3]. Highly silicic melts have >60% silica content which form polymerised networks of SiO_4^{4-} tetrahedra. Due to the abundance of network forming cations (Si, Al) and fewer network modifying cations (Mg, Ca, Na, K) the SiO_4^{4-} polymerised chains create ring structures which surround cavities in the melt. The presence of large cages >2.5 Å in diameter [46], is greatest in silica rich melts due to their strong network forming ability. These silicic melts have interesting properties, and in comparison to less polymerised melts, such as basalt, have

higher viscosity and lower density. As these types of melts are important during crust formation, understanding their structure and how they behave *in situ* will further our knowledge about the properties of melts in subduction zone settings, and how elements are transported between the mantle and the crust in these environments. In crustal settings fluids such as H_2O can be involved in the system so the comparison between hydrous and non-hydrous melts is important in order to understand the influence of water on magmatic systems. For example, studies have shown that in subduction zones, volatiles such as water can influence the incorporation of metals into magmatic fluids [112, 113]; however, little is understood about the exact structural changes that may occur within the melt at the conditions of formation (high $P-T$) to account for this. Trace elements, such as Y and Zr, are known to accommodate within haplogranite melt structures [114, 115]. In order to understand trace element incorporation within silicate melt structures that contain these elements, the trace element free structure must be understood. This study was carried out in order to provide insight into the interactions of major elements within this composition for comparison with trace element doped studies on the same composition completed in Chapters 6 and 7.

5.2 Data Acquisition and Analysis

Synthetic haplogranite (HPG) glass was synthesised by high temperature homogenisation and flash cooling as described in Chapter 4.4. This composition is a model for other silicic compositions with a high degree of polymerisation and has the advantage of containing only four oxides in order to minimise the number of element contributions in the structure factor. Water was added to the HPG in order to lower the melting temperature so that melting could be achieved within a resistively heated diamond anvil cell. Water was added via high pressure addition in a piston-cylinder press as detailed in Chapter 4.4 and the composition of the HPG is shown in Table 5.1.

Measurements on HPG glass were carried out up to 12 GPa by cold compression, and the HPG melts were measured up to 5 GPa using angle and energy-dispersive x-ray diffraction techniques (Table 5.2). Angle dispersive measurements were collected on beamlines I15 at the Diamond Light Source and PSICHE at the synchrotron Soleil, with some high $P-T$ molten data collected using energy dispersive x-ray diffraction on HP-CAT beamline at the Advanced Photon Source, USA (Chapter 4.2.3). Not all the data collected on the experiments was of high

Sample	SiO_2	Al_2O_3	Na_2O	K_2O	Total
Initial Dry	78.7 (3)	11.9 (2)	4.3 (1)	4.5 (2)	99.4 (5)
Initial Hydrous	71.4 (2)	10.5 (2)	3.6 (1)	3.9 (1)	89.4* (5)
Recovered Sample C8	73.4 (2)	11.0 (2)	3.9 (1)	4.3 (1)	92.6* (4)
Recovered Sample C10	73.8 (2)	11.1 (2)	3.8 (1)	4.1 (1)	92.8* (4)

Table 5.1 *Compositions from electron microprobe analysis for the original starting glass, after water addition, and average for fully glass samples recovered after the experiments. Analyses are based on average of 10 sample spots and standard deviations are shown in brackets. * indicates where the low totals are due to the addition of 8-10 wt.% water.*

enough quality to use; for full experimental details of unsuccessful collection see Appendix One, Table 9.1. For angle-dispersive measurements, to create high $P-T$ conditions, resistively heated diamond anvil cells (DAC) were used (Chapter 4.3.2). The Pt heating coils surrounded a 4×4 mm rhenium gasket of 200 μm thickness. Finely ground HPG sample powder was loaded into the 250 μm electro-eroded hole previously indented to 90 μm thickness. The powder was packed into the hole thoroughly to avoid collapse of the sample chamber. In order to access the highest possible Q-range the diamonds were glued with stycast on to 70° opening Boehler-Almax seats. Temperatures were recorded by a K-type thermocouple placed on the very edge of the gasket indent as close to the sample chamber as possible. Thermocouples were previously calibrated as in Section 4.3.2. To achieve maximum signal intensity from the low scattering sample the x-ray beam (wavelengths in Table 5.2) was focussed to 70×70 μm. Diffraction patterns were collected in the glass and melt for 60 s using a Perkin Elmer (I-15) or MAR image plate (PSICHE) detector at each pressure point (Table 5.2). For Perkin Elmer data a background 'dark image' was collected after each measurement in order to subtract any background noise inherent in the detector and the MAR was cleared between each measurement to reduce any possible contamination from background scattering. All DAC measurements covered a Q-range up to 11-12 $Å^{-1}$, with free-standing glass measurements covering up to 20 $Å^{-1}$. Pressure was determined in the DAC before each experiment by ruby fluorescence, and at high temperature it was monitored by a Pt foil inserted into the sample chamber. Diffraction on the Pt calibrant was collected for 10 s at each pressure point before and during heating. At each pressure, glass, melt, and quench measurements were collected where possible. After quenching the gasket was unloaded, the sample recovered, and the empty gasket replaced in the cell in order to collect

Sample	Beamline	Technique	Wavelength (Å)	P (GPa)	T (K)
Ambient Dry	ID-15 ESRF	FS glass	0.1701	amb	amb
Ambient Hydrous	ID-15 ESRF	FS glass	0.1701	amb	amb
C1	PSICHE Sol.	rh-DAC	0.2647	0.7 (3)	na
				0.8 (3)	880 (50)
C2	I-15 DLS	rh-DAC	0.2637	1.4 (4)	na
C3	I-15 DLS	rh-DAC	0.2637	1.6 (5)	na
C4	I-15 DLS	rh-DAC	0.2637	2.3 (5)	na
C5	HP-CAT APS	PEP	EDXD	2.3	1700 (50)
C6	HP-CAT APS	PEP	EDXD	3.3	1800 (50)
C7	I-15 DLS	rh-DAC	0.2637	3.5 (5)	na
C8	I-15 DLS	rh-DAC	0.2637	4.1 (5)	na
				4.3 (5)	950 (50)
C9	I-15 DLS	rh-DAC	0.2637	5.1(6)	na
C10	HP-CAT APS	PEP	EDXD	5.4	1900 (50)
C11	I-15 DLS	rh-DAC	0.2637	11.8 (5)	na

Table 5.2 *HPG data collected at various synchrotron sources with experimental conditions for each sample. FS glass - free standing glass. Ambient temperature data was collected at every pressure point and the highest temperature reached during heating is listed for each sample. Abbreviations for beamlines are as follows: DLS - Diamond Light Source, APS - Advanced Photon Source, ESRF - European Synchrotron Radiation Facility, Sol. - Synchrotron Soleil. Angle dispersive x-ray diffraction measurements are given with the wavelengths used during the experiment and the high pressure techniques used (rh-DAC - resistively heated DAC, PEP - Paris-Edinburgh press) are stated. EDXD states where energy dispersive x-ray diffraction measurements were undertaken and a white beam was used. Samples C1 to C11 are all hydrous HPG.*

the background scattering signal from the diamond anvils.

Free standing ambient glass measurements were performed by Dr S. Kimber using x-ray diffraction on I-15A beamline at the ESRF, Grenoble. Energy dispersive x-ray diffraction measurements were made in a Paris-Edinburgh press using the zirconia 14/3 mm gasket described in Section 4.3.4. The collection techniques and data processing methods are fully described in Chapter 4.5 and 4.6.

Diffraction patterns collected with angle-dispersive techniques were analysed using the methodology presented in Chapter 4.5. The $S(Q)$ was obtained by normalising the diffraction pattern to the inelastic (Compton) and self scattering profiles for the HPG composition, and the radial distribution function, $G(r)$, was then produced through a Fourier transform of the $S(Q)$. A smooth cosine function was applied between 11-14 Å^{-1} to the $S(Q)$ in order to ensure the $S(Q)$ oscillates around 1 at high Q. This function was fit based on the oscillations in

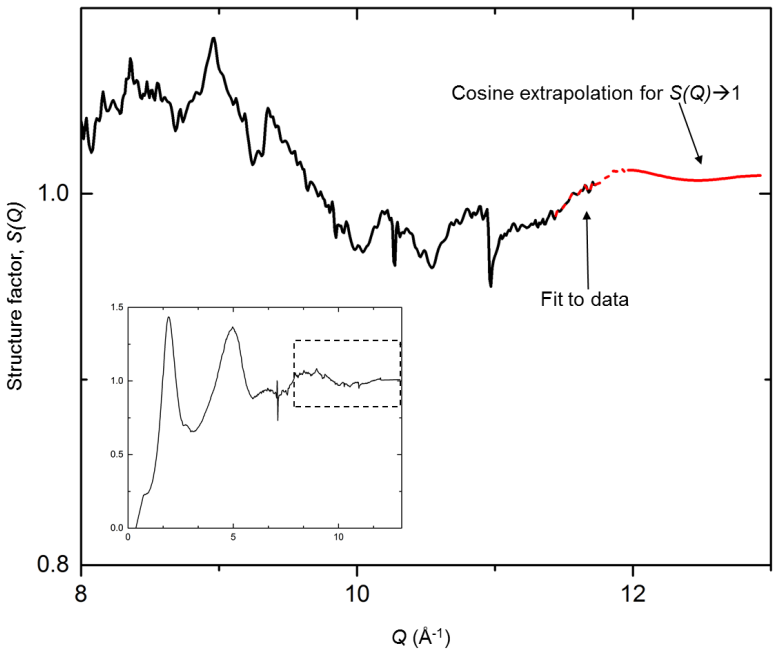

Figure 5.1 *The extrapolation of $S(Q)$ with a cosine function at high Q. Fit to data is shown by dashed red line with extrapolated function shown by the solid red line. The oscillation is forced around $S(Q)$=1 at high Q where there is no further signal from the sample. Inset Main image is region in dotted line box on full $S(Q)$.*

the data (Figure 5.1). Self consistency checks were used to ensure reliability of the data by various methods (Chapter 4.5.4).

During heating, at temperatures >850 K the samples either recrystallised or remained non-crystalline. In the cases where crystallisation occurred the runs were stopped and discarded as the temperature required to melt the crystals exceeded the heater limits (>1300 K). On these time scales (>1 hour) recrystallization would be expected to occur above the solidus at ∼840 K, before melting, unless a liquid phase is reached above the glass transition temperature. Therefore, if recrystallization did not occur at temperatures above the solidus the samples are assumed to be in the super-cooled liquid state at >880-900 K and chemically similar to the melt (temperatures above the liquidus). In any case, from these results the melt phase and the ambient temperature phase are identical as no changes were observed between runs at room temperature, and clearly above melting (Figure 5.2) as seen in C8 where temperatures far exceeded the liquidus temperature for hydrous haplogranite [116].

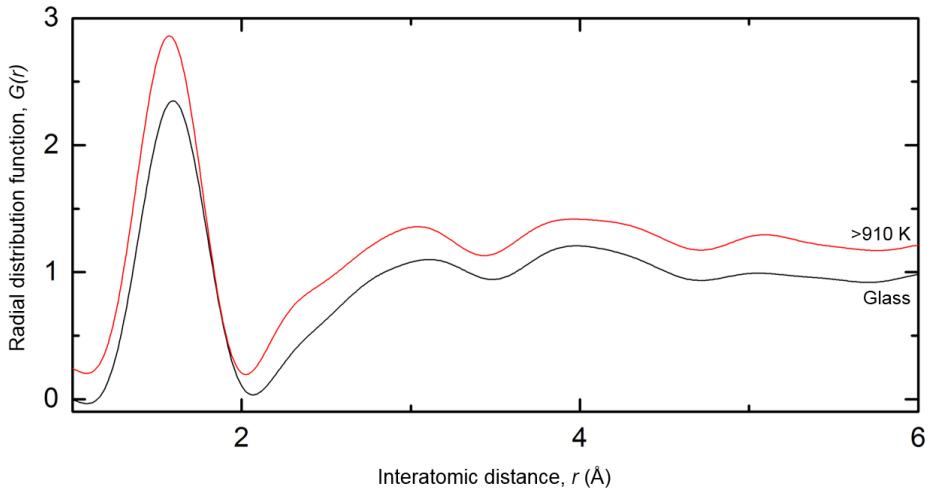

Figure 5.2 *Real space $G(r)$ from a haplogranitic sample (C8 at 4.1 GPa) displaying the compressed glass measurement and one at high temperature above the liquidus for HPG [116]. It can be seen from the $G(r)$ that no major structural change occurs between the glass and liquid state.*

5.2.1 Recovered Sample Analysis

On quenching, the heated samples predominantly appeared glassy from both the DAC and PEP experiments. Two of the recovered samples contained quartz crystals around the edge of the sample (Figure 5.3 A and C). These samples had slightly reduced SiO_2 content in the bulk glass, and as no evidence of crystals was seen in the diffraction experiments the crystals must be a quench product. Recovered quenched samples were polished for electron microprobe analysis at the EMMAC (The Edinburgh Materials and Micro-Analysis Centre), University of Edinburgh. Analyses were carried out using a CAMECA SX100 electron microprobe with a current of 30 nm, a voltage of 15 keV and 8 μm beam size. Where fully glass samples were recovered (C6, C8, C10) the samples retained a stoichiometry nearly identical to their starting compositions (Table 5.1), including totals; therefore it is unlikely the samples underwent any chemical change or significant water loss. Bubbles were present in some of the quenched DAC samples (Figure 5.3B), which are likely to be the product of water containing vesicles that appeared during quenching. This indicates that water remained in the samples during the experiments.

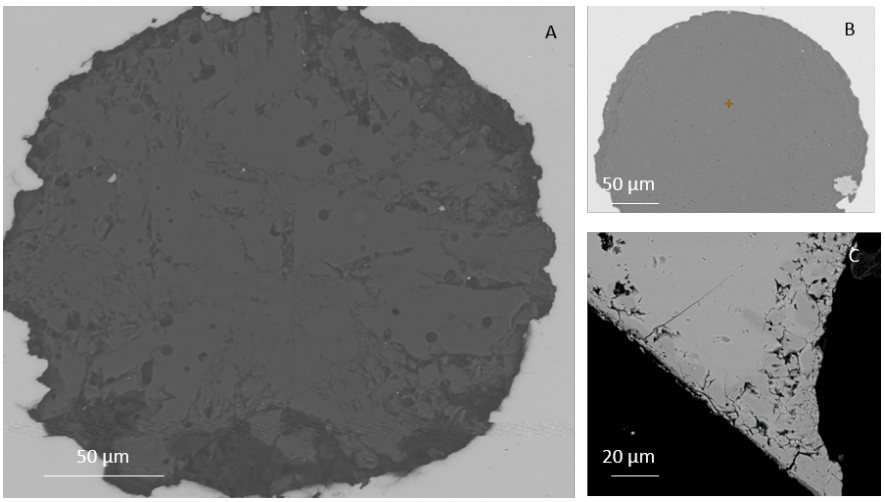

Figure 5.3 *Image of quenched glass from A: DAC experiment C1 showing quench quartz crystal growth. B: DAC experiment C8 with vesicles in glass. C: Recovered Paris-Edinburgh press HPG sample (C5) with crystals around edge of capsule.*

5.3 Structure of Haplogranite

The structure of the HPG glass and melt phases were measured at increasing P points up to 12 GPa (Table 5.2). Glass measurements were made at ambient conditions for both the dry and hydrous starting glass, and at P in the hydrous glass at 0.7, 1.4, 1.6, 2.3, 3.5, 4.1, 5.1, and 11.8 GPa, with high temperature melt data successfully collected at 0.8, 2.3, 3.3, 4.3 and 5.4 GPa at >880 K. The measured structure factors, $S(Q)$, and calculated radial distribution functions, $G(r)$, are shown in Figures 5.4 and 5.5. The $S(Q)$ is of high quality to 11-12 $Å^{-1}$ in reciprocal space, and a decrease in the intensity of the first sharp diffraction peak (FSDP), at pressures <4 GPa, with increasing temperature is observed. This is due to the lower density of the melt and more open structure at high temperature. Any data collected to less than 12 $Å^{-1}$ was discarded to ensure consistent processing between the data sets.

In the $S(Q)$ (Figure 5.4) the FSDP can be seen at 1.75(2) $Å^{-1}$ in the hydrous ambient glass. This rapidly increases to 1.93(2) $Å^{-1}$ with compression of the glass to 0.7 GPa, and increases gradually to 1.98(1) $Å^{-1}$ at 5.1 GPa until it reaches 2.09(2) $Å^{-1}$ at 11.8 GPa. In the molten samples no immediate increase is observed between the ambient hydrous glass and the first melt at 0.8 GPa, and it increases to 1.93(2) $Å^{-1}$ by 4.5 GPa where it matches that of the glass. It is likely that the ambient P melt (for which no data was collected here), has a lower FSDP

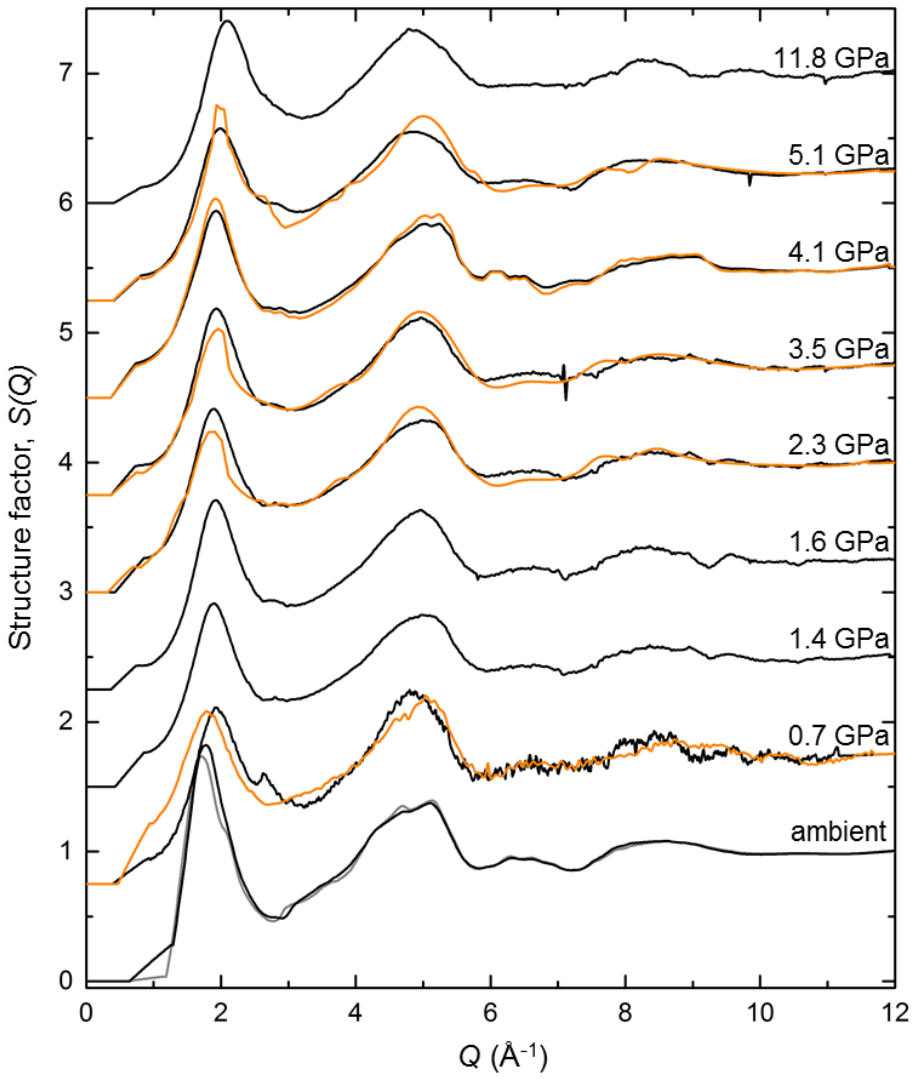

Figure 5.4 *S(Q) for HPG measurements documented in text and listed in Table 5.2. Black curves show cold compressed glass at high P with orange curves showing high T molten data collected within 0.5 GPa of glass. Grey curve is the dry sample at ambient conditions.*

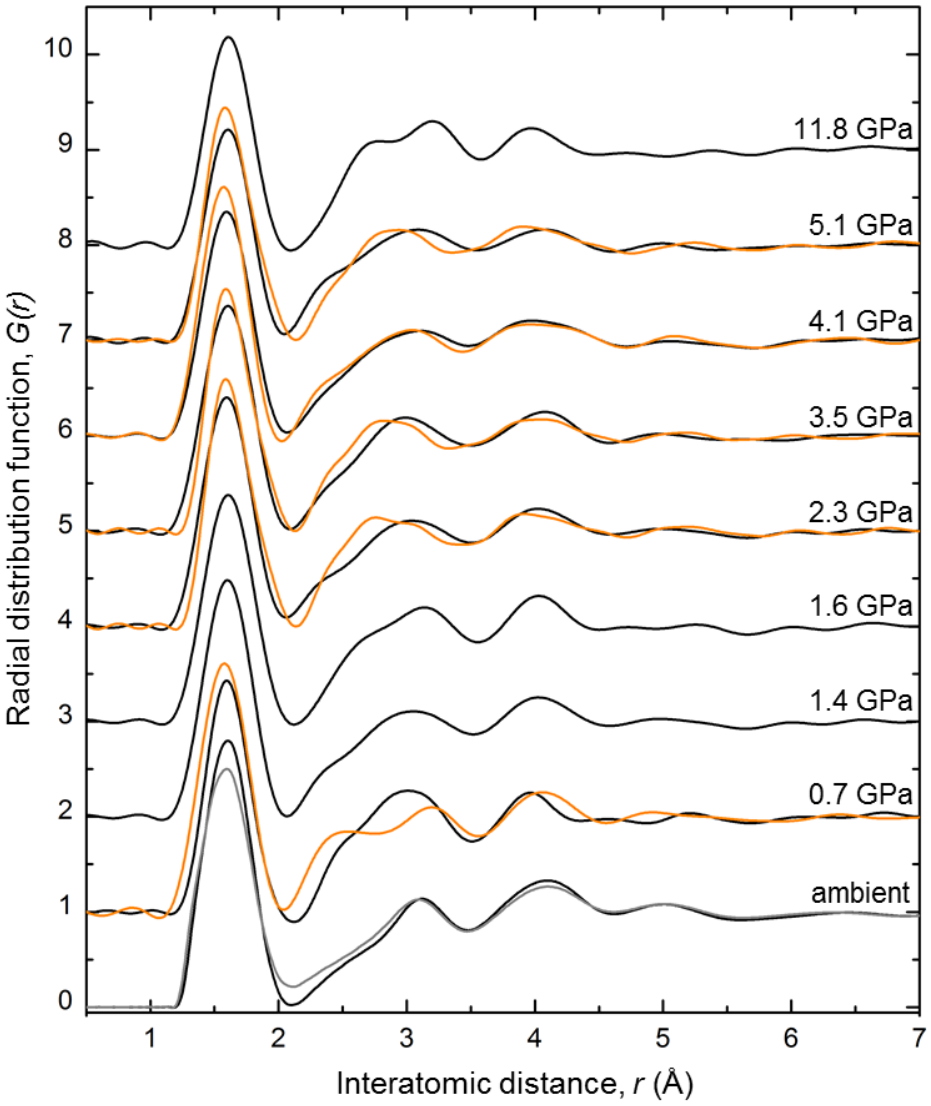

Figure 5.5 *$G(r)$ for the $S(Q)$ in Figure 5.4. Black curves show cold compressed glass, and orange, the melt at similar pressure (within 0.5 GPa). Grey curve is the dry sample at ambient conditions.*

position than the ambient glass as the melt is less dense than the glass. As discussed in Chapter 2.1, the FSDP is attributed to the intermediate range order in silicates and therefore the size and number of cages present in the sample. The shift to higher Q of the FSDP can be linked to the collapse of the interconnected rings during compression, which appears to be mostly complete in the melt by 4-5 GPa, as the FSDP positions of the glass and melt are identical at 4.1 and 5.1 GPa. If it is assumed that the FSDP position of the ambient liquid would be at a shorter reciprocal distance than the ambient glass, over the presented P range there appears to be a greater increase in shift (i.e. cage collapse) in the melt from 0.7-4.1 GPa, than in the glass, as might be expected in the more compressible and lower viscosity liquid (Figure 5.6). As seen in Figure 5.6 as temperature increases in samples below 4 GPa, the FSDP decreases in position and intensity, whereas above 4-5 GPa very little shift is observed. The melt network is initially more open due to the thermal disorder, and it is more likely to be able to rearrange on compression compared to the more rigid glass structure. By 4.1 GPa this difference has reduced completely and the FSDP in the melt and glass are similar, potentially indicating that the melt network has been compressed until it resembles that of the glass structure by 4-5 GPa. This indicates that below 4-5 GPa the melt network is highly compressible compared to the glass at the same pressure. The higher Q oscillations however, above 2.5 Å^{-1}, are consistently similar between the glass and the melt indicating that the short range structure, bond distances and atomic positions, are analogous between the glass and melt structures, which is confirmed by the $G(r)$.

The $G(r)$ are of high quality to 6 Å in real space, which includes up to the 2nd coordination sphere of silica tetrahedra. Between the glass and melt measurements, the intensity of the first peak, r_1, increases for a given P. This is related to the thermal expansion of the sample upon heating. The r_1 peak is attributed to the Si-O bond distance and is the most prominent feature in any silica rich glass or liquid. This occurs consistently at 1.6 Å in good agreement with other literature data on compositions over this P-range [17, 117, 118]. At the same temperature this peak decreases in intensity as pressure increases (Figure 5.5), as expected due to the increase in density under compression. The second peak, r_2 at 3 Å, with a shoulder at 2.5-2.6 Å, arises from the overlapping correlations between the O-O and Si-Si contributions at 2.8 and 3.2 Å respectively (Figure 5.7). A third broad peak, r_3, is also observed at 4.1 Å which represents the second nearest neighbour interactions of Si-O. All the features observed in the $G(r)$ are consistent between different beamlines, x-ray techniques and cell designs,

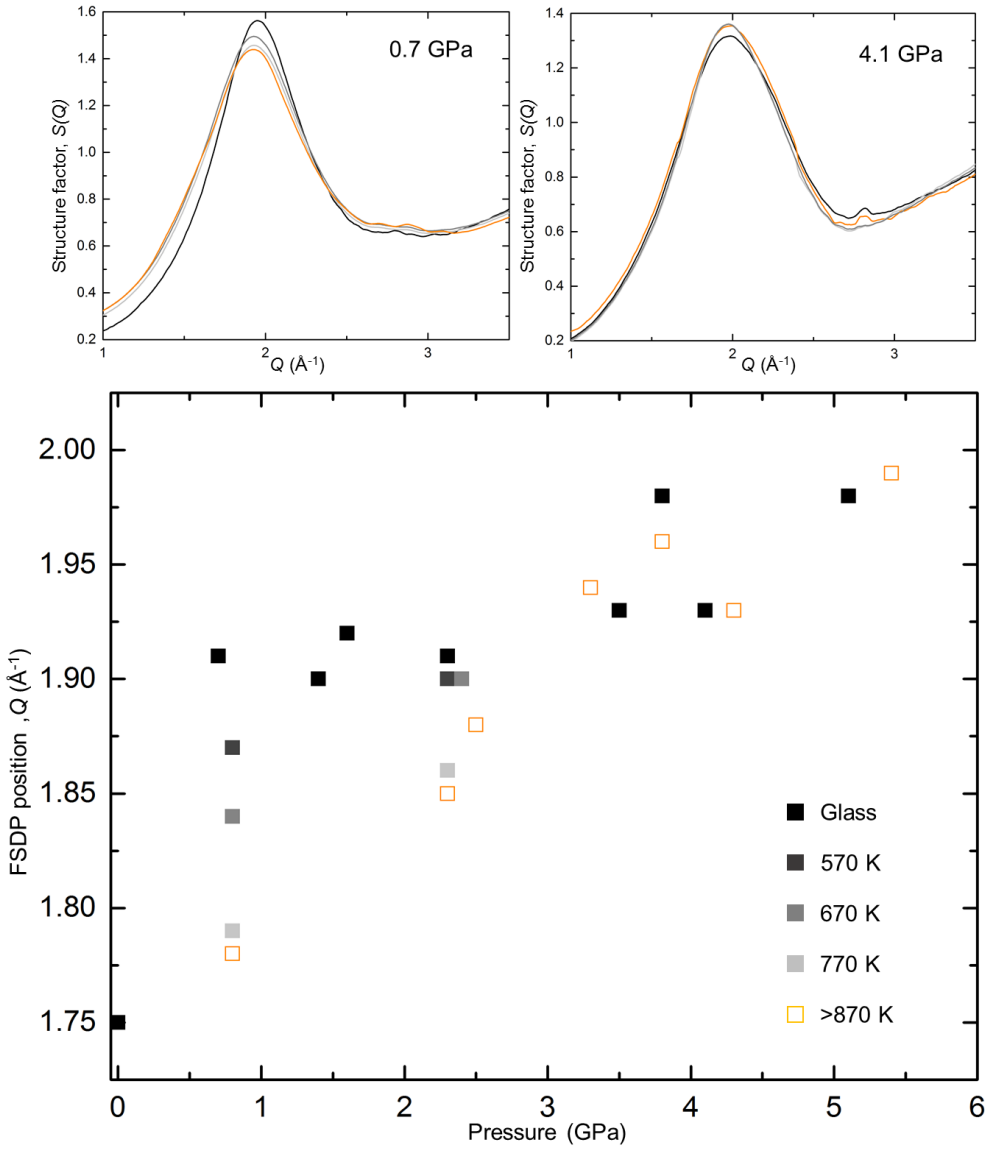

Figure 5.6 *Shift of the FSDP position with P for different temperatures ranging from glass to melt. Low pressure, 0.7 GPa, data shows clear decrease in FSDP position whereas 4.1 GPa data show very little variation.*

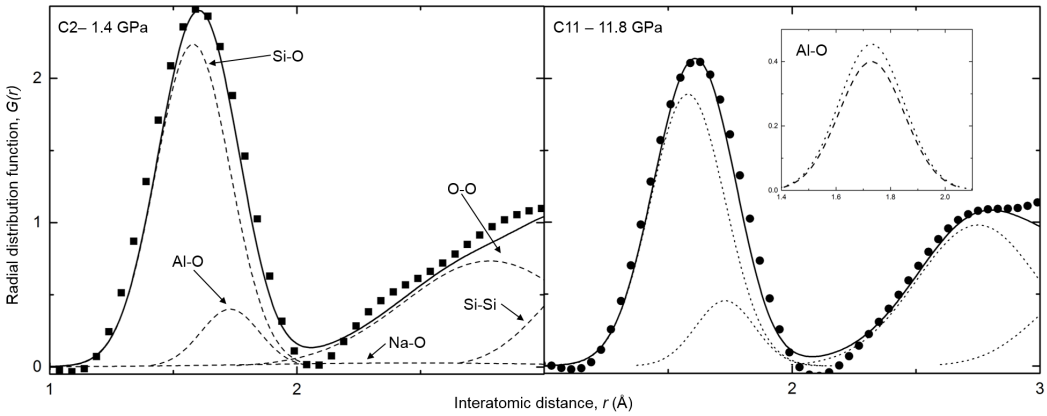

Figure 5.7 *Fitting procedure for hydrous HPG glasses (same for melts). Left is a low P sample (square markers), right is the highest P glass (round markers). Solid lines are the total fits from a sum of the individual fits (dashed and dotted lines). Fits are labelled on left figure and are the same correlations on the right. Inset shows the change in Al-O fit with P. Na-O contributions are only shown on left to show how minor the correlation is.*

indicating the high quality, consistency and reproducability of these data and data analysis methods used. As seen in Figure 5.2, there is no distinct difference between the glass and molten state. These results are similar to those measured for SiO_2 and rhyolitic compositions [16, 17, 119] and predicted by MD models [49].

In order to understand the individual pair correlations present in the HPG structure the data were fit with individual Gaussians that represent each ion-ion contribution (Figure 5.7). Two major assumptions had to be made in order to fit via this technique: (1) That all the correlations are symmetrical, and (2) that the density, n_0, can be predicted through fixing the Si-O correlation with a known coordination of CN_{Si-O}=4 and distance r_{Si-O} =1.6 Å over this P range. The first assumption can be made at short distances because the correlations are nearly symmetric and there are no contributions from secondary oscillations at r <3 Å. The second is in agreement with many previous studies on the coordination and bond distance of Si-O [17, 19, 117, 118], and as the width of the Si-O contribution is clearly visible, $g(r)_{Si-O}$ can be given a fixed width, CN, and r, allowing an estimate for the density by integrating under the Si-O contribution. The densities obtained via this method for each P and used in Equation 4 are shown in Figure 5.9. Self-consistency checks were also completed to confirm the reliability of the extracted density (see Chapter 4.5.4). For the $g(r)_{Al-O}$, initial CN_{Al-O} and r_{Al-O}

Ion-Ion	r_i	k	CN_i	Lit. r_i	Lit. CN_i
Si-O	1.6 (2)	0.12	4	1.61	4.0
Al-O	1.73 (1)	0.09	4.3-5.1 (2)	1.73	4.1
O-O	2.79 (2)	0.2	8.2	2.65	8
Na-O	2.46	0.2	8	2.46-2.68	8
Si-Si	3.2 (2)	0.13	6	3.08	na

Table 5.3 *Ion-ion contributions used to model individual Guassians, g(r)$_{ind}$, in the compositions at ambient conditions. Where bond distances evolved with pressure this is discussed in the text. r_i = bond length, k =width parameter of Gaussian, CN_i = coordination of individual bond. Si-O literature values from [17, 19, 117, 118], Al-O values from [20, 38], and O-O correlations from [49, 110], Na-O values from [49, 93, 121].*

from [20, 38], were used to refine the fit and the estimated $CN_{\mathrm{Al-O}}$ and $r_{\mathrm{Al-O}}$ obtained here are in good agreement with these studies. The correlations for Na-O and K-O are so small due to their low Z and concentration that they make very little contribution to the total $G(r)$ (Figure 5.7 left) as predicted in models by [49]. O-O correlations were initially fit with $CN_{\mathrm{O-O}}$ and $r_{\mathrm{O-O}}$ from [49, 110, 120]. In order to fit the r_2 contribution a sum between the O-O and Si-Si correlations was made to estimate the overlaps that might occur at lower r. Although fitting to 3 Å is not required for the HPG, this was critical in Chapter 7. The parameters used to model the data are listed in Table 5.3.

The fit results indicate that the Si-O peak has a variation from 1.58 to 1.61 Å which can be attributed to the error in the Fourier transform. There do not appear to be any significant changes in $r_{\mathrm{Si-O}}$ with melting as no alteration occurs between the high temperature and corresponding ambient T glass measurements. This is as expected for such a high silica content composition due to the strong glass forming nature of these liquids, as seen in SiO_2 glass and liquids. In the 11.8 GPa glass, the fits to the first peak in the $G(r)$ do suggest that a change in $CN_{\mathrm{Al-O}}$ may occur (Figure 5.7 right). This is because the density required to fit the contribution, without an increase in Al coordination, would be the same as the lowest P data which seems unreasonable. This suggests that either the $CN_{\mathrm{Si-O}}$ or $CN_{\mathrm{Al-O}}$ increases. Numerous studies have shown that $CN_{\mathrm{Si-O}}$ in glasses remains constant at 4 until >20 GPa; therefore it is most likely an affect of $CN_{\mathrm{Al-O}}$. This has been observed previously in silicate glasses by x-ray diffraction [110] and nuclear magnetic resonance spectroscopy [38], where studies witness 50% 6-fold Al by 12 GPa. The results here suggest an increase of $CN_{\mathrm{Al-O}}$

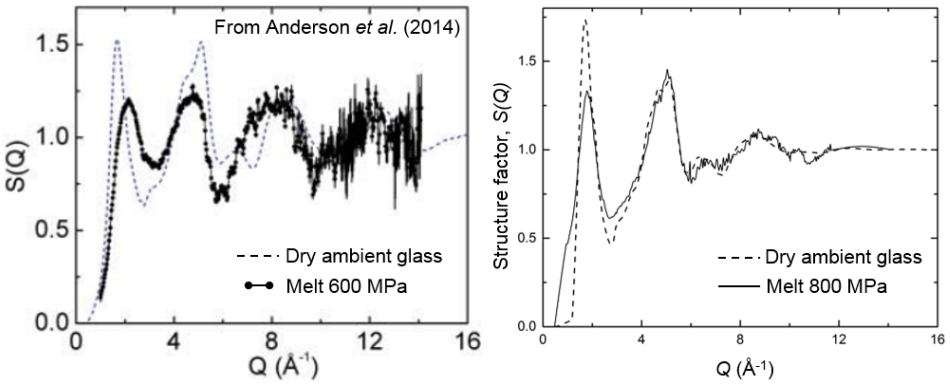

Figure 5.8 *Comparison of data presented here with that of [119] at similar conditions (600 and 800 MPa - 0.6 and 0.8 GPa).*

to an average of 5.3(2), suggesting at least 50% 6-fold coordinated Al by 12 GPa.

5.3.1 Anhydrous and Hydrous Haplogranite

The $S(Q)$ and $G(r)$ for the ambient dry and hydrous glasses are shown at the base of Figures 5.4 and 5.5 and show no variation on the addition of water in the glass structure except a decrease in Si-O intensity related to a decrease in density with the addition of water. Anderson *et al.* [119] also measured an HPG composition using DAC x-ray diffraction techniques at a similar pressure and using the same data processing methodology. They proposed that in water saturated HPG melts at low P, the bond distance of the Si-O increases by 0.095 Å to 1.71 Å from the glass to the melt phase. They also observe a dramatic shift in the $S(Q)$ FSDP position from 1.67 $Å^{-1}$ in the dry ambient HPG glass to 2.14 $Å^{-1}$ in the hydrous HPG melt at 600 MPa (0.6 GPa). This has not been observed here with 10 wt.% H_2O in the composition and there is no observable structural change between the anhydrous and hydrous compositions in the results of this study (Figure 5.8). Although there is no molten hydrous data at ambient P presented here, there is no observable shift in r_{Si-O} or in the FSDP, for the 0.8 GPa melt from the dry glass. The difference between observations is most likely to be down to the level of noise and normalisation of the $S(Q)$ in [119] at high temperature compared to similar high temperature data collected in this study (Figure 5.8). The ambient dry glass data between the two studies appears very similar, although the high levels of noise from 8-14 $Å^{-1}$ in the melt data of [119] would make correct normalisation very difficult. This could lead to incorrect peak height and width in the lower

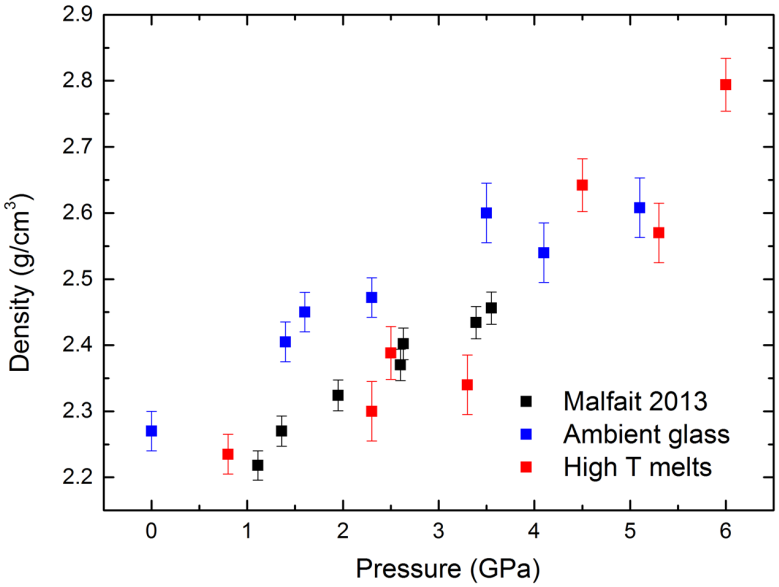

Figure 5.9 *Comparison of the densities obtained here with Malfait [122] density data collected using x-ray absorption on natural granitic samples. Melt data from this study is shown in red, and glass in blue. Black squares are reported melt data from [122]. Some data points (6 and 2.5 GPa are from Lu-HPG data shown in Chapter 7.*

Q region in the $S(Q)$, which induces incorrect distances in r after the Fourier transform.

5.3.2 Density Properties

The density, ρ, of the HPG was estimated via fixing the $CN_{\mathrm{Si-O}}$=4 and distance $r_{\mathrm{Si-O}}$=1.6 Å. In order to compare with reported densities in the literature, the calculated atomic number density, n_0, must be converted to g/cm^3. This is done using the formula $\rho = n_0 M/A_0$ where M is the atomic mass of the sample and A_0 is Avagadro's constant. The densities for the hydrous glass and melt samples are shown in Figure 5.9 and compared to hydrous granitic melt densities reported by [122], collected using x-ray absorption techniques on natural samples. The high temperature HPG measurements are in excellent agreement up to 4 GPa suggesting that densities extracted using this method are reasonable. The hydrous glass densities are consistently higher than those of the melt until 4-5 GPa where the densities of the glass and melt become similar within error and are less distinct. The initial lower densities of the melt at P <4 GPa would be expected due to the more flexible structure and lower viscosity of the HPG at high temperature. At 4-5 GPa the similarity of the densities may

corroborate the observations in the FSDP position in the $S(Q)$ (Figure 5.6), that compression of the silicate melt structure is more rapid until 4-5 GPa but subsequently becomes similar to that of the glass. Both these observations suggest that the collapse of voids formed by large cages within the more relaxed melt network is predominantly complete by 4-5 GPa in highly polymerised structures.

5.4 Conclusion

Platinum wire resistive heaters were successful at producing high $P-T$ conditions within DAC up to 950 K. Limitations in the number of heater coils and oxidation of the connectors prevented access to higher temperatures, which would be required to melt more basaltic or anhydrous compositions. X-ray diffraction techniques were used to gain insight into the structure of silica rich HPG melts and glasses at high pressure up to 12 GPa. Although little structural change was observed over the $P-T$ range, it can be seen that the density of the HPG studied here is consistent with previous studies and that both the FSDP and experimental densities reflect a collapse of voids and compression within the melt structure up to 4-5 GPa. The melt appears considerably more compressible than the glass up to this P, but further compression causes little differentiation between the melt and glass structures. The strong glass forming nature of this silica rich composition produces no overall structural difference between the glass and melt, dry or hydrous, in contrast to the findings of [119]. This result would suggest that quenched granitic glasses would be ideal analogues of the melt structure up to 6 GPa; although for density measurements it is critical, especially at P <5 GPa, that studies are carried out in the molten state. The coordination increase to 50% 6-fold Al-O observed by [20] and [38], also appears confirmed by results presented here.

Chapter 6

Trace Elements in Haplogranite using X-ray Absorption

This chapter begins detailing the results on the incorporation of trace elements within melt structures using x-ray absorption spectroscopy (XAS). It is a preliminary study to Chapter 7 in order to corroborate novel x-ray diffraction results, as XAS is a well established technique for looking at minor elements in silicates. The first part of this study, on Br in granitic melts, was completed in collaboration with Dr. B. Cochain and resulted in the publication 'Bromine speciation in hydrous silicate melts at high pressure' (Cochain *et al.* (2015) which can be found in Publications at the end of this thesis [1]). The structural results of this work were carried out predominantly by Dr. B. Cochain, although the initial stages of the analysis were completed by the author and are included to show the development of high $P-T$ EXAFS and analytical techniques that are applied in Section 6.3, where analysis was solely undertaken by the author. Any work carried out by Dr. Cochain is clearly highlighted in the relevant section.

6.1 Introduction

Minor elements, ranging from REE to noble gases, can be incorporated within silicate melt structures, and depending on the concentration and type of element contained within a typical melt these elements can play an important role in a range of magmatic processes. In this chapter the incorporation of trace elements

Br, Y and Zr within a composition similar to that presented in Chapter 5 will be discussed. XAS is particularly useful for studying minor elements as it provides information on the local structure around the specific element being studied. Quantitative information can be obtained on the number, interatomic distance and type of nearest neighbour atom interactions.

6.2 Preliminary Study - Bromine in Granitic Melts

Extended X-ray Absorption Spectroscopy (EXAFS) will be used to study the effect of bromine on the melt structure. Bromine, along with the other halogens (F, Cl, I), is thought to have an important role during the degassing of magmas in volcanic eruptions and, subsequently, the transport of these elements from the mantle and the evolution of the atmosphere [123–125]. Br has also been linked to the destruction of O_3 molecules in the atmosphere [126]. The solubility of these elements within the melt could influence how these elements are cycled as they are commonly linked to the degassing of H_2O [125]. Experimental studies have shown that Br could have multiple cycles that include Br returning to the mantle via silicate melts rather than the atmosphere through volcanism [127]. Understanding how Br incorporates in silicate melts, and how it is bonded to other elements, will therefore, help further understanding of its chemical behaviour.

6.2.1 Experimental Techniques and Analysis

Samples (supplied by C. Martel) for EXAFS were naturally erupted rocks from Mt Pelee with a nominally similar composition to the synthetic HPG in Chapter 5 (Table 6.1). In order to ensure homogeneity they were remelted, quenched in water and crushed by R. Champalier and G. Prouteau. They added Br and H_2O by high temperature pressurisation in an Ar-H_2 gas mixture at 1250^{o}C and 0.2 GPa for 42 hours. This composition would not have been suited to x-ray diffraction in the same way as the HPG due to the complication of having multiple higher scattering elements (Ti and Fe), but for XAS it is ideal as this only probes the local structure around the chosen element, in this case, Br.

Samples doped with Br were measured in transmission mode in a Paris Edinburgh press at the Br K-edge (13,470 eV) on beamline BM23 at the ESRF (Chapter 4.2.4). The energy of the beam was tuned by a Si(111) monochromator and

Oxide	Original Glass	Recovered Glass
SiO_2	73.27 (70)	71.40 (72)
TiO_2	0.30 (1)	0.29 (1)
Al_2O_3	12.20 (30)	12.58 (91)
FeO	0.83 (16)	0.03 (12)
MgO	0.41 (4)	0.40 (19)
MnO	0.08 (1)	0.07 (3)
CaO	2.29 (14)	2.23 (14)
Na_2O	4.19 (21)	4.82 (29)
K_2O	1.60 (13)	1.68 (18)
P_2O_5	0.01 (1)	0.01 (1)
Cl	0.01 (1)	0.01 (1)
Br	2.2 (22)	2.27 (31)
H_2O	3.50 (50)	4.00 (50)
Totals	100.89 (120)	99.79 (130)

Table 6.1 *Composition of the original parent glass doped with Br and H_2O, and the average recovered sample composition based on 10 sample spots for the quenched glass (2.1 and 3.4 GPa).*

the beamsize was $0.1 \times 0.5\,\mathrm{mm}^2$. The cell assembly, from [94], comprised of a boron-epoxy gasket and graphite furnace surrounding a boron-nitride cylinder and nano-polycrystalline diamond (NPD) capsule [128]. This capsule was used in order to minimise any Bragg peaks from single or poly-crystalline diamond that would cause interference and noise in the EXAFS spectra. In order to minimise the loss of water from the capsule Pt-Rh5% discs were placed at either end of the NPD cylinder. The boron-nitride (BN) capsule acted as the pressure transmitting medium within the gasket. Pressure was determined via diffraction from the BN and a Pt foil inserted at the side of the diamond capsule, and their equations of states were used to estimate the $P-T$ conditions within the sample (Chapter 4.3.5). Samples where cold compressed and heated by increasing power at a constant oil regulated pressure until any Bragg peaks within the sample had disappeared, ensuring a homogeneous molten state. $P-T$ conditions for the data collected are listed in Table 6.3. After high $P-T$ measurements, power to the press was shut off in order to quench the sample. If successfully quenched, recovered samples were analysed by electron microprobe (EMP) for their final composition and the presence of any crystals at EMMAC at the University of Edinburgh with a 15 keV accelerating voltage and 10 μm defocused beam. EMP collection and analysis was carried out with Dr. Cochain and no major change in sample composition occured during the experiment (Table 6.1). The Br content

of the samples was determined by C. Leroy using proton-induced x-ray emission (PIXE) analyses as detailed in [127] and H_2O content was estimated by Dr. B. Cochain using Raman spectroscopy.

EXAFS scans on the starting glass sample and references were run for 20 minutes from 13,300 to 14,300 eV to collect data up to 10-12 $Å^{-1}$ in k-space. The NaBr reference was collected to 8 $Å^{-1}$ due to the number of glitches at high k. Due to the low intensity of signal in the molten samples spectra were only collected to 13,710 eV. At each $P-T$ condition a minimum of three EXAFS spectra were collected in order to minimise the level of noise. During each run, a pellet of NaBr was recorded on channel I_2 after the sample chamber, I_1, in order to calibrate the edge energy and compensate for any beam drift (Chapter 4.7). Data collected via absorption spectroscopy was analysed using the theory outlined in Chapter 3.2. The data were processed using the ATHENA and ARTEMIS software by Ravel and Newville [129]. Multiple spectra collected under the same conditions were normalised to an edge jump of 1, merged in energy and were fit with a cubic-spline background. In this study the R_{bkg} was set at 1.35 Å for the references and 1.4 Å for the sample analysis undertaken by Dr. B. Cochain. Once normalised, the data were plotted as $\chi(k)$ and weighted by k^2 in order to increase the high k signal. $\chi(k)\cdot k^2$ spectra were then Fourier transformed using a Hanning window over an appropriate k-range for the reference and samples (Table 6.2 and Section 6.2.2).

6.2.2 Results

References

The analysis in this section was undertaken by the author. Reference spectra were collected on crystalline Br compounds ($FeBr_2$, NaBr, KBr, $KBrO_3$) in order to fit Br bonding environments of known structures that can subsequently be used for fitting the samples. $\chi(k)\cdot k^2$ spectra were Fourier transformed in ARTEMIS over a k-range specified in Table 6.2. These k-ranges were chosen to minimise the noise at high k that could be introduced into the Fourier transform and produce artefacts in real space. The fit parameters used to model the EXAFS data were coordination number (CN), amplitude reduction factor (S_0^2), attenuation due to thermal disorder in the bond length (σ^2), and shift in energy from the model to the measured distance (ΔE_0) (Table 6.2). The amplitude reduction

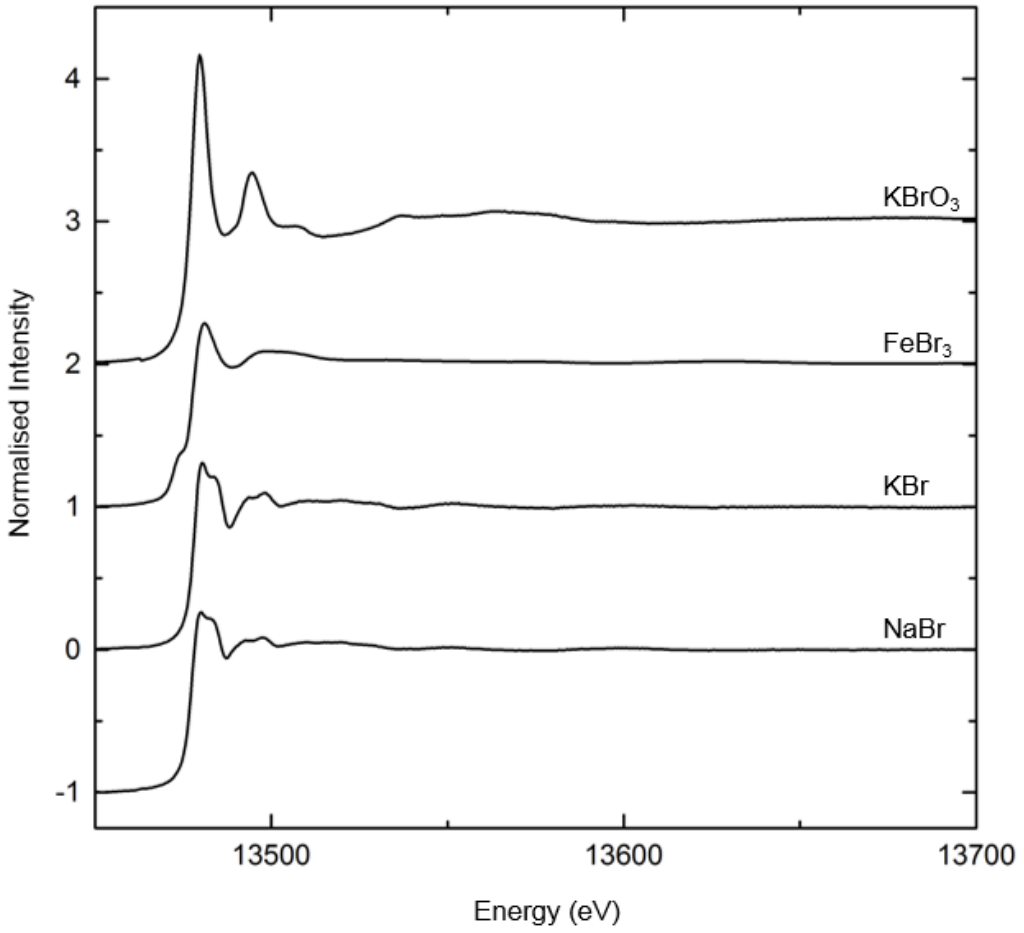

Figure 6.1 *Normalised XAS spectra for Br containing crystalline reference compounds.*

Reference	Bond	k-range	R (Å)	CN	R-factor	σ^2	ΔE_0	S_0^2
KBr	Br-K	2.5-10	3.25 (5)	5.5 (5)	0.006	0.02 (1)	0.57 (40)	0.49 (2)
$KBrO_3$	Br-O	2.5-10.5	1.65 (5)	3.3 (3)	0.03	0.001 (3)	5.5 (5)	0.51 (7)
$FeBr_2$	Br-Fe	4.2-12	2.3 (4)	6.1 (4)	0.004	0.005 (4)	-1.85 (82)	0.50 (1)
NaBr	Br-Na	2.6-8	2.98 (2)	6.0 (5)	0.019	0.008 (2)	5.6 (3)	0.55 (4)

Table 6.2 *Derived fitting parameters for Br containing reference compounds.*

factor, S_0^2, is related to the sample CN number and arises from the interactions between multielectron excitations [130, 131]. This factor is dependant on the beamline conditions and local environment of the element. For unknown sample environments it is usually measured on a reference sample of known CN and fixed for determination of CN for experimental samples [131]. All fits aimed to reduce the correlations between parameters, such as CN and σ^2 or R and ΔE_0, by fitting over k-weightings of 1, 2 and 3 simultaneously [132]. ΔE_0 never exceeded ± 6 eV, which showed that the fit procedure was reasonable [133]. The R-factor, the sum-of-squares of the displacement between the model and data (often described as the goodness of fit), was minimised during each fitting procedure and are listed in Table 6.2.

The normalised XAS spectra for the Br reference compounds are shown in Figure 6.1. The absorption edge, E_0 for the bromide samples is 13,478 eV with a very slight increase to 13,480 eV for the oxide, $KBrO_3$. This shift is due to the increase in oxidation state to +5 in potassium bromate. A clear change in the EXAFS oscillations is also seen in the oxide, with much more broad oscillations and a single peak at 13,500 eV. These oscillations produce distinctive differences in k. The pre-edge feature seen in $FeBr_3$ is related to the number of 1s-4d transitions that can occur and the less centro-symmetric environment of Fe. Within the NaBr and KBr samples a split of the absorption crest can be seen, which reflects the difference in site and symmetry of these compounds compared to the $FeBr_3$ and $KBrO_3$.

Theoretical backscattering amplitudes and model functions were calculated from CIF files [134–137] using IFEFFIT [129] after known crystallographic structures. Analysis of KBr produced a modelled distance for K-Br at 3.2-3.3 Å and a coordination of 5, in good agreement with [138]. The $KBrO_3$ structure was fit well with an average bond distance for Br-O of 1.65 Å and CN of 3 as observed by [139, 140]. The NaBr structure was fit with an Na-Br bond distance of 2.98 Å with 6 coordination, as found by [141, 142], and $FeBr_2$ structure of Fe-Br 6 CN at 2.36 Å. For $FeBr_2$ the coordination obtained is similar to that found in [143–145]

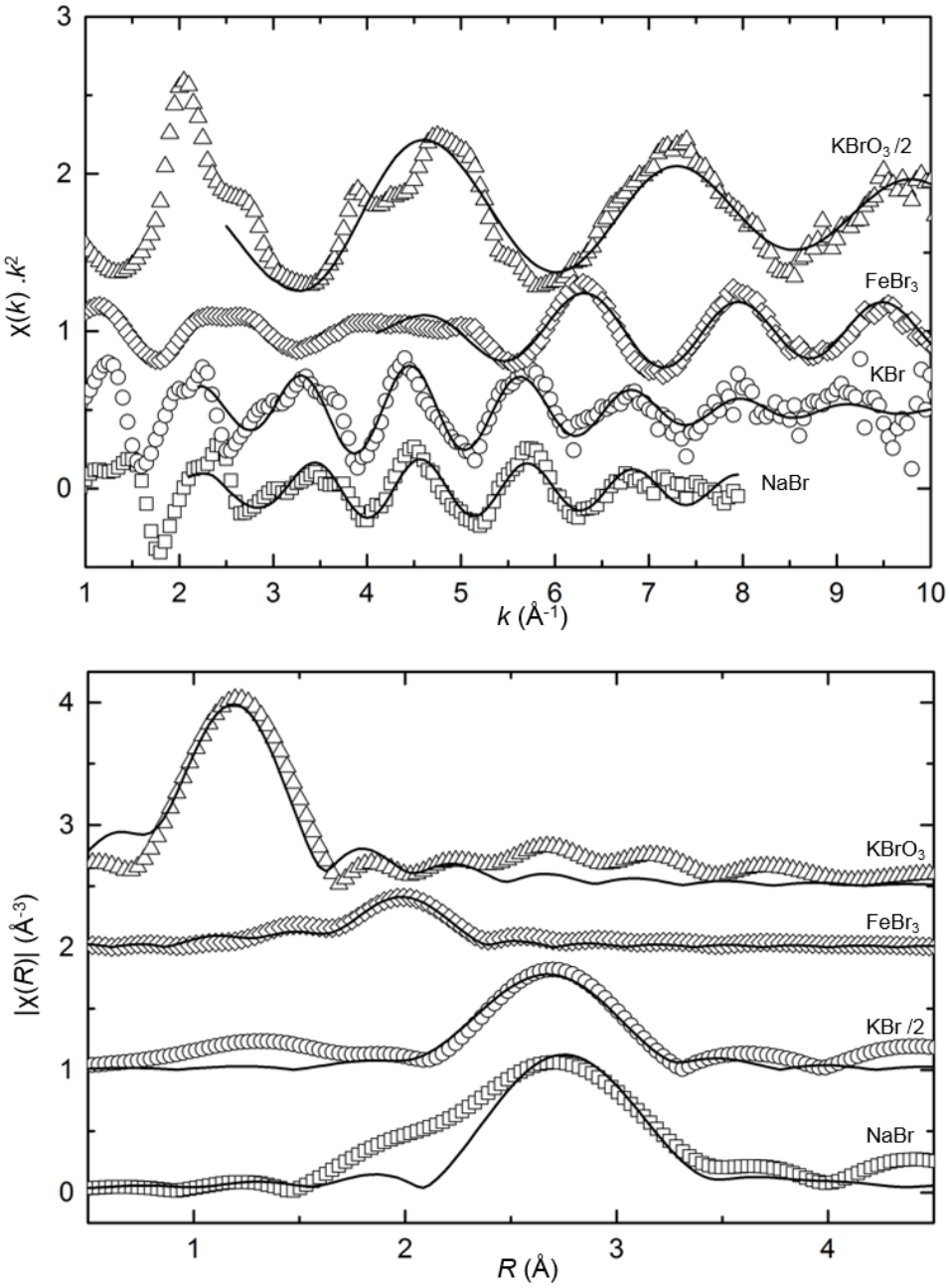

Figure 6.2 *Top: k^2-weighted EXAFS oscillations from EXAFS in Figure 6.1. $KBrO_3$ has been divided by a factor of 2 for scale. Collected data are shown as points, with fits (Table 6.2) in solid lines. Bottom: Fourier transform of top panel spectra with final fits.*

but the bond distance is 0.3 Å shorter than these studies suggest. In reference [1] Dr. Cochain fit the $FeBr_2$ structure with slightly different parameters, suggesting error can arise in the models due to the poor quality at low k of the EXAFS spectra and subsequently the chosen parameters for the fit. The $CN_{\mathrm{Fe-Br}}$ in [1] of 3 is low compared to literature values [145], although the bond distance produced by Dr. Cochain is in better agreement. The bond distance presented here is likely affected by the small range of the Fourier transform; however the CN seems more reasonable. This is one of the limitations of EXAFS analysis, as the chosen fitting range, window positions and background are at the author's discretion, leading to differences in the final fits. Many fits can produce equally low R-factors, which is often used to present the statistically most likely result, as multiple energy minima exist depending on the chosen starting values for the fit parameters [133, 146]. As σ^2, CN and S_0^2 all contribute to the amplitude of the fit oscillations; if one is initially input as too high/low this can directly affect the other. In this case the fit value of σ^2 was considerably lower than that of Dr. Cochain and therefore enabled a higher CN parameter to be estimated. As the R-factors are both very low the fits are equally as likely; this difference indicates the need for an excellent k-range and multiple reference compounds to establish a reasonable amplitude reduction factor for the data. The other fit parameters were in good agreement and within error of those reported in [1].

Samples

High $P-T$ data were collected at 2.1, 3.4 and 7.6 GPa, with quench measurements made at 2.1 and 3.4 GPa. Ambient glass measurements on the free standing starting glass were also collected. All the analysis in this section was completed by Dr. Cochain apart from the lowest pressure liquid where the author has compared derived results to that of Dr. Cochain. As can be seen in Figure 6.3 the noise levels in the data increase considerably at high $P-T$ conditions, making fitting of the data at $k > 6$ Å^{-1} difficult. The two maxima in the real space data also indicate the presence of multiple contributions in the data (Figure 6.4) which complicates fitting procedures. As can be seen in Figure 6.4 the same features are observed in all the quench and melt measurements, with peaks at 1.5 and 2.7 Å (uncorrected for phase shift). Using the references these were identified as most likely to be correlations from Br-O and Br-alkali (Na or K).

The same method of fitting as for the references was used, with the exception

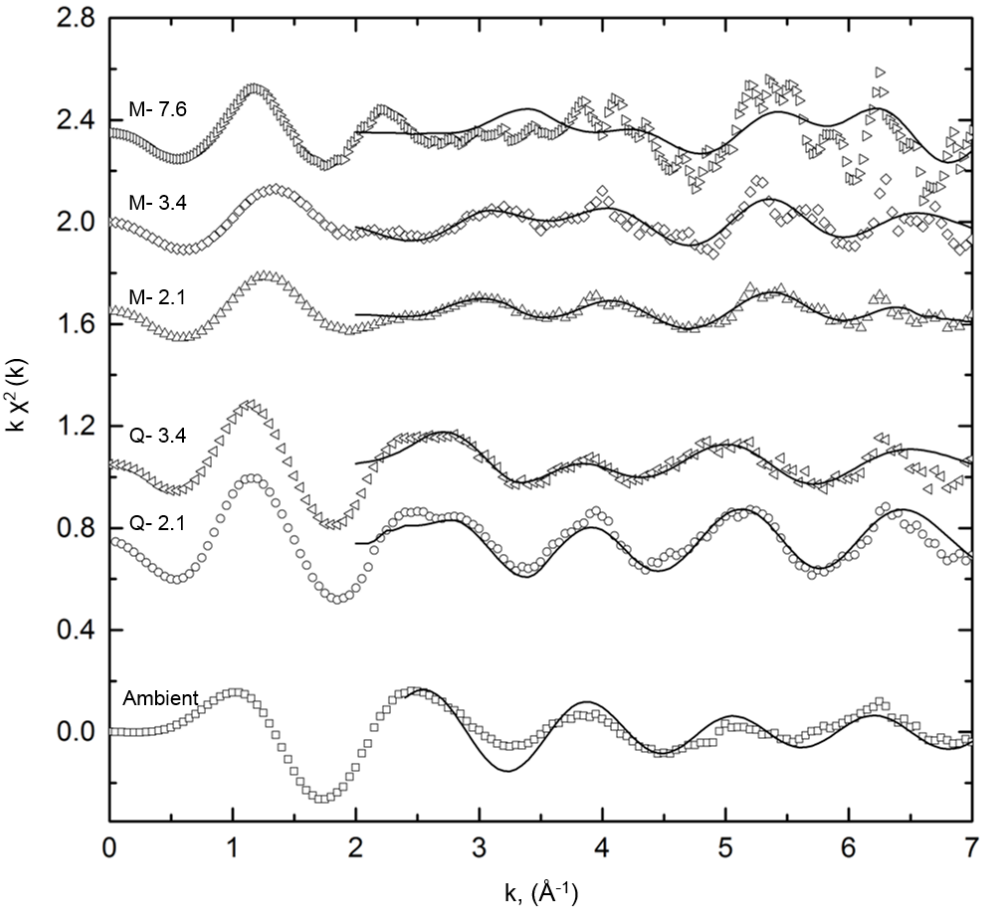

Figure 6.3 *k^2-weighted EXAFS oscillations for the parent glass (Ambient), quench (Q) and molten (M) samples. Data are points listed in Table 6.3, with fits shown in solid lines.*

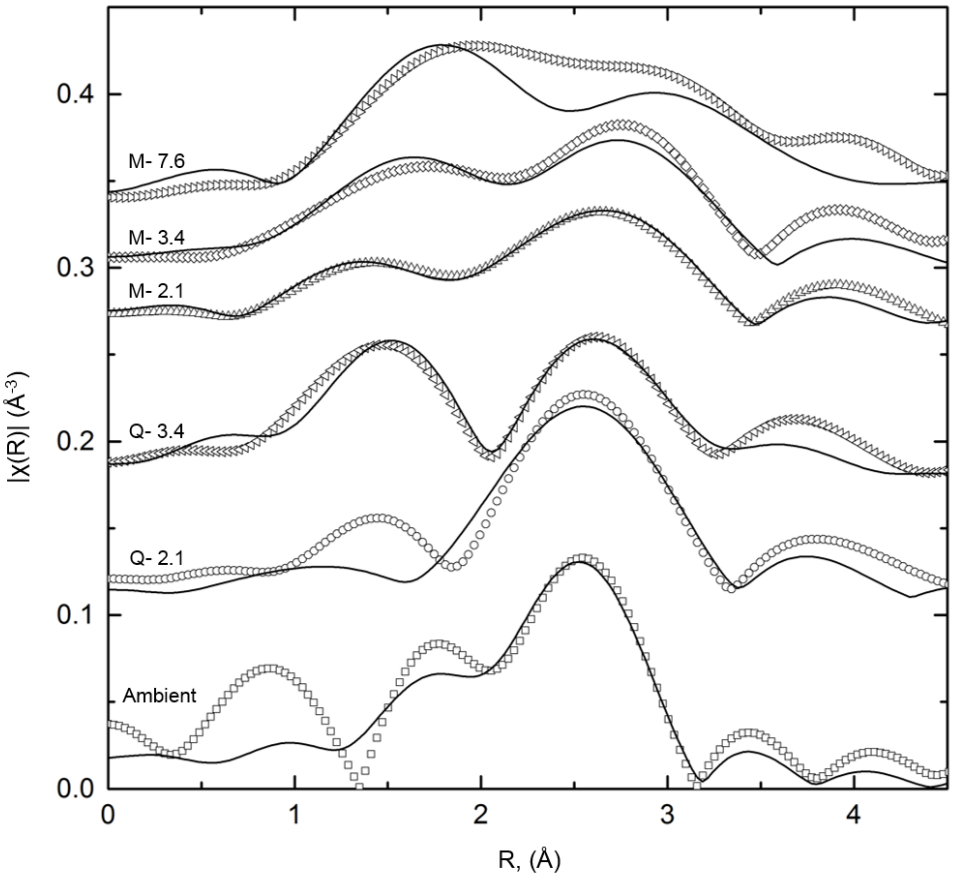

Figure 6.4 *Real space Fourier transforms of k^2-weighted data shown in Figure 6.3*

P (GPa)	T (K)	Bond	R (Å)	CN	σ^2	R-factor	ΔE_0	σ^3
2.1 M	2000	Br-O	1.67 (2)	2.0 (2)	0.07 (3)	0.02	3.79 (1.19)	0.005
		Br-Na	3.49 (5)	5.8 (2)	0.05 (1)			
This work		Br-O	*1.75 (6)	*3.2 (5)	*0.05 (3)	*0.02	*-0.2 (9)	*0.005
2.1 M	2000	Br-Na	*3.15 (10)	*6.1 (2)	*0.02 (3)			
2.1 Q	amb	Br-Na	3.63 (18)	6.5 (4)	0.09 (1)	0.12	-4.58 (11)	0.008
3.4 M	2000	Br-O	1.83 (18)	2.2 (3)	0.19 (2)	0.03	5.95 (2.42)	0.012
		Br-Na	3.63 (38)	6.1 (4)	0.06 (3)			
3.4 Q	amb	Br-O	1.68 (33)	1.5 (6)	0.03 (2)	0.04	3.25 (1.02)	0.024
		Br-Na	3.54 (87)	5.3 (3)	0.01 (7)			
7.6 M	2000	Br-O	1.91 (23)	2.1 (6)	0.05 (3)	0.19	1.90 (92)	0.001
		Br-Na	3.72 (57)	6.6 (7)	0.03 (1)			
Amb	amb	Br-Na	2.91 (37)	2.5 (1)	0.02 (2)	0.02	4.39 (61)	-
		Br-O (-H)	3.36 (9)	3.5 (7)				

Table 6.3 *EXAFS derived fitting parameters extracted by Dr. Cochain for the parent glass, quench (Q) and melt (M) data. 'This work' is the same sample as 2.1 M (2.1 GPa melt) with parameters derived by the author; these parameters are highlighted by * for clarity.*

of a much shorter k-range of 2-7 $Å^{-1}$ due to the noise at high energies, and the initial input parameters were obtained from the reference fits parameters. For the data it was important to always use the same k-range to ensure no artificial oscillations were introduced. Data were first compared to reference spectra to identify the most likely type of bonding to be present in the sample and reference spectra bond distances and coordination numbers were used as the initial fitting parameters. The second correlation in R in all of the samples (Figure 6.4), was fit much better with NaBr rather than KBr leading to the choice of this alkali in the fits. Amplitude (S_0^2) was set to 0.82(4) for the analysis by Dr. Cochain, based on the amplitude reduction factor for NaBr, and 0.52(2) for the lowest P glass analysed by the author. Parameters for the 2.1 GPa melt determined by the author are shown alongside results by Dr. Cochain in Table 6.3 and presented in Figure 6.5. The only distinct difference between both sets of results is the bond distance required to fit the Br-Na correlation which differ by 0.35 Å; this could be related to the lower S_0^2 value chosen by the author based on the reference parameters. This value can often vary for the same material [131] and arises from the use of a different NaBr dataset to that of [1] for comparison. It can be seen in Figure 6.5 in k-space, that the oscillations >6 Å are more accurately represented by B. Cochain, enabling a more precise fit of the second correlation in R to be obtained.

The results by Dr. Cochain were obtained as follows. The first contribution fitted well with Br-O from $NaBrO_3$. This indicates that the first shell surrounding Br

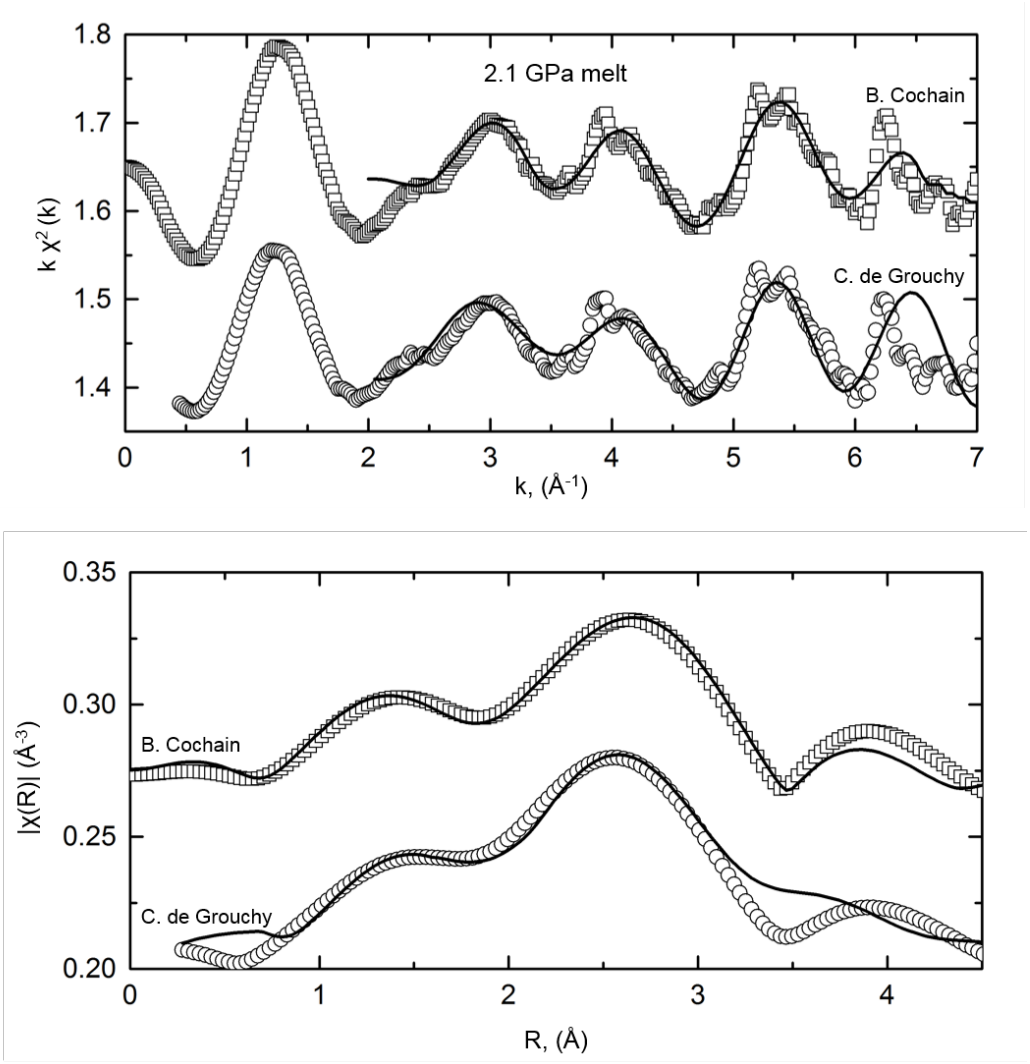

Figure 6.5 *Comparison of fits made by the author and Dr. Cochain for 2.1 GPa melt to show similarity of results.*

in the structure is O at a distance of $R_{\mathrm{Br-O}}$ =1.67 Å and $CN_{\mathrm{Br-O}}$ =2, which increases to $R_{\mathrm{Br-O}}$ =1.91 Å with increasing P. The second coordinating sphere is comprised of Na with $CN_{\mathrm{Br-Na}}$ =6 and $R_{\mathrm{Br-Na}}$ =3.49 Å increasing to 3.72 Å at 7.6 GPa. The contributions within the quench measurements are at slightly shorter distances of 1.5 Å; however a reasonable fit could not be attained for lowest P. The possibility of Br-Si correlations were tested for by including this correlation in the original fits, however none were found. The results from the molten and glass samples show that Br is predominantly surrounded by Na in a similar environment to that of NaBr with two oxygens within the Na coordination shell. These could be either a result of -OH molecules from the water, or from silica tetrahedra within the melt structure. Similar structures to NaBr have been found for Cl where Cl-Ca environments in salt-like arrangements dominate in Cl-bearing silicate melts [147].

The ambient glass structure could not be fit with the same parameters as for the melt and quench data. A structure similar to [114] of hydrated Br $[\mathrm{Br}(\mathrm{H_2O})_6]^-$ of 6 $\mathrm{H_2O}$ molecules at 3.4 Å and an Na-Br contribution at 2.91 Å were used. The hydration model approach provided a reasonable fit of the data with 3.5 Br-O(-H) contributions at 3.36 Å and $CN_{\mathrm{Br-Na}}$=2.5 at $R_{\mathrm{Br-Na}}$=2.91 Å.

6.2.3 Discussion

The results show that there is a distinct difference between the incorporation of Br in silica rich ambient glass to that of the molten and quenched samples at high pressure up to 7.6 GPa. A hydrated Br complex consisting of $\mathrm{Br}[\mathrm{Na}_x(\mathrm{H_2O})_y]$ appears to dominate at ambient conditions, similar to results presented by Louvel *et al.* [148]. In contrast, with increasing pressure and temperature, a change to a Br environment similar to crystalline NaBr occurs (Figure 6.6). A slight increase in $CN_{\mathrm{Br-O}}$ and $R_{\mathrm{Br-O}}$ up to 7 GPa is observed, indicating that minor elements also undergo coordination changes with P in silicate melts, as observed for major elements such as Si, Al and Ca [19, 20].

The exact nature of the oxygens that coordinate the Br within the melt and quench structures is not possible to identify using EXAFS. However, Dr. Cochain proposed the most likely scenario to be the presence of -OH molecules linked to water present near the alkali 'salt-like' structure (Figure 6.6). As Br appears to bond with alkalis in the melt structure, this would suggest that with increasing alkali content in the melt, the solubility of Br in the melt structure may also

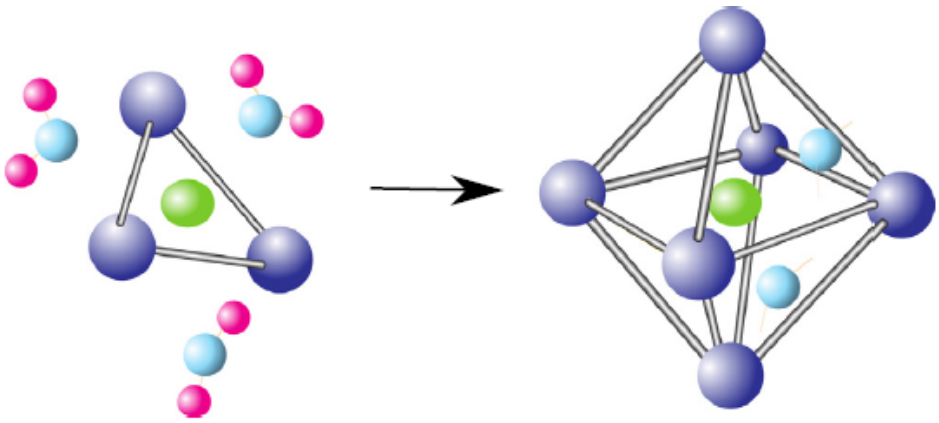

Figure 6.6 *Schematic view of how Br atoms (green) may incorporate in the ambient glass structure (left) by $Br[Na_x(H_2O)_y]$ complexation, to the incorporation at high $P-T$ in the melt (right), where Br is surrounded by Na atoms (purple). Oxygen atoms - light blue, hydrogen atoms - pink. From [1].*

increase. The results corroborate existing studies on the increasing partitioning of Br into silicate melts with a higher number of network modifying cations and alkalis [127]. Although halogens are most soluble in aqueous fluids, Br solubility is known to be high in alkali rich hydrous silicate melts [149], and therefore the incorporation of Br by alkalis in the melt may allow silicate melts to act as carriers of Br within subduction zones. If any Br was retained within the slab after initial fluid dehydration, subsequent melting of crustal material at depth may mobilise any remaining halogens from the slab to the mantle wedge, and possibly transport halogens into the volcanic arc.

Although there is a very slight difference in coordination (<1) and bond distance (<0.1 Å) between the melt and the glass, the overall Br environments are consistent, and the slight changes in CN and R are most likely due to the high thermal motion within the liquid. There does not appear to be any major structural difference between the melt and quenched samples, indicating glasses quenched from high T could be used analogously to the melt, as in Chapter 5. This study showed the possibility of studying trace elements in HPG at high $P-T$ conditions using XAS, and how the use of NPD capsules provided a glitch free signal in the melt under pressure. On the basis of this work a similar study on Y and Zr in HPG melts was carried out by the author and is presented below in Section 6.3.

Oxide	Original Glass	Y Recovered Glass
SiO_2	72.1 (2)	69.6 (3)
Al_2O_3	10.6 (2)	9.75 (3)
Na_2O	3.7 (1)	4.1 (2)
K_2O	3.9 (1)	3.6 (2)
Y_2O_3/ZrO_2	2.5(1)/2.2(1)	1.2 (2)
Total	92.8/92.5 (5)*	88.25 (7)*

Table 6.4 *Composition of original starting HPG glasses both Y and Zr doped, and recovered sample analysis of Y containing HPG data as no Zr containing samples were succesfully recovered. Samples are based on a minimum of 10 analysis spots. * The low totals are due to the addition of water in the sample which cannot be measured by microprobe but matches well with added H_2O quantities.*

6.3 Yttrium and Zirconium in Haplogranite

The local structure of Y and Zr within HPG silicate melts (of the same composition as Chapter 5) at high pressure and temperature were investigated to identify the effect of pressure on REE speciation. Trace elements Y and Zr were chosen as they are chemically similar to Lu and Hf, which are important trace elements in early Earth dating and formation (Chapter 2.2). Results from x-ray diffraction on Lu within the same composition are presented in the following chapter for comparison. Although the intention of this thesis is to collect information on the incorporation of REE and HFSE in silicate melts at high P, the absorption K-edge energies of Lu and Hf are too high (>63 keV) to obtain good quality EXAFS data, and the relatively small atomic numbers of Y and Zr make them difficult to detect at low concentrations by x-ray diffraction. Therefore Y and Zr were used in this EXAFS study as proxies for Lu and Hf, with Lu later studied by x-ray diffraction (Chapter 7), due to their excellent K-edge energies for EXAFS (17,047 and 17,997 eV respectively) that provide a good absorption signal even at low concentration.

6.3.1 Data Acquisition and Analysis

The HPG was synthesised as for Chapter 5, with the addition of high purity (>99.99%) Y_2O_3 and ZrO_2 at 2.5 wt.% to separate samples (Table 6.4). Glasses were fused in a furnace at 1600°C and fast quenched by immersion of the crucible

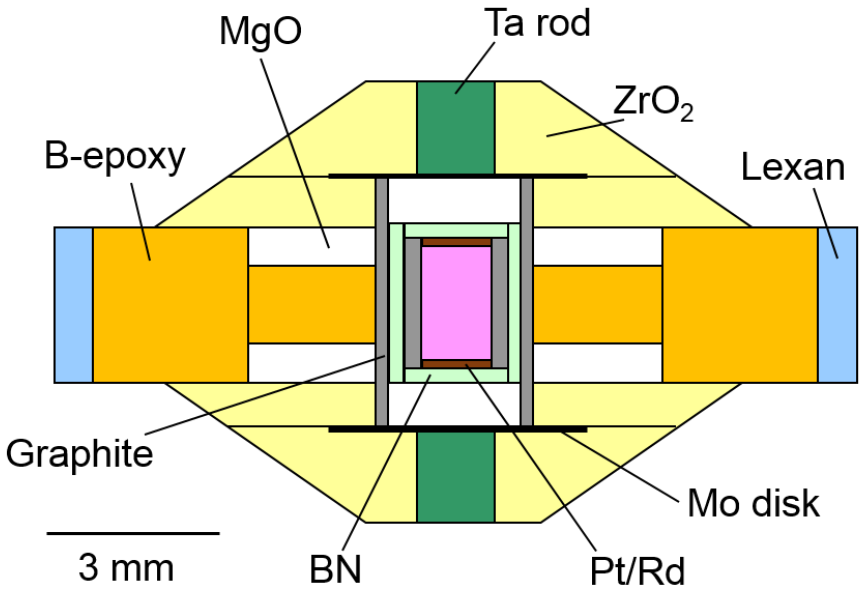

Figure 6.7 *Modified cell assembly with BE 'windows' [86] first used in this study for EXAFS measurements on Y and Zr. BE 'windows' in the MgO gasket provide increased transmission from the sample.*

in cold water. Full homogenisation was achieved by repeating this step 3 times and finely grinding the sample under acetone between each melting. The data acquisition and analysis techniques employed in Section 6.2.1 were used for the study of Y and Zr incorporation within the HPG from Chapter 5; however, modifications were made to the cell assembly in order to maximise the signal from the sample. A cell design developed by Y. Kono [86] was trialled with boron-epoxy (BE) 'windows' in the MgO ring of the gasket to minimise absorption from the cell assembly (Figure 6.7). As they were successful in minimising glitches in section 6.2.1, nano-polycrystalline diamond capsules were used, and high $P-T$ conditions were generated by a Paris-Edinburgh press on BM-23 at the ESRF. Experiments were conducted in a similar set-up to Section 6.2.1 with cold compression of the sample and resistive heating through a graphite heater. Temperature estimates were made from previous calibration measurements of the cell-assembly [94] and the pressure was derived from the cell volume of Pt and MgO within the cell assembly. In order to monitor the onset of melting, XRD was used to assess the appearance and subsequent disappearance of Bragg peaks in the spectra during heating. A minimum of four spectra were collected for each measurement and a reference foil of Y (or Zr) was measured in channel I_2 to monitor any beam drift (Chapter 4.7).

EXAFS signal analysis was undertaken as described in Section 4.7 with the

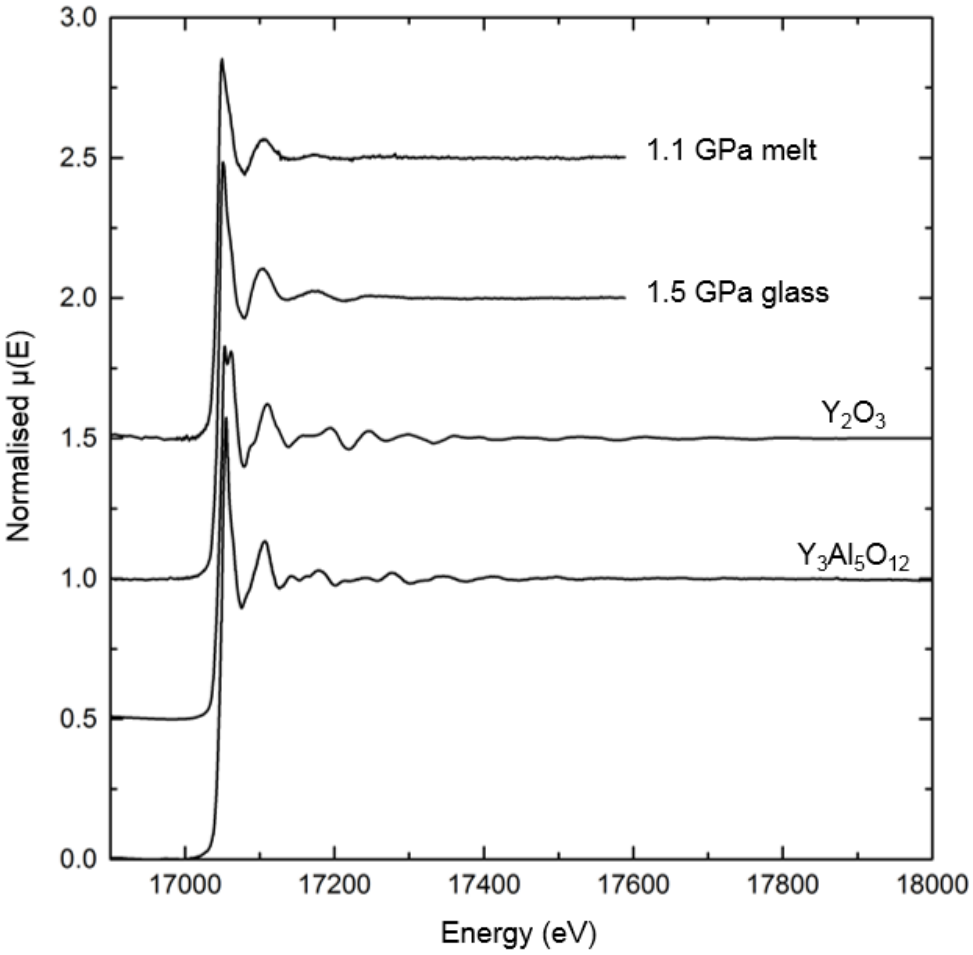

Figure 6.8 *XAS spectra for Y containing reference compounds and an example of one glass and melt spectrum for comparison to references.*

specific details as follows. The minimum R_{bkg} for all analyses was 1.25 Å, set as the distance at which below no atom-atom interactions could take place. The spectra were normalised for an edge jump height of 1 and shifted for any beam drift that occurred over the scan time. The k-range used in the Fourier transforms was consistent for all measurements of the same type; for the references a Hanning window over 3-15 $Å^{-1}$ in k was used, and for the glass and high $P-T$ measurements the k-range was 2-7 $Å^{-1}$ in order to minimise any artefacts arising from the lower quality data at high energy. Fourier transforms and fits were made over all k-weights (1-3) in order to reduce the correlations between fit parameters [132] and the results are presented as $\chi(k).k^3$-weighted in order to view the high k oscillations.

6.3.2 Results for Yttrium-doped Haplogranite

Reference spectra were collected from 16,820 to 18,280 eV with a scan time of 30 minutes. Glass and high $P-T$ measurements were collected from 16,820 to 17,580 eV over 15-20 minutes. Normalised XANES and EXAFS spectra collected on the references and samples are shown in Figure 6.8. Only one glass and one melt spectra are plotted as the spectra remained identical over all $P-T$ conditions. In a qualitative description of the XANES spectra it can be seen that the edge position of the samples and references is at 17,050($\pm$0.5) eV indicating no change in oxidation state of Y^{3+}. As in the Br data in Section 6.2.2 the height of the edge decreases in the molten state due to the thermal disorder within the sample. There are also noticeable differences in the shape of the absorption crest, and as a first inference the samples could be assumed to have a more similar Y structure to the $Y_3Al_5O_{12}$ from the absence of a 2nd crest peak at 17,062 eV which is seen in the Y_2O_3. The splitting of the crest in Y_2O_3 most likely represents the inequivalent Y sites of regular and distorted octahedral sites, Y1 and Y2, as reported by [150, 151]. The slight shoulder at 17,087 eV on the first EXAFS oscillation is caused by multiple scattering paths that were not fit here. This XANES comparison between the reference and sample spectra was used as a starting point for the fits described later in this section.

Yttrium references

Y-containing references (Y_2O_3 and $Y_3Al_5O_{12}$) were collected in order to represent possible coordination sites for Y in silicate melts and glasses. These were fit using the same methodology as described in Section 6.2.2 with four fit parameters: CN, σ^2, ΔE_0 and S_0^2 with the amplitude and phase shift calculated by IFEFFIT [129] from crystalline reference compounds [151, 152]. Only relevant bond environments that contributed to the EXAFS spectra were included in the fit and these were identified by individually modelling interactions up to 6 Å and seeing the largest contributors. Figure 6.9 shows the k^3-weighted EXAFS spectra for the reference compounds and subsequent Fourier transforms and their fits with fitting parameters listed in Table 6.5. These fits and parameters compare well with existing EXAFS data on both references [41, 153–155].

For Y_2O_3 an R-factor of 0.02 shows the goodness of fit and three main contributions can be seen at 1.9, 3.1 and 3.7 Å (uncorrected for phase shift).

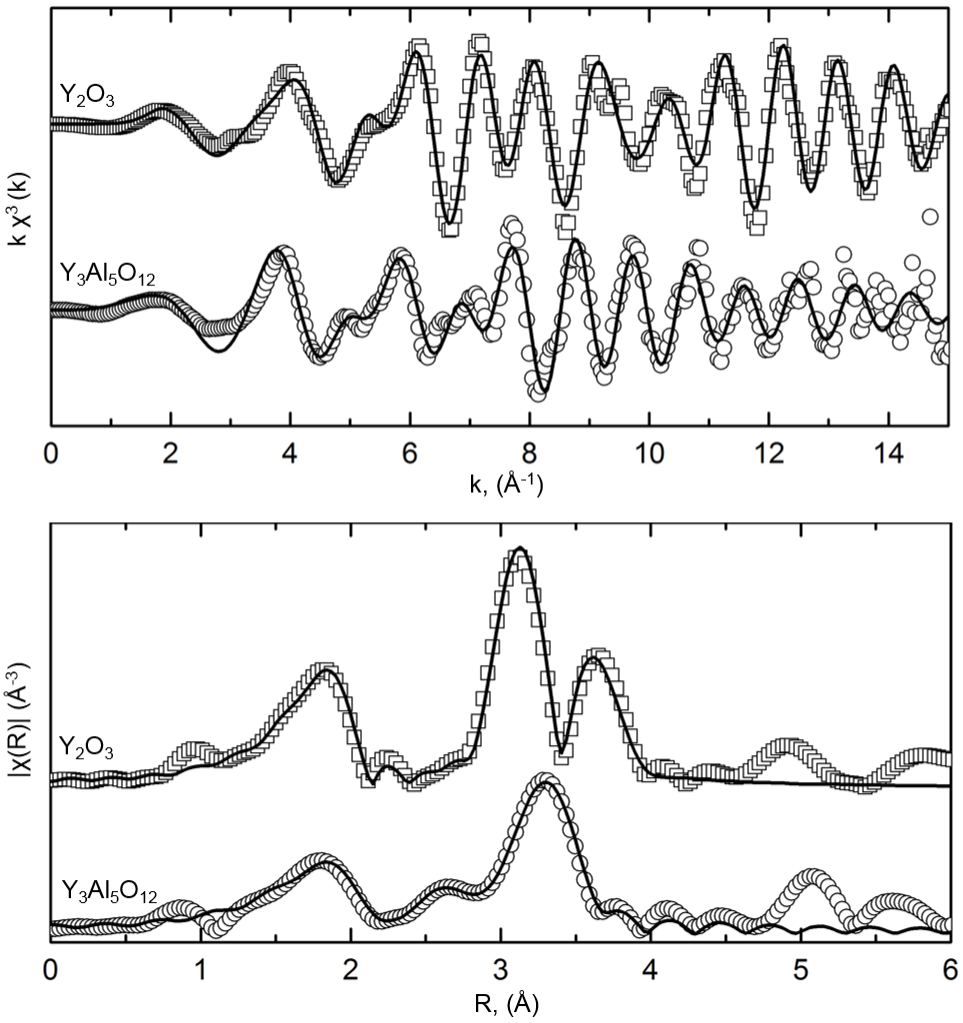

Figure 6.9 *Top: k^3-weighted EXAFS oscillations for the Y containing reference compounds and their subsequent fits (solid lines). Bottom: Real space data Fourier transformed from k^3-weighted data above.*

Y_2O_3	R-factor = 0.02	ΔE_0 = -4.5 (9)	S_0^2 = 1.23 (5)
Bond Type	R (Å)	CN	σ^2
Y-O	2.28 (2)	6.1 (3)	0.006 (3)
Y-Y_1	3.52 (3)	6.3 (3)	0.005 (2)
Y-Y_2	3.99 (2)	6.0 (4)	0.006 (3)
Y-O_1	4.20 (4)	6.4 (3)	0.006 (3)
Y-O_2	4.32 (3)	5.8 (4)	0.006 (3)
$Y_3Al_5O_{12}$	R-factor = 0.03	ΔE_0 = -4.12 (1.0)	S_0^2 = 1.15 (9)
Bond Type	R (Å)	CN	σ^2
Y-O	2.30 (3)	4.1 (2)	0.01 (1)
Y-O	2.44 (3)	4.2 (3)	0.01 (1)
Y-Al_2	3.01 (2)	2.0 (2)	0.006 (3)
Y-Al_1	3.36 (3)	3.9 (3)	0.02 (1)
Y-$Al_{2.1}$	3.68 (4)	4.2 (4)	0.01 (2)
Y-Y	3.68 (4)	4.1 (3)	0.007 (3)
Y-O_1	3.82 (5)	4.5 (4)	0.01 (2)

Table 6.5 *EXAFS Fitting parameters derived for the Y containing crystalline reference compounds.*

Initially the first contribution, arising from the shell of O surrounding Y ions in the crystal structure, was fit in order to fix ΔE_0. The first maxima in R is solely from the first coordination sphere of Y-O and represents octahedral coordination of 6 oxygens at 2.28 Å as reported in [156] and [157] where they identified 6 coordinated Y in two sites with an average Y-O bond distance of 2.26 and 2.29 Å. For the 2nd and 3rd shells ΔE_0 was fixed in order to minimise the number of fit parameters as various σ^2 were required for the fits of individual bonds. The 2nd maxima comprises of 6 Y-Y_1 at 3.52 Å, Y_1 being the first shell of Y atoms surrounding the starting Y position. The third shell was fit in the same way and comprised of 6-coordinated Y-Y_2 (the 2nd shell of Y interactions) at 3.99 Å, 6-coordinated O at 4.2 Å and 6-coordinated O at 4.32 Å.

For $Y_3Al_5O_{12}$ three maxima are seen at 1.9, 2.7 and 3.3 Å (uncorrected for phase shift) and as with the Y_2O_3 the first two represent shells of a single type of atom surrounding Y. During fitting ΔE_0 was fixed by fitting the first maxima, representing contributions from 8 oxygens in a distorted dodecahedra configuration with 4 oxygens at 2.30 Å and 4 at 2.43 Å, similar to 2.32 and 2.44 Å as reported by [158]. The 2nd shell arises from two Y-Al bonds at 3.01 Å, with the third maxima comprised of multiple bond environments including Y-Al, Y-

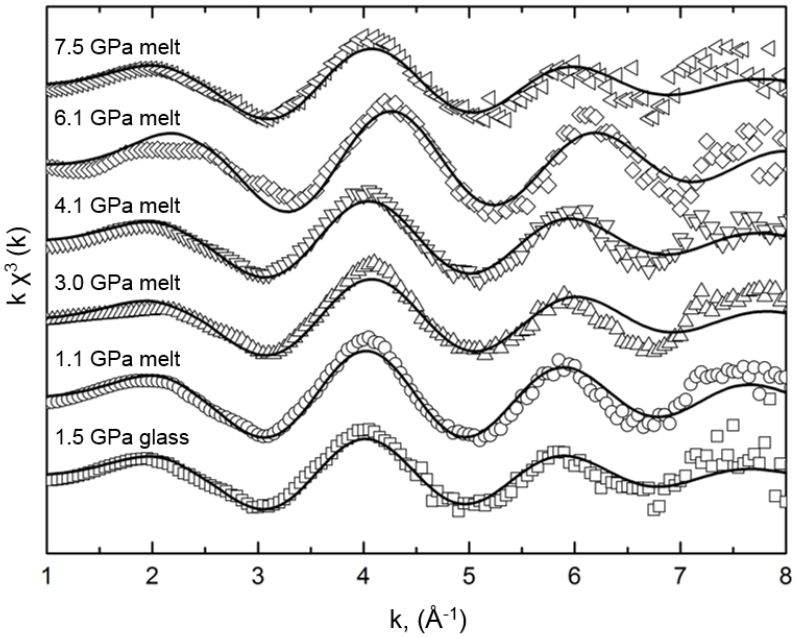

Figure 6.10 *k^3-weighted EXAFS oscillations for Y-doped HPG samples at high pressure and temperature as detailed in Table 6.6. Fits to data are shown in solid black lines.*

Y and Y-O in various shells and distances (Table 6.5). The higher R (>4 Å) correlations in both references come from higher shell interactions and multiple scattering paths that were not fit here. Goodness of the fits is indicated by the small R-factors and deviation from E_0 (Table 6.5). The fit to these model compounds could then be used to fit the measured data as known parameters could be used in the initial fitting procedures.

Yttrium High Pressure Melts and Glasses

High pressure glass data were collected at 1.5 GPa, with melt data collected at 1.1, 3.0, 4.1, 6.1, and 7.5 GPa and >1450 K (Table 6.6). The k^3-weighted EXAFS spectra with fits and corresponding Fourier transforms (uncorrected for phase shift) for the glass and melts are shown in Figures 6.10 and 6.11. Fits were made using initial bond distances and coordination numbers obtained from the crystalline reference samples, and the amplitude for all the melts was fixed at 0.95(5) from the glass data. The R-factors were all <0.02 with ΔE_0 consistently <6 eV which confirms the validity of the fitting procedure. The errors for coordination where obtained by varying the coordination number until

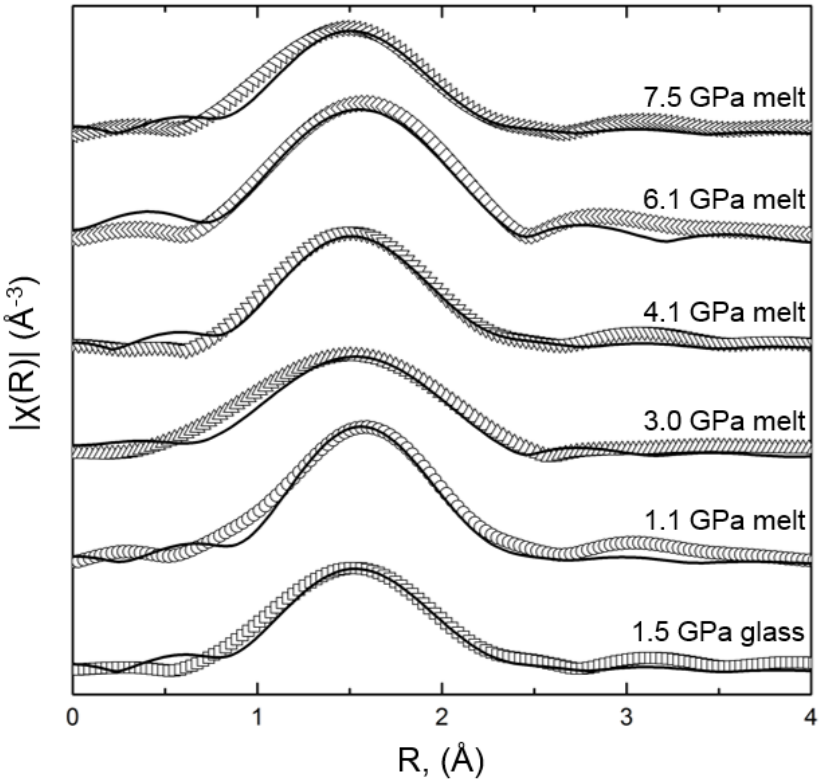

Figure 6.11 *Real space data for samples shown in Figure 6.10.*

P (GPa)	T (K)	Bond type	CN	r (Å)	R-factor	σ^2	ΔE_0 (eV)
1.5 (3)	300	Y-O	8.1 (2)	2.38 (2)	0.02	0.008 (3)	-3.0 (2)
1.1 (3)	1450 (50)	Y-O	8.1 (3)	2.40 (4)	0.01	0.02 (1)	-3.68 (80)
3.0 (5)	1500 (50)	Y-O	7.8 (4)	2.39 (3)	0.017	0.02 (1)	-4.17 (40)
4.1 (5)	1580 (60)	Y-O	8.1 (3)	2.37 (3)	0.008	0.02 (1)	-1.37 (10)
6.1 (4)	1600 (50)	Y-O	8.5 (4)	2.37 (4)	0.005	0.022 (4)	-4.2 (10)
7.5 (5)	1650 (50)	Y-O	7.8 (3)	2.37 (4)	0.004	0.024 (5)	-4.2 (10)

Table 6.6 *Experimental conditions and fit parameters for the Y-doped HPG samples.*

a fit was no longer reached or the R-factor drastically increased representing a considerable worsening of the derived parameters. The first maximum in R is the Y-O correlation which is consistent across all $P-T$ conditions, including both glass and melt spectra. This correlation was fit with Y-O at an average distance of 2.37 Å and CN_{Y-O}=8. This fit was based on the $Y_3Al_5O_{12}$ standard and could not be fit with any lower coordinated correlations (Table 6.6). Quenched samples which were recovered for analysis contained crystals of quartz and micron sized blobs concentrated in Y (Figure 6.12), within an HPG glassy matrix. The glass retained a stoichiometry similar to the starting composition (Table 6.4), apart from a slight reduction in SiO_2 and Y_2O_3 due to the quartz crystals and nodules. It is known that crystals were not present during the high $P-T$ experiments due to the lack of Bragg peaks in the sample from XRD, and the absence of glitches in the EXAFS spectra which would be caused by crystals floating within a liquid.

The coordination and bond length found for Y-O in these melts is consistent with those reported for Y-O in other highly polymerised glasses at ambient conditions. Simon *et al.* [41] present an increase in coordination and bond length from CN_{Y-O}=6 and R_{Y-O}=2.27 Å to CN_{Y-O}=8 and R_{Y-O}=2.4 Å as the polymerisation of the glass increases. The bond length and coordination derived in this study, within a silica rich, highly polymerised HPG composition is therefore consistent with their results and other studies that indicate REE adopt 8-fold coordination in highly polymerised compositions [39]. The results within the high $P-T$ melts, show that no structural change of Y incorporation within the HPG occurs up to at least 8 GPa. The similarity between the incorporation within the glass [41] and melt in this study is consistent with the results of Chapter 5, that silica rich compounds are strong network formers with nearly identical glass and melt structures.

In silica rich compositions, the high coordination is attributed to the lack of

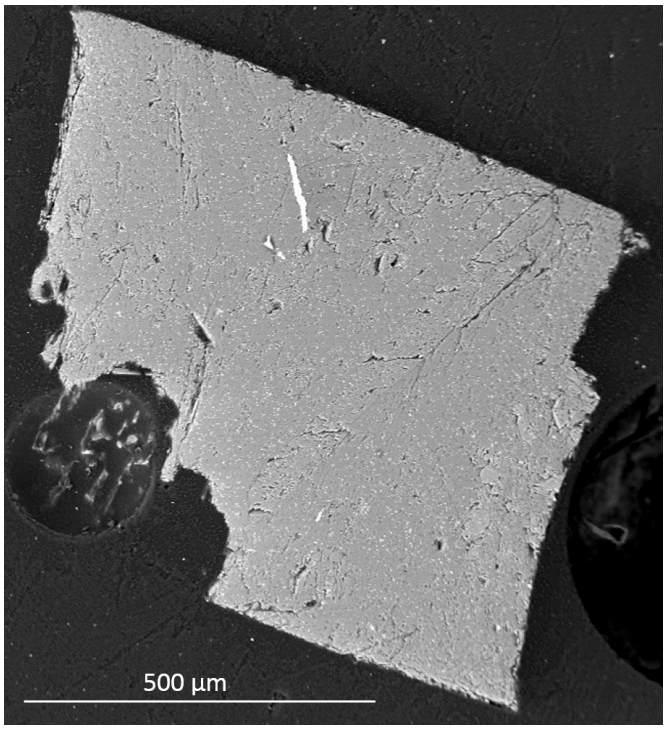

Figure 6.12 *Recovered Y-containing sample from 3 GPa and polished lengthwise down the capsule. White speckles are nodules of concentrated yttrium and SiO_2. Large white strip is Pt from the pressure calibrant that has moved into the sample. Large crystals of quartz can be seen towards the right hand side of the capsule.*

non-bridging oxygens where large numbers of interconnected silica tetrahedra form cages within the structure. This reduces the number of available non-bridging oxygens to bond with large, highly charged elements such as Y and as a result they therefore adopt high coordination numbers, predominantly bonded to bridging oxygens. Within the melt network, the 4-7 member ring structures are unlikely to accommodate Y or other REE within them due to the cavity size of <2.5 Å; therefore Y is most likely situated within the larger cages in the structure surrounded by 8 nearest neighbour oxygens. It would appear from this result that with increasing P the larger sites that contain Y must remain open up to 8 GPa as no change in bond distance or coordination for Y is observed. This would indicate that the compression of the melt must arise from the collapse of smaller cages and those that do not contain REE.

Due to the thermal disorder within the samples at high temperature, and the noise at high k *in situ*, the pair correlation functions in real space (Figure 6.11) are quite broad. These could be fit by a combination of coordination and bond distances representing different sites. For example, two Y-O bonds of 4-fold coordination at distances that combined to an average of 2.37 Å, as in $Y_3Al_5O_{12}$. However, due to the fitting procedures and necessity to reduce the number of fitting parameters, this accuracy could not be achieved here. Simon *et al.* [41] suggest that within silica rich compositions the Y-O site is asymmetric, and this accounts for the longer bond distance than for lower coordinated Y-O. This would appear realistic in a melt network due to the increased flexibility of the sites and the presence of various sites with different coordination in the structure. Results collected within melt structures provide an average over the time of the scan and present a snapshot of the melt at these conditions. The lack of variation with increase in P indicates that any structural compression within the melt network does not affect the incorporation of Y. This is most likely due to the initial collapse of the cages in which Y is unlikely to be accommodated. As Y must accommodate in the larger sites due to its radius, there is less influence upon compression than there would be for lower coordinated species such as Al, because as the network is more closely packed the number of nearest neighbours of network forming cations will increase.

6.3.3 Results for Zirconium-doped Haplogranite

Normalised XAS spectra are shown in Figure 6.13 for the Zr containing reference compounds, both dry and hydrous Zr bearing HPG glasses, and an example of one hydrous melt collected. Reference spectra were collected from 17,770 to 18,800 eV with a scan time of 25 minutes for the glasses, and high $P-T$ measurements collected from 17,770 to 18,550 eV over 15 minutes due to the increase in noise levels at higher energy in the molten samples. Only one hydrous glass and a melt spectrum are shown in Figure 6.13 as subsequent glass and melt patterns remained similar over all $P-T$ conditions in this study. The absorption edge, E_0, was set to 18,010 eV for the reference and hydrous samples, and 18,008 eV for the dry glasses, as can be seen in the XANES spectra.

The $ZrSiO_4$ (zircon) reference spectrum shows a split edge crest with two peaks at 18,010 and 18,020 eV; this is also seen in the ambient hydrous glass where the zircon and glass spectra are nearly identical, indicating the environment of Zr in the HPG may be similar. The molten hydrous spectra also shows the split crest and the same small peak at 18,055 eV on the first EXAFS oscillation which represents multiple scattering paths from Zr-Zr atoms [159]. In the molten case the signal is damped due to the thermal disorder and the 2nd peak on the crest is not so well defined. The split edge crest represents the distinctive single site of Zr symmetrically placed within 8 oxygens which are at two different distances from the central Zr [148]. The monoclinic ZrO_2 spectrum shows no edge shift compared to the $ZrSiO_4$ spectrum indicating no change in valence of Zr^{4+}. However, the distinct single peak of the ZrO_2 represents the lower symmetry within the monoclinic structure as Zr is coordinated by a range of oxygens at different interatomic distances. The double peak, seen clearly in the first derivative of the XANES (main peak and B in Figure 6.14) is strongly pronounced in zircon and the hydrous HPG samples, but heavily damped in the dry glass indicating the hydrous and dry glass local environment of Zr may differ.

In the dry glass the XANES spectrum has a broad white line and the presence of two small peaks (C in Figure 6.14) on the edge crest. There is noticeably no multiple scattering peak on the first EXAFS oscillation and the EXAFS oscillations are broader with a much longer wavelength than those of the zircon-like spectra. Although the dry glass looks nominally similar to the ZrO_2 spectrum the edge peak is split, broader and the pre-edge region contains a well defined peak (seen clearly at A in Figure 6.14). These features indicate a different environment

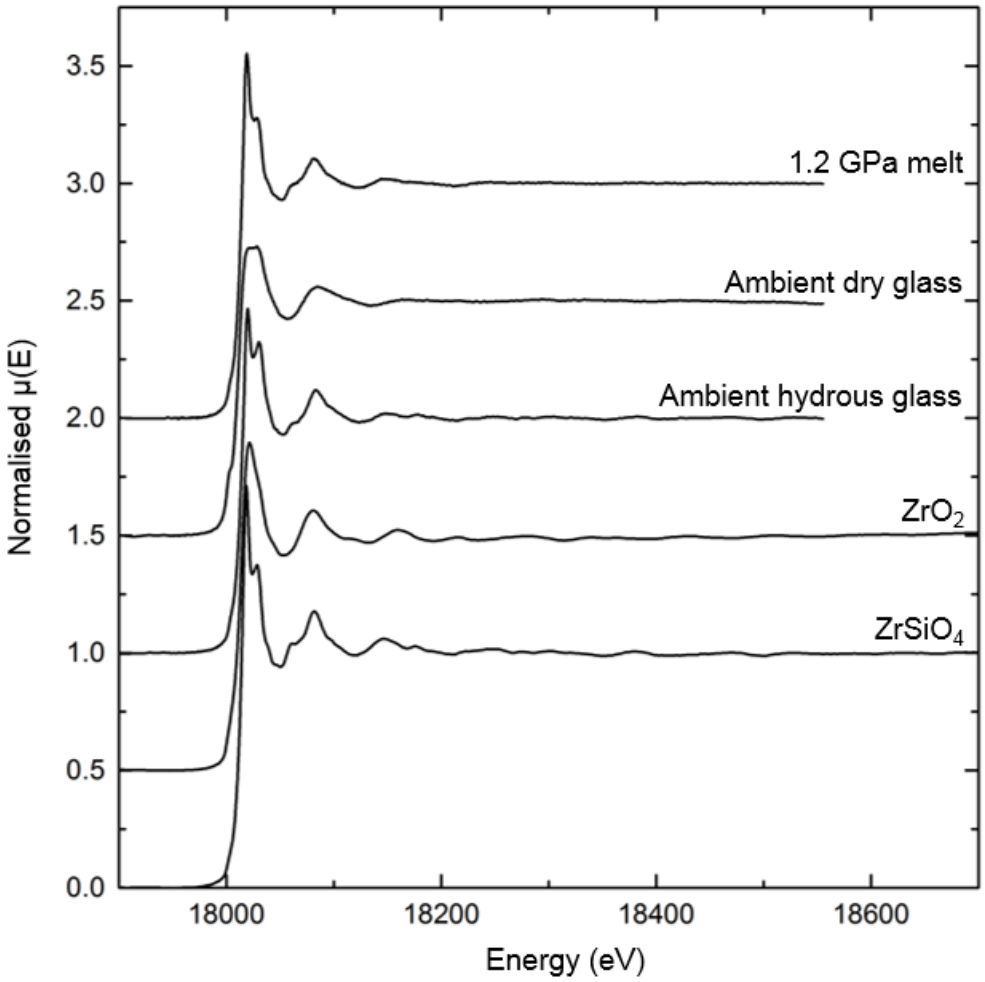

Figure 6.13 *XAS spectra collected for the Zr containing references compounds, the dry and hydrous ambient glasses, and a hydrous high pressure melt for comparison.*

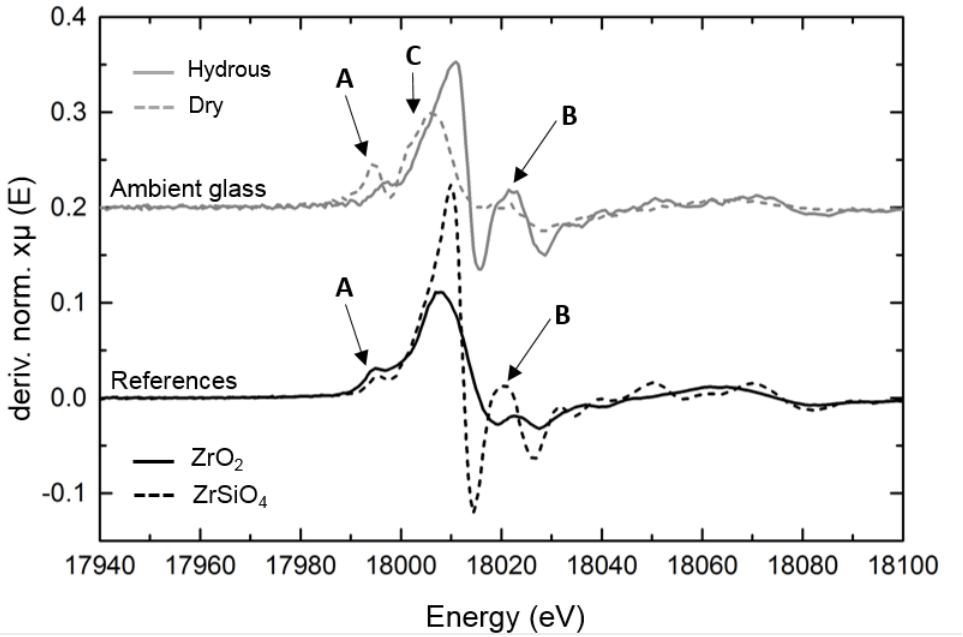

Figure 6.14 *Normalised first derivative of XANES spectra for Zr reference compounds and dry and hydrous ambient glasses. Highlighting A) Pre-edge feature, B) Multiple scattering contribution, C) splitting of the edge crest and lower energy of edge in dry glass.*

to either reference sample, but potentially more similar to that of ZrO_2. The pre-edge feature, which is present in all the samples but much more pronounced in the dry glass, is the result of 1s-4d transitions where electrons in lower shells transition to empty bound states [160]. These occur due to p-d mixing if dipole or quadrupolar transitions are allowed and are related to less centro-symmetric states. Octahedral states tend to have the lowest pre-edge features due to the high centro-symmetry and lack of p-d mixing, with the largest pre-edge intensity present in tetrahedral sites. The very low pre-edge feature within the zircon and hydrous samples would be consistent with a nearly centro-symmetric octahedral site, perhaps with some variation in bond lengths.

Zirconium References

Zr-containing references (ZrO_2 and $ZrSiO_4$) were fit using the same methodology as described for Y containing samples, with four fit parameters: CN, S_0^2, σ^2, and ΔE_0. The k^3-weighted EXAFS spectra for the reference compounds and subsequent Fourier transforms are shown in Figure 6.15 along with the final fits, and the fitting parameters used are listed in Table 6.7. During fitting, all the

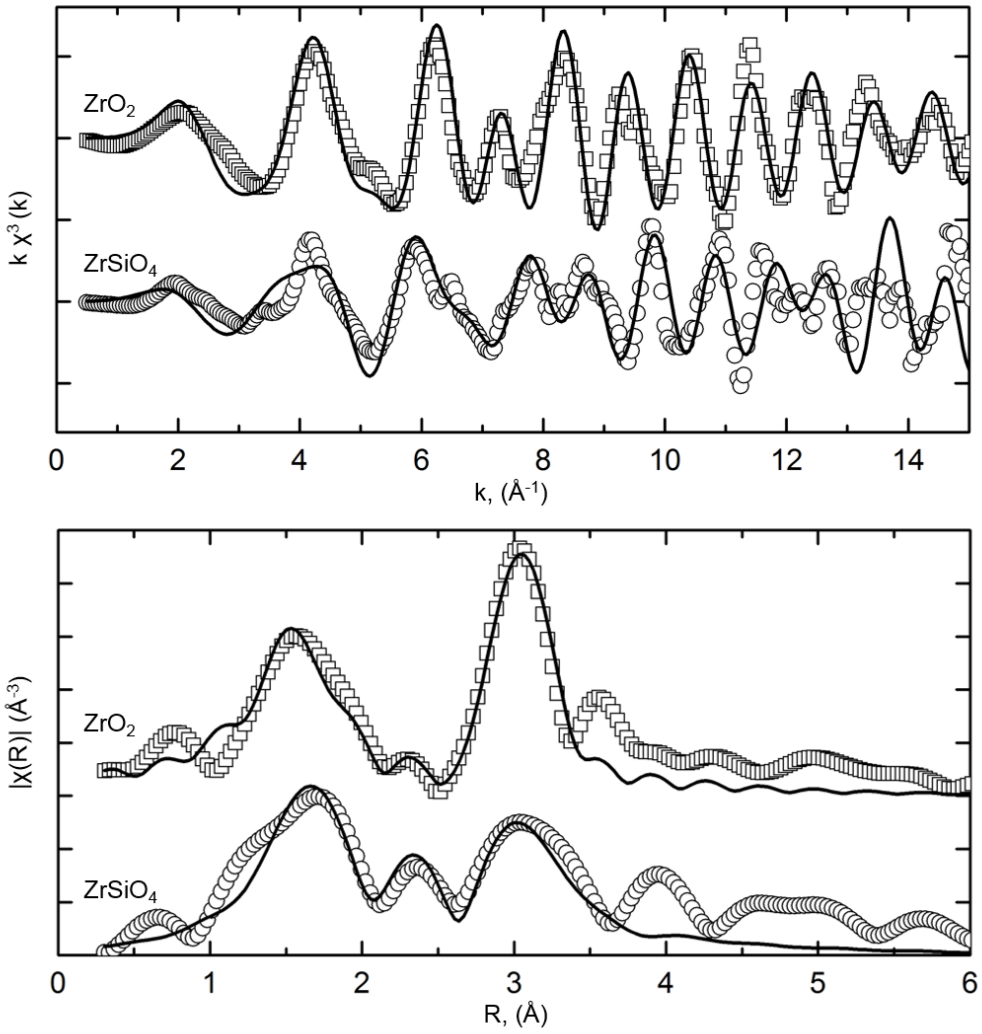

Figure 6.15 *Reference spectra for two Zr containing crystalline compounds. Top panel is the k-weighted spectra with Fourier transforms shown below in R.*

coordination parameters were fixed from known crystal structure studies [161–163], and the final fits compare well with previous structural studies on these compositions, and EXAFS data on Zr containing compounds [114, 115].

For ZrO_2 two distinct maxima can be seen at 1.55 and 3.05 Å in real space (uncorrected for phase shift). Unlike in the Y compounds all of the paths were fit simultaneously with one ΔE_0 and only two σ^2 parameters. This is due to there only being two main sites for Zr, with O or with Zr. The first maximum in R represents 7-fold coordination of Zr-O with two oxygens at 2.05 Å and 5 at 2.18 Å as reported in [163]. For the 2nd shell, 7 Zr are found at an average distance of 3.46 Å with multiple different bond lengths (Table 6.7). This 7-fold

ZrO_2	R-factor = 0.02	ΔE_0 = -5.3 (5)	S_0^2 = 1.23 (2)
Bond Type	CN	R (Å)	σ^2
Zr-O	2	2.05	0.003 (2)
Zr-O	2	2.16	0.003 (2)
Zr-O	3	2.23	0.003 (2)
Zr-Zr	1	3.33	0.005 (2)
Zr-Zr	4	3.44	0.004 (1)
Zr-Zr	1	3.47	0.004 (1)
Zr-Zr	1	3.58	0.004 (1)
$ZrSiO_4$	R-factor = 0.03	ΔE_0 = -4.12 (10)	S_0^2 = 0.96 (3)
Bond Type	CN	R (Å)	σ^2
Zr-O	4	2.14	0.006 (4)
Zr-O	4	2.29	0.006 (4)
Zr-Si	2	3.01	0.002 (4)
Zr-Si	4	3.63	0.002 (4)
Zr-Zr	4	3.63	0.05 (5)

Table 6.7 *Fitting parameters for Zr containing reference compounds. See text for detailed discussion on values fixed from literature.*

coordination in both shells is due to the monoclinic structure of low temperature ZrO_2 where 7 oxygens coordinate Zr in a distorted octahedral-like structure [164]. The single peak in the XANES spectra and less prominent pre-edge feature is due to the reasonable symmetry of the site and dominance of one set of bond lengths, compared to zircon, where two clear sets of bond lengths for one site are present.

For $ZrSiO_4$ (zircon) three maxima are seen at 1.7, 2.35 and 3.02 Å in real space (uncorrected for phase shift) and, as in ZrO_2, the first maximum represents coordination of Zr by O. In the zircon this distance is longer and represents 8-fold coordination of Zr in large sites within the silicate network. Four Zr-O bonds are found at 2.14 Å and four at 2.29 Å in a much more regular arrangement than in ZrO_2, in agreement with [162]. These two distinct bond lengths are reflected by the presence of two peaks on the edge crest in the XANES spectra (Figure 6.14) and the weaker pre-edge feature confirms the higher centro-symmetry of the Zr sites. The 2nd shell comprises of Zr-Si atoms at 3.01 Å, with the third shell being a contribution of both Zr-Si and Zr-Zr at 3.63 Å (Table 6.7). The higher R (>4 Å) correlations in the $ZrSiO_4$ arise from longer R interactions and multiple scattering paths that were not fit here. Goodness of both fits is indicated by the small R-factors and deviation from E_0 (Table 6.7). By modelling these

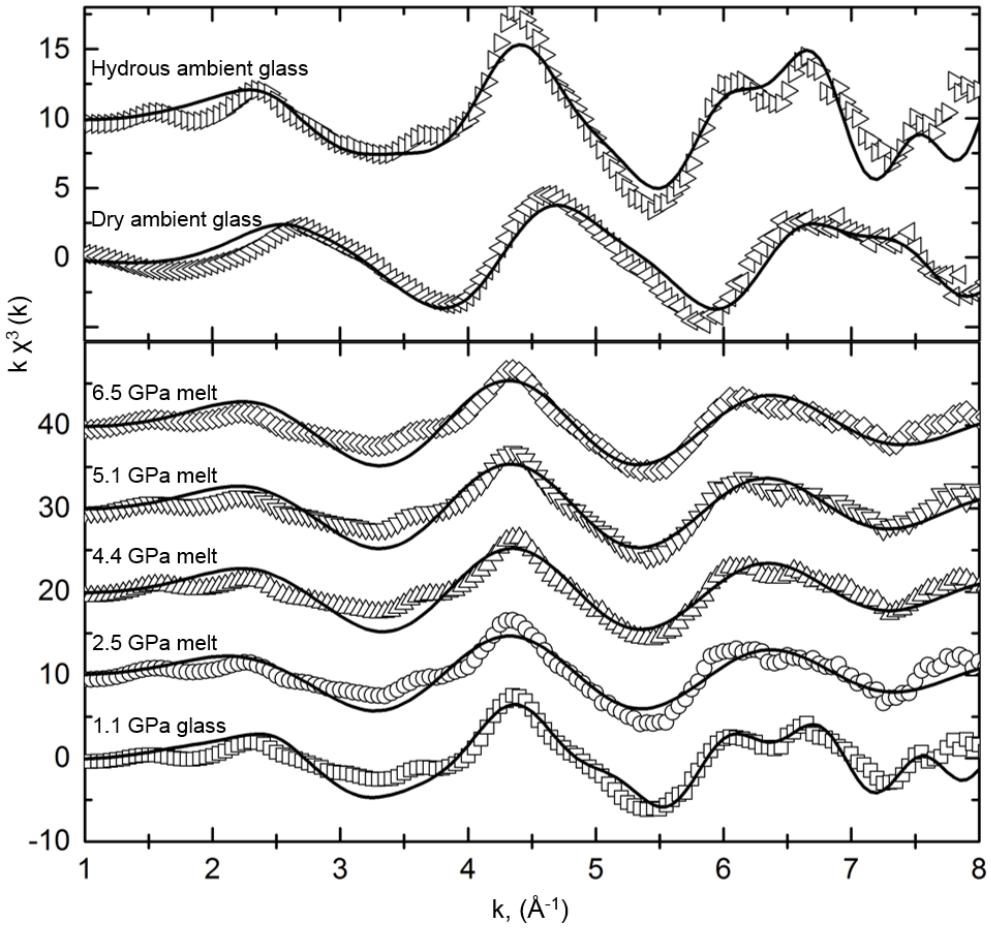

Figure 6.16 *k^3-weighted spectra for Zr-doped HPG data. Top panel shows ambient glass data for both the dry and hydrous starting glass. Lower panel are the high pressure glass and melt results. In both cases fits made to the data are shown with a solid black line.*

correlations they can be used to fingerprint the unknown coordination in the glass and melt samples.

Zirconium High Pressure Melts and Glasses

Ambient glass data were collected on both the dry and hydrous Zr-containing HPG glass. High P glass measurements were collected at 1.1 GPa and high temperature melt measurements were made at 2.5, 4.4, 5.1 and 6.5 GPa at >1500 K (Table 6.8). The k^3-weighted spectra and their fits are shown in Figure 6.16, with the Fourier transformed real space correlations (uncorrected for phase shift) and fits shown in Figure 6.17. Fits were made using the same procedures as for Y by using known parameters from the reference files and fixing S_0^2 =1.2,

P (GPa)	T (K)	Bond type	CN	R (Å)	R-factor	σ^2	ΔE_0 (eV)
amb. Hyd	300	Zr-O	4.0 (3)	2.14 (2)	0.03	0.001 (2)	-3.5 (5)
		Zr-O	4.2 (3)	2.29 (2)		0.001 (3)	
		Zr-Si	3.8 (2)	3.6 (3)		0.03 (1)	
		Zr-O	8.3 (2)	4.36 (4)		0.002 (2)	
amb. Dry	300	Zr-O	7.9 (3)	2.20 (2)	0.04	0.009 (3)	1.5 (6)
		Zr-Si	4.5 (3)	3.98 (4)		0.003 (1)	
1.1 (3)	300	Zr-O	8.2 (3)	2.22 (3)	0.03	0.001 (2)	-2.5 (7)
		Zr-Si	4.3 (2)	3.45 (3)		0.06 (2)	
		Zr-O	8.0 (3)	2.63 (3)		0.001 (2)	
2.5 (4)	1600 (50)	Zr-O	7.7 (4)	2.21 (3)	0.006	0.006 (1)	-2.0 (7)
4.4 (5)	1650 (50)	Zr-O	8.1 (3)	2.23 (3)	0.005	0.008 (2)	3.2 (5)
5.1 (5)	1450 (50)	Zr-O	8.0 (4)	2.22 (3)	0.009	0.007 (2)	-2.3 (7)
6.5 (6)	1500 (50)	Zr-O	8.1 (3)	2.20 (3)	0.008	0.007 (1)	-2.7 (6)

Table 6.8 *Experimental conditions for Zr-doped HPG data collected and derived fit parameters for nearest neighbour interactions used to fit Figures 6.16 and 6.17.*

that of the crystalline references. CN and r were refined until the best fit and lowest R-factor were arrived at. The k-range for the fitting was 2.1-7.9 Å^{-1} for all the glass and melts. The final parameters and R-factors are detailed in Table 6.8 which shows R-factors consistently lower than 0.05 and ΔE_0 <6 confirming the validity of the fitting methods.

For the ambient glasses (top panels in Figures 6.16 and 6.17) as predicted from the qualitative XANES description, there are clear differences between the dry and hydrous Zr-HPG samples. The first maximum in the dry sample is fit with 8-fold coordinated Zr-O at 2.20(2) Å. This distance is slightly shorter than the average distance for the hydrous glass which is fit with 8-fold coordinated Zr-O at an average of 2.23 Å with two bond distances (2.14 and 2.29 Å) each with 4-fold coordination, as in the zircon reference and in agreement with data from [115] for rhyolitic glasses. This confirms the XANES fingerprint that the well defined split of the edge of the hydrous HPG was similar to the zircon reference compound. In the dry HPG there is a 2nd small shell identifiable from the EXAFS at 3.98 Å in Figure 6.17 which was fit by 4-fold Zr-Si. The 2nd shell of coordinating Si would be expected in this dry silica rich HPG composition. The Zr-O distance is similar to that found in the high temperature tetragonal phase of ZrO_2 (two sites of 4-fold coordination at 2.08 and 2.37 Å [160]). This is also reflected in the XANES spectra, where two dampened peaks are observed at the edge compared to the single peak for monoclinic ZrO_2, indicating the presence of two sites of differing bond length, but not as well defined as in the zircon. The pre-edge

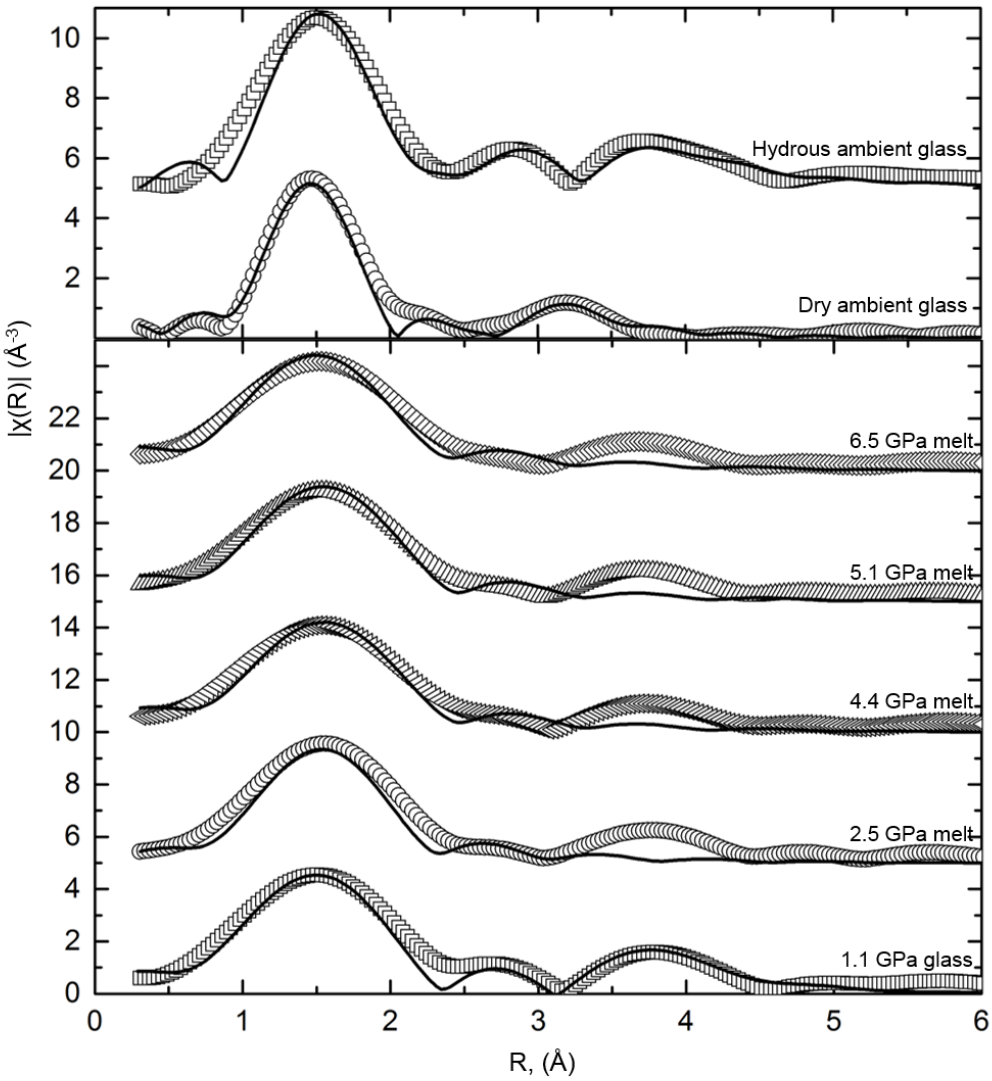

Figure 6.17 *Fourier transforms of 6.16 in real space with fits for Zr glasses and melts shown and parameters listed in Table 6.8.*

features observed in the dry glass also indicate the presence of enhanced p-d mixing, and a greater number of 1s-4d transitions caused by a lack of centro-symmetry which would favour the presence of tetragonal ZrO_2. Although it was not possible to resolve two separate bond distances for Zr-O during the fitting of the dry glass, the split of the edge crest would indicate the possible presence of two sites which could not be resolved here. In the hydrous glass the EXAFS oscillations in k-space can be seen to decrease in wavelength and move to lower k. This produces a first maximum of coordinating oxygens identical to zircon. The small 2nd and 3rd shells are fit with the same environments as found in the zircon reference with Zr-Si and Zr-Zr at 3.6 and 4.64 Å respectively. The presence of a 2nd shell of Zr-Si indicates there is unlikely to be any complexation with water. The increase in intensity of the peaks on the edge crest is consistent with other studies [115] where the structural relaxation in the water bearing samples caused large changes around the edge.

The high pressure glass and melts were fit with the same parameters as for the ambient hydrous glass as all the high P data collected was in the hydrous sample. Fits were not made above 2.5 Å due to the thermal disorder present in the sample, as the fitting procedure used was unable to account for any high R contributions. The decrease in intensity of the Zr-O contribution with high $P - T$ is consistent with thermal relaxation and increased disorder. It is most likely that the broad oscillation around 3.9 Å in Figure 6.17 is due to the same contributions as in the ambient glass, of Zr-Si and Zr-Zr. Up to 6.5 GPa in the melt no change in bond distance or coordination for Zr-O was observed.

The damping of the edge crest peaks in the dry glass represents the presence of a more rigid structure. This is potentially similar to tetragonal ZrO_2 formed at high temperature. Due to the lack of water the structure will have less flexibility in site size and coordination and the results suggest that on average in the dry HPG that Zr is accommodated by 8 oxygens with an average bond length of 2.2 Å. In tetragonal ZrO_2, Zr is accommodated within tetragonal sites coordinated by four oxygens at 2.08 Å and four at 2.37 Å (an average 2.22 Å) [164] which would be consistent with results collected here. The two tetragonal sites would decrease the centro-symmetry of the structure and cause the well defined pre-edge features observed in the XANES. As Zr is smaller in diameter than REE, Zr could be incorporated within the smaller 4 to 6-member cages within the network.

The well defined split of intense peaks on the crest of the hydrous glass represent a single symmetrical 8-fold coordinated site, with 2 distinct bond lengths. The

high polymerisation of this melt but more relaxed structure due to the presence of water, would allow Zr to adopt 8-fold coordination in a more regular symmetric environment as water produces a more open structure and higher number of NBO [165]. Farges and Rossano [115] found evidence for predominantly 6-coordinated Zr at 2.08 Å in albite glasses, but observed 7-8 fold coordinated species in the most polymerised (rhyolitic with NBO<0.12) glasses. As the HPG in this study is even more highly polymerised it is in good agreement with the results by [115]. Louvel *et al.* [114] suggested Na may coordinate with two oxygens bonded to Zr in a complexation of Zr-Si/Na with 7 CN at 2.1 Å, and that the presence of alkalis greatly influences the bonding environment and therefore solubility of Zr in silicates. The composition here contains considerably less alkalis and due to the high number of NBO in the structure, a greater number of zircon-like ZrO_8 species are observed in the highly polymerised melt.

6.3.4 Discussion

In both the hydrous Y and Zr containing HPG samples there appears to be no effect of pressure on the Y or Zr local environments within the melt structure. Both elements are coordinated in the first shell by 8 oxygens in a similar configuration to Y and Zr silicate crystalline compounds. There also appears to be no change between the hydrous glass and melt structures as might be expected for such a strongly polymerised silica rich composition and as observed in Chapter 5 for the HPG structure. The accommodation of Zr and Y on large 8-fold sites is caused by the lack of non-bridging oxygens available in the polymerised network. These sites are less energetically favourable due to the requirement to bond with predominantly bridging oxygens, and as seen in partitioning data from [33, 34], these elements preferentially incorporate in minerals or less polymerised melts when highly polymerised silica rich melts are present. If coordination remains consistent with P it could be expected that measured partition coefficients at ambient P with strongly polymerised melts could be good representations of partitioning at the depth that granitic magmas would be formed at (P <5 GPa). In more alkali rich granitic compositions it is possible that the Zr and Y would adopt slightly lower coordination, increasing their preference for partitioning into the melt rather than crystals. As discussed in [114], greater solubility of these elements in water rich environments could impact the mobilisation of Zr. As hydrous melts are prevalent in subduction zones, where melting of subducting crustal material may produce granitic melts, Zr could be mobilised from the

subducting slab during melting. Melting of the slab at any depth <6 GPa will produce the same environment for Zr within the melt and therefore there will be no effect of P on Zr mobilisation.

6.3.5 Conclusion

X-ray absorption spectroscopy has been used to study the incorporation of trace elements, Y and Zr, within a highly polymerised melt at high pressures up to 8 GPa. This was the first study to use the BE-window high pressure cell design for the PEP and data were succesfully collected with a high signal intensity. In the Y-doped HPG melts up to 7.5 GPa, Y appears to be coordinated by 8 oxygens at R_{Y-O}=2.37 Å. This is consistent with results presented on quenched glasses by [41] and is most likely due to the requirement for the large radii Y to accommodate within the larger cage structures within the highly polymerised network. For hydrous Zr-doped HPG melts, Zr appears to be coordinated by 8 oxygens, at an average distance of R_{Zr-O}=2.23 Å, up to 8.1 GPa. This site appears to be reasonably symmetric and similar to that found in crystalline zircon. The decrease in bond distance from Y to Zr is consistent with the difference in atomic radii between the two elements (Y = 1.04 Å, Zr = 0.86 Å). This would suggest that the large cages within the network are modified by the cation which is present in the melt structure, as the larger Y appears to prop open the silicate network more than the Zr. With P, both Y and Zr prevent the sites they are accommodated on from collapsing and compression of the silicate network must occur via collapse of the unoccupied large cages and smaller rings. This indicates the importance of undertaking structural studies on low concentrations of trace elements, as at higher concentrations they may artificially alter the structure to a greater extent than would occur at natural concentrations. Within the anhydrous glass, Zr adopts a less symmetric environment within the more rigid structure. The results on Zr incorporation in the HPG are similar to those found by [115] in quenched highly polymerised rhyolitic compositions.

For both Zr and Y-doped HPG samples, where glass measurements were made at a similar pressure to those of the melt, there appeared to be no structural difference between the incorporation of the trace elements between the glass and melt structures. This result would suggest that for highly silicic compositions quenched glass measurements on trace element incorporation using EXAFS would be analogous to those of the melt. Quenched glass measurements are

advantageous as they provide an increased signal intensity due to the lack of high $P-T$ equipment required; therefore lower concentrations can be used that represent more natural conditions.

Chapter 7

Structure of Lutetium-doped Melts and Glasses

This chapter presents the first results on minor REE structural incorporation in silicate liquids at high pressure using x-ray diffraction. This work follows on from that of Chapter 6 and uses x-ray diffraction techniques to identify the bonding environment of Lu, for comparison with the data on Y collected by x-ray absorption methods. Not all the data collected during the experiments presented in this chapter was of high enough quality to use for analysis and for full experimental details of the unsuccessful runs see Appendix One, Tables 9.1 and 9.3.

7.1 Introduction

The structure of two Lu doped (4000 ppm) model end member silicate liquids, a highly polymerised haplogranite (Si-Al-Na-K-O) of the same composition as Chapters 5 and 6, and a less polymerised anorthite-diopside (Si-Al-Mg-Ca-O) are investigated. These have been studied up to 8 GPa using *in situ* angle and energy dispersive x-ray diffraction techniques. The haplogranite and anorthite-diopside compositions represent different end members of mantle melting and identify whether observed partitioning changes between melts of varying SiO_2 composition could be related to changes of REE environment within the melt structure.

7.2 Experimental Procedures

The haplogranite (HPG) and anorthite-diopside (AnD) glasses were synthesised as outlined in Chapter 4.4. The HPG composition is identical to that of Chapter 5 with the only addition to the starting glass composition being the doping of 4 wt.% of high purity (>99.99%) Lu_2O_3 within a portion of each glass. This equates to 4000 ppm atomic wt.% of Lu. The samples were free from iron so that the number of elements with bond lengths between 2.2-2.4 Å might be minimised, as these overlap the Lu-O bond distance. Two experimental methods were used to obtain structural data at high pressure and temperature conditions. (1) Measurements on HPG doped melts were carried out up to 8 GPa and 1100 K using angle-dispersive x-ray diffraction in resistively heated diamond anvil cells on beamline I15 at the Diamond Light Source (Harwell Campus, UK). Undoped HPG measurements used in this chapter are the same as detailed in Chapter 5. (2) Experiments on the AnD doped and undoped melts up to 8 GPa and 2000 K were collected on beamline 16-BM-B, HP-CAT, at the Advanced Photon Source (Argonne National Laboratory, USA) by energy-dispersive x-ray diffraction. High $P-T$ conditions were generated by use of a Paris-Edinburgh press. Ambient AnD glass data were collected on the PSICHE beamline at Synchrotron Soleil, Paris, France (for Lu doped AnD glass) and at P02.2 beamline at PETRA III synchrotron in Hamburg, Germany (for plain AnD glass).

The experimental conditions for all measurements are detailed in Table 7.2. High $P-T$ DAC measurements carried out on I15 are described in Chapter 5 with glass, melt and quench measurements collected for 60 s at each pressure where possible. Pressure was monitored in the same way as Chapter 5, by ruby fluorescence before heating, and on a Pt foil inserted into the sample chamber during the experiment. A detailed description of the Paris-Edinburgh press experiment techniques and cell design can be found in Chapters 4 and 5. Pressure was determined from the cell-volume change of the pressure transmitting medium in the form of an MgO cylinder and temperature was estimated by previous power calibrations using this cell assembly [92]. This calibration also accounts for the effect on pressure of the distance between the sample and MgO ring at high temperature using the P-V-T relation of MgO and elastic wave velocity measurements. Diffraction patterns on the MgO were collected at room temperature and above the melting temperature. X-ray diffraction was collected for 2 hours using an energy-dispersive germanium solid-state detector at 2θ angles (2°, 2.7°, 3.5°, 5°, 7°, 10°, 15°, 20°, 27°, 35°)

Oxide	HPG initial	HPG recovered	AnD Initial	AnD Recovered
SiO_2	71.6 (7)	73.2 (4)	48.8 (5)	46.9 (7)
Al_2O_3	10.5 (3)	10.7 (1)	14.7 (2)	14.4 (4)
Na_2O	3.3 (3)	3.6 (2)	-	-
K_2O	3.7 (1)	3.8 (1)	-	-
MgO	-	-	10.2 (2)	14.2 (2)
CaO	-	-	22.7 (2)	21.6 (2)
Lu_2O_3	3.9 (1)	3.9 (1)	3.6 (1)	3.3 (1)
Totals	93.0* (6)	95.7* (3)	100.2 (6)	100.5 (6)

Table 7.1 *Compositions from electron microprobe analysis of both initial and recovered samples. HPG (haplogranite) and AnD (anorthite-diopside) compositions given in wt.% oxide. Analyses are based on average of a minimum of 10 sample spots; standard deviations are shown in brackets. * The low totals for the HPG composition are due to the presence of water in the sample and correspond well with the amounts added during synthesis.*

covering up to 20 $Å^{-1}$ in reciprocal space with $Q = 4\pi E \sin\theta/12.398$, where E is the energy of the x-rays in keV up to >100 keV.

7.2.1 Recovered Sample Analysis

Recovered HPG quenched samples were polished for electron microprobe analysis at the EMMAC (The Edinburgh Materials and Micro-Analysis Centre), University of Edinburgh. Analyses were carried out using a CAMECA SX100 electron microprobe with an accelerating voltage of 15 keV and 8 μm beam size. Where glass was recovered the samples retained a stoichiometry nearly identical to their starting compositions (Table 7.1); therefore it is unlikely the samples underwent any major chemical change during the experiments and no loss of Lu. Back scattered electron images taken of the sample show no evidence for quench crystallisation and the sample appears glassy (Figure 7.1b). Bubbles are present in the HPG which is probably due to exsolution of water during quenching indicating that water remained in the sample during the experiment. The low microprobe totals (Table 7.1) for the HPG composition are due to the presence of water in the sample. Quenched AnD samples were analysed at the Centre de Microanalyse Camparis, University Pierre and Marie Curie. These results (Table 7.1) show that when the sample quenched to a glass (Figure 7.1a) the composition after the experiment was nearly identical.

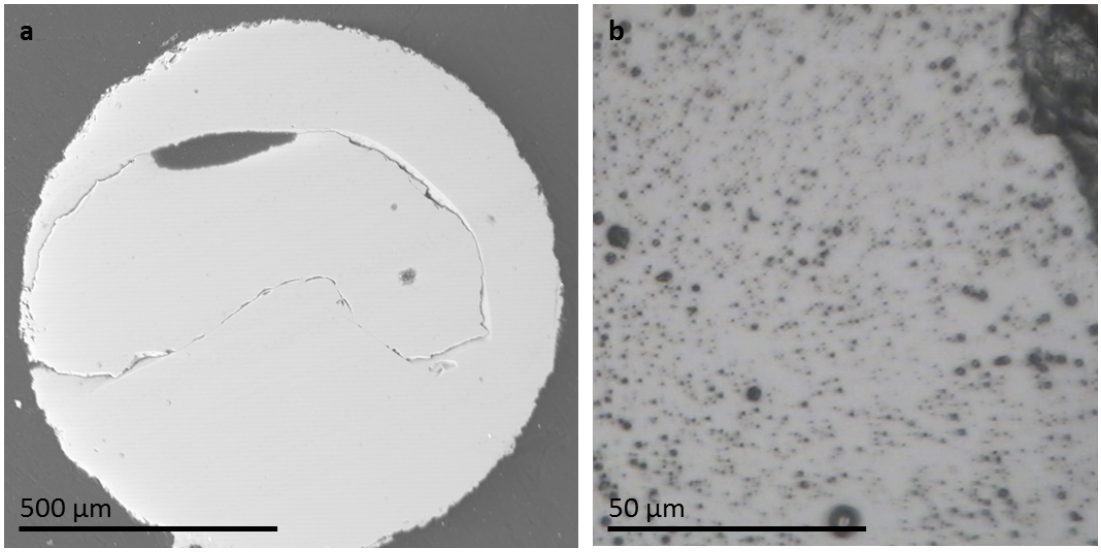

Figure 7.1 *a: Recovered sample from AnD experiment A8-a using a Paris-Edinburgh press. b: Recovered sample from HPG experiment D5 from resistive heated DAC polished within Re gasket. Spots are bubbles within the hydrous sample.*

7.3 Data Analysis Procedure

A detailed background to the data processing of x-ray diffraction data is presented in Chapters 4 with data analysis for angle dispersive x-ray diffraction already presented for the HPG experiments in Chapter 5. The Q_{max} and normalisation parameters established in Chapter 4 are used here throughout, as well as the fitting parameters for undoped HPG obtained in Chapter 5. For the AnD, energy dispersive x-ray diffraction techniques were used and the data analysis procedure is described in Chapter 4.6 with specific experimental details below.

7.3.1 Energy Dispersive X-ray Diffraction

Multi angle energy dispersive x-ray diffraction (EDXD) was used to collect *in situ* liquid data using a Paris-Edinburgh press. Data were collected for periods of 2 hours *in situ* within the capsule from [93] (Chapter 4.3.4). This provides a large sample volume and subsequently high signal intensity from the sample. As data is collected at fixed angles multiple spectra representing each angle are collected. At least two spectra were collected at each detector angle and these were summed in order to improve the counting statistics. Bragg peaks arising from the diffraction of graphite in the cell assembly, and fluorescence of indium on the detector and

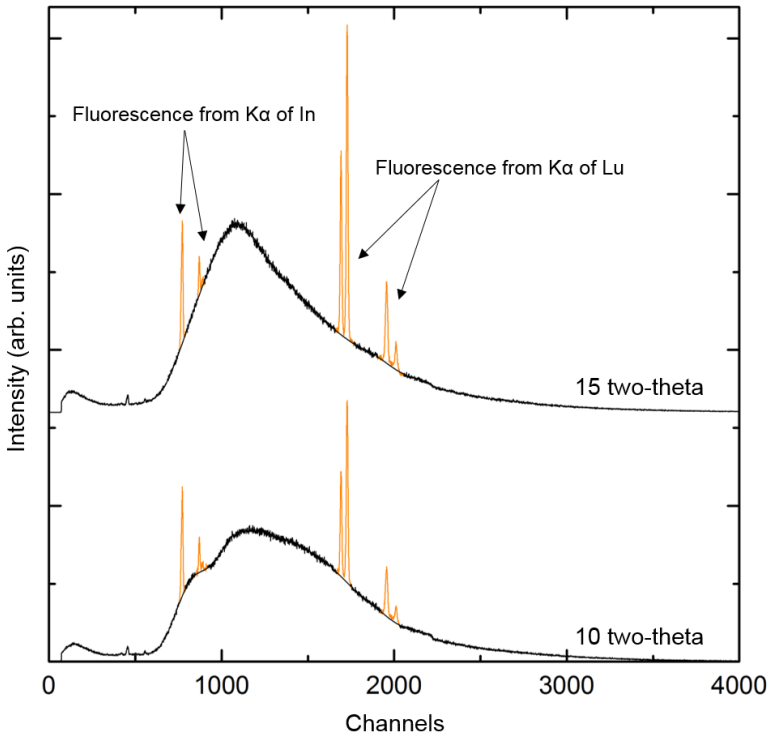

Figure 7.2 *Examples of two fixed angle energy dispersive x-ray diffraction spectra showing the presence of Kα fluorescence lines from indium and lutetium. These peaks are removed and a fit made between the data points from the energies on either side. Channel number is converted to energy, E, through E=offset + slope × channel where offset and slope are beamline parameters.*

Lu were removed at each angle (Figure 7.2). If peaks were at >30% concentration between the energies of interest (25 to 55 keV) the data were discarded. Where required, fits were made to the data to extrapolate the signal after the Bragg and fluorescence peaks were removed. The aEDXD program developed by Changyong Park (see [92]) was then used to scale the primary beam by least squares fitting at the highest 2θ angle, and an evenly spaced $S(Q)$ function was produced by error weighted spline smoothing of the merged data in Q-space. This technique is based on the highest diffraction angle oscillating around 1 because as $Q \to \infty$, $S(Q) \to 1$. The $G(r)$ was then obtained by Fourier transform of the spline smoothened $S(Q)$.

Run no.	Comp.	P (GPa)	T (K)	n_0 (Å^{-3})	$G(r)$ positions (Å)		
Exp. 1					r_1	r_2	r_3
D1	HPG + Lu	0.5 (2)	910* (50)	0.069 [0.066]	1.59	2.33	2.98
D2	HPG + Lu	2.1 (3)	900* (50)	[0.071]	1.6	2.37	2.98
D3	HPG + Lu	2.5 (3)	290	0.073	1.59	2.36	3.01
D4	HPG + Lu	3.8 (2)	973 (40)	0.079 [0.078]	1.6	2.36	3.0
D5	HPG + Lu	5.8 (4)	1073 (40)	0.083 [0.082]	1.59	2.35	2.99
Exp. 2							
Amb1	AnD (†)	0	290	0.081	1.62	2.41	3.24
Amb2	AnD + Lu (‡)	0	290	0.081	1.62	2.36	3.25
A1-b	AnD	0.8 (3)	1570 (50)	0.082	1.59	2.78 s	3.28
A2-b	AnD	2.4 (2)	1670 (50)	0.084	1.61	2.76 s	3.27
A3-b	AnD	3.5 (3)	1720 (50)	0.087	1.59	2.76 s	3.27
A4-b	AnD	4.8 (3)	1770 (50)	0.09	1.59	-	3.27
A5-b	AnD	6.5 (3)	1870 (50)	0.092	1.60	-	3.27
A6-b	AnD	8.0 (4)	2070 (60)	0.092	1.61	-	3.24
A7-b	AnD + Lu	0.8 (3)	1570 (50)	0.082	1.59	2.34	3.22
A8-a	AnD + Lu	2.1 (3)	2020 (80)	0.084	1.61	2.34	3.25
A9-b	AnD + Lu	3.1 (3)	1570 (50)	0.087	1.59	2.32	3.17
A10-b	AnD + Lu	4.2 (3)	1750 (50)	0.091	1.62	2.32	3.24
A11-a	AnD + Lu	5.2 (3)	1850 (50)	0.094	1.62	2.41	3.24
A12-b	AnD + Lu	7.0 (3)	2120 (50)	0.093	1.61	2.43	3.16

Table 7.2 *P-T conditions of each experimental run as well as estimated densities and results on positions of the first three peaks in the $G(r)$, r_{1-3}. Errors for P and T shown in brackets. Experiment 1: Glass and melt measurements on the haplogranite carried out on I-15 at the Diamond Light Source. Where both glass and high T data were collected, the density in square brackets (e.g. [0.066]) is from the molten phase. Peak positions are shown only for high T phases unless none was collected. * on temperature indicates where the thermocouple failed during the run and a minimum T was estimated from recrystallisation of Pt and previous thermocouple calibrations. Experiment 2: Molten anorthite-diopside data collected on HP-CAT at the Argonne Photon Source in June 2014 (-a) and February 2016 (-b). Within r_2, 's' represents where the 2nd peak arises from the O-O contribution producing a shoulder on the r_3 peak and not from a distinct 2nd oscillation. † denotes collection at synchrotron Soleil, PSICHE. ‡ denotes collection at Petra P.02 DESY.*

7.4 Results

7.4.1 Haplogranitic Melts

In situ data on the HPG Lu-doped melts were collected between 900-1070 K at 0.5, 2.1, 3.8, and 5.8 GPa (Table 7.2). As in Chapter 5, at temperatures >850 K the samples either recrystallised (1 in 5 high temperature runs) or remained amorphous. In the cases where crystallisation occurred water loss may have occurred, and the runs were discarded as the temperature required to melt the crystals exceeded the heater limits. If recrystallization did not occur at these temperatures it is assumed that the samples were in the super-cooled liquid state at >900 K in agreement with [166]. As in Chapter 5, from the results here the Lu-doped HPG melt and ambient temperature phases are identical as no changes were observed in the $G(r)$ between runs at room temperature or above melting (grey solid line on Figure 7.4) as seen in D4 where temperatures exceeded the liquidus temperature for haplogranite [116]. This indicates for the HPG at these pressures that the glass structure is analogous to the melt, as seen in Chapters 5 and 6. As the glass and melt structures are identical in the HPG, and the most similar P measurements between the undoped and Lu-doped data were collected in the glass, only the glass data is presented in the $S(Q)$ and $G(r)$ here. The $S(Q)$ and $G(r)$ are shown in the upper panels (A) of Figures 7.3 and 7.4. In Figure 7.3A the first sharp diffraction peak (FSDP) is seen at 1.98 Å^{-1} with a slight increase to 2.01Å^{-1} at 5.8 GPa. Alteration to the $S(Q)$ from the scattering of Lu is seen in the 2nd peak between 3-5 Å^{-1}, where the peak appears less broad in the Lu-doped case with slightly greater intensity on the upward slope at 3-4 Å^{-1}.

7.4.2 Anorthite-Diopside Melts

Liquid data on the Lu doped AnD were collected at 0.8, 2.1, 3.1, 4.2, 5.2 and 7 GPa at 1570-2120 K, with ambient glass measurements collected at room $P-T$ on both the doped and undoped AnD compositions. Undoped AnD liquid measurements were also collected at similar regularly spaced pressure intervals (Table 7.2). At 3 GPa data were collected at three temperatures (in steps of 200 K) to show there was no effect of temperature on the results (Figure 7.5). The measured $S(Q)$ for the Lu-doped AnD compositions are shown in the lower panel (B) of Figure 7.3 along with the undoped samples for comparison. The FSDP shows a gradual

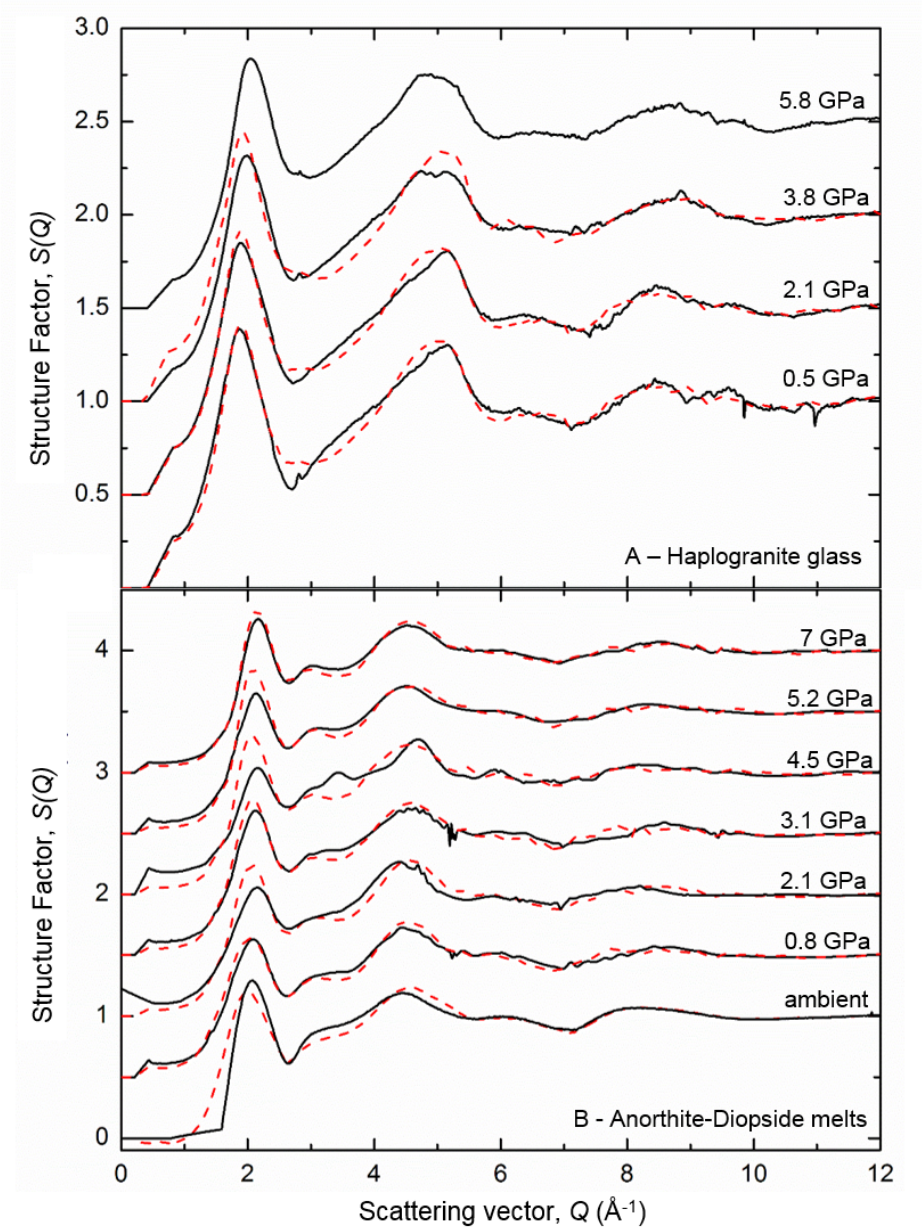

Figure 7.3 *A - S(Q) for HPG Lu-doped (black) and undoped (red dashed) glass measurements. B - Lu-doped AnD melts (black) and undoped AnD (red dashed) melts. See Table 7.2 for details. Pressures shown are for the Lu-doped data with the undoped data collected within 0.5 GPa of the doped.*

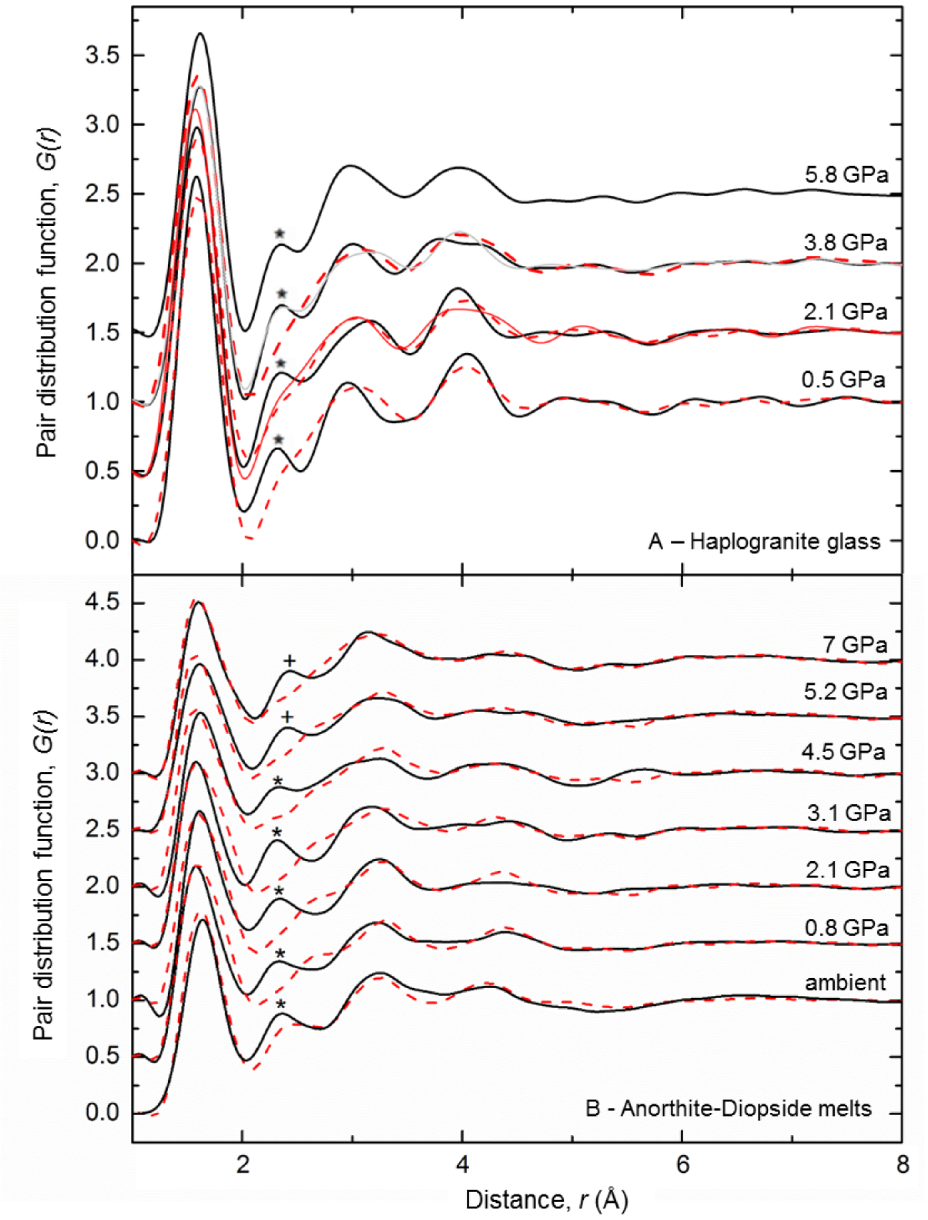

Figure 7.4 *$G(r)$ for the $S(Q)$ shown in 7.3. A - $G(r)$ for HPG Lu-doped (black) undoped (red dashed) glasses, with grey solid line a Lu-doped melt at $>970\,K$ for comparison with the glass at 3.8 GPa from D4. B - AnD melts.*

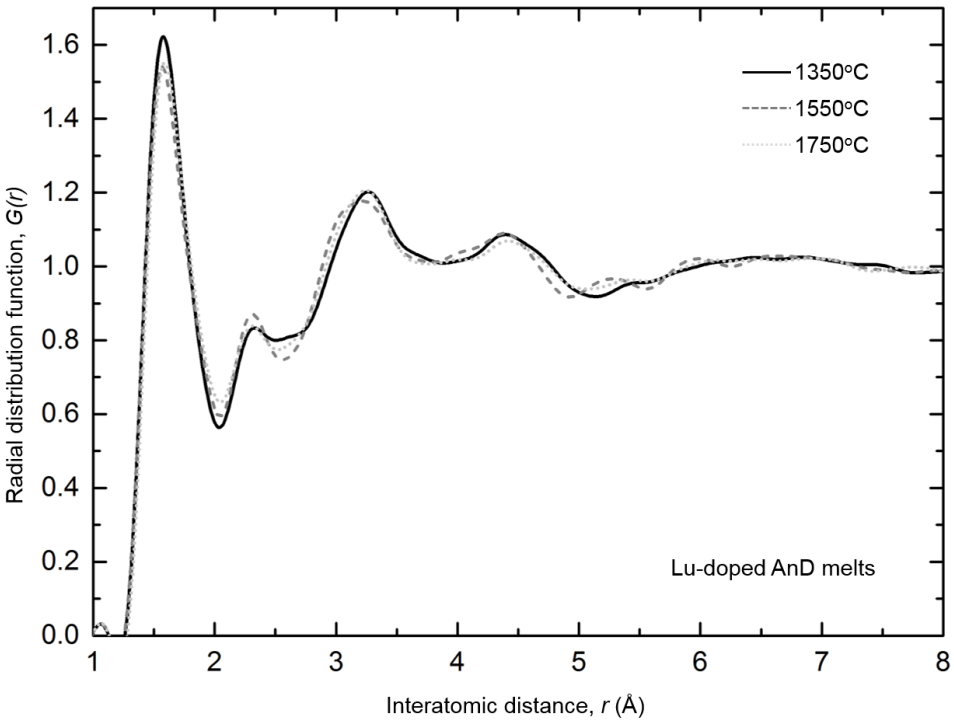

Figure 7.5 *Radial distribution functions, $G(r)$, collected for Lu-doped anorthite-diopside melts at various temperatures above melting. As can be seen from the $G(r)$ there is no difference within error between the samples and therefore temperature appears to have no effect on the bonding environment of Lu within these melts.*

increase from 2.05 to 2.1 Å^{-1} from ambient conditions to 4.5 GPa. As discussed in Chapter 5, an increase in the FSDP has been observed for other silicate glass and melt compositions and is attributed to the collapse of voids in the SiO_2 network [14, 17, 118]. A similar increase in intensity between 3-4 Å^{-1}, as observed in the HPG, is seen in the Lu-doped AnD $S(Q)$. The resulting real space distribution functions, $G(r)$, are shown in Figure 7.4B. The main peak positions, atomic densities and uncertainties in real space for each data point are detailed in Table 7.2.

7.4.3 Structural Results

In both compositions the first peak in the $G(r)$, r_1, is attributed to the $r_{\text{Si}-\text{O}}$ at 1.61(2) Å with 4-fold coordination as shown in other silicate glass, liquid and crystalline structures [16, 118]. In the HPG, the second peak, r_2, only appears within the Lu-doped samples at 2.36(3) Å and is attributed to the Lu-O bond distance. This distance is similar to modelled Lu-O bond distances

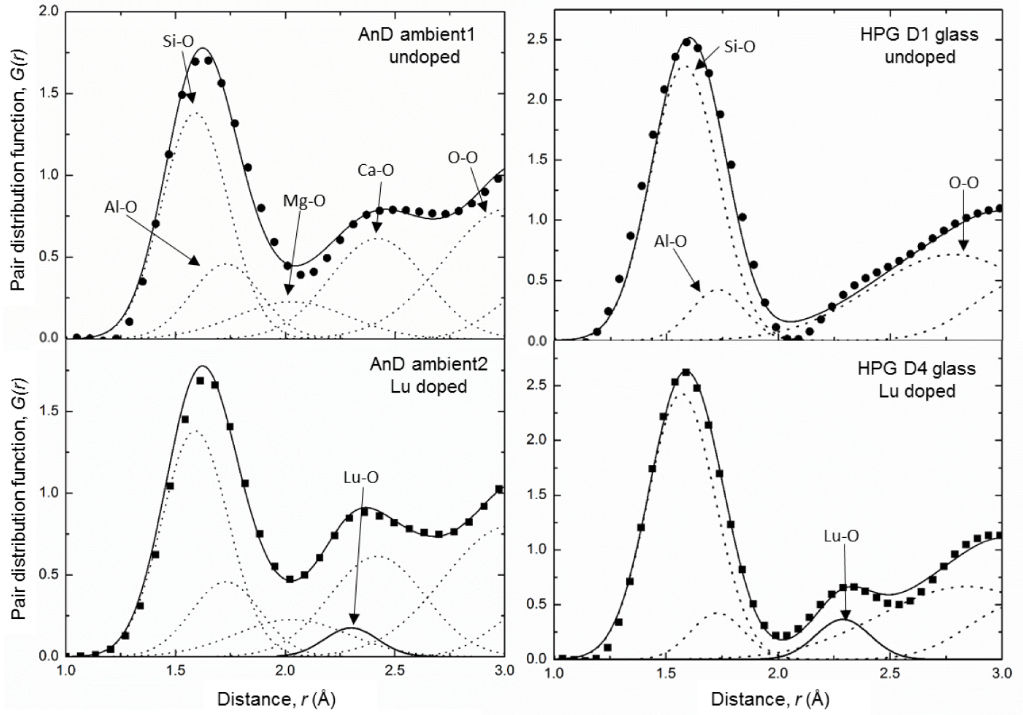

Figure 7.6 *Measured $G(r)$ (black markers) from Figure 7.4 shown with Gaussian fits to both the plain (upper panels) and doped (lower panels) samples. Individual Gaussians, $g_{\mathrm{ind}}(r)$, for ion-ion contributions are labelled (dotted lines) along with the total sum of Guassians (solid black line). Left panels show the AnD compositions and right panels, the HPG. Lu-O contributions are shown in the doped figures by a thick black line and are labelled as Lu-O. Major element fit parameters are identical between the doped and undoped samples using parameters described in Table 7.3.*

in aluminosilicate glasses at 2.29 Å [167]. In the undoped AnD, the second contribution arises from the Ca-O correlations at ∼2.4 Å and overlaps the Lu-O distance. However, the r_2 peak in the doped AnD can be clearly seen to increase in intensity and shift to lower r with the introduction of Lu in the ambient samples (Figure 7.4B). The correlations observed at 3.0(2) Å in the HPG and 3.2(3) Å in the AnD are attributed to the sum of the O-O and Si-Si contributions and match well with $G(r)$ observed in other studies [14, 168, 169], and with MD simulations by [49] on similar compositions. In the HPG a fourth correlation is visible at 4 Å; this can be attributed to the secondary interactions of Si-O and is much more pronounced in the HPG due to the higher concentration of SiO_2.

Ion-Ion	r		k		CN	
elements	HPG	AnD	HPG	AnD	HPG	AnD
Si-O	1.6 (2)	1.6 (2)	0.12		4	4
Al-O	1.73 (1)	1.75 (2)	0.09		4.3*	4.3*
Mg-O	-	2.00 (5)	-	0.2	-	5
Ca-O	-	2.40 (2)	-	0.15	-	8.1*
Na-O	2.46	-	0.2*	-	8	-
Lu-O	2.36	2.29*	0.08	0.07	8.1	6.2*

Table 7.3 *Ion-ion contributions used to model individual Gaussians, $g(r)_{\mathrm{ind}}$, in the compositions at ambient conditions. * indicates that coordination or bond distances evolved with pressure. The coordination numbers obtained for Lu are an average over a minimum of 10 fits with error of ±0.3 for each final value. d_i = bond length, k = width parameter of Gaussian, CN_i = coordination of individual bond.*

7.4.4 Fitting Parameters

Initially the undoped data for each pressure were fitted with a sum of Gaussians (Figure 7.6). Over this pressure and temperature range it is assumed that the Si-O coordination, $CN_{\mathrm{Si-O}}$, of 4 and bond length, $r_{\mathrm{Si-O}}$, of 1.61 Å remain unchanged [14, 16, 17], due to the incompressibility of the relatively rigid silica tetrahedra. Other known peak positions and coordination numbers were fixed using data from literature [20, 49, 170] (Table 7.3). The undoped HPG fit parameters were used from Chapter 5. The Al-O contribution at 1.73(2) Å occurs under the Si-O peak and has a calculated coordination of 4.3(2) from [20, 171]. Na and K contributions are insignificant to the total $G(r)$ due to their light scattering so are not shown here, as in rhyolitic $G(r)$ models by [49]. In the AnD, special care had to be taken to correctly fit both Mg-O and Ca-O as these produce broad oscillations and introduce additional pair correlations. Ca-O correlation parameters, coordination and bond distance, were taken from literature [20, 49, 170, 172, 173] and a bond distance of $r_{\mathrm{Ca-O}}$ of 2.41(2) Å, as observed from the ambient $G(r)$ (Figure 7.4B), is in good agreement with $r_{\mathrm{Ca-O}}$ in silicates from other studies (2.41 Å in [170] and 2.37 Å in [172]). For this bond length an average coordination, $CN_{\mathrm{Ca-O}}$, of between 7-8 is widely accepted [20, 49, 173] and was used in the fits for the undoped spectra (Figure 7.6). Based on neutron studies by [170] a slight increase in $CN_{\mathrm{Ca-O}}$ with increasing P is estimated, and this was included in the fitting. However, variations in the $CN_{\mathrm{Ca-O}}$ between 7-9 have little impact on the average Lu-O coordination for the doped compositions.

$CN_{\mathrm{Lu-O}}$ and $r_{\mathrm{Lu-O}}$ were calculated by refining the fits until a reasonable match was achieved within the input parameters. The undoped major element parameters remained consistent in both the Lu-doped and undoped compositions to isolate any Lu-O contributions (Figure 7.6). The $g(r)_{\mathrm{ind}}$ for Lu-O were then integrated to obtain the area under the peak. This technique limits the uncertainty that arises from fitting complex pair distribution functions but errors in the average coordination arise from the asymmetry of the real $g(r)_{\mathrm{ind}}$ correlations and their high r oscillations. Above 3 Å considerable uncertainty also arises from the overlapping complex interactions of the partial distribution functions which makes it impossible to fit the data at r >3 Å.

7.4.5 Lutetium Incorporation

In the HPG melt, a bond distance up to 6 GPa of $r_{\mathrm{Lu-O}}$ =2.36(3) Å was observed and found to be invariable with pressure within the accuracy of this technique. The average $CN_{\mathrm{Lu-O}}$ was determined to be 8.1(3) at all pressure and temperature conditions. For the AnD a $CN_{\mathrm{Lu-O}}$ of 6.2(3) and a $r_{\mathrm{Lu-O}}$ of 2.29(2) Å were determined for the lowest pressure data (<5 GPa) and the ambient doped glass. The higher pressure points show a clear shift in fit correlation to a higher $r_{\mathrm{Lu-O}}$ of 2.40(3) Å and an estimated $CN_{\mathrm{Lu-O}}$ of 7.9 (3) (Table 7.2, Figure 7.7). This change appears to be abrupt and occurs within 1-2 GPa (from the accuracy of the data). This is unlike major element coordination changes which undergo a transition over a broad pressure range [16, 20, 38] and is most likely caused by reaching the packing limit of the melt at ∼5 GPa [174].

Crystalline oxide bond lengths for Lu-O are in good agreement with the distance of the r_2 correlation at ambient pressure. Tabulated ionic radii by [175] give six-fold coordinated Lu-O as reported to be 2.24 Å and 8-fold coordinated Lu-O at 2.32 Å. Studies on other REE glasses, e.g. YbSiAlO/N, have found similar parameters with Yb-O coordination at 6 and a bond length of 2.22 Å [176]. Other REE-O such as Dy and La in sodium silicates show decreasing bond length with atomic radii due to the lanthanide contraction, with 6-fold Dy-O at 2.29 Å and La-O at 2.48 Å. In this study, a coordination $CN_{\mathrm{Lu-O}}$ of 6 gives rise to a bond distance of 2.29 Å, and $CN_{\mathrm{Lu-O}}$ of 8 gives 2.36-2.4 Å; as might be expected in the liquid this distance is slightly longer than those of the solids.

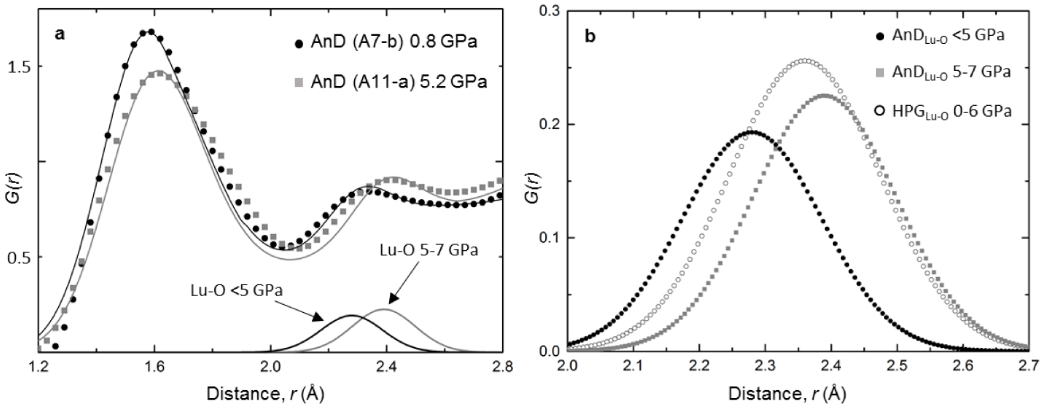

Figure 7.7 *a - Change in fits for Lu-O in AnD with P increase above 5 GPa. G(r) for a low P AnD melt (black circles) and high P AnD melt above the Lu-O coordination change (grey squares) and their respective fits (solid lines) are shown. Individual* $g(r)_{\mathrm{Lu-O}}$ *are marked with a clear shift to higher r seen above 5 GPa. b - Individual* $g(r)_{\mathrm{Lu-O}}$ *for low P AnD (black circles), high P AnD (grey squares) and average for HPG (high silica) over the P range studied (open circles).*

7.5 Discussion

At the time of writing, this was the first experimental study of its kind to identify the structural incorporation of trace elements at high pressure within silicate melt structures using x-ray diffraction. As the results here are in agreement with REE-O bond environments given above, and corroborate EXAFS results for the coordination ($CN_{\mathrm{Y-O}}$=8) and bond lengths ($r_{\mathrm{Y-O}}$=2.37 Å) of Y (a geochemical proxy for Lu) in silica-rich glasses at ambient P [41] and high $P-T$ (Chapter 6), this method appears to provide a reliable tool for determining REE speciation within silicate melts. A major consideration for this technique is that it is reliant on the applicability of Henry's law as in order to use trace elements in models it is assumed that the activity, and hence partitioning of trace elements is independant of concentration below a given limit. This is because at such low concentrations they form an insignificant structural part of a phase and do not alter the thermodynamics of the system. Although Lu here is not at natural levels of concentration (<2 ppm), in this system we propose that Henry's law is still obeyed as: (1) At concentrations of 4000 ppm Lu ions are highly unlikely to interact with each other; (2) many studies on partitioning of trace elements have shown that Henry's law is still obeyed even at several wt. % concentration

of trace elements [177, 178]; (3) there is a close similarity here with other results on REE (Y and La) at much lower concentrations [39, 41].

7.5.1 Compositional effect

At low pressure, <5 GPa, the results presented show an increase in Lu coordination from 6 to 8 with increasing silica content of the melt, from AnD to HPG, coincident with an increase in bond length of 0.07(3) Å, a 7% bond length increase (Figure 7.7b). This is consistent with observations on Y-O from Chapter 5 where in the highly polymerised HPG, CN_{Y-O}=8 and r_{Y-O}=2.37 Å. Other studies have also observed an increase in coordination in silicate and aluminosilicate glasses at ambient conditions where an increase to 8-fold coordination was observed on changing the glass composition [40, 41]. This compositional effect at ambient conditions is attributed to the higher availability of non-bridging oxygens in the basaltic network.

The number of non-bridging oxygens is thought to have a major role in trace element bonding. Silicate melts are often classified by their ratio of non-bridging oxygens (NBO) versus tetrahedrally coordinated cations (NBO/T) which defines their degree of polymerisation. The equation $NBO/T = 2(NM - T^{3+})/T^{4+}$ is used to determine the polymerisation by the number of network modifying cations (NM) and tetrahedral cations, charge balanced by network modifiers (T^{3+} = Al^{3+}, Fe^{3+}) in ratio with the number of network forming cations (Si^{4+}). When NBO/T = 0 the melt is fully polymerised, and an NBO/T = 4 would describe a fully depolymerised melt where four non-bridging oxygens are free to bond with cations. Most natural silicate melts have an NBO/T between 0 and 1 [165]. As REE will preferentially bond with NBO they therefore have higher coordination in environments where NBO are not freely available (i.e. highly polymerised melts). The results presented show an increase in the Lu coordination from 6 to 8 with increasing polymerisation of the melt (for HPG the NBO/T=0.03, and AnD has NBO/T=1.1) with a coincident increase in bond length of 0.07(3) Å. Many studies on silica rich compositions [33, 41, 46] suggest that there is a larger number of interconnected tetrahedra in these compositions compared to lower silica compositions (Chapter 2.1). This polymerisation increases the number of cages in the structure and reduces the number of NBO available to coordinate large REE. It is unlikely that Lu, with such a large radius, is able to enter any 4-7 member ring structures. In this situation Lu must be accommodated within

larger cages in the melt structure (diameter $\gtrsim$2.5 Å) surrounded by at least 8 nearest-neighbour oxygens. Within the AnD composition, however, the network is less polymerised. This allows a greater freedom of sites for Lu incorporation and more non-bridging oxygens are preferentially available for 6-fold coordination at P <4-5 GPa.

The results for the HPG presented here are all for a hydrous composition, but for $CN_{\mathrm{Lu-O}}$ or $r_{\mathrm{Lu-O}}$, it is not likely that the absence of water would affect the results. Water is proposed to depolymerise the melt structure [179] and as Lu is already behaving as in a polymerised system it is only expected that this higher coordination environment would also be present in the anhydrous case.

7.5.2 Pressure Effects

Within the HPG there is no observable pressure effect on Lu incorporation within the melt structure up to 6 GPa, as also observed for Y and Zr in Chapter 6. As described in [174] and [46], silica rich melts are predominantly comprised of interconnected rings of tetrahedra that form cages. Due to the very low concentrations of network modifying cations in the HPG studied here the structure of this highly polymerised composition is dominated by these interconnected tetrahedra. As pressure increases the cages collapse as the network is compressed. As Lu is unlikely to be accommodated within the predominant 4-7 membered cages there is little compressional effect on its speciation within the melt as Lu must remain in any available larger cages (Figure 7.8A-B). As the number of available sites for Lu in highly polymerised melts would be small, Lu may also prevent the larger cages from collapsing on compression.

Within the AnD an increase in P causes an abrupt Lu-O coordination increase from 6 to 8 between 4-5 GPa, accompanied by an increase in the bond length from 2.29 to 2.40 Å (Figure 7.7). Therefore, above 5 GPa the $CN_{\mathrm{Lu-O}}$ and $r_{\mathrm{Lu-O}}$ is similar to that of the HPG. The difference between the behaviour at pressure of the AnD and HPG melts is due to the initial structure of the melt at <5 GPa. At low pressure, in the AnD, Lu is free to bond within the network in any available space and preferentially adopts lower CN. At higher pressure, as the packing limit of the melt is reached, Lu is forced on to 'crystal-like' sites and coordination increases (Figure 7.8C-D). The lower silica content and higher concentration of network modifying cations in the AnD composition prevent the structure forming polymerised network cages on compression as there are fewer silica tetrahedra,

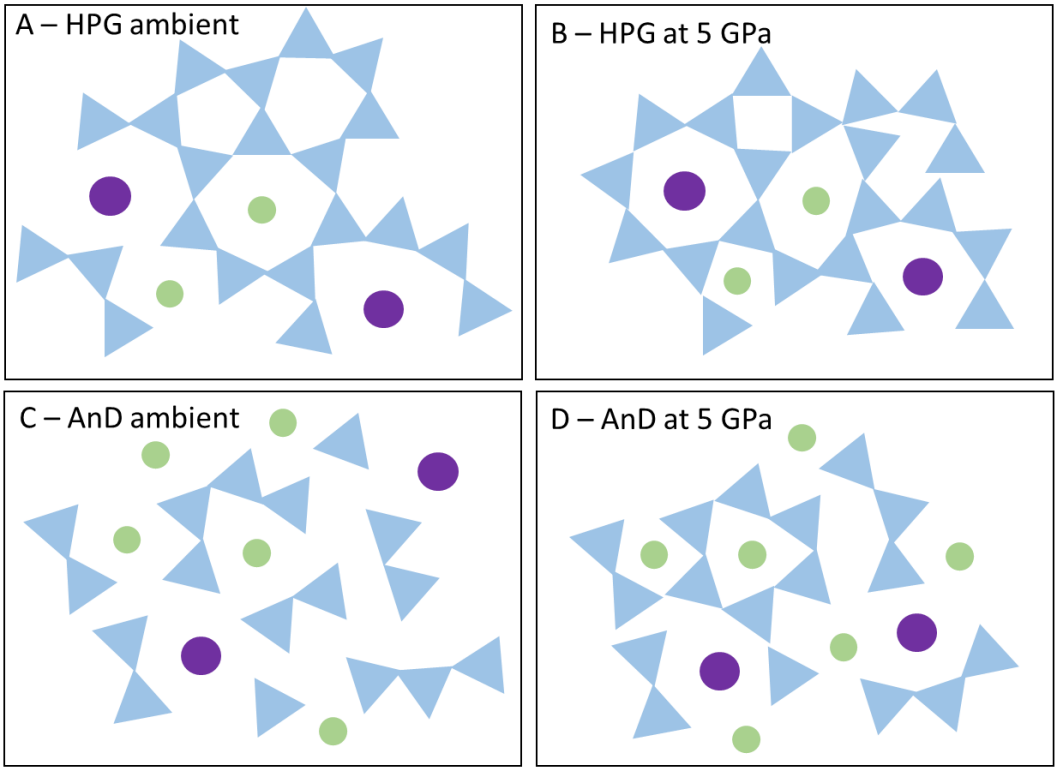

Figure 7.8 *Two-dimensional schematic representations of the HPG and AnD melt structures at ambient pressure (A and C) and at 5 GPa (B and D). Silica tetrahedra = blue triangles, network modifying cations = green, Lu atoms = purple. A - A possible HPG structure at ambient conditions. The silicate network forms rings (2D) and cages (3D) where cations can be accommodated. B - Upon compression of the HPG, the interconnected silicate network rings and cages collapse but Lu (purple) remains in the largest sites available surrounded by 8 nearest neighbour oxygens. C - A possible ambient structure of the less polymerised AnD melt. The greater availability of NBO and higher concentration of cations allow octahedral and tetrahedral cation sites to exist within the silicate network. D - After compression up to 5 GPa, the AnD melt network is packed closer together and Lu is coordinated by 8 nearest neighbour oxygens from both silica tetrahedra and octahedral cation sites, as found in minerals such as garnet.*

and oxygens are available to coordinated cations in tetrahedral or octahedral configurations similar to those found in minerals. This results in a close packed network distinctly different from that of the HPG (Figure 7.8) with the presence of 'crystal-like' sites. The idea of these sites in the melt were developed in silicates (specifically clinopyroxene) by [180], who proposed that oxide-like, 6-fold sites might exist in the melt structure and influence partition coefficients due to the site elasticity and radii. Van Westrenen *et al.* [181] showed that partitioning behaviour between silicate melt and garnets could be better explained by the presence of $J_3Al_5O_{12}$ sites with 8-fold coordination within the melt, rather than 6-fold J_2O_3 sites. As pressure increases in the initially less polymerised structure, and the melt is packed more closely together it is likely that more 'crystal-like' sites are created within the melt with a higher coordination environment. These have a similar bonding environment to sites within minerals such as garnet, and therefore a reduction at high P in partition coefficient between the melt and minerals, where REE^{3+} are usually slightly compatible, would be expected. This same transition to 'crystal-like' sites could occur in the silica-rich melts with P, however, as the initial CN is already 8 it would be indistinguishable to resolve using this methodology. This is also unlikely due to the fundamental difference in structures at ambient conditions.

As pressure increases, the density of the AnD sample also increases, as discussed for the HPG results presented in Chapter 5. This is due to the increase in pressure causing a tightening of the tetrahedral network. Molecular dynamic simulations combined with x-ray diffraction by [174] suggest that compression within a polymerised network is different to that of a less polymerised melt. For a depolymerised network, as pressure increases, the packing fraction of the tetrahedra increases and the number of NBO will decrease as they are forced to bridge on compression. As they were not initially in ring or cage structures these are unlikely to form on compression and a close packed structure is generated. In a highly polymerised melt, the already highly interconnected tetrahedral network that makes up the cages, collapses to form smaller cages with only a slight change in the number of NBO [174], preserving some of the ring and cage structures at P. Wang [174] proposes, in depolymerised systems, that the packing limit of the melt is reached between a number density of 0.082-0.088 atoms/$Å^{-3}$, which corresponds to approximately 3-7 GPa in the case of the diopside melts. This pressure range overlaps where the observed change in Lu coordination within the AnD occurs (Table 7.2). The estimated densities used in this study are shown in Figure 7.9 with increasing pressure. It can be seen that between 1-5 GPa

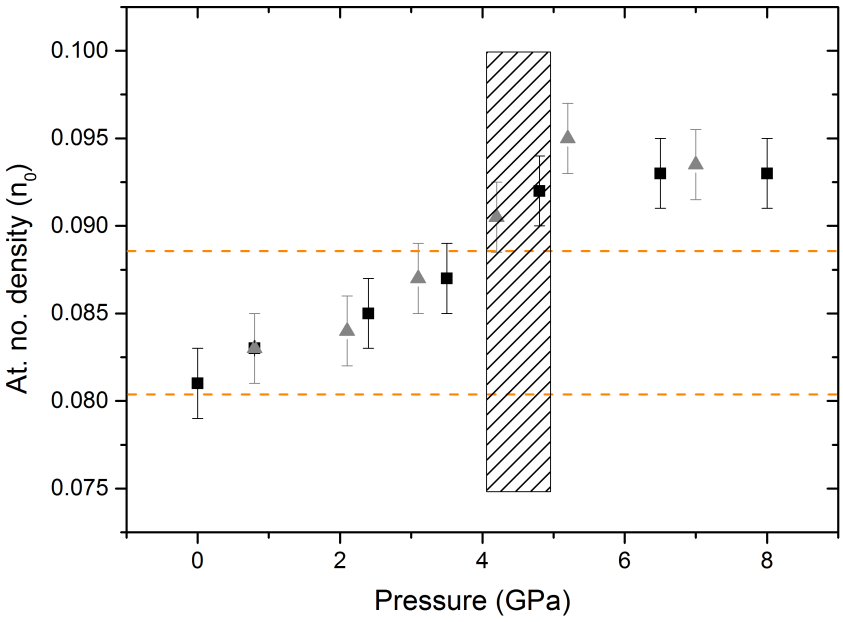

Figure 7.9 *Atomic number densities, n_0 in atoms/Å^3, for Lu-doped (grey triangles) and undoped (black squares) AnD melts in this study from Table 7.2. Dotted lines are the suggested tetrahedral packing fraction limits from Wang [174] on compression of diopside. The observed CN change in this study is represented by the hashed box. Errors on the densities arise from errors on the $G(r)$.*

there is rapid density increase as the sample is packed, which then appears to slow with a further increase in pressure. The observed coordination change is between pressures marked with the grey box; this appears to be after the sample has undergone the initial stages of compression. The results on the coordination change of Lu within these melts corroborate that of [174] in suggesting there is a distinctly different behaviour between polymerised and depolymerised melts with increasing pressure, and that the AnD melt is more closely packed than the HPG at pressures >4-5 GPa, due to the lack of cages formed by the silica tetrahedra.

7.5.3 Impact on Partition Coefficients

The coordination change from 6 to 8 as melt polymerisation increases (i.e. from the AnD to the HPG) corresponds with results presented by [33] and [34] on the dramatic increase in REE partition coefficients with melt polymerisation. This increase in compatibility and preference to incorporate in the mineral as

polymerisation of the melt increases has been proposed to be due to the energetics associated with bonding to predominantly bridging oxygens. In depolymerised melts the freely available non-bridging oxygens mean that at lower P the REE can more easily incorporate into the melt structure than in the crystal lattice.

From these results it is clear that the melt could have a much stronger influence on $D_{\mathrm{min/melt}}$ with pressure than previously expected. The observed decrease in compatibility between Lu and minerals such as garnet and clinopyroxene with P (Chapter 2, Figure 2.6) could occur due to the appearance of 'garnet-like' sites within the melt. The coordination change in the melt at 5 GPa results in the plateauing of the $D^{\mathrm{Lu}}_{\mathrm{min/melt}}$ as there is little preference for either the mineral or melt at this pressure. Although Lu has the same coordination in polymerised melts as the basaltic melts at >5 GPa existing partitioning studies would suggest that the site or mechanism for Lu incorporation in these melts is different, at least for low P polymerised melts. This is because opposite partitioning behaviour is observed; for low pressures an increase in D_{Lu} is witnessed with a preference for crystals over granitic melts, but a decrease in D_{Lu} between low pressure and >5 GPa basaltic melts, indicating a preference for basaltic melts at high pressures. As no partitioning data is available for granitic melts at P >4 GPa it could be possible that at these pressures D_{Lu} also decreases but from this study it is suggested that the incorporation of Lu in the structure between the depolymerised and polymerised melts is different; therefore this would be unlikely. If partition coefficients in basaltic melts increase with P, as suggested by some authors [66, 67] this would not alter any results presented in this chapter, and it may suggest that as pressure is increased in depolymerised systems, the REE incorporation mechanism between polymerised and depolymerised melts becomes similar. Changes in partitioning would also be affected by the influence of other coexisting P effects such as compression of the crystal lattice. Green and Pearson [72] did observe a small increase of $D^{\mathrm{REE}}_{\mathrm{cpx/melt}}$ with P up to 2-3 GPa between clinopyroxene-andesitic melts which suggests that the change in partitioning cannot only be attributed to one factor as it may vary for different mineral-melt systems where the influence of the crystal or melt is stronger. In the case of [72] the melts comprised of ∼60% SiO_2 content and REE may have coordination environments in the melt similar to the HPG in this study.

If the coordination increase for Lu at 5 GPa (∼150 km depth) in basaltic-like melts is consistent with a subsequent decrease and plateau of partition coefficient, this could significantly affect partitioning at depth. Within the Lu/Hf system during

mantle melting there is distinctive partitioning behaviour at ambient pressure where Lu is preferentially incorporated over Hf in crystallising phases. However, if D_{Lu} values decrease with pressure (Figure 2.6), above 5 GPa D_{Lu} will approach D_{Hf}, and would result in a much lower partitioning ratio between Lu/Hf than expected. This decrease in partitioning ratio could have two implications: (1) if Lu/Hf at depth are no longer partitioned distinctively, Lu/Hf signatures in melts extracted from the mantle at >4-5 GPa could indicate prior depletion even though none has occured. (2) radiogenic Lu/Hf signatures in crustal rocks could be evidence of a superchondritic mantle source rather than a depleted mantle. Both implications throw greater uncertainty into the debate on when and how the early Earth crust was formed. Although this structural data cannot identify exactly what changes would occur at depth it indicates that there is likely to be a strong melt effect on partitioning that cannot be ignored in partitioning models and adds further complications to studies dependant on partitioning ratios as geochemical tracers.

7.6 Conclusion

This chapter presents the first x-ray diffraction measurements on trace elements *in situ* within melt structures. It shows that x-ray diffraction techniques can be used to study trace element incorporation in liquids and can reliably determine a nearest-neighbour bond distance for minor elements. This technique is applicable to Lu due to the length of the Lu-O bond distance, as it appears within the $G(r)$ where there are few correlations. If Fe or other higher scattering elements were present in the sample it is unlikely this methodology would have been successful.

The results show an increase in coordination from 6 to 8 of Lu with increasing polymerisation of the melt at lower pressures up to 4-5 GPa, consistent with an increase in the $D_{\mathrm{mineral/melt}}$ partitioning ratio from <1 to >100 at ambient pressures. These results are consistent with the results presented for Y in Chapter 5 and show no variation in REE incorporation (CN or bond distance) with increasing P in polymerised systems. As for Y, this would suggest that the large atomic radius of Lu prevents the larger occupied cages in the melt collapsing with P, and compression is caused by collapse of the unoccupied sites. These results show that both x-ray absorption and diffraction techniques can be used to identify REE incorporation at high pressure and temperature. Apart from the higher compressibility within the melt phase, as seen for the undoped HPG in

Chapter 5, the Lu-doped HPG also appears identical between the glass and melt phases, indicating quenched glass measurements on REE provide good analogues for molten silica-rich systems up to 6 GPa.

With pressure, an abrupt coordination increase from 6 to 8 is observed at 4-5 GPa in less polymerised systems. This coordination change suggests that at >4-5 GPa compression of the melt results in the formation of 'crystal like' sites that accommodate Lu at high pressure. This change in Lu incorporation is likely to strongly affect the partitioning of Lu at depth, and subsequently cause distinct changes in the predicted Lu/Hf ratios during early Earth crustal formation. This may produce a depleted mantle Lu/Hf isotope signatures in crustal samples extracted from a non-fractionated source at 4-5 GPa, or during shallow melting produce chondritic signatures from a superchondritic reservoir.

Overall these results indicate that there are important structural changes in silicate melts that occur with variations in both composition and pressure that cannot be neglected in standard models. As the melt structure changes with pressure, using a single melt term to normalise the effects of melt on trace element partitioning will not accurately predict partitioning behaviour at depth during magma formation or differentiation. In order to fully understand how partitioning is affected by melt structural changes, detailed insight into the exact nature of the Lu sites within the melt network is still required.

Chapter 8

Structure of Neodymium-doped Silicate Melts at High Pressure

8.1 Introduction

This chapter continues with the subject of trace element incorporation in depolymerised melts. In this chapter the speciation of neodymium (Nd) is studied in the same anorthite-diopside composition as Chapter 7. Nd was used to identify whether incorporation mechanisms within the melt differ for changing REE, and to observe whether the same changes seen for Lu occur with other lanthanide elements. As with Lu, the radioactive decay of ^{146}Sm-^{142}Nd is commonly used for dating crust formation, and interpreting the bulk composition of the early Earth. Here, the structure of the Nd-doped anorthite-diopside melt is measured using laser heated diamond anvil cells (LH-DAC) and in the Paris-Edinburgh press (PEP).

8.2 Experimental Procedures

The anorthite-diopside (AnD) composition was synthesised as described in Chapter 4.4, and the composition is detailed in Table 8.1. This composition was doped with 3.8 wt.% Nd_2O_3 of >99.99% purity in order to have a similar concentration to the Lu concentrations in Chapter 7. Nd was chosen due to its larger radius as it falls towards the opposite end of the lanthanide series from Lu.

Oxide	Initial	DAC recovered	PEP Recovered
SiO_2	48.8 (5)	49.4 (4)	45.7 (5)
Al_2O_3	14.7 (3)	15.24 (3)	13.4 (3)
MgO	10.2 (2)	9.8 (2)	15.9 (3)
CaO	22.7 (2)	22.2 (5)	21.4 (4)
Nd_2O_3	3.4 (1)	3.4 (1)	2.9 (1)
Totals	99.8 (5)	100.4 (6)	98.7 (5)

Table 8.1 *Compositions from electron microprobe analysis of both initial and recovered samples. Compositions given in wt.% oxide. Analyses are based on average of a minimum of 10 sample spots, standard deviations are shown in brackets. Results from both experiments (DAC and PEP) are shown in columns 3 and 4 to show comparison between recovery of different experiment types.*

It also has the ability to couple with the YAG laser required for laser heating [182]. The Nd-doped glass was transparent and pale purple in colour with the colour deepening at higher concentrations of doping; this was significantly different to the Lu doped glass which was always colourless. The glass was checked after synthesis for a lack of bubbles or crystals and was very finely crushed for one hour before loading. Data up to 8 GPa at >1500 K in 1 GPa pressure steps were collected on HP-CAT at the Advanced Photon source to study the low pressure sample in detail using a Paris-Edinburgh press. These data were collected and analysed by the same method as described in Chapter 7 for the Lu-doped AnD samples and the undoped samples used for comparison are the same as described in Chapter 7. LH-DAC experiments were carried out on the GSECARS beamline at the APS and measurements on the melt structure were made up to 36 GPa at >2000 K, with high pressure doped and undoped glass measurements made up to 60 GPa. As with Chapters 5 and 7 not all of the data collected during the experiments could be presented in the final results due to varying quality, and the reasons for not analysing certain data are listed in Appendix One, Tables 9.3 and 9.2.

8.2.1 Laser Heating Experiments

Laser heated diamond anvil cells were used in this study in order to access melting up to higher pressures relevant to those of the entire upper mantle to mid-lower mantle. For loading, the sample was initially compressed in a 1 mm culet DAC

to create very thin (∼5-10 μm) platelets that could be loaded into the the gasket hole. This enabled very efficient packing of the sample in order to prevent collapse of the hole during pressurisation or heating. Three platelets of amorphous SiO_2 were initially placed in the gasket hole to prevent any contact between the sample and the diamonds and to act as a pressure transmitting medium. Platelets of SiO_2 were created in the same way and each platelet was checked for a similar thickness to a standard one made and kept at the beginning of the experiment. Three platelets of sample were then loaded and the hole was filled with another three layers of SiO_2. Platelets of the same thickness were used in every loading to ensure the gasket hole was filled each time and there would be identical sample intensity for each experiment. For these experiments pressure was monitored by a ruby loaded into the sample chamber before and after heating. Due to the small beamsize (<20 μm) it was easy to ensure the laser heating spot was never close to the edge of the gasket or the ruby.

During laser heating, melting was known to occur by coupling of the laser to the sample and visually observing the luminescence of the sample. Laser power was increased incrementally by 0.5 W before opening the shutters and observing if melting occurred. Once melting occurred no further measurements were taken and a quench pattern was collected. Patterns were collected at each pressure on the glass, on melting with the lasers and subsequently on the quench. Patterns on the glass were collected for up to 60 s using a Perkin Elmer detector, whereas melt spectra were only collected for a maximum of 10 s in order to prevent damage to the detector. Backgrounds, as for the DAC experiments in Chapters 5 and 7, were collected by inserting the empty gasket (after the sample had been recovered) into the cell and collecting empty patterns. Carbon mirrors were used to focus the lasers on both sides of the sample; these produce diffuse scattering on the detector that must be accounted for when subtracting the background. In order to account for these and other background effects both mirror and non-mirror background patterns were collected.

8.2.2 Recovered Sample Analysis

After laser heating the samples were recovered as small glass spheres within the SiO_2 pressure medium (Figure 8.1A) with the diameter of the laser size (20 μm). These were recovered from the gasket using a needle and were mounted and polished in epoxy resin for electron microprobe analysis. Electron microprobe

analysis was undertaken at the Centre de Microanalyse Camparis, University Pierre and Marie Curie using an accelerating voltage of 20 keV and 10 nA for the major elements (Si, Al, Mg and Ca) and 40 nA for Nd detection. The beamsize was set at a nominal 1 μm diameter. The initial and recovered sample compositions are shown in Table 8.1. The recovered DAC samples show practically identical content indicating there was very little or no diffusion from the SiO_2 pressure transmitting medium and no loss of Nd during heating. From the presence of spheres within the SiO_2 layers we can conclude that the sample was molten in localised areas with limited diffusion of elements in or out of the heating spot. This may have been limited due to the very short collection times (<10 s) at high temperature and the excellent coupling of Nd to the laser. Samples recovered from the PEP experiments were glassy (Figure 8.1B) but show a slight change in composition occurred during the experiment. Silica content decreased by $\sim$4 wt % with MgO increasing by $\sim$5-6 wt %. MgO is likely to have diffused into the capsule from the cell assembly at high pressure and temperature as the samples were held for up to 8 hours at high $P-T$. Silica could also have diffused out of the sample into the cell assembly at these conditions. However, as the silica content decreased the polymerisation of the melt was not affected and the melt still remained depolymerised; the other cation concentrations were also similar so it is unlikely that the results were dramatically affected.

8.3 Data Analysis Procedure

Data analysis was carried out using the same method as described in Chapters 5 and 7 for both the PEP and DAC experiments. Due to the high background scattering from the carbon mirrors (Figure 8.2) special care had to be taken to ensure background removal was consistent for all measurements. This was completed by scaling the background at the same 2θ angle for every spectrum. As can be seen in Figure 8.2, the compressed glass measurements were made without the carbon mirrors to increase the signal intensity, these could then be compared to the melt measurements where the mirrors were required to assess the reliability of the decreased signal. Due to the pressure transmitting medium, in the compressed glass samples the signal collected contained scattering from both the sample and the amorphous SiO_2. This contribution was removed by collecting data on a compressed sample with no SiO_2 at similar pressure intervals. This was then compared to the diffraction patterns containing sample and SiO_2

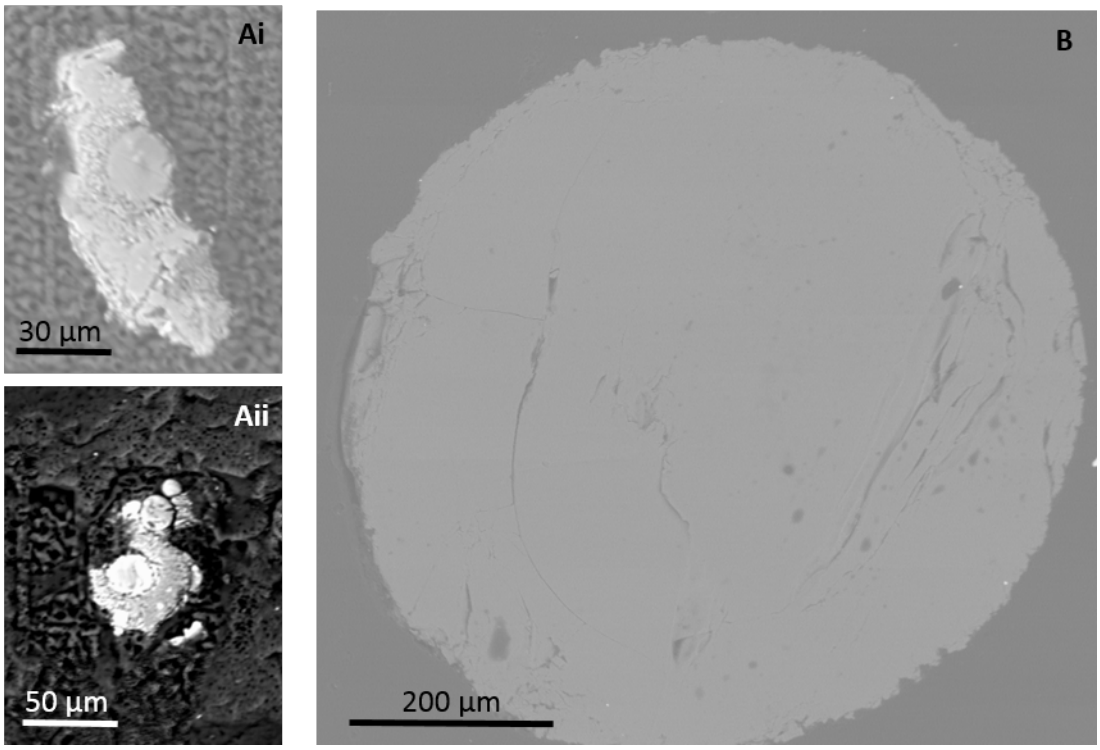

Figure 8.1 *Recovered samples both DAC (Ai-ii) and PEP (B) experiments, taken on the electron microprobe. Ai and Aii clearly show the 20 µm spheres caused by laser heating.*

and the contribution arising from SiO_2 was removed from the diffraction signal (Figure 8.2A). During heating, stishovite and coesite Bragg peaks are produced as SiO_2 recrystallises at high temperature. If this occurred, the Bragg peaks were removed by masking the diffraction spots on the image plate. These were useful for corroborating the estimated pressure from the ruby using the phase diagram of quartz at high pressure and temperature. In some cases during heating the SiO_2 did not recrystallise and the SiO_2 contribution was removed via the same method as the compressed glass.

8.4 Results

8.4.1 Neodymium as a Laser Coupler

This is the first time Nd has been reported as a coupler for LH-DAC experiments and previous couplers have included other metals such iron and platinum [14, 182]. In order to couple with the YAG laser an element which absorbs at the same

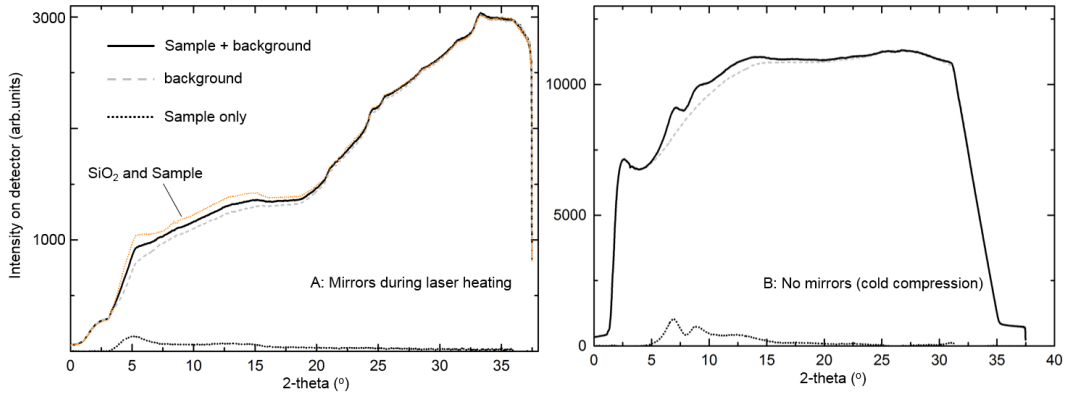

Figure 8.2 *Diffraction patterns for examples of the Nd-doped glass samples contained in the DAC, with (A) and without (B) carbon mirrors for laser heating. In A, the sample signal with and without SiO_2 contributions is shown.*

wavelength of the YAG (1064 nm) is required. Nd was chosen due to its ability to absorb and fluoresce at this wavelength. The Nd coupler has many advantages over previous iron coupling measurements including the ability to re-melt the sample with identical quality, very localised heating, and preservation of the diamond anvils even at P >50 GPa and T >2000 K. When Fe has been used as a coupler [14], if the same sample was melted more than once with the laser a considerable decrease in intensity was observed, indicating that Fe appeared to diffuse away from the sample spot. With Nd no such decrease in intensity was observed and the recovered sample analysis suggests that Nd remained homogeneously distributed. The localisation of heating is improved with Nd compared to Fe as observed by the partial recrystallisation of the SiO_2 thermal insulation layer. In Fe-doped samples this layer always recrystallised resulting in considerably more Bragg peaks to remove and additional uncertainty in the data processing. It is also this improvement in localisation of heating that appears to protect the diamond anvils from damage at high $P-T$. With Fe, at $P > 40$ GPa, laser heating spots on the culets or cracking of the diamond anvils nearly always occurred; however no damage was observed at the same conditions with Nd. This is likely due to greater heat escape from the sample in the case of Fe, which is inferred by the SiO_2 recrystallisation.

Run no.	P (GPa)	Power (W)	n_0 (Å^{-3})	$G(r)$ positions (Å)		
Exp. 1				r_1	r_2	r_3
Nd doped	amb.	amb.	[0.081]	1.61 (1)	2.48 (2)	3.24 (3)
N1	2.1 (3)	40	0.084 [0.085]	1.59 (2)	2.44 (2)	3.07 (3)
N2	6 (2)	14	0.093 [0.093]	1.59 (2)	2.43 (2)	3.11 (3)
N3	8.2 (3)	13	0.092	1.62 (2)	2.41 (2)	3.19 (2)
N4	12 (2)	15	0.093	1.61 (2)	2.50 (5)	3.17 (4)
N5	17.5 (5)	27	0.096 [0.094]	1.61 (1)	2.49 (3)	3.21 (3)
N6	29.3 (9)	82	0.097 [0.094]	1.65 (2)	2.61 (4)	3.18 (4)
N7	35.7 (5)	81	0.097 [0.097]	1.68 (2)	2.51 (4)	3.37 (6)
N8	44.9 (2.0)	amb.	[0.099]	1.69 (2)	2.47 (5)	3.16 (4)
N9	60 (3.0)	amb.	[0.098]	1.67 (2)	2.56 (3)	3.22 (3)
Undoped	amb.	amb.	[0.081]	1.61 (1)	2.46 (2)	3.23 (3)
	7.6 (3)	amb.	[0.094]	1.62 (2)	2.44 (2)	3.18 (3)
	18.5 (5)	amb.	[0.096]	1.63 (1)	2.65 (2)	3.15 (3)
	28.8 (5)	amb.	[0.097]	1.66 (2)	2.43 (3)	3.15 (3)
	35.6 (10)	amb.	[0.098]	1.67 (1)	2.39 (3)	3.15 (3)
	45.3 (10)	amb.	[0.098]	1.68 (2)	2.42 (3)	3.14 (2)
	58.0 (20)	amb.	[0.099]	1.68 (2)	2.45 (3)	3.07 (4)
Exp. 2		T (K)				
P1	0.6 (3)	1570 (50)	0.082	1.60 (1)	2.43 (2)	3.05 (2)
P2	3.5 (2)	1820 (50)	0.087	1.59 (1)	2.44 (2)	3.10 (3)
P3	5.5 (3)	1850 (50)	0.092	1.59 (2)	2.41 (3)	3.18 (5)

Table 8.2 *Experimental conditions of each experiment as well as estimated densities and results on positions of the first three peaks in the $G(r)$, r_{1-3}. Brackets in T and P are errors. Experiment 1 was using laser heating at GSECARS, and experiment 2 results are from HP-CAT using the Paris-Edinburgh press. Densities given in [] denote the density of the glass samples at the same pressure as the melt. As described in the text all undoped data collected in Exp. 1 were glass due to the lack of laser coupler. Undoped data collected up to 8 GPa on HP-CAT is described in Chapter 7.*

8.4.2 Structural Results

Details of experimental data collected at each pressure are listed in Table 8.2. Laser heating melt data on the Nd-doped samples were collected up to 35.7 GPa with doped glass measurements for comparison also taken at each pressure step. The highest pressure measurements at 44.9 and 60 GPa were successfully collected on the glass only due to the low signal intensity of the melt. PEP data using EDXD were collected on the doped samples in the molten state at 0.6, 3.5 and 5.5 GPa along with undoped AnD melt measurements up to 8 GPa (described in Chapter 7.4.2). Undoped glass samples were collected up to 60 GPa; no melt could be collected on the undoped samples in the DAC setup due to the lack of laser coupler (Nd) in the sample. The structure factors are shown in Figure 8.3 with the lower panel showing comparison between molten Nd-doped samples (either by LH-DAC or PEP) and molten undoped samples up to 8 GPa, and the upper panel displaying molten doped data (where possible) from LH-DAC experiments compared against compressed glass at the same pressure over the range 8-60 GPa. The subsequent $G(r)$ obtained via Fourier transform are shown in Figure 8.4. The positions of the prominent peaks and densities used for the calculation are given in Table 8.2.

In the $S(Q)$ the FSDP of the Nd-doped samples increases from 1.99 Å^{-1} at ambient conditions to 2.08 Å^{-1} by 8 GPa. This is similar to the shift seen in the Lu-doped AnD over the same P-range and is also observed in the undoped AnD. There is good consistency between the $S(Q)$ collected via PEP and LH-DAC measurements although as can be seen at 2.1, 6 and 8.2 GPa, the noise at Q >4 Å^{-1} is much greater in the LH-DAC measurements due to the lower signal intensity, and subsequently the resolution of oscillations at Q >7 Å^{-1} is poorer than in the PEP experiments. This causes broadening of the resolved peaks in the $G(r)$ which is discussed below. As in the Lu-doped melts, the $S(Q)$ for the doped and undoped melts are similar except for a slight increase in $S(Q)$ intensity in the doped spectra between 3-4 Å^{-1} on the shoulder of the second peak. This is less distinct than in the Lu-doped samples and not as consistent. At higher pressures, the FSDP visibly decreases in intensity, broadens and shifts further to a higher Q of 2.36 Å^{-1} at 29 GPa until it reaches 2.5 Å^{-1} by 45 GPa and appears to remain in this position up to 60 GPa. This is attributed to the increase in mean Si-O distance as Si coordination increases at high pressure, and therefore a distortion of the silicate network. A second diffuse peak at 3.2 Å^{-1} is observed to increase in intensity from 17 GPa in the glass structure whilst the

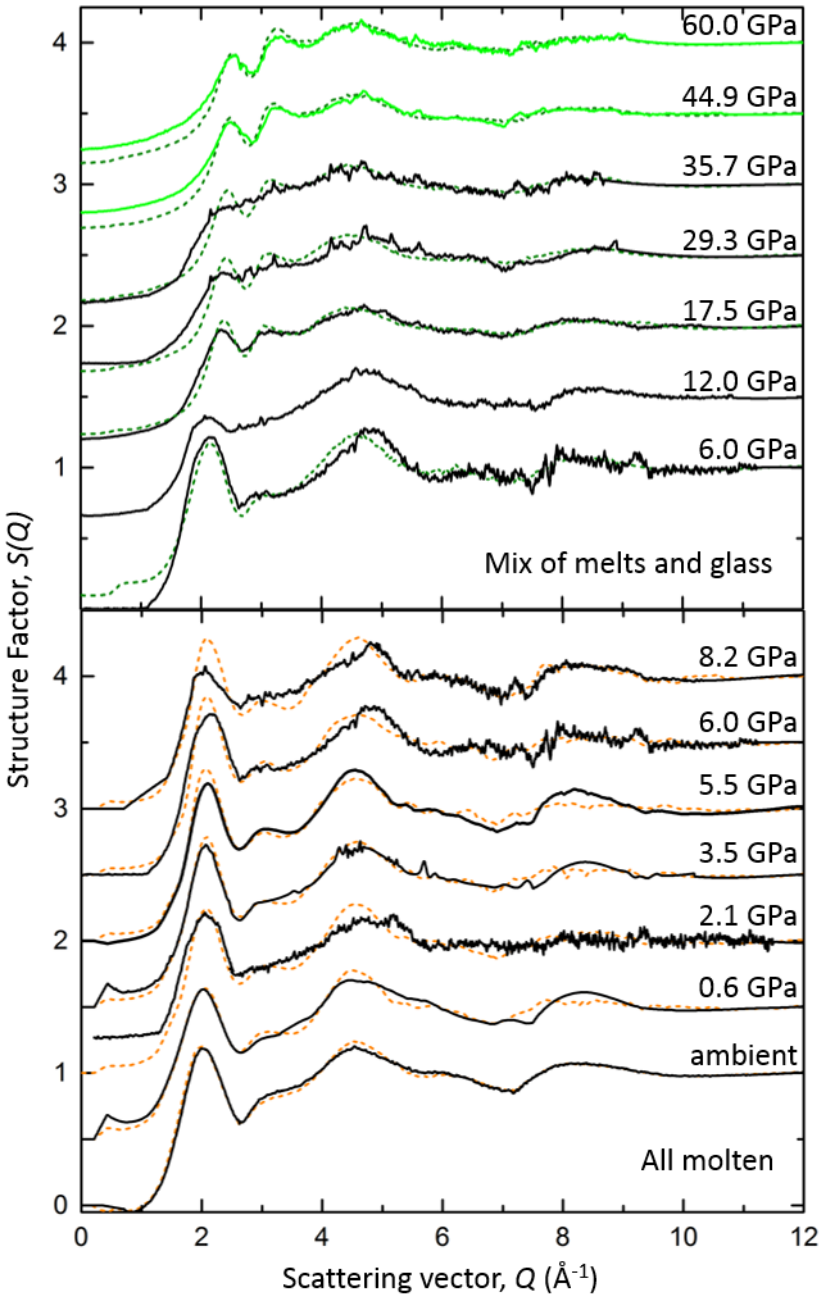

Figure 8.3 *Structure Factors, $S(Q)$, for Nd-doped (black) and undoped (orange and green) melts and glasses up to 60 GPa. Lower panel shows 1 GPa pressure steps in the low pressure regime up to 8 GPa with both the Nd-doped and undoped collected in the molten state at high temperature. Green patterns in the top panel are undoped glass measurements for comparison.*

third peak broadens and decreases in intensity. These results are consistent with data presented on basaltic melts by [14] and SiO_2 glasses at high pressure [16, 17]. As can be seen in the LH-DAC samples at 29.3 and 35.7 GPa, the signal intensity is much lower than that of the glass at the same pressure. This is due to the short collection time for the melts and carbon mirrors required to align the laser heating system, as well as the very low scattering of the molten sample at these pressures. Although the Fourier transform of these spectra appears reasonable, the peaks appear very broad due to the lack of resolution in the $S(Q)$. This affects the real intensities of the peaks and makes fitting with appropriate densities difficult as will be discussed in Section 8.4.4.

In the $G(r)$ the first peak at r_1=1.61 Å in the low P data arises from the Si-O and Al-O contributions as discussed in Chapter 7. The second peak at r_2=2.4 Å in the undoped samples is the result of the Ca-O contribution and is seen to increase in intensity in all the Nd-doped samples, assumed to be a result of the Nd-O correlation as witnessed for Lu-O in Chapter 7. The third peak, r_3 at 3.1-3.2 Å is a sum of the O-O and Si-Si correlations (Table 8.2). The change in intensities of the $S(Q)$ peaks above 17.5 GPa is represented in the $G(r)$ by noticeable changes in the correlations. The first peak in the $G(r)$ which is dominantly the Si-O contribution is seen to shift to 1.65 Å at 17.5 GPa to 1.68 Å by 35.7 GPa; the alteration in the first peak height and position is consistent with an increase in Si-O coordination from 4 to 6 over this range. At 29.3 GPa in the undoped glasses it can be seen that the second correlation in the $G(r)$ gains intensity and a broad band is seen to appear at 2.5 Å. Both these changes have been observed in other silicate melts and glasses [14, 16, 17]. This contribution has been attributed to the presence of tetrahedral edge-sharing giving rise to O-O correlations at this distance as compression forces the tetrahedra closer together [17]. The decrease in the Si-O contribution height with pressure is due to the increasing density of the sample with compression as observed in Chapters 5 and 7. Above 17.5 GPa this decrease slows with further increasing pressure which is consistent with the FSDP shift rate which also slows above this pressure suggesting the rate of densification is much greater below 20 GPa, and dominant between 0-5 GPa as discussed in Chapter 7 and by Sanloup [14].

As mentioned, the low signal intensity from the liquid sample may cause artefacts in the $G(r)$ during the data processing. As this study is focussed on minor correlations, specifically Nd-O, it is important to be able to distinguish artefact oscillations from real contributions, especially as slight changes in intensity caused

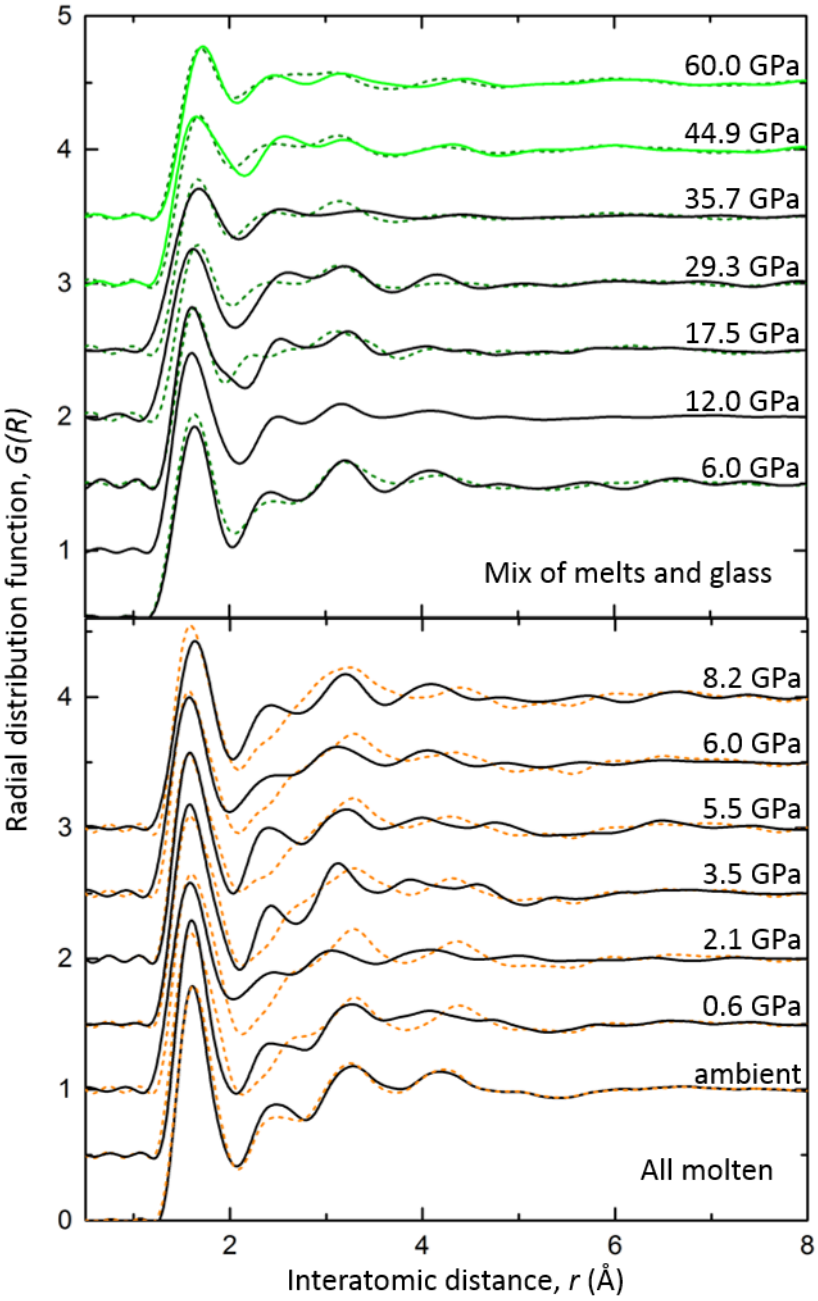

Figure 8.4 *Radial distribution functions, $G(r)$, Fourier transformed from the $S(Q)$ shown in Figure 8.3. Lower panel shows 1 GPa pressure steps in the low pressure regime up to 8 GPa with both the Nd-doped and undoped collected in the molten state at high temperature. Green patterns in the top panel are undoped glass measurements for comparison.*

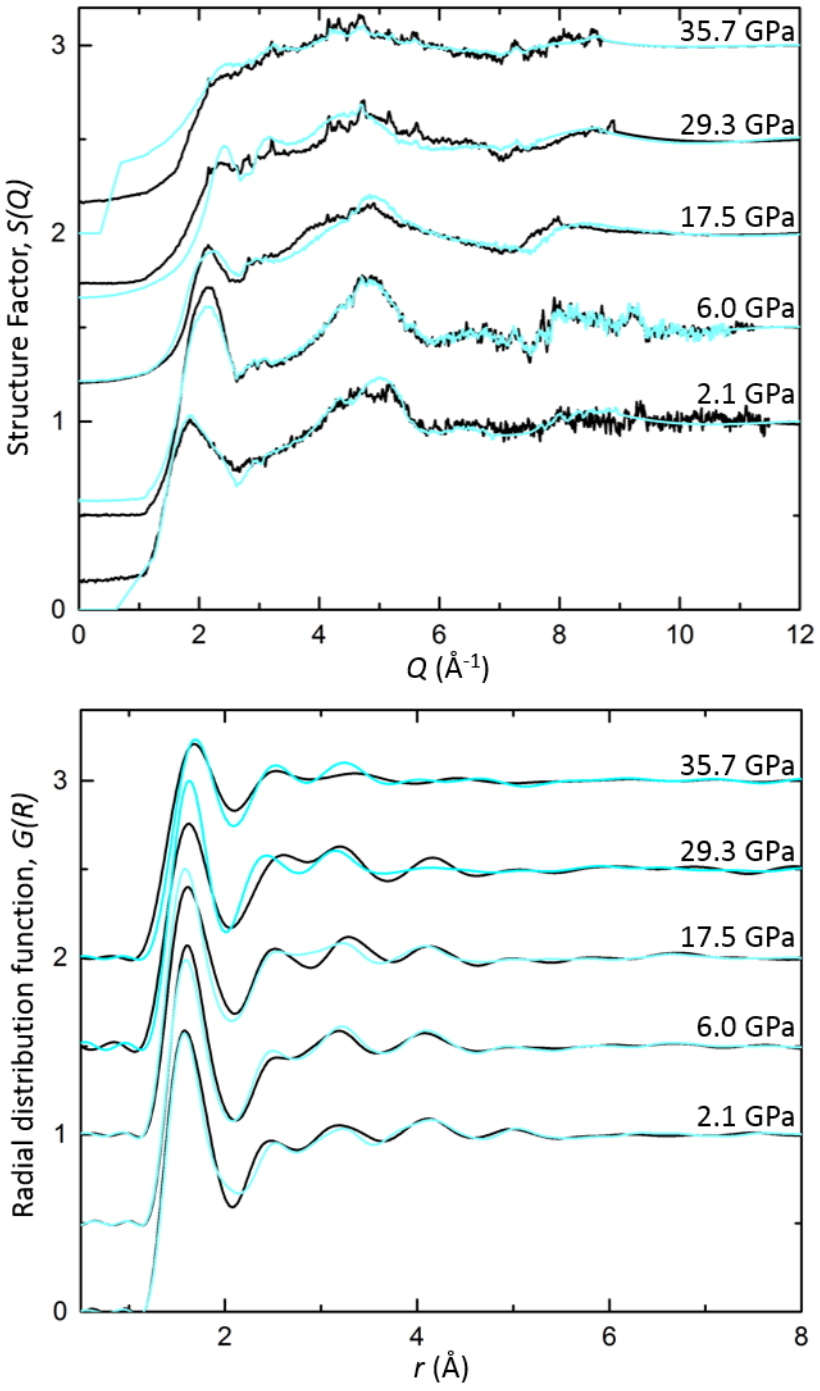

Figure 8.5 *Nd-doped melt data (blue) compared to Nd-doped glass data (black) at the same pressure. Top panel shows the $S(Q)$ with lower panel shows the subsequent $G(r)$.*

Ion-Ion	r			k			CN		
elements	P_1	P_2	P_3	P_1	P_2	P_3	P_1	P_2	P_3
Si-O	1.6 (2)	1.6 (2)	1.68 (2)	0.12	0.12	0.14	4	4	5.8
Al-O	1.75 (2)	1.75 (2)	1.80 (2)	0.09	0.09	0.12	4.3	4.3-5.2	5.2
Mg-O	2.00 (5)	2.00 (5)	2.05 (3)	0.2	0.2	0.12	5	5	5.5
Ca-O	2.40 (2)	2.45 (9)	2.50 (9)	0.15	0.15	0.14	8.1	9	10.5
O-O	3.05 (4)	3.05 (4)	3.00 (4)	0.18	0.18	0.15	9	9	10
Nd-O	2.38 (3)	2.45 (3)	2.45 (3)	0.1	0.1	0.08	5.8(3)	8.2(3)	8.2(4)

Table 8.3 *Ion-ion contributions used to model individual Gaussians, $g(r)_{\mathrm{ind}}$, in the compositions over different pressure ranges. Errors from fitting the bond distances are given in brackets. The coordination numbers obtained for Nd are an average over a minimum of 10 fits with error of ±0.3 for each final value. r_i = bond length, k = width parameter of Gaussian, CN_i = coordination of individual bond. P_1 = ambient and 1 GPa data. P_2=2-12 GPa, P_3=17.5 GPa and above*

by data processing could alter extracted coordination numbers from $CN_{\mathrm{Nd-O}}$. In Figure 8.5 Nd-doped melts are plotted against their ambient glass spectra to identify whether the Nd-O correlations considered to be part of r_2 in the $G(r)$ are consistent. As can be seen, most of the $G(r)$ pairs in both the glass and melts are very uniform, apart from the increase in Si-O correlation length to 1.65 Å which occurs at lower P in the melt phase, at 17.5 GPa, and not until 30 GPa in the glass. The only significant correlation differences are seen in 29.3 GPa where an increase in r_1 intensity and decrease in the r_2 position is seen in the glass relative to the melt. Obviously differences between the glass and melt spectra could be the result of structural changes between the phases, although it is unlikely that this would be seen at just one pressure. This data suggest that the glass and melt spectra are predominantly similar in structure over the P-range of this study, with the only observed difference being the lower P increase of the Si-O distance in the melt. The overall consistency between the data sets shows that most of the contributions can be considered real, but that some artefacts may arise during data processing over the same Q-range due to the varying noise levels in the data at high Q and should be considered with care in the analysis.

8.4.3 Nd-O at Low Pressure, 1-8 GPa

By comparing the doped and undoped molten data up to 8 GPa the Nd-O contribution can be seen to appear in the structure from ambient conditions

at 2.36-2.43 Å (Figure 8.4). The undoped data up to 8 GPa were fit with the same parameters as in Chapter 7 (Table 8.3) and the $CN_{\mathrm{Nd-O}}$ and $r_{\mathrm{Nd-O}}$ could be extracted by the same method as for Lu-O in Chapter 7, where the same parameters for the undoped data were fit to the doped where possible, so that the Nd-O correlation could be extracted (Figure 8.6). For the lowest P (ambient and 1 GPa) data, identical fitting parameters for Nd-O were obtained and resulted in a $CN_{\mathrm{Nd-O}}$=5.8 and $r_{\mathrm{Nd-O}}$=2.38 Å. This distance is consistent with the calculated 6-coordinated Lu-O in AnD (Chapter 7), where $r_{\mathrm{Lu-O}}$=2.29 Å. The increase in Nd-O bond distance compared to Lu-O by 0.1 Å is expected, due to the larger atomic radii of Nd (1.12 Å) compared to Lu (1.001 Å) [175]. This coordination is also similar to $CN_{\mathrm{Lu-O}}$=6 in Chapter 7, showing that both REE adopt the same coordination in basaltic-like melts at low pressure. Although this distance is greater than would be predicted by tabulated ionic crystal radii of 2.33 Å for 6-fold Nd^{3+} coordination [175], this would be expected in the molten phase due to thermal vibrations and the less rigid structure, and is the same difference from tabulated radii as observed for Lu. Molecular dynamic modelling of Nd in ambient pressure silicate glasses obtained $CN_{\mathrm{Nd-O}}$=5.5-5.7 and $r_{\mathrm{Nd-O}}$=2.32 Å similar to the results presented here [183]. EXAFS measurements on Nd within phosphate glasses [184], where $CN_{\mathrm{Nd-O}}$=6.4 and $r_{\mathrm{Nd-O}}$=2.37 Å, are also very consistent. In Figure 8.6 (right), it can be seen that in some cases the required Ca-O correlation fit differed between the doped and undoped samples. This is due to the overlapping Ca-O and O-O correlations that mean the Ca-O contribution cannot be resolved explicitly enough to refine a true bond distance. The difference in the $r_{\mathrm{Ca-O}}$ required between some of the doped and undoped data is 0.05 Å and is given as the error on the fits in Table 8.3. If the undoped correlation position is used for the doped spectra, fitting a $CN_{\mathrm{Nd-O}}$ >10 is required which seems unreasonable; therefore the extracted fit parameters are still considered reliable estimates within error.

As can be seen in Figure 8.7 and from the parameters in Table 8.3, at 2 GPa there is an increase to $CN_{\mathrm{Nd-O}}$=8.2(3) and $r_{\mathrm{Nd-O}}$=2.45 Å. The undoped sample fitting parameters remain as expected over this range, strongly indicating that there is a change in Nd-O environment. The average coordination appears to abruptly increase with only slight compression above 1 GPa. This is accompanied by a slight increase in bond length but due to the underlying Ca-O correlation this is not precisely resolvable and the large error means this distance could be anywhere between 2.4-2.5 Å. The Nd-doped melt data collected at 5.5 GPa could not be fit with anything less than 10-fold coordination. This seems unexpectedly

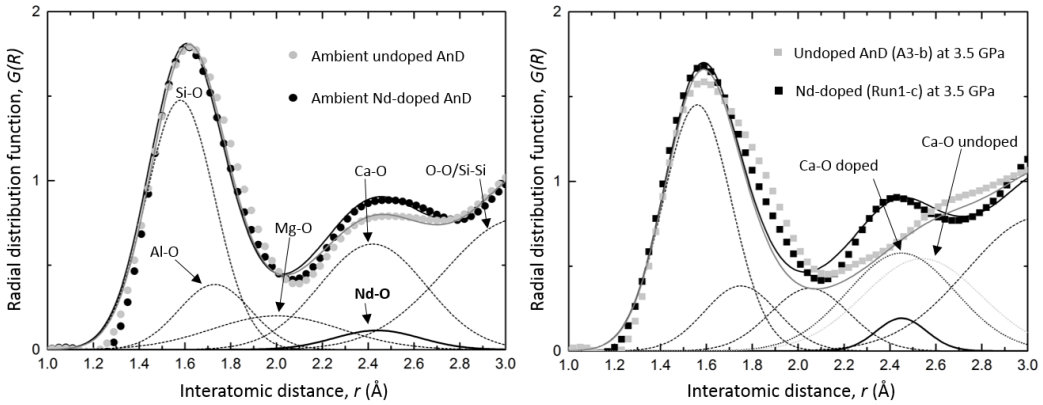

Figure 8.6 *Left: Ambient Nd-doped and undoped spectra with fits (solid lines). Individual ion-ion correlations, $g(r)_{\mathrm{ind}}$, used to make the fits are labelled and the same correlations are used in the doped spectra with the addition of Nd-O. Right: Fitting of high temperature and pressure data at 3.5 GPa and the correlations (same labels as ambient). The error in the Ca-O correlation between the doped and undoped data is highlighted and the higher r Nd-O correlation can be seen.*

high and is not consistent with the other pressures and is put down to spline normalisation errors in the data processing, as the oscillations at $Q > 8\,\mathrm{Å}^{-1}$ seem unusually intense. No further CN or distance change occurs up to 8 GPa within the resolution of this technique.

8.4.4 Nd-O at High Pressure, 8-60 GPa

Above 8 GPa the $CN_{\mathrm{Nd-O}}$ remains at 8.2(4) with possibly a slight increase to $r_{\mathrm{Nd-O}}$=2.45 Å from 17.5 GPa and above. The predicted high pressure increase of $CN_{\mathrm{Ca-O}}$ to 10-fold was taken from [20, 185] and fit well with the undoped spectra over the P_3 range; however, the coincident decrease of $r_{\mathrm{Ca-O}}$ to 2.3 Å was not observed and could not be fit to the undoped data of this range. Here, the $r_{\mathrm{Ca-O}}$ has to increase to 2.5 Å to allow any realistic fitting of the undoped spectra. Above 29.3 GPa, however, resolving the Ca-O and broadened O-O contribution becomes increasingly difficult, and both correlations were used to fit one broad correlation to the r_2 contribution in the undoped data. Therefore, the specific parameters obtained for Ca-O and O-O in this range may not be accurate for their individual correlations. This should not impact on the Nd-O correlation

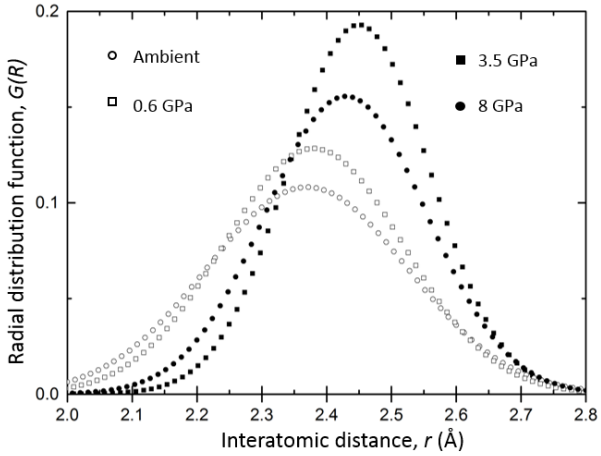

Figure 8.7 *Individual $g(r)_{\mathrm{Nd-O}}$ correlations to highlight increase in bond distance and coordination (increased total area of peak). At <1 GPa (open symbols), correlations are less intense and at lower r, with increasing r and intensity at >2 GPa (close symbols). The difference in intensities between data of the same coordination number is due to the density differences between the samples.*

methodology as the contribution of the Nd-O correlation on the $G(r)$ is still fit separately, minus the undoped correlation parameters. The $CN_{\mathrm{Si-O}}$ and $r_{\mathrm{Si-O}}$ were fit accordingly with their expected increased bond distance and coordination number of 1.68 Å and 6, as well as the known $CN_{\mathrm{Al-O}}$ change from 4.3 to 5.2 (Chapter 5). Up to 29.3 GPa, the $CN_{\mathrm{Nd-O}}$=8.2 and $r_{\mathrm{Nd-O}}$=2.45 Å are consistent with the observations from the P_2 range; but for data above 35 GPa it was not possible to identify the individual Nd-O contribution successfully. This was due to the increase in the r_2 correlation in the undoped samples due to the O-O interactions. No distinct shift in r_2 position was observed from 29.3 GPa and 35.7 GPa, so it could be assumed that no major change had occurred to $CN_{\mathrm{Nd-O}}$ and $r_{\mathrm{Nd-O}}$; however it is unresolvable due to the low signal intensity of the data at these pressures and therefore broadening of the $G(r)$ peaks. If data could be collected to a higher Q-range, or from a larger sample volume, it should be possible to trace the Nd-O contribution to higher pressures.

8.5 Discussion

This study follows on the results of Chapter 7 on the incorporation of Lu within basaltic-like melts at high pressure and the same assumptions on Henry's law

behaviour are made for the concentrations of Nd in this study (<3800 ppm). The results presented show an increase in Nd-O coordination from 5.8 to 8.2 above 1 GPa in the AnD melt structure. The $CN_{\mathrm{Nd-O}}$ of 5.8(3) at <1 GPa is consistent with $CN_{\mathrm{Lu-O}}$=6 at the same pressures, although an increase in coordination number appears to occur at considerably lower P for Nd than for Lu, as for the same composition $CN_{\mathrm{Lu-O}}$ increased from 6 to 8 between 4-5 GPa. As for Lu, it is most likely at ambient and very low P that Nd is free to accommodate anywhere within the open depolymerised network, and is not forced to occupy ring or cage structures due to the low silica content of the AnD. Nd therefore preferentially adopts the lower CN as the structure is more open and flexible and requires bonding to only non-bridging oxygens. For Lu, it was proposed that at 4-5 GPa, after significant compression of the network, the increased network connectivity forced the Lu on to 'crystal-like' sites of higher CN. As the atomic radii of Nd is significantly larger than that of Lu (1.12 to 1.002 Å), this transition may be forced to occur at lower P for Nd as it can only accommodate in the largest voids in the melt structure that immediately reduce in number on compression. During compression, the large atomic radii of Nd could prevent the collapse of certain voids but the number of nearest-neighbour oxygens surrounding the site will increase as the network is rapidly compressed between 0-5 GPa. As discussed in Chapter 7, the density increase is most rapid over this low P range, and perhaps it is only the smaller radii of Lu that allows it to accommodate more freely on other lower CN sites within the network before being forced to adopt 8-fold CN. This difference between the structural incorporation with P of a HREE (Lu) and LREE (Nd) suggests that the incorporation of REE in silicate liquids cannot be considered uniform for all REE despite their similar ionic charge, and presents the question of how the different REE will behave and where the division in behaviour arises. As Lu and Nd represent near end members of the light and heavy REE, perhaps the majority of HREE from Eu to Lu will incorporate as Lu, and the LREE as Nd. Particularly in systems where there are no crystal lattice site changes with P, there could be a gradual trend in partitioning with P within the REE series entirely due to the melt composition. Further structural data on the incorporation with P on a variety of REE would be required to monitor this.

8.5.1 Implications for Partitioning

At ambient pressures the LREE are known to only be compatible in minerals with large 8-fold regular lattice sites available, such as garnet, when a basaltic

melt is present [45]. In minerals with smaller cation sites large REE are usually incompatible unless the melt is highly polymerised. At high P it appears that the basaltic melt network becomes increasingly favourable to REE incorporation as the melt network generates garnet-like 8-fold sites. For Lu, when this increase in coordination in the melt site was observed, a coincident decrease in partition coefficient is also witnessed between basaltic melts and major minerals. It was suggested in Chapter 7 that the decrease in compatibility, so that Lu incorporates equally in the melt and mineral, was due to the presence of the crystal-like sites in the liquid leaving no distinct preference for either phase. Due to the large radii of Nd it is generally incompatible in most mineral phases and prefers to incorporate in the melt [55]; this could be due to the low pressure structural changes within the melt that allow it to be accommodated on the 'crystal-like' sites in the melt network from between 1-2 GPa. As garnet is not stable at low P in the mantle it is difficult to interpret whether Nd would be more compatible at very low P.

There appears to be no distinct change in partition coefficients for Nd between garnet and basaltic melts (Figure 2.6) from 3-10 GPa [69, 73, 74], unlike for Lu where a distinct decrease was observed over this range. This possibly confirms that any structural changes occurring within Nd-doped melts are at lower P, particularly as a distinct decrease in partitioning is observed for Nd between clinopyroxene and basaltic melts between 0-3 GPa [73, 75], where partitioning drops from 0.7 to 0.05, a greater decrease than for any other REE discussed here (Y, Sm, Lu). The observed partitioning behaviour for REE, of increasing compatibility in minerals with decreasing ionic radii, can be explained by a difference in structural behaviour of the melt phase and not only the elasticity of the crystal lattice. Previously, this trend has always been attributed to the difficulty of accommodating the LREE with large atomic radii within the crystal lattice. However this study suggests that the structure of the melt could also strongly influence this behaviour. As the incorporation of REE in silicate melt structures appears to differ with P, there may be greater influence of the melt on partitioning trends and behaviour at depth than previously expected.

8.6 Conclusion

The structural incorporation of Nd in anorthite-diopside melts at high pressure is different to the heavy REE Lu. Neodymium proved to be an excellent coupler for laser heating DAC experiments producing homogeneous melting throughout

the sample and little damage to the diamond anvils. Nd-doped AnD melts were studied using x-ray diffraction techniques in both laser-heated DAC and PEP experiments up to 35 GPa. $CN_{\mathrm{Nd-O}}$ increases from 5.8 to 8.2 between 1-2 GPa, at much lower pressure than for Lu where $CN_{\mathrm{Lu-O}}$ increased from 6 to 8 at 4-5 GPa. The increase in coordination for Nd-O is also not coincident with a distinctive increase in bond length as clearly observed for Lu-O, where $r_{\mathrm{Nd-O}}$ ranges from 2.36-2.45 Å, compared to Lu-O where $r_{\mathrm{Lu-O}}$ increased from 2.29 to 2.42 Å. The shorter distance of the Lu-O bond means it is more easily resolvable in this composition than the Nd-O due to less overlap with the Ca-O contribution. This highlights the limitations in using x-ray diffraction to monitor REE incorporation, as only elements with bond lengths distinct from other major element correlations can be resolved using current techniques.

The results show that the incorporation of REE within silicate melts is distinctly different and that the size of the REE affects the sites it can accommodate on within the silicate melt network. If it is assumed that all LREE behave in a more similar way to Nd than Lu, the partitioning of Sm/Nd will not be strongly affected by this change as the ratio will be maintained across the P-range of the mantle. The distinct partitioning trend of REE with increasing atomic radii (increasing compatibility with decreasing radii), could be the result of the changes within the silicate melt network rather than purely elasticity of the crystal site as presumed in current models. As with Chapter 7, these results highlight the importance of collecting structural data on trace element incorporation within silicate melts and that the effect of the melt cannot be considered negligible in partitioning models.

The current methodology appears to be applicable on molten AnD up to 35 GPa, although above this the signal intensity from such thin samples becomes too low and only glass measurements can successfully resolve the structure. With developments in high pressure techniques with larger sample volumes at high pressure, and brighter synchrotron sources, it may be possible in the future to resolve REE incorporation at P >35 GPa. Apart from the previously observed onset of Si-O coordination change at lower P within basaltic melt structures [14], glass measurements at corresponding pressures to the AnD melt studied here appear structurally identical over this P-range up to 35 GPa. This would suggest that x-ray diffraction measurements performed on REE doped quenched glasses would have increased signal intensity and could provide good analogues of the melt phase.

Chapter 9

Conclusions and Future Work

In this thesis the structure of two end-member melt compositions have been investigated at high pressure and temperature: a highly polymerised haplogranite melt up to 8 GPa, and a less polymerised anorthite-diopside composition to 60 GPa. The structure of the granitic melts when doped with trace elements Br, Y, Zr, and Lu has been studied, including any local environment changes around the trace elements with pressure and temperature. The incorporation of Lu within both end member compositions has been studied to identify the different bonding environments of REE within both highly polymerised and less polymerised melts. The bonding environment of Nd has also been studied within the less polymerised AnD melt for comparison between the incorporation mechanisms of varying REE.

Novel experimental techniques have been implemented throughout the work presented in this thesis. Results in Chapter 6 present the first studies to use the boron-epoxy 'window' cell design for x-ray absorption studies in the Paris-Edinburgh press. These cells were successfully used to increase transmission from the low scattering samples. New Pt wire resistive heaters suitable for DAC experiments have been developed and successfully used to access T >900 K within the sample chamber. The Pt wire heaters have been calibrated and produce consistent temperature measurements and power curves between different heaters. The limitation of this design is the maximum achievable temperature of <1000 K, although this could potentially be improved with more precise coiling. For YAG laser heating DAC experiments, neodymium was trialled as a laser coupler with favourable results. At low concentrations (<1 at.%) Nd was able to act as a laser coupler without causing extensive damage to the diamond anvils.

The haplogranite melts studied in Chapters 5, 6 and 7 are structurally identical to those of their corresponding glass up to 8 GPa in both the doped and undoped studies. This would suggest that quenched haplogranitic or granitic glasses from high $P - T$ could be used as successful analogues for studies on the molten structure. However, for density studies data must be collected on molten samples due to the high compressibility of granitic melts compared to their glass up to 5 GPa as observed in Chapter 5. Within the haplogranite structure, Y and Zr were investigated using x-ray absorption spectroscopy at high pressure and temperature. Up to 8 GPa the local environment of Y and Zr in the melt structure remains consistent. Both Y and Zr are found in high, 8-fold coordination with oxygen at bond distances of 2.37 and 2.22 Å respectively, and no evidence for complexation with water was observed. The Y and Zr environment within the glass of the same composition is identical to that of the melt; however, in the dry haplogranite the Zr local environment appears to become more irregular.

The first x-ray diffraction measurements on trace elements *in situ* within silicate melt structures have been presented. The results of Chapters 7 and 8 indicate that x-ray diffraction techniques can be used to study trace element incorporation in liquids and can reliably determine nearest-neighbour bond distances for minor elements. The results show that between a less polymerised to highly polymerised melt there is a significant change in Lu coordination, from 6 to 8, coincident with an increase in bond length of 0.07 Å from $r_{\mathrm{Lu-O}}$=2.29 to 2.36 Å. This coordination change can explain why large REE prefer to incorporate in crystalline structures when partitioning between minerals and highly polymerised melts, as there are less available sites for accommodating large REE in highly interconnected networks. An abrupt coordination increase for Lu-O from 6 to 8 was also observed at 4-5 GPa within the less polymerised system, indicating that pressure has a substantial effect on REE incorporation within less polymerised silicate melts. This is corroborated by the results presented on Nd-O coordination within the same composition, where an increase from 6 to 8-coordinated Nd is observed between 1-2 GPa in the AnD melt. The difference in behaviour between the incorporation of REE in highly polymerised (HPG) and less polymerised (AnD) systems is most likely due to the nature of the silicate network. In the HPG the high silica content produces a strongly interconnected network, as found in silica glass, with different sized cages. The large radii REE can only be accommodated within the largest void structures, and upon compression may prevent these sites from collapsing. Within the AnD melt network, the higher concentration of cations prevents a polymerised network forming at low P; therefore the REE

may be accommodated in multiple sites within the network. Upon compression, the cations and silica tetrahedra are packed closer together but do not form rings or cages as in the HPG network. Instead, 'crystal-like' sites are generated where REE can incorporate in a similar configuration to minerals such as garnet.

Although results presented in this thesis indicate the potential for determining the incorporation of rare Earth and other trace elements in silicate melts, there are limitations in the methodologies presented. Currently, reasonably high concentrations (4 wt.% oxide) of the trace elements are required to generate a large enough signal. This could result in the interaction of these elements within the sample or alterations to the structure due to the incorporation of these elements that may not occur at natural (ppm) concentrations. With increasing brightness of synchrotrons and improved flux, it may be possible in the future to carry out these measurements at more realistic concentrations. The other main limitation arises from the overlapping contributions within the $G(r)$. In this study the REE-O bond distances were resolvable as they occur at a distance distinctly different to most other ion-ion interactions in the silicates studied. For smaller radii cations such as Hf, the bond distance prevents a distinct peak being resolved as it overlaps with the main Si-O and Al-O contributions. If natural samples were used, that contain elements such as Fe, this would also prevent the resolution on the REE-O bonding environments required for this study. In order to study more natural compositions, partial structure factors could be obtained using isotopic substitution and neutron diffraction.

X-ray absorption and diffraction measurements are useful to corroborate results on similar elements, although in complicated molten samples, absorption spectroscopy is limited due to the high number of multiple scattering interactions which are difficult to model. X-ray diffraction is advantageous over EXAFS in this study as it provides the bonding environments of the entire sample, but with both techniques, data processing can introduce artefacts that misrepresent the structure. For x-ray diffraction it is critical that a high Q-range and excellent background is collected. With higher energy the Q-range can be increased, and this will decrease the artefacts that arise from the current limits on the Fourier transform. Currently, at high energy the signal:background ratio is too high to obtain a useful scattering signal from the sample. As synchrotron sources are developed with higher flux it will be possible to use higher energy x-rays and, therefore, access higher Q to study low scattering samples. Paris-Edinburgh press experiments using energy dispersive diffraction were particularly

successful at providing high Q-range and good signal intensity in this study and are only limited by the $P-T$ conditions that are accessible. As new experimental techniques are developed it will be possible to increase the sample volumes that can be used at high $P-T$. A larger volume provides a greater signal intensity, and the current small ($<100\mu m$) sample size required for high P DAC measurements is the reason why results on the molten state in Chapter 8 are limited in P to <30 GPa. Zhai and Ito [186] have developed sintered diamond anvils for multi-anvil experiments that can reach pressures of up to 90 GPa. These would be ideal for providing a much greater signal intensity from a larger sample volume at high pressure, compared to DAC experiments, and more accurate temperature measurements than laser heated diamond anvil cells. As high pressure-temperature techniques develop, x-ray diffraction structural measurements on trace element incorporation in melts at natural levels of concentration should be achievable, if the elements have high enough scattering (i.e. Z>52). In the future, in order to better constrain the behaviour of a wider variety of trace elements with pressure at different bond distances, a larger Q-range would be required to enable greater resolution between correlations in the $G(r)$. This could be achieved with higher energy x-rays as discussed, and would need to be combined with larger sample volumes or greater flux of x-rays so that signal intensity from the sample is not comprised.

The results presented in this thesis indicate clearly that important structural changes occur within silicate melts, even for minor elements, and that changes within the melt structure can explain variations in existing partitioning data with pressure. For different REE there is a substantial change in the structural incorporation within less polymerised melts similar to basaltic magmas, indicating that the behaviour of different sized REE cations cannot only be attributed to changes in the crystal lattice during partitioning. The data presented here are in agreement with existing partitioning data for the REE series, where HREE (such as Lu) are more compatible in minerals than the LREE at $P<5$ GPa. On the basis of this thesis, further work should be carried out on other REE within the lanthanide series to establish whether the change in local environment with pressure is element dependent, or if a gradual trend with decreasing atomic radii is present.

Based on the difference in behaviour between Nd and Lu in the AnD composition in this study, if structural changes within the melt impact partitioning of Lu and Nd at different pressures, the partitioning behaviour of these elements is

expected to be different with increasing P. At P >4-5 GPa, partitioning between Lu and Hf may become similar if Lu becomes more incompatible at depth in certain minerals. For Nd, as the change occurs at much lower P between 1-2 GPa, Nd may remain incompatible over the range of melt formation. The results presented in this thesis provide clear evidence that melt structural changes influence the local environment of trace elements and these local changes need to be taken into account in future geochemical models. It is clear that individual partitioning measurements, not only for different minerals with pressure but also melt compositions, is required at the $P-T$ conditions of interest, and attempting to predict partitioning behaviour at depth without experimental data for the mineral-melt system of interest at high $P-T$ is likely to be unsuccessful.

From the work undertaken in this thesis, it is clear that existing partitioning data cannot be extrapolated beyond the pressure and temperature conditions of the experiments due to changes in the melt structure and trace element environments. This implies that studies need to be focused on constraining and understanding the trace element sites within melt structures and not just the crystal lattice sites of minerals present during partial melting. Current understanding of large-scale melting processes, that are interpreted using partitioning studies, are therefore limited by the current pressure and temperature range of existing partitioning data. In order to understand processes such as magma ocean crystallisation, melting during the moon-forming impact, and early crustal formation, partitioning experiments and structural studies on melts under the conditions relevant to these processes must be undertaken.

Appendix One

Data tables for all the $P-T$ points collected at various beamlines and the reasons for not including the data in the main text of this thesis. Data was collected over the course of many different experiments, and for three of the main experiments that were undertaken during the course of this work, some data could not be analysed. The reasons for not including some data are listed in the following tables for the experiments:

1) Haplogranite and Lu-doped haplogranitic collected in resistive heated DAC experiments on I-15 at the Diamond Light Source in October 2013 (Table 9.1).

2) Anorthite-diopside laser heated DAC experiments on GSECARS at the Advanced Photon Source in February 2015 (Table 9.2).

3) Anorthite-diopside Paris-Edinburgh press experiments at HP-CAT at the Advanced Photon Source in February 2016 (Table 9.3).

Exp. no.	Thesis no.	Comp.	P (GPa)	T (K)	In results?	Reason if not included
Cell 1	D4	HPG + Lu	3.8 (2)	973 (40)	YES Chap. 7	na
Cell 2	D5	HPG + Lu	5.8 (4)	1073 (40)	YES Chap. 7	na
Cell 3	C4	HPG	2.3 (3)	290	YES Chap. 5,7	na
Cell 4	C3	HPG	1.6 (5)	290	YES Chap. 5	na
Cell 5	-	HPG + Lu	1.5 (3)	290	NO	image plate poor
Cell 6	C10	HPG	5.1 (6)	290	YES Chap. 5	na
Cell 7	C2	HPG	1.4 (2)	290	YES Chap. 5,7	na
Cell 8	C7	HPG	3.5 (5)	290	YES Chap. 5	na
Cell 9	-	test	na	na	NO	test cell
Cell 10	-	-	-	-	NO	incorrect sample loading
Cell 11	-	-	-	-	NO	sample contaminated
Cell 12	-	-	-	-	NO	sample contaminated
Cell 13	-	HPG	na	290	NO	no pressure calibrant
Cell 14	-	HPG	na	290	NO	no pressure calibrant
Cell 15	C9	HPG	4.0 (5)	950 (50)	Yes Chap. 5	na
Cell 16	-	HPG	na	290	NO	image plate not symmetric
Cell 17	-	HPG	na	290	NO	not enough Q-range collected
Cell 18	D1	HPG + Lu	0.5 (2)	910 (50)	YES Chap. 7	na
Cell 19	D2	HPG + Lu	2.1 (3)	900 (50)	YES Chap. 7	na
Cell 20	D3	HPG + Lu	2.5 (3)	290	YES Chap. 7	na
Cell 21	C8	HPG	4.1 (3)	950 (50)	YES Chap. 5,7	na
Cell 22	C12	HPG	11.8 (5)	290	YES Chap. 5	na
Cell 23	-	HPG + Lu	2.5 (3)	290	NO	low signal intensity

Table 9.1 *Complete list of experimental runs from Diamond Light Source in October 2013.*

Exp. no.	Thesis no.	Comp.	P (GPa)	Melt	In results?	Reason if not included
Cell 1	N2	AnD + Nd	6 (2)	Y	YES Chap. 8	na
Cell 1b	-	AnD + Nd	9.0 (3)	na	NO	no appropriate background
Cell 2	N1	AnD + Nd	2.1 (3)	Y	YES Chap. 8	na
Cell 2b	-	AnD + Nd	7.4 (3)	na	NO	no appropriate background
Cell 2c	N4	AnD + Nd	12.0 (3)	Y	YES Chap. 8	na
Cell 3	-	AnD + Nd	11.0 (4)	na	NO	poor Q-range
Cell 4	-	AnD + Nd	20.8 (6)	na	NO	Too many qtz peaks in spectra
Cell 5	GLASS	AnD + Nd	1-60	na	YES Chap. 8	na
Cell 6	N3	AnD + Nd	8.2 (3)	Y	YES Chap. 8	na
Cell 6b	-	AnD + Nd	15.8 (7)	na	NO	Identical to Cell 7 (N5)
Cell 7	N5	AnD + Nd	17.5 (5)	Y	YES Chap. 8	na
Cell 7b	-	AnD + Nd	26.1 (5)	na	NO	Unable to normalise correctly
Cell 7c	N7	AnD + Nd	35.7 (5)	Y	YES Chap. 8	na
Cell 8	-	AnD + Nd	26.1 (5)	na	NO	Rings in diffraction pattern
Cell 8b	N6	AnD + Nd	29.3 (9)	Y	YES Chap. 8	na
Cell 9	N8	AnD + Nd	44.9 (2.0)	N	YES Chap. 8	na
Cell 10	N9	AnD + Nd	60 (3.0)	N	YES Chap. 8	na
Cell 11	GLASS	AnD	1-60	na	YES Chap. 8	na

Table 9.2 *Complete list of experimental runs from GSECARS at the Advanced Photon Source in February 2015.*

Exp. no.	Thesis no.	Comp.	P (GPa)	T (K)	In results?	Reason if not included
Cell 1	P1	AnD + Nd	0.6 (3)	1570 (50)	YES Chap. 8	na
	-	AnD + Nd	2.1 (3)	1400 (50)	NO	Too many peaks in spectra
	P2	AnD + Nd	3.5 (3)	1820 (50)	YES Chap. 8	na
	-	AnD + Nd	4.5 (4)	1550 (50)	NO	Too many peaks in spectra
	P3	AnD + Nd	5.5 (3)	1850 (50)	YES Chap. 8	na
Cell 2	A1-b	AnD	0.8 (3)	1570 (50)	YES Chap. 7,8	na
	A2-b	AnD	2.4 (2)	1670 (50)	YES Chap. 7,8	na
	A3-b	AnD	3.5 (3)	1720 (50)	YES Chap. 7,8	na
	A4-b	AnD	4.8 (3)	1770 (50)	YES Chap. 7,8	na
	A5-b	AnD	6.5 (3)	1870 (50)	YES Chap. 7,8	na
Cell 3	-	AnD + Nd	4.5 (4)	1650 (50)	NO	Too many peaks in spectra
Cell 4	A7-b	AnD + Lu	0.8 (3)	1570 (50)	YES Chap. 7	na
	A9-b	AnD + Lu	3.1 (3)	1570(50)	YES Chap. 7	na
	A10-b	AnD + Lu	4.2 (3)	1750 (50)	YES Chap. 7	na
	-	AnD + Lu	5.3 (3)	1750 (50)	NO	not fully molten
Cell 5	A12-b	AnD + Lu	7.0 (3)	2120 (50)	YES Chap. 7	na
Cell 6	-	AnD + Lu	2.8 (4)	1350 (50)	YES Appendix 1	na
	-	AnD + Lu	2.8 (4)	1750 (50)	YES Appendix 1	na
Cell 7	A6-b	AnD	8.0 (4)	2070 (50)	YES Chap. 7,8	na

Table 9.3 *Complete list of experimental runs from HP-CAT data collected at the Advanced Photon Source in February 2016.*

Bibliography

[1] B. Cochain, C. Sanloup, C. de Grouchy, C. Crépisson, H. Bureau, C. Leroy, I. Kantor, and T. Irifune, "Bromine speciation in hydrous silicate melts at high pressure," *Chem. Geol.*, vol. 404, pp. 18–26, 2015.

[2] G. Caro, B. Bourdon, B. J. Wood, and A. Corgne, "Trace-element fractionation in Hadean mantle generated by melt segregation from a magma ocean.," *Nature*, vol. 436, pp. 246–9, jul 2005.

[3] M. Best, *Igneous and Metamorphic Petrology*. Blackwell Publishing Company, 2003.

[4] A. Working Group, "University of Lehigh Tectonics - Student Resources." http://www.ei.lehigh.edu/learners/tectonics/heatflow/heatflow2.html. Accessed: May 2016.

[5] D. Bercovici and S.-i. Karato, "Whole–mantle convection and the transition–zone water filter," *Nature*, vol. 425, pp. 39–44, 2003.

[6] J. Revenaugh and S. Sipkin, "Seismic evidence for silicate melt atop the 410 km mantle discontinuity," *Nature*, vol. 369, pp. 474–477, 1994.

[7] J. E. Vidale and M. A. H. Hedlin, "Evidence for partial melt at the coremantle boundary north of Tonga from the strong scattering of seismic waves," *Nature*, vol. 391, pp. 682–685, 1998.

[8] G. K. Pradhan, G. Fiquet, J. Siebert, A.-L. Auzende, G. Morard, D. Antonangeli, and G. Garbarino, "Melting of MORB at core-mantle boundary," *Earth Planet. Sci. Lett.*, vol. 431, pp. 247–255, 2015.

[9] P. H. Warren, "The magma ocean concept and lunar evolution," *Ann. Rev. Earth Planet. Sci*, vol. 13, pp. 201–240, 1985.

[10] L. Elkins-Tanton, "Magma Oceans in the Inner Solar System," *Ann. Rev. of Earth and Planet. Science*, vol. 40, pp. 113–139, 2012.

[11] J. Loveday, *High Pressure Physics*. Taylor & Francis, 2012.

[12] S. Tateno, K. Hirose, Y. Ohishi, and Y. Tatsumi, "The structure of iron in Earth's inner core," *Science*, vol. 330, pp. 359–362, 2010.

[13] N. Funamori, S. Yamamoto, T. Yagi, and T. Kikegawa, "Exploratory studies of silicate melt structure at high pressures and temperatures by in situ x-ray diffraction," *J. Geophys. Res.*, vol. 109, p. B03203, 2004.

[14] C. Sanloup, J. Drewitt, Z. Konôpková, P. Dalladay-simpson, D. M. Morton, N. Rai, W. van Westrenen, and W. Morgenroth, "Structural change in molten basalt at deep mantle conditions," *Nature*, vol. 503, pp. 104–107, 2013.

[15] P. D. Asimow and T. J. Ahrens, "Shock compression of liquid silicates to 125 GPa: The anorthite-diopside join," *J. Geophys. Res. Solid Earth*, vol. 115, no. 10, p. B10209, 2010.

[16] T. Sato and N. Funamori, "High-pressure structural transformation of SiO_2 glass up to 100 GPa," *Phys. Rev. B*, vol. 82, p. 184102, 2010.

[17] C. J. Benmore, E. Soignard, S. A. Amin, M. Guthrie, S. D. Shastri, P. L. Lee, and J. L. Yarger, "Structural and topological changes in silica glass at pressure," *Phys. Rev. B*, vol. 81, p. 054105, 2010.

[18] C. J. Benmore, "A review of high-energy x-ray diffraction from glasses and liquids," *ISRN Mater. Sci.*, pp. 1–19, 2012.

[19] C. Sanloup, J. Drewitt, C. Crépisson, Y. Kono, C. Park, C. McCammon, L. Hennet, S. Brassamin, and A. Bytchkov, "Structure and density of molten fayalite at high pressure," *Geochim. Cosmochim. Acta*, vol. 118, pp. 118–128, 2013.

[20] J. W. E. Drewitt, S. Jahn, C. Sanloup, C. de Grouchy, G. Garbarino, and L. Hennet, "Development of chemical and topological structure in aluminosilicate liquids and glasses at high pressure," *J. Phys. Condens. Matter*, vol. 27, no. 10, p. 105103, 2015.

[21] W. McIntire, "Trace element partition coefficients–a review of theory and applications to geology," *Geochim. Cosmochim. Acta*, vol. 27, pp. 1209–1264, 1963.

[22] F. A. Frey, "Trace element geochemistry: Applications to the igneous petrogenesis of terrestrial rocks," *Rev. Geophys. Sp. Phys.*, vol. 17, no. 4, pp. 803–823, 1979.

[23] F. Albarède, J. Blichert-toft, J. D. Vervoort, J. D. Gleason, and M. Rosing, "Hf-Nd isotope evidence for a transient dynamic regime in the early terrestrial mantle," *Nature*, vol. 404, no. March, pp. 30–32, 2000.

[24] G. Caro, B. Bourdon, A. N. Halliday, and G. Quitté, "Super-chondritic Sm/Nd ratios in Mars, the Earth and the Moon.," *Nature*, vol. 452, pp. 336–339, 2008.

[25] M. Boyet and R. W. Carlson, "A new geochemical model for the Earth's mantle inferred from ^{146}Sm–^{142}Nd systematics," *Earth Planet. Sci. Lett.*, vol. 250, pp. 254–268, 2006.

[26] I. Campbell and H. O'Neill, "Evidence against a chondritic Earth," *Nature*, vol. 483, pp. 553–558, 2012.

[27] J. Blichert-Toft and F. Albarède, "The Lu-Hf isotope geochemistry of chondrites and the evolution of the mantle-crust system," *Earth Planet. Sci. Lett.*, vol. 148, pp. 243–258, 1997.

[28] M. Bizzarro, J. a. Baker, H. Haack, D. Ulfbeck, and M. Rosing, "Early history of Earth's crust-mantle system inferred from hafnium isotopes in chondrites," *Nature*, vol. 421, pp. 931–3, 2003.

[29] T. M. Harrison, A. K. Schmitt, M. T. McCulloch, and O. M. Lovera, "Early (4.5 Ga) formation of terrestrial crust: LuHf , δ^{18}O, and Ti thermometry results for Hadean zircons," *Earth Planet. Sci. Lett.*, vol. 268, pp. 476–486, 2008.

[30] M. Guitreau, J. Blichert-toft, H. Martin, S. J. Mojzsis, and F. Albarède, "Hafnium isotope evidence from Archean granitic rocks for deep-mantle origin of continental crust," *Earth Planet. Sci. Lett.*, vol. 337-338, pp. 211–223, 2012.

[31] E. Watson, "Two–liquid partition coefficients–Experimental data and geochemical implications," *Contrib. Mineral. Petrol.*, vol. 56, pp. 119–134, 1976.

[32] F. Ryerson and P. Hess, "Implications of liquid-liquid distribution coefficients to mineral-liquid partitioning," *Geochim. Cosmochim. Acta*, vol. 42, pp. 921–932, 1978.

[33] S. Prowatke and S. Klemme, "Effect of melt composition on the partitioning of trace elements between titanite and silicate melt," *Geochim. Cosmochim. Acta*, vol. 69, pp. 695–709, 2005.

[34] M. W. Schmidt, J. a. D. Connolly, D. Günther, and M. Bogaerts, "Element partitioning: the role of melt structure and composition.," *Science*, vol. 312, pp. 1646–50, 2006.

[35] G. D. Bromiley and S. T. Redfern, "The role of TiO_2 phases during melting of subduction-modified crust: Implications for deep mantle melting," *Earth Planet. Sci. Lett.*, vol. 267, pp. 301–308, 2008.

[36] T. Evans, H. O'Neill, and J. Tuff, "The influence of melt composition on the partitioning of REEs, Y, Sc, Zr and Al between forsterite and melt in the system CMAS," *Geochim. Cosmochim. Acta*, vol. 72, pp. 5708–5721, 2008.

[37] T. Imai, E. Takahashi, T. Suzuki, and T. Hirata, "Element partitioning between olivine and melt up to 10 GPa: Implications for the effect of pressure," *Phys. Earth Planet. Inter.*, vol. 212-213, pp. 64–75, 2012.

[38] J. Yarger, K. Smith, R. Nieman, J. Diefenbacher, G. Wolf, B. Poe, and P. McMillan, "Al coordination changes in high-pressure aluminosilicate liquids," *Science*, vol. 270, pp. 1964–1967, 1995.

[39] C. Ponader and G. Brown, "Rare earth elements in silicate glass/melt systems: I. Effects of composition on the coordination environments of La, Gd, and Yb," *Geochim. Cosmochim. Acta*, vol. 53, pp. 2893–2903, 1989.

[40] F. Farges, "Structural environment around Th^{4+} in silicate glasses: Implications for the geochemistry of incompatible Me^{4+} elements," *Geochim. Cosmochim. Acta*, vol. 55, pp. 3303–3319, 1991.

[41] S. Simon, M. Wilke, R. Chernikov, S. Klemme, and L. Hennet, "The influence of composition on the local structure around yttrium in quenched silicate melts - Insights from EXAFS," *Chem. Geol.*, vol. 346, pp. 3–13, 2013.

[42] G. S. Henderson, G. Calas, and J. F. Stebbins, "The structure of silicate glasses and melts," *Elements*, vol. 2, pp. 269–273, 2006.

[43] C. Sanloup, "Density of magmas at depth," *Chem. Geol.*, vol. 429, pp. 51–59, 2016.

[44] J. Stebbins, P. McMillan, and D. Dingwell, *Structure, Dynamics and Properties of Silicate Melts*. Mineralogical Society of America, reviews in mineralogy ed., 1995.

[45] W. Nesse, *Introduction to Mineralogy*. Oxford University Press, 2000.

[46] S. Kohara, J. Akola, H. Morita, K. Suzuya, J. K. R. Weber, M. C. Wilding, and C. J. Benmore, "Relationship between topological order and glass forming ability in densely packed enstatite and forsterite composition glasses," *Proc. Natl. Acad. Sci.*, vol. 108, no. 36, pp. 14780–14785, 2011.

[47] P. Y. Huang, S. Kurasch, A. Srivastava, V. Skakalova, J. Kotakoski, A. V. Krasheninnikov, R. Hovden, Q. Mao, J. C. Meyer, J. Smet, D. A. Muller, and U. Kaiser, "Direct imaging of a two-dimensional silica glass on graphene," *Nano Lett.*, vol. 12, pp. 1081–1086, 2012.

[48] B. O. Mysen, "The structure of silicate melts," *Annu. Rev. Earth Planet. Sci.*, vol. 11, pp. 75–97, 1983.

[49] R. Vuilleumier, N. Sator, and B. Guillot, "Computer modeling of natural silicate melts: What can we learn from ab initio simulations," *Geochim. Cosmochim. Acta*, vol. 73, pp. 6313–6339, 2009.

[50] S. R. Elliott, "Origin of the first sharp diffraction peak in the structure factor of covalent glasses and liquids," *J. Phys. Condens. Matter*, vol. 4, pp. 7661–7678, 1992.

[51] P. S. Salmon, "Real space manifestation of the first sharp diffraction peak in the structure factor of liquid and glassy materials," *Proc. Math. Phys. Sci.*, vol. 445, no. 1924, pp. 351–365, 1994.

[52] J. H. Lee and S. R. Elliott, "Simulation evidence for the origin of the first sharp diffraction peak," *J. Non. Cryst. Solids*, vol. 192-193, pp. 133–136, 1995.

[53] P. S. Salmon, R. A. Martin, P. E. Mason, and G. J. Cuello, "Topological versus chemical ordering in network glasses at intermediate and extended length scales.," *Nature*, vol. 435, pp. 75–78, 2005.

[54] J. Du and L. R. Corrales, "First sharp diffraction peak in silicate glasses: Structure and scattering length dependence," *Phys. Rev. B*, vol. 72, no. 9, p. 092201, 2005.

[55] W. White, *Geochemistry*. John Wiley & Sons, 2013.

[56] Y. Amelin, D.-C. Lee, A. N. Halliday, and R. T. Pidgeon, "Nature of the Earth's earliest crust from hafnium isotopes in single detrital zircons," *Nature*, vol. 399, pp. 252–255, 1999.

[57] J. D. Vervoort, P. J. Patchett, G. E. Gehrels, and a. P. Nutman, "Constraints on early Earth differentiation from hafnium and neodymium isotopes," *Nature*, vol. 379, pp. 624–627, 1996.

[58] T. M. Harrison, J. Blichert-Toft, W. Müller, F. Albarède, P. Holden, and S. J. Mojzsis, "Heterogeneous Hadean hafnium: Evidence of continental crust at 4.4 to 4.5 Ga," *Science*, vol. 310, pp. 1947–50, 2005.

[59] N. Onuma, H. Higuchi, H. Wakita, and H. Nagasawa, "Trace element partitioning between two pyroxenes and the host lava," *Earth Planet. Sci. Lett.*, vol. 5, pp. 47–51, 1968.

[60] J. Blundy and B. J. Wood, "Prediction of crystal-melt partition coefficents from elastic moduli," *Lett. to Nat.*, vol. 372, pp. 452–554, 1994.

[61] J. Brice, "Some thermodynamic aspects of the growth of strained crystals," *J. Chrystal Growth*, vol. 28, pp. 249–253, 1975.

[62] J. Blundy and B. Wood, "Crystal-chemical controls on the partitioning of Sr and Ba between plagioclase feldspar, silicate melts and hydrothermal solutions," *Geochim. Cosmochim. Acta*, vol. 55, pp. 193–209, 1991.

[63] S. R. Hart and K. E. Davis, "Nickel partitioning between olivine and silicate melt," *Earth Planet. Sci. Lett.*, vol. 40, pp. 203–219, 1978.

[64] W. van Westrenen, B. J. Wood, and J. D. Blundy, "A predictive thermodynamic model of garnet–melt trace element partitioning," *Contrib. to Mineral. Petrol.*, vol. 142, pp. 219–234, 2001.

[65] B. J. Wood and J. D. Blundy, "A predictive model for rare earth element partitioning between clinopyroxene and anhydrous silicate melt," *Contrib. to Mineral. Petrol.*, vol. 129, pp. 166–181, 1997.

[66] W. van Westrenen and D. Draper, "Quantifying garnet–melt trace element partitioning using lattice–strain theory: new crystal-chemical and thermodynamic constraints," *Contrib. to Mineral. Petrol.*, vol. 154, pp. 717–730, 2007.

[67] D. Draper and W. van Westrenen, "Quantifying garnet–melt trace element partitioning using lattice–strain theory: assessment of statistically significant controls and a new predictive model," *Contrib. to Mineral. Petrol.*, vol. 154, pp. 731–746, 2007.

[68] W. van Westrenen, J. Blundy, and B. J. Wood, "Crystal-chemical controls on trace element partitioning between garnet and anhydrous silicate melt," *Am. Mineral.*, vol. 84, pp. 838–847, 1999.

[69] D. S. Draper, D. Xirouchakis, and C. B. Agee, "Trace element partitioning between garnet and chondritic melt from 5 to 9 GPa: implications for the onset of the majorite transition in the martian mantle," *Phys. Earth Planet. Inter.*, vol. 139, pp. 149–169, 2003.

[70] T. Dunn, "Partitioning of Hf, Lu, Ti, and Mn between olivine, clinopyroxene and basaltic liquid," *Contrib. to Mineral. Petrol.*, vol. 96, pp. 476–484, 1987.

[71] D. Frei, A. Liebscher, G. Franz, B. Wunder, S. Klemme, and J. Blundy, "Trace element partitioning between orthopyroxene and anhydrous silicate melt on the lherzolite solidus from 1.1 to 3.2 GPa and 1,230 to 1,535 C in the model system Na_2O-CaO-MgO-Al2O_3-SiO_2," *Contrib. to Mineral. Petrol.*, vol. 157, pp. 473–490, 2009.

[72] T. H. Green and N. J. Pearson, "Effect of pressure on rare earth element partition coefficients in common magmas," *Nature*, vol. 305, pp. 414–416, 1983.

[73] V. J. M. Salters and J. Longhi, "Trace element partitioning during the initial stages of melting beneath mid-ocean ridges," *Earth Planet. Sci. Lett.*, vol. 166, pp. 15–30, 1999.

[74] K. T. M. Johnson, "Experimental cpx/ and garnet/melt partitioning of REE and other trace elements at high pressures: Petrogenetic implications," *Mineralogical Mag.*, vol. 58A, pp. 8–9, 1994.

[75] R. Vannucci, P. Bottazzi, E. Wulff-Pedersen, and E. R. Neumann, "Partitioning of REE, Y, Sr, Zr and Ti between clinopyroxene and silicate melts in the mantle under La Palma (Canary Islands): implications for the nature of the metasomatic agents," *Earth Planet. Sci. Let.*, vol. 158, pp. 39–51, 1998.

[76] H. Keppler and D. Rubie, "Pressure-induced coordination changes of transition-metal ions in silicate melts," *Nature*, vol. 364, pp. 54–56, 1993.

[77] B. Warren, *X-ray Diffraction*. Dover Publications inc. New York, 1969.

[78] J. H. Eggert, G. Weck, P. Loubeyre, and M. Mezouar, "Quantitative structure factor and density measurements of high-pressure fluids in diamond anvil cells by x-ray diffraction: Argon and water," *Phys. Rev. B*, vol. 65, p. 174105, 2002.

[79] F. Hajdu, "Analytic approximation for incoherent scattered x-ray intensities," *Acta Crystallogr.*, vol. A27, pp. 73–74, 1971.

[80] F. Hajdu, "Revised parameters of the analytic fits for coherent and incoherent scattered x-ray intensities of the first 36 atoms," *Acta Crystallogr.*, vol. A28, pp. 250–252, 1972.

[81] D. T. Cromer and J. T. Waber, "Scattering factors computed from relativistic Dirac-Slater wave functions," *Acta Crystallogr.*, vol. 18, pp. 104–109, 1965.

[82] A. Compton, "A quantum theory of the scattering of x-rays by light elements," *Phys. Rev.*, vol. 21, no. 5, pp. 483–502, 1923.

[83] P. Debeye, "Zerstreuung von Rontgenstrahlen," *Ann. Phys.*, vol. 46, pp. 809–823, 1915.

[84] T. Faber and J. Ziman, "A theory of the electrical properties of liquid metals," *Philos. Mag.*, vol. 11, pp. 153–173, 1965.

[85] M. Newville, "Fundamentals of XAFS," in *Consort. Adv. Radiat. Sources*, 2004.

[86] A. Rosa, J. Pohlenz, C. de Grouchy, B. Cochain, Y. Kono, S. Pasternak, O. Mathon, T. Irifune, and M. Wilke, "In-situ characterisation of liquid network structure at high pressure and temperature using XAS coupled with Paris-Edinburgh Press," *High Press. Res.*, vol. Online, pp. 1477–2299, 2016.

[87] L. Dubrovinsky, N. Dubrovinskaia, E. Bykova, M. Bykov, V. Prakapenka, C. Prescher, K. Glazyrin, H.-P. Liermann, M. Hanfland, M. Ekholm, Q. Feng, L. V. Pourovskii, M. I. Katsnelson, J. M. Wills, and I. A. Abrikosov, "The most incompressible metal osmium at static pressures above 750 gigapascals," *Nature*, vol. 525, pp. 226–229, 2015.

[88] R. Boehler and K. De Hantsetters, "New anvil designs in diamond-cells," *High Press. Res.*, vol. 24, 2004.

[89] J. Chaston, "The oxidation of the platinum metals," *Platin. Met. Rev.*, vol. 19, no. 4, pp. 135–140, 1975.

[90] G. Smolik, D. Petti, and S. Schuetz, "Oxidation and volatilization of molybdenum from TZM alloy in air," *J. Nucl. Mater.*, vol. 283-287, pp. 1458–1462, 2000.

[91] S. Klotz, J. Besson, G. Hamel, R. J. Nelmes, J. S. Loveday, and W. G. Marshall, "High pressure neutron diffraction using the Paris-Edinburgh cell: Experimental possibilities and future prospects," *High Press. Res.*, vol. 14, no. 4-6, pp. 249–255, 1996.

[92] Y. Kono, C. Park, C. Kenney-Benson, G. Shen, and Y. Wang, "Toward comprehensive studies of liquids at high pressures and high temperatures: Combined structure, elastic wave velocity, and viscosity measurements in the Paris-Edinburgh cell," *Phys. Earth Planet. Inter.*, vol. 228, pp. 269–280, 2014.

[93] A. Yamada, Y. Wang, T. Inoue, W. Yang, C. Park, T. Yu, and G. Shen, "High-pressure x-ray diffraction studies on the structure of liquid silicate using a Paris-Edinburgh type large volume press," *Rev. Sci. Instrum.*, vol. 82, p. 015103, 2011.

[94] M. van Kan Parker, C. Sanloup, E. J. Tronche, J.-P. Perrillat, M. Mezouar, N. Rai, and W. van Westrenen, "Calibration of a diamond capsule cell assembly for in situ determination of liquid properties in the ParisEdinburgh press," *High Press. Res.*, vol. 30, no. 2, pp. 332–341, 2010.

[95] R. A. Forman, G. J. Piermarini, J. D. Barnett, and S. Block, "Pressure measurement made by the utilization of ruby sharp-line luminescence," *Science*, vol. 176, no. 4032, pp. 284–285, 1972.

[96] H. Mao, J. Xu, and P. Bell, "Calibration of the ruby pressure gauge to 800 kbar under quasi-hydrostatic conditions," *J. Geophys. Res.*, vol. 91, no. B5, pp. 4673–4676, 1986.

[97] F. Datchi, a. Dewaele, P. Loubeyre, R. Letoullec, Y. Le Godec, and B. Canny, "Optical pressure sensors for high-pressurehigh-temperature studies in a diamond anvil cell," *High Press. Res.*, vol. 27, no. 4, pp. 447–463, 2007.

[98] Y. Fei, J. Li, K. Hirose, W. G. Minarik, J. a. Van Orman, C. Sanloup, W. van Westrenen, T. Komabayashi, and K.-i. Funakoshi, "A critical evaluation of pressure scales at high temperatures by in situ x-ray diffraction measurements," *Phys. Earth Planet. Inter.*, vol. 143-144, pp. 515–526, 2004.

[99] Y. Fei, A. Ricolleau, M. Frank, K. Mibe, G. Shen, and V. Prakapenka, "Toward an internally consistent pressure scale," *Proc. Natl. Acad. Sci.*, vol. 104, no. 22, pp. 9182–9186, 2007.

[100] F. Birch, "Finite strain isotherm and velocities for single-crystal and polycrystalline NaCl at high pressures and 300 K," *J. Geophys. Res.*, vol. 83, pp. 1257–1268, 1978.

[101] F. Birch, "Equation of state and thermodynamic parameters of NaCl to 300 kbar in the high-temperature domain," *J. Geophys. Res.*, vol. 91, no. B5, pp. 4949–4954, 1986.

[102] P. I. Dorogokupets and a. Dewaele, "Equations of state of MgO, Au, Pt, NaCl-B1, and NaCl-B2: Internally consistent high-temperature pressure scales," *High Press. Res.*, vol. 27, no. 4, pp. 431–446, 2007.

[103] A. F. Goncharov, J. C. Crowhurst, J. K. Dewhurst, S. Sharma, C. Sanloup, E. Gregoryanz, N. Guignot, and M. Mezouar, "Thermal equation of state of cubic boron nitride: Implications for a high-temperature pressure scale," *Phys. Rev. B*, vol. 75, p. 224114, 2007.

[104] A. Hammersley, "FIT2D: An introduction and overview," *ESRF Intern. Rep.*, vol. ESRF97HA02, 1997.

[105] C. Prescher and V. B. Prakapenka, "DIOPTAS: a program for reduction of two-dimensional x-ray diffraction data and data exploration," *High Press. Res.*, vol. 35, no. 3, pp. 223–230, 2015.

[106] J. Krogh-Moe, "A method for converting experimental x-ray intensities to an absolute scale," *Acta Crystallogr.*, vol. 9, pp. 951–953, 1956.

[107] N. Norman, "The Fourier transform method for normalizing intensities," *Acta Crystallogr.*, vol. 10, pp. 370–373, 1957.

[108] R. Hoseman and S. Bagchi, *Direct Analysis of Diffraction by Matter*. North Holland Publishing Company, 1962.

[109] A. Zeidler, J. W. E. Drewitt, P. S. Salmon, A. C. Barnes, W. a. Crichton, S. Klotz, H. E. Fischer, C. J. Benmore, S. Ramos, and A. C. Hannon, "Establishing the structure of GeS_2 at high pressures and temperatures: a combined approach using x-ray and neutron diffraction," *J. Phys. Condens. Matter*, vol. 21, p. 474217, 2009.

[110] J. Drewitt, C. Sanloup, A. Bytchkov, S. Brassamin, and L. Hennet, "Structure of $(Fe_xCa_{1-x}O)_y(SiO_2)_{1-y}$ liquids and glasses from high-energy x-ray diffraction: Implications for the structure of natural basaltic magmas," *Phys. Rev. B*, vol. 87, p. 224201, 2013.

[111] M. Newville, "IFEFFIT: interactive XAFS analysis and FEFF fitting," *J. Synchrotron Radiat.*, vol. 8, pp. 322–324, 2001.

[112] M. Louvel, C. Sanchez-Valle, W. J. Malfait, H. Cardon, D. Testemale, and J.-L. Hazemann, "Constraints on the mobilization of Zr in magmatic-hydrothermal processes in subduction zones from in situ fluid-melt partitioning experiments," *Am. Mineral.*, vol. 99, pp. 1616–1625, 2014.

[113] Y.-F. Zheng and J. Hermann, "Geochemistry of continental subduction-zone fluids," *Earth, Planets Sp.*, vol. 66, no. 1, p. 93, 2014.

[114] M. Louvel, C. Sanchez-valle, W. J. Malfait, D. Testemale, and J.-L. Hazemann, "Zr complexation in high pressure fluids and silicate melts and implications for the mobilization of HFSE in subduction zones," *Geochim. Cosmochim. Acta*, vol. 104, pp. 281–299, 2013.

[115] F. Farges and S. Rossano, "Water in Zr-bearing synthetic and natural glasses," *Eur. J. Mineral.*, vol. 12, pp. 1093–1107, 2000.

[116] F. Holtz, M. Pichavant, P. Barbey, and W. Johannes, "Effects of H_2O on liquidus phase relations in the haplogranite system at 2 and 5 kbar," *Am. Mineral.*, vol. 77, pp. 1223–1241, 1992.

[117] T. Sato and N. Funamori, "High-pressure in situ density measurement of low-Z noncrystalline materials with a diamond-anvil cell by an x-ray absorption method," *Rev. Sci. Instrum.*, vol. 79, p. 073906, jul 2008.

[118] C. Meade, R. J. Hemley, and H. K. Mao, "High-pressure x-ray diffraction of SiO_2 glass," *Phys. Rev. Lett.*, vol. 69, no. 9, pp. 1387–1391, 1992.

[119] A. J. Anderson, H. Yan, R. a. Mayanovic, G. Solferino, and C. J. Benmore, "High-energy x-ray diffraction of a hydrous silicate liquid under conditions of high pressure and temperature in a modified hydrothermal diamond anvil cell," *High Press. Res.*, vol. 34, no. 1, pp. 100–109, 2014.

[120] L. B. Skinner, C. J. Benmore, J. K. R. Weber, S. Tumber, L. Lazareva, J. Neuefeind, L. Santodonato, J. Du, and J. B. Parise, "Structure of molten $CaSiO_3$: neutron diffraction isotope substitution with aerodynamic levitation and molecular dynamics study," *J. Phys. Chem. B*, vol. 116, pp. 13439–13447, 2012.

[121] F. Angeli, O. Villain, S. Schuller, S. Ispas, and T. Charpentier, "Insight into sodium silicate glass structural organization by multinuclear NMR combined with first-principles calculations," *Geochim. Cosmochim. Acta*, vol. 75, no. 9, pp. 2453–2469, 2011.

[122] W. J. Malfait, R. Seifert, S. Petitgirard, J.-P. Perrillat, M. Mezouar, T. Ota, E. Nakamura, P. Lerch, and C. Sanchez-Valle, "Supervolcano eruptions driven by melt buoyancy in large silicic magma chambers," *Nat. Geosci.*, vol. 7, no. 12, pp. 122–125, 2014.

[123] V. Y. Chevychelov, R. E. Botcharnikov, and F. Holtz, "Experimental study of fluorine and chlorine contents in mica (biotite) and their partitioning

between mica, phonolite melt, and fluid," *Geochemistry Int.*, vol. 46, no. 11, pp. 1081–1089, 2008.

[124] T. A. Mather, "Volcanism and the atmosphere: the potential role of the atmosphere in unlocking the reactivity of volcanic emissions," *Philos. Trans. R. Soc.*, vol. 366, pp. 4581–4595, 2008.

[125] H. Balcone-Boissard, B. Villemant, and G. Boudon, "Behavior of halogens during the degassing of felsic magmas," *Geochemistry, Geophys. Geosystems*, vol. 11, no. 9, 2010.

[126] S.-M. Fan and D. Jacob, "Surface ozone depletion in Arctic spring sustained by bromine reactions on aerosols," *Nature*, vol. 359, pp. 522–524, 1992.

[127] H. Bureau, E. Foy, C. Raepsaet, A. Somogyi, P. Munsch, G. Simon, and S. Kubsky, "Bromine cycle in subduction zones through in situ Br monitoring in diamond anvil cells," *Geochim. Cosmochim. Acta*, vol. 74, pp. 3839–3850, 2010.

[128] T. Irifune and R. J. Hemley, "Synthetic diamond opens windows into the deep Earth," *EOS Trans. Am. Geophys. Union*, vol. 93, no. 7, pp. 65–66, 2012.

[129] B. Ravel and M. Newville, "ATHENA, ARTEMIS, HEPHAESTUS: Data analysis for x-ray absorption spectroscopy using IFEFFIT," *J. Synchrotron Radiat.*, vol. 12, pp. 537–541, 2005.

[130] J. Rehr, E. Stern, R. Martin, and E. Davidson, "Extended x-ray-absorption fine-structure amplitudes - Wave-function relaxation and chemical effects," *Phys. Rev. B*, vol. 17, no. 2, 1978.

[131] S. D. Kelly, S. R. Bare, N. Greenlay, G. Azevedo, M. Balasubramanian, D. Barton, S. Chattopadhyay, S. Fakra, B. Johannessen, M. Newville, J. Pena, G. S. Pokrovski, O. Proux, K. Priolkar, B. Ravel, and S. M. Webb, "Comparison of EXAFS foil spectra from around the world," *J. Phys. Conf. Ser.*, vol. 190, p. 012032, 2009.

[132] G. S. Pokrovski, B. R. Tagirov, J. Schott, E. F. Bazarkina, J. L. Hazemann, and O. Proux, "An in situ x-ray absorption spectroscopy study of gold-chloride complexing in hydrothermal fluids," *Chem. Geol.*, vol. 259, pp. 17–29, 2009.

[133] A. Michalowicz and G. Vlaic, "Multiple solutions in data fitting: a trap in EXAFS structural analysis and some ideas to avoid it," *J. Synchrotron Radiat.*, vol. 5, pp. 1317–20, 1998.

[134] H. Ott, "Die Strukturen von Mn O, Mn S, Ag F, Ni S, Sn I_4, $SrCl_2$, Ba F_2, Praezisionsmessungen einiger Alkalihalogenide," *Zeitschrift fuer Krist. Krist. Krist. Krist.*, vol. 63, 1926.

[135] S. Abrahams and J. Bernstein, "Remeasurement of optically active $NaClO_3$ and $NaBrO_3$," *Acta Crystallogr.*, vol. B33, pp. 3601–3604, 1977.

[136] N. Gregory, "The crystal structure of ferric bromide," *J. Am. Chem. Soc.*, vol. 73, p. 472, 1951.

[137] M. Ahtee, "Lattice constants of some binary alkali halide solid solutions.," *Ann. Acad. Sci. Fenn.*, vol. 313, pp. 1–11, 1969.

[138] V. Meisalo and O. Inkinen, "An x-ray diffraction analysis of potassium bromide," *Acta Crystallogr.*, vol. 22, pp. 58–65, 1967.

[139] M. Szafranski and K. Staahl, "Refinements of the crystal-structures and UV-absorption properties of $KBrO_3$, $RbBrO_3$ and $CsBrO_3$," *Zeitschrift fuer Krist.*, vol. 209, pp. 491–494, 1994.

[140] W. Levason, J. S. Ogden, M. D. Spicer, and N. A. Young, "Characterization of dibromine monoxide (Br_2O) by bromine K-edge EXAFS and IR spectroscopy," *J. Am. Chem. Soc.*, vol. 112, pp. 1019–1022, 1990.

[141] R. Ingalls, E. D. Crozier, J. E. Whitmore, A. J. Seary, and J. M. Tranquada, "Extended x-ray absorption fine structure of NaBr and Ge at high pressure," *J. Appl. Phys.*, vol. 51, pp. 3158–3163, 1980.

[142] B. S. Rao and S. P. Sanyal, "Structural and elastic properties of sodium halides at high pressure," *Phys. Rev. B*, vol. 42, no. 3, p. 1810, 1990.

[143] K. Waizumi, H. Masuda, and H. Ohtaki, "X-ray structural studies of $FeBr_2.4H_2O$, $CoBr_2.4H_2O$, $NiCl_2.4H_2O$ and $CuBr_2.4H_2O$. *cis/trans* Selectivity in transition metal (II) dihalide tetrahydrate," *Inorganica Chim. Acta*, vol. 192, pp. 173–181, 1992.

[144] Z. Ropka, R. Michalski, and R. Radwanski, "Electrical and magnetic properties of $FeBr_2$," *Phys. Rev. B*, vol. 63, p. 172404, 2001.

[145] J. Haberecht, H. Bormann, and R. Kniep, "Refinement of the crystal structure of iron dibromide, $FeBr_2$," *Zeitschrift für Krist. - New Cryst. Struct.*, vol. 216, p. 510, 2001.

[146] A. Michalowicz, K. Provost, S. Laruelle, A. Mimouni, and G. Vlaic, "F-test in EXAFS fitting of structural models," *J. Synchrotron Radiat.*, vol. 6, pp. 233–235, 1999.

[147] K. A. Evans, J. A. Mavrogenes, H. S. O'Neill, N. S. Keller, and L.-Y. Y. Jang, "A preliminary investigation of chlorine XANES in silicate glasses," *Geochemistry, Geophys. Geosystems*, vol. 9, no. 10, 2008.

[148] M. Louvel, *Trace elements in subduction zone fluids: Speciation , partitioning and the geochemical cycle of halogens and HFSE.* PhD thesis, 2011.

[149] H. Bureau and N. Métrich, "An experimental study bromine behaviour in water–saturated silicic melts," *Geochim. Cosmochim. Acta*, vol. 67, pp. 1689–1697, 2003.

[150] M. Bonnet, A. Delapalme, H. Fuess, and M. Thomas, "Refinement of the structure of yttrium iron garnet (YIG). A case of severe extinction and absorption," *Acta Crystallogr.*, vol. B31, pp. 2233–2240, 1975.

[151] M. Faucher and J. Pannetier, "Refinement of the Y_2O_3 structure at 77 K," *Acta Crystallogr.*, vol. B36, pp. 3209–3211, 1980.

[152] A. Emiraliev, A. G. Kocharov, R. V. Bakradze, I. Karimov, and Z. I. Akhmedzhanov, "Neutron diffraction refinement of the coordinates of oxygen atoms in yttrium-aluminum garnet," *Kristallografiya*, vol. 21, pp. 211–213, 1976.

[153] M. Winterer, R. Nitsche, and H. Hahn, "Local structure in nanocrystalline ZrO_2 and Y_2O_3 by EXAFS," *NanoStructural Mater.*, vol. 9, pp. 397–400, 1997.

[154] I. Jonane, K. Lazdins, J. Timoshenko, A. Kuzmin, J. Purans, P. Vladimirov, T. Graning, and J. Hoffmann, "Temperature-dependent EXAFS study of the local structure and lattice dynamics in cubic Y_2O_3," *J. Synchrotron Radiat.*, vol. 23, pp. 510–518, 2016.

[155] A. Longo, F. Giannici, A. Balerna, C. Ingrao, F. Deganello, and A. Martorana, "Local environment of yttrium in Y-doped barium cerate compounds," *Chem. Mater.*, vol. 18, no. 24, pp. 5782–5788, 2006.

[156] Y.-N. Xu, Z.-q. Gu, and W. Y. Ching, "Electronic, structural, and optical properties of crystalline yttria," *Phys. Rev. B*, vol. 56, no. 23, pp. 14993–15000, 1997.

[157] M. Paton and E. Malsen, "A refinement of the crystal structure of yttria," *Acta Crystallogr.*, vol. 19, p. 307, 1965.

[158] Z. Pan, W. Li, Y. Xu, Q. Hu, and Y. Zheng, "Structure and redshift of Ce^{3+} emission in anisotropically expanded garnet phosphor $MgY_2Al_4SiO_{12}$:Ce^{3+}," *RSC Adv.*, vol. 6, pp. 20458–20466, 2016.

[159] F. Farges, "Does Zr-F "complexation" occur in magmas?," *Chem. Geol.*, vol. 127, pp. 253–268, 1996.

[160] G. Mountjoy, D. M. Pickup, R. Anderson, G. W. Wallidge, M. A. Holland, R. J. Newport, and M. E. Smith, "Changes in the Zr environment in zirconia-silica xerogels with composition and heat treatment as revealed by ZrK-edge XANES and EXAFS," *Phys. Chem. Chem. Phys.*, vol. 2, pp. 2455–2460, 2000.

[161] J. Li, S. Meng, J. Han, and X. Zhang, "Valence electron structure and properties of the ZrO_2," *Sci. China, Ser. E Technol. Sci.*, vol. 51, no. 11, pp. 1858–1866, 2008.

[162] K. Robinson, G. V. Gibbs, and P. H. Ribbe, "The structure of zircon: A comparison with garnet," *Am. Mineral.*, vol. 56, pp. 782–790, 1971.

[163] D. K. Smith and H. W. Newkirk, "The crystal structure of baddeleyite (monoclinic ZrO_2) and its relation to the polymorphism of ZrO_2," *Acta Crystallogr.*, vol. 18, pp. 983–991, 1965.

[164] P. Li, I.-W. Chen, and J. E. Penner-Hahn, "X-ray-absorption studies of zirconia polymorphs. I. Characteristic local structures," *Phys. Rev. B*, vol. 48, no. 14, pp. 10063–10073, 1993.

[165] B. Mysen, "Water-melt interaction in hydrous magmatic systems at high temperature and pressure," *Prog. Earth Planet. Sci.*, vol. 1, no. 4, pp. 1–18, 2014.

[166] D. B. Dingwell, "The glass transition in hydrous granitic melts," *Phys. Earth Planet. Inter.*, vol. 107, pp. 1–8, 1998.

[167] S. Iftekhar, B. Pahari, K. Okhotnikov, A. Jaworski, B. Stevensson, J. Grins, and M. Edén, "Properties and structures of RE_2O_3-Al_2O_3-SiO_2 (RE=Y, Lu) glasses probed by molecular dynamics simulations and solid-state NMR : The roles of aluminium and rare-Earth ions for dictating the microhardness," *J. Phys. Chem. C*, vol. 116, no. 34, pp. 18394–18406, 2012.

[168] C. Crépisson, G. Morard, H. Bureau, G. Prouteau, Y. Morizet, S. Petitgirard, and C. Sanloup, "Magmas trapped at the continental lithosphereasthenosphere boundary," *Earth Planet. Sci. Lett.*, vol. 393, pp. 105–112, 2014.

[169] L. Cormier, D. R. Neuville, and G. Calas, "Structure and properties of low-silica calcium aluminosilicate glasses," *J. Non. Cryst. Solids*, vol. 274, pp. 110–114, 2000.

[170] R. N. Mead and G. Mountjoy, "A molecular dynamics study of densification mechanisms in calcium silicate glasses $CaSi_2O_5$ and $CaSiO_3$ at pressures of 5 and 10 GPa," *J. Chem. Phys.*, vol. 125, p. 154501, 2006.

[171] J. W. E. Drewitt, S. Jahn, V. Cristiglio, A. Bytchkov, M. Leydier, S. Brassamin, H. E. Fischer, and L. Hennet, "The structure of liquid calcium aluminates as investigated by neutron and high energy x-ray diffraction in combination with molecular dynamics simulation methods," *J. Phys. Condens. Matter*, vol. 23, p. 155101, 2011.

[172] M. C. Eckersley, P. H. Gaskell, a. C. Barnes, and P. Chieux, "Structural ordering in a calcium silicate glass," *Nature*, vol. 335, pp. 525–527, 1988.

[173] G. Chiari, "On metal-oxygen moordination. A statistical method to determine coordination number. I. Calcium," *Acta Crystallogr.*, vol. B46, pp. 717–723, 1990.

[174] Y. Wang, T. Sakamaki, L. B. Skinner, Z. Jing, T. Yu, Y. Kono, C. Park, G. Shen, M. L. Rivers, and S. R. Sutton, "Atomistic insight into viscosity and density of silicate melts under pressure.," *Nat. Commun.*, vol. 5, p. 3241, 2014.

[175] R. D. Shannon, "Revised effective ionic radii and systematic studies of interatomic distances in halides and chalcogenides," *Acta Crystallogr.*, vol. A32, pp. 751–767, 1976.

[176] H. Uhlig, M. J. Hoffmann, P. Lamparter, and S. Steeb, "Atomic structure of rare Earth Si-Al-O-N glasses," *Zeitschrift für Naturforsch.*, vol. 53a, pp. 259–264, 1998.

[177] P. Beattie, "On the occurrence of apparent non-Henry's Law behaviour in experimental partitioning studies," *Geochim. Cosmochim. Acta*, vol. 57, no. 1, pp. 47–55, 1993.

[178] S. Prowatke and S. Klemme, "Rare earth element partitioning between titanite and silicate melts: Henry's law revisited," *Geochim. Cosmochim. Acta*, vol. 70, pp. 4997–5012, 2006.

[179] B. Mysen, D. Virgo, W. Harrison, and C. Scarfe, "Solubility mechanisms of H_2O in silicate melts at high pressures and temperatures: a Raman spectroscopic study," *Am. Mineral.*, vol. 65, pp. 900–914, 1980.

[180] J. Blundy, T. Falloon, B. Wood, and J. Dalton, "Sodium partitioning between clinopyroxene and silicate melts," *Journal of Geophys. Research*, vol. 100, pp. 501–515, 1995.

[181] W. van Westrenen, N. Allan, J. Blundy, J. Purton, and B. J. Wood, "Atomistic simulation of trace element incorporation into garnets comparison with experimental garnet-melt partitioning data," *Geochim. Cosmochim. Acta*, vol. 64, no. 9, pp. 1629–1639, 2000.

[182] G. Shen, H. Mao, and R. J. Hemley, "Laser-heated diamond anvil cell technique: Double-sided heating with multimode Nd:YAG laser," *Adv. Mater. '96 – New Trends in High Pressure Research*, pp. 149–152, 1996.

[183] A. B. Corradi, V. Cannillo, M. Montorsi, C. Siligardi, and A. N. Cormack, "Structural characterization of neodymium containing glasses by molecular dynamics simulation," *J. Non. Cryst. Solids*, vol. 351, pp. 1185–1191, 2005.

[184] M. Karabulut, G. Marasinghe, E. Metwalli, a. Wittenauer, R. Brow, C. Booth, and D. Shuh, "Neodymium and erbium coordination environments in phosphate glasses," *Phys. Rev. B*, vol. 65, pp. 1–7, 2002.

[185] N. De Koker, "Structure, thermodynamics, and diffusion in $CaAl_2Si_2O_8$ liquid from first-principles molecular dynamics," *Geochim. Cosmochim. Acta*, vol. 74, pp. 5657–5671, 2010.

[186] S. Zhai and E. Ito, "Recent advances of high-pressure generation in a multianvil apparatus using sintered diamond anvils," *Geosci. Front.*, vol. 2, no. 1, pp. 101–106, 2011.

Publications

B. Cochain, C. Sanloup, C. de Grouchy, C. Crépisson, H. Bureau, C. Leroy, I. Kantor, and T. Irifune. Bromine speciation in hydrous silicate melts at high pressure. *Chemical Geology*, 404, 18-26 (2015).

C. de Grouchy, C. Sanloup, B. Cochain, J. Drewitt, Y. Kono and C. Crépisson. Lutetium incorporation in magmas at depth: Implications for partitioning and geochemical tracing. *Submitted to Earth and Planetary Science Letters June 2016.*